Detection and Characterisation of Micro- and Nano-plastics in Water using Optical Spectroscopy

Syed Atif Iqrar

Doctor of Philosophy

Aston University

March 2025

S.A. Iqrar, PhD Thesis, Aston University, 2025.

ABSTRACT

Detection and Characterisation of Micro- and Nano-plastics in Water using Optical Spectroscopy

Syed Atif Iqrar
Doctor of Philosophy
2025

Micro- and nanoplastic (MNP) contamination in various environmental matrices has become an increasing global concern due to its potential ecological and health impacts. However, detecting and characterising these minuscule plastic particles remains challenging due to the limitations of conventional spectroscopic techniques. This thesis explores the potential of photoluminescence (PL) spectroscopy as an alternative technique for detecting and characterising MNPs in aqueous media. The research encompasses the optimisation of fluorescence excitation-emission (FLE) features for MNP detection, the development of a protocol for generating model MNPs, and the proof-of-concept demonstration of a semi-portable PL spectrometer for microplastic detection.

In the first set of experiments, Fluorescence (FL) spectroscopy was utilised to investigate the intrinsic excitation-emission features of common microplastics, including polystyrene (PS), polyethylene terephthalate (PET), and polypropylene (PP). Through systematic analysis, distinct fluorescence signatures were identified for each polymer type, enabling precise and label-free identification. These spectral characteristics, linked to polymer-specific molecular transitions, form the basis for a non-destructive fluorescence-based microplastic detection method.

The second set of experiments established a protocol for generating model MNPs through a high-power direct ultra-sonication technique. This method significantly improved the efficiency of MNP production compared to conventional methods, eliminating the need for chemical additives and achieving high suspension stability in an aqueous medium. The generated MNPs, ranging from 100 nm to 150 µm, closely resembled environmental plastic pollutants in terms of size distribution and morphology. Their characterisation using Raman spectroscopy, infrared spectroscopy combined with machine learning, UV-Vis spectroscopy, and SEM imaging confirmed their suitability as reference materials for microplastic research.

Furthermore, the third phase of the study examined the effectiveness of FLE mapping for detecting and characterising MNPs in aqueous media. The study demonstrated that ultrasonicated MNPs, including PS, PET, and PP exhibited strong and distinct FL spectra, including those smaller than 100nm. This study confirmed that optimised excitation wavelengths provide distinct FL fingerprints for MNPs and enhance their FL signal strength, improving the technique's sensitivity for real-time detection.

Finally, the development of a semi-portable PL spectrometer further highlighted the feasibility of real-time, on-site MNP detection. Although challenges such as background noise require further optimisation, this proof-of-concept system represents a significant step toward field-deployable MNP pollution monitoring.

Keywords: micro- and nanoplastics, photoluminescence spectroscopy, ultrasonication, semi-portable spectrometer, microplastic detection, intrinsic fluorescence, machine learning.

ACKNOWLEDGMENTS

In the name of Allah, the Most Gracious, the Most Merciful. All praise is due to Him, who blessed me with good health, guided my efforts, and granted me the strength and perseverance to complete this work.

I extend my deepest gratitude and appreciation to the many individuals and institutions that have been crucial in completing this doctoral thesis.

First and foremost, I would like to express my sincere gratitude to my advisors, Alex Rozhin and Daniel Hill, for their unwavering support, invaluable guidance, and continuous encouragement throughout this research journey. Their expertise, insightful feedback, and dedication to my academic growth have been instrumental in shaping the direction of this work.

Secondly, I am extremely grateful to Raghavan Chinnambedu Murugesan, one of the best mentors I have found in my research career, for his continuous support and encouragement, constructive feedback on research ideas, and scholarly insights to ensure the quality of this research. His collective expertise has enriched the depth and breadth of my work.

I appreciate the Aston Institute of Photonic Technologies (AIPT) for providing a conducive research environment and access to resources essential for the successful completion of this thesis. I am also thankful to Professor Heidi Ottevaere from Vrije Universiteit Brussel for giving me the opportunity to work at Photonics Centre VUB during my secondment.

Special thanks go to my colleagues and fellow researchers, Aisha Bibi, Jordi Valls, and Mehrdad Lotfi Chobari, who have provided valuable discussions, shared their expertise, and provided an opportunity for excellent collaborative research work.

Above all, I owe my deepest gratitude to my wife, Fasiha Syed, whose unwavering support, patience, and sacrifices have been a cornerstone of this journey. Her belief in me, even in the most challenging times, has been a constant source of strength and motivation. I am also deeply thankful to my family back home in Pakistan for their prayers, encouragement, and emotional support throughout this journey.

Lastly, I sincerely thank the European Union for their invaluable support and funding (Horizon 2020 Marie Curie project – MONPLAS Grant number: 860775) throughout my research at Aston University. This project has provided financial assistance and a platform for collaboration, fostering a rich and dynamic academic environment. I am grateful for the chance to be part of a program that champions excellence in research and facilitates international collaboration. I am deeply thankful for the opportunities it has provided to advance my knowledge and pursue academic excellence.

DEDICATION

This thesis is dedicated to the memory of my beloved mother, Balqees Fatima, whose unwavering love, guidance, and strength continue to inspire me. Though she is no longer with us, her spirit lives on in the resilience and determination she instilled in me.

Mom, your sacrifices and encouragement have been the driving force behind my academic journey. This achievement is a tribute to your enduring influence and the lessons of perseverance you imparted. Your memory will forever be a source of inspiration, and I dedicate this work to the woman whose love shaped the person I am today.

I would also like to express my deepest gratitude to my father, Syed Iqrar Hussain, whose continued support has always encouraged me to pursue my goals with dedication.

LIST OF CONTENTS

List of abbreviations

μFTIR – Fourier-Transform Infrared Microscopy

μm – Micrometre/Micron

μRaman – Raman Microscopy

2D – Two Dimensional

3D – Three Dimensional

ATR – Attenuated Total Reflection

AU – Aston University

CARS – Coherent Anti-stokes Raman Spectroscopy

CCD – Charge Coupled Device

CFC – Continuous-Flow Ultracentrifugation

CFU – Cross-Flow Ultrafiltration

CPR – Continuous Plankton Recorders

DDT – Dichloro Diphenyl Tri-chloroethane

DI – Deionised

DOM – Dissolved Organic Matter

DR – Dimensional Reduction

DSC – Differential Scanning Calorimetry

EEM – Excitation-Emission Mapping

FBCI – Fast Background Correction and Identification

FC – Flow Cytometry

FL – Fluorescence

FLE – Flourescence Excitation Emission

FPA – Focal Plane Array

FTIR – Fourier-Transform Infrared

He-Cd – Helium and Cadmium

HDPE – High-Density Polyethylene

HRS – Handheld Raman Spectrometer

LCD – Liquid Crystal Display

LDPE – Low-Density Polyethylene

ML – Machine Learning

MMT – Metric Million Tonnes

MNPs – Micro and Nano plastic

MOCNESS – Multiple Opening and Closing Nets and Environmental Sampling System

MP – Microplastic

MPSS – Microplastic Sediment Separator

MW – Molecular Weight

NA – Numerical Aperture

NPs – Nanoplastics

OM – Optical Microscopy

PA – Poly-Amide

PAHs – Polycyclic Aromatic Hydrocarbons

PARAFAC – Parallel Factor Analysis

PBDEs – Poly-Brominated Diphenyl Ethers

PCA – Principal Component Analysis

PCBs – Polychlorinated Biphenyls

PCMF – Polycarbonate Membrane Filter

PCV-U – Unplasticised Polyvinyl Chloride

PBI – Perylene-Bisimide

PE – Polyethylene

PES – Polyester

PET – Polyethylene terephthalate

PFAS – Poly-Fluoroalkyl Substances

PL – PhotoLuminescence

PMMA – Poly(Methyl Methacrylate)

PMPs – Primary Microplastics

PMT – Photomultiplier Tube

POPs – Persistent Organic Pollutants

POSS – Polyhedral Oligomeric Silsesquioxane

PP – Poly (Propylene)

PPMA – Polypropylene Maleic Anahydride

ps – Picosecond

PS – Polystyrene

PS-NPs – Polystyrene Nanoplastics

PVC – Polyvinyl Chloride

Pyr-GC-MS – Pyrolysis Gas Chromatography-Mass Spectrometry

QCL – Quantum Cascade Laser

RDF – Random Decision Forests

RF – Random Forest

SDCM – Signal Dissection by Correlation Maximisation

SED – Secondary Diffraction Mode

SEM – Scanning Electron Microscopy

SERS – Surface Enhanced Raman Spectroscopy

SMA – Sub-Miniature Version A

SML – Surface Microlayer

SPPL – Semi-Portable Photoluminescence

SMPs – Secondary Microplastics

SPA – Solid-Phase Absorbers

TECS – Technology Enhance Clad Silica

TEM – Transmission Electron Microscopy

TGA – Thermogravimetry Analysis

PMPs – Primary Microplastics

TGA-DSC – Thermogravimetric Analysis with Differential Scanning Calorimetry

TGA-MS – Thermogravimetric Analysis with Mass Spectrometry

TGA-TDU-GC-MS – Thermogravimetric Analysis with Thermal Decomposition Unit, Gas Chromatography, and Mass Spectrometry

TRPL – Time-Resolved Photoluminescence Spectroscopy

US – Ultrasonicated

USB – Universal Serial Bus

US-MNP – Ultrasonicated Micro-and Nanoplastics

UV – Ultraviolet

UV-vis – Ultraviolet and Visible

UV-vis-NIR – Ultraviolet, visible, and Near-Infrared

WTA – Winner-Takes-All

XPS – X-Ray Photoelectron Spectroscopy

List of symbols

λ_{ex}	Excitation wavelength (nm)
λ_{em}	Emission wavelength (nm)
υ_0	Initial frequency (Hz)
υ_{vib}	vibrational frequency (Hz)
λ_{in}	Incident Light wavelength (nm)
$\delta\lambda$	Scan Interval (nm)
M	Molar
$\Delta\lambda_{ex}$	Step size of excitation wavelength (nm)
$\Delta\lambda_{em}$	Step size of emission wavelength (nm)
$\upsilon_0 - \upsilon_{vib}$	Stokes Raman Scattering
$\upsilon_0 + \upsilon_{vib}$	Antistokes Raman Scattering
S_0	Low energy state (Ground state)
S_1	First excited singlet electronic state
S_2	Second excited singlet electronic state
T_1	Excited triplet state
T_n	Lowest triplet state
θ_f	Angle at which FL emissions are recorded
P_{max}	Maximum output power of ultrasound sonotrode
$\bar{x}$	Mean size of ultrasonicated microplastics
σ	Standard deviation of USMP particles
γ	Skewness of distribution curve

List of Figures

List of Tables

List of Publications

Journal Publications:

1. S.A. Iqrar, A. Bibi, R.C. Murugesan, D.Hill, A. Rozhin “Excitation–Emission Fluorescence Mapping Analysis of Microplastics That Are Typically Pollutants” Published in Photochem, 2024. 4(4): page 488-500 [1].
2. S.A. Iqrar, J.V. Conesa, M.L. Choobbari, C.M. Raghavan, P.M. Lutsyk, Stephen Luttjohann, H. Ottevaere, A.G. Rozhin “Efficient generation of suspensible secondary reference micro/nano plastic through high power direct ultrasound treatment”, in preparation.
3. S.A.Iqrar, R.C. Murugesan, A. Rozhin “Fluorescence Excitaion-Emission mapping analysis of secondary ultra-sonicated microplastics in water”, in preparation.

Conference Publications:

1. S.A.Iqrar, A. Bibi, R.C. Murugesan, D.Hill, A. Rozhin “Exploring the potential of photoluminescence spectroscopy for the detection of microplastics” Micro 2022 International Conference, Aalborg, Denmark.
2. S.A.Iqrar, R.C. Murugesan, D.Hill, A. Rozhin “Fluorescence mapping analysis of ultrasonicated microplastics” 18th International Conference on chemistry and the environment, 2022, Venice, Italy.

Chapter 1: Introduction and Background

Plastic pollution is one of the most crucial environmental challenges on a global scale. Since 1950, a substantial amount of plastic waste has entered the environment, where its degradation resulted in the formation of smaller plastic particles down to the micro- and nanoscale [2]. These particles are classified as micro- and nanoplastics (MNPs). Microplastics (MPs) are defined as particles with a diameter smaller than 5 mm [3], while nanoplastics (NPs) have diameters ranging from 1 to 100 nm or 1000 nm [4]. The definition of nanoplastics remains a topic of debate, with some researchers setting the upper size limit at 1000 nm [5-7], while others define it as 100 nm [8-10]. These minuscule plastic fragments, often invisible to the naked eye, have become widespread, raising serious environmental and health concerns [11]. They have penetrated terrestrial and aquatic ecosystems, from the highest mountain peaks to the depths of ocean channels [12]. Of particular concern in recent years are nanoplastics, which, due to their nanoscale size, are exceptionally difficult to detect and manage [13]. These particles present a serious environmental threat due to their potential to disrupt ecosystems and pose risks to human health [14].

The detection and quantification of these MNPs is not straightforward, given their minuscule size, irregular morphology, diversity of materials, adsorption of toxic chemicals, and the complexity of environmental matrices [15]. Many techniques, including microscopy, spectroscopy, chemical analysis, and a combination of these, have been employed to detect and identify these MNP particles [16]. Yet, challenges persist, as detecting MNPs in different environmental samples, i.e., water, soil, air, biota, and food, requires sophisticated equipment and specialised training. Moreover, standardising detection procedures and classifying MNPs based on size, shape, and polymer composition remains challenging [17].

1.1 Aim and Objectives

This thesis aims to investigate the potential of fluorescence (FL) spectroscopy as an emerging analytical method for detecting and identifying MNPs in the water. This aim will be achieved through the following objectives:

1. Investigation of intrinsic fluorescence emissions from microplastics (> 500 μm) in water under multiprobe excitation wavelengths. This will involve using a novel two-dimensional (2D) fluorescence excitation-emission (FLE) mapping method aimed at exploring the detection and identification capabilities of fluorescence spectroscopy for commonly encountered microplastics such as polystyrene (PS), polyethene terephthalate (PET), and polypropylene (PP). Additionally, the study will analyse the observed optical features, providing insights into their fluorescence characteristics. The findings are expected to contribute to the advancement of fluorescence spectroscopy as a reliable method for environmental monitoring and pollution control of microplastics in water.
2. Development of a laboratory-scale method for generating reference MNPs to facilitate real-time environmental micro- and nanoplastic studies. This objective addresses the challenges associated with obtaining secondary environmental MNPs, which are often labour-intensive and time-consuming. The proposed method will enable the simple and rapid production of reference MNPs using a direct ultrasonication technique, including polystyrene (PS), polymethyl methacrylate (PMMA), polypropylene (PP), and polyvinyl chloride (PVC). These reference materials will serve as controlled samples for validating spectroscopic methods as detection and identification tools, ultimately contributing to the advancement of analytical techniques for environmental microplastic monitoring.
3. Investigating the detection capability of fluorescence spectroscopy for micro- and nanoplastics (MNPs) in water. This objective aims to evaluate the effectiveness of FL spectroscopy in determining the detection limits for micro- and nanoplastics. The study

will involve recording fluorescence excitation-emission (FLE) maps for ultrasonically produced MNPs, including polystyrene (PS), polypropylene (PP), and polyethylene terephthalate (PET), to identify their distinct fluorescence emission characteristics. These findings will enhance the chemical characterisation and identification of MNPs in water, reinforcing the role of fluorescence spectroscopy as a reliable tool for environmental microplastic detection.

4. Development of a photoluminescence (PL)-based semi-portable analytical platform for the rapid and label-free detection of microplastics in water. The initial phase will validate pre-determined optimal excitation wavelengths to achieve strong fluorescence emissions from three microplastic types with diameters of ≥ 500 μm. These optimised excitation wavelengths will guide the design requirements for a semi-portable PL spectrometer. The subsequent phase will focus on the design and construction of the semi-portable PL spectrometer, including the establishment of measurement protocols for microplastic analysis. This development supports the aim of advancing fluorescence spectroscopy as a practical and efficient tool for detecting and identifying microplastics in environmental water samples.

1.2 Thesis Structure

The structure of this thesis comprises six chapters, outlined as follows:

Chapter 1: introduces micro- and nanoplastics, covering their origins, fate, impact, and prevalence across various environmental matrices. It also provides a detailed overview of the preliminary steps involved in MNP analysis, including sampling methods and sample preparation techniques. Additionally, it presents a comprehensive review of state-of-the-art methods for analysing MNPs. Finally, a literature review on fluorescence spectroscopy for microplastic detection and identification is also covered.

Chapter 2: explores the intrinsic fluorescence emissions of microplastics larger than 500 μm when subjected to multiprobe excitation wavelengths. It introduces a novel approach using two-dimensional (2D) fluorescence excitation-emission (FLE) mapping to detect and identify commonly found microplastics, including polystyrene (PS), polyethylene terephthalate (PET), and polypropylene (PP). By analysing the fluorescence characteristics of these microplastics, the study aims to enhance the application of fluorescence spectroscopy for environmental monitoring and pollution assessment.

Chapter 3: outlines the development of a laboratory-scale method for generating reference MNPs, which are essential for studying real-time environmental microplastics. The acquisition of secondary environmental microplastics is known to be challenging, labour-intensive, and time-consuming. Therefore, the chapter focuses on introducing a simple and rapid production of reference MNPs (PS, PP, PMMA, PVC) using a direct ultrasonication technique.

Chapter 4: presents FLE mapping analysis for ultrasonicated micro- and nanoplastics (US-MNPs) in water. Building on the findings from Chapter 3, where a laboratory-scale ultrasonication technique was used to generate reference MNPs, this chapter investigates their fluorescence properties to evaluate the detection capabilities of fluorescence spectroscopy. FLE maps were recorded for ultrasonically produced polystyrene (PS), polypropylene (PP), and polyethylene terephthalate (PET) to identify their distinct fluorescence signatures and establish the detection limits of this method. The findings contribute to advancing fluorescence spectroscopy as a reliable tool for microplastic identification, offering an alternative to traditional spectroscopic methods while addressing their inherent limitations.

Chapter 5: focuses on developing a photoluminescence (PL)-based semi-portable analytical platform designed for rapid and label-free micro- and nanoplastics (MNP) detection. Initial developments focused on using optimal excitation wavelengths for strong fluorescence emissions from three different types of microplastics with diameters ≥ 500 μm, as reported in Chapter 2. Subsequently, the recorded optimal excitation wavelengths were utilised to establish the system

design requirements of a portable PL spectrometer. Finally, this chapter details the complete design and construction of the semi-portable PL spectrometer, including measurement protocols for MNPs.

Chapter 6: presents an overall conclusion of the thesis.

1.3 Microplastics: Origin, Fate, and Impacts

Plastic pollution stands as one of the paramount environmental challenges of our era, stemming from the annual influx of over 8-16 million metric tonnes (MMT) into the oceans [18]. This issue arises from inadequate management of synthetic plastic produced, ranging from 1.5 to 299 MMT between 1950 and 2013, and the anticipated cumulative production is expected to soar to 34 billion metric tonnes by 2050 [19]. As shown in Figure 1.1, a significant rise in plastic production has been noticed since 2004. The surge in plastic production from 225 MMT in 2004 escalated to 367 MMT by 2020 [20]. After plastic enters the environment, it undergoes rigorous weathering conditions, hydrolysis, photo-oxidation by ultraviolet (UV) radiations from sunlight, and mechanical breakage caused by sand abrasion or water turbulence [21].

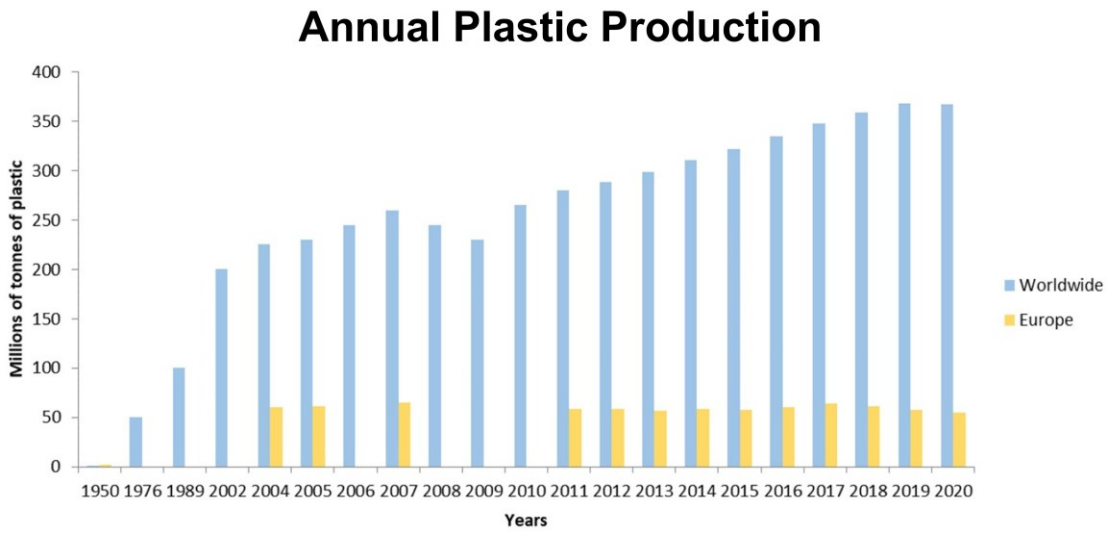

Figure 1.1 shows the different categories of plastic waste generated globally from 1950 to 2020. The blue lines represent global plastic production, while the yellow bars indicate European production in metric million tonnes (MMT) [22].

The environmental MPs have been categorised into two main types, primary and secondary microplastics. Primary microplastics (PMPs) are tiny plastic particles that are intentionally manufactured to be small in size, typically with dimensions less than 5 millimetres [23]. These microplastics are produced for various purposes, i.e., cosmetics and personal care products [24], textiles [25], and industrial abrasives [26]. The intentional production of primary microplastics contributes to their direct release into the environment. Their small size makes them particularly challenging to manage and can lead to ecological and environmental concerns as they may be ingested by marine organisms, affecting the food chain and ecosystem health. On the contrary, secondary microplastics (SMPs) refer to small plastic particles that result from the breakdown or fragmentation of larger plastic items. SMPs can be shaped into various forms, including microbeads, microfibers, thin films, and smaller plastic fragments [27]. As shown in Figure 1.2, SMPs are the dominant contributors to microplastic pollution. These include synthetic textiles (35%), tyre wear (28%), and city dust (24%), which together account for the majority of emissions [28]. In contrast, PMPs contribute a much smaller fraction, including road markings (7%), marine coatings (3.7%), personal care products (2%), and plastic pellets (0.3%) [28]. The origin of these plastics highlights the need for improved waste management, sustainable material alternatives, and pollution control measures to mitigate their environmental impact. Additionally, these particles pose environmental concerns as they can be ingested by marine organisms, potentially entering the food chain and affecting ecosystem health.

MNPs have been found in various environmental matrices, indicating their pervasive presence across different ecosystems. The common environmental matrices where microplastics have been detected include water bodies (surface water and oceans) [29], soil [30], air [31], sediments [32], biota (plants and animals) [33], food and beverages [34], drinking water [35], and recently human blood [36] and clouds [37]. The widespread distribution of microplastics across different environmental matrices raises concerns about their potential impact on ecosystems, human

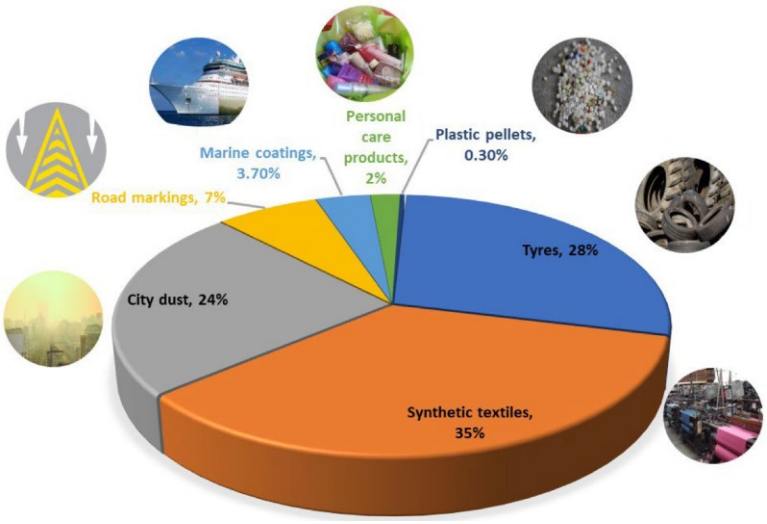

Figure 1.2: The proportional distribution of primary and secondary microplastic sources. City dust, tyre wear, and the synthetic industry contribute significantly to the majority of microplastic pollution [28].

health, and the overall health of the planet [14]. The toxicity and environmental effects of microplastics are primarily influenced by their physiochemical properties, such as size, shape, surface chemistry, density, colour, and bioavailability. The toxicity of MNPs is size-dependent, as smaller particles have higher toxicity due to factors like increased surface area, persistent retention times, and the potential for the accumulation of pollutants [38-40]. The shape of the MNPs also has an impact on ingestion, depending on how long they stay in the body after consumption [41]. For instance, Daphnia magna quickly ingests polyethylene particles with both regular and irregular shapes. However, the irregularly shaped microplastic particles had longer gut clearance compared to regular particles [42]. The presence of MNP particles at different levels in water bodies is greatly influenced by the density that projects their distribution and destination, which further leads to their distribution in different habitats and biota [43-45]. The colour of MNPs is another feature that can mislead visual predators and disrupt their foraging behaviour, depending on their ingestion preferences. Research shows that the MPs resembling the prey were more likely to be consumed, i.e., blue microplastic particles were consumed because they were confused with blue copepods [46]. Furthermore, based on the polarity and affinity of different

functional groups of MPs, various toxic contaminants can be adsorbed on their surface, such as persistent organic pollutants (POPs), polychlorinated biphenyls (PCBs), heavy metals, polycyclic aromatic hydrocarbons (PAHs), dichlorodiphenyltrichloroethane (DDT), polybrominated diphenyl ethers (PBDEs), and other contaminants such as poly-fluoroalkyl substances (PFAS) [47].

The identification and characterisation of MNP are of utmost significance owing to their potential toxicity and substantial environmental impact. The MNP detection process necessitates a systematic approach that starts with meticulous sampling methodologies. After sampling, the subsequent phases involve diverse pre-treatments and sample preparations, which are integral to ensuring the accuracy and reliability of the identification process [48]. The forthcoming sections will elaborate on these crucial steps, specifically delving into the latest techniques employed and addressing the challenges inherent in the processes.

1.4 Sampling Processes

Sampling stands as the primary and crucial stage in achieving precise characterisation of MNP. However, it is quite challenging due to the varied physicochemical properties of MNPs and the intricate composition of environmental matrices. The selection of an appropriate sampling method primarily relies on the type of matrix, i.e., water, soil, snow, sediments, organisms, and air, and the physicochemical attributes of MNP, encompassing factors like size, shape, surface chemistry, density, and polarity. Sampling MNP in environmental waters involves different techniques that consider the hydrological conditions, such as currents, wind, and water density, that change the distribution of MNP in water [49]. To this end, different sampling methods have been developed for sampling MNPs from river water [50], seawater [51], lakes [52], ponds [53], and wastewater [54].

The sampling of MNP from water bodies has been mainly classified into two categories: (a) net sampling and (b) bulk sampling methods. The net sampling method involves using different nets with varying mesh sizes from 1-500 μm. This technique can only sample MP and cannot capture

NP because the mesh size manufacturing limit is 1µm [55]. Additionally, the heterogeneous distribution of MP in water bodies necessitates the collection of large volumes, typically ranging from 100 L to several cubic meters, to obtain a more representative sample [56]. This method enables the collection of MP from marine and river matrices [57]. Figure 1.3 shows all devices that are used for net, bulk, and other sampling techniques. The most common devices for net sampling are Manta, Neuston, Bongo, and MOCNESS nets. The Manta and Neutson are mainly used to collect MP from surface water. On the other hand, the Bongo net is used for sampling MP in water columns at depths of 1-212 m [58]. However, neither of these nets is suitable for vertical water columns. These nets are designed for horizontal or oblique towing and lack the structural features, such as rigid frames or flow meters, needed for controlled vertical descent and retrieval. As a result, they are not suitable for precise vertical column sampling where depth-resolved data is required. To collect MP in vertical columns, different multi-stage technologies have been developed, such as multiple opening and closing net environmental sampling systems (MOCNESS) [59], continuous plankton recorders (CPR) [60], and multi-net trawl [61]. The bulk sampling method involves the collection of a substantial volume of water, typically ranging from 200 to 1,100 L, and often at least 500 L in scenarios with low particle abundance, to obtain a representative sample and account for uneven microplastic distribution in the water column [62]. The collected volume is then transported to a laboratory for further physical and chemical treatments to make it ready for analysis.

Compared to net-based sampling methods, bulk sampling has the capability to collect both MP and NP from the water using glass or steel buckets and bottles to avoid contamination. This method can be used to sample surface water and verticle water columns with a volume capacity between 2 and 50 L [63]. The most common devices used for bulk sampling of MNP are buckets, Niskin, Rosette, and immersible pumps. The stainless steel buckets were formerly employed for collecting bulk samples from the surface waters of the Bohai Sea [58] and the effluent of

wastewater treatment plants in urban river basins [64]. Niskin bottles, which are cylindrical water samplers designed to collect discrete samples at specific depths, are used in various configurations to collect bulk water samples, with deep-sea models capable of operating at depths exceeding 10,000 meters [65]. The Rosette device comprises multiple Naskin bottles arranged in a circular manner with a conductivity temperature depth sensor. This device is used during the diving process to collect MNP-contaminated water samples in deep water columns [51, 66]. This method has been utilised to sample the microplastics (MP) in the water column down to around 4 km. The findings indicate that the predominant concentration of microplastics is located within the vertical layer spanning depths from 8 to 51 meters [67]. Among bulk sampling techniques, the immersible pump is also a standard method to sample at a specific depth of water columns. However, this method demands increased operational energy and involves intricate processes, making it inconvenient for water sampling [68].

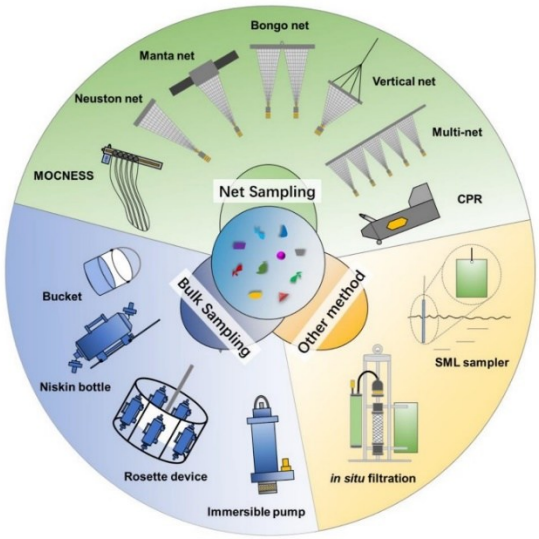

Figure 1.3 The devices commonly employed for sampling micro- and nanoplastics (MNPs) in different environmental water bodies, categorised into net sampling, bulk sampling, and other methods. [55].

Different specialised sampling devices have been employed in recent years to achieve specific objectives related to MNP sampling in water. These devices include cross-flow ultrafiltration (CFU) [69], continuous-flow ultracentrifugation (CFC) [70], surface microlayer (SML) sampling

[71], and in-situ filtration [56]. The CFU has recently been reported as a novel method for sampling NP up to 50 nm in size [72]. In this method, the sample passes through a set of hollow fibre membranes composed of polysulfone, collected at a flow rate of 4 litres per minute. However, this method cannot be used for microparticles (MP) exceeding 100 µm in size, given the restricted internal diameter of the fibre membranes, set at 200 µm [73]. CFC is a promising technique for sampling microplastics (MP) and nanoplastics (NP) from water. This method exhibits the capacity to sample at a rate of 5 litres per hour, revealing a 76% presence of 150 nm PS-NPs within the sample volume [70]. However, it's important to note that increasing the pump speed in CFC results in a reduction of MNP concentration, rendering it unsuitable for sampling large volumes. Additionally, this method is not optimal for low-density MNPs, as they tend to float on the water surface post-centrifugation. Furthermore, the in-situ filtration approach combines fine meshes with immersible pumps, ensuring efficient and high-volume sampling exclusive to MP, while it is not capable of sampling NP [74].

Sampling MNP from other matrices, such as soil, sediments, snow, and water, requires specific tools and methods. In agricultural soil, microplastic pollution is primarily attributed to the use of mulches, coated fertilisers, and sewage sludge [75]. However, inadequate disposal of municipal waste and littering also contribute to the accumulation of secondary microplastics in the soil [76]. MNPs with varying densities disperse across different levels of the ocean. Biofouling further amplifies the weight of MNPs, causing them to sediment in the water [77]. Approximately 13% of the entire marine plastic waste settles in the deep sea, posing a threat to the deep-sea ecosystem [49]. Sampling heterogeneously distributed MNPs in sediments proves to be a challenging task, necessitating specialised tools like box corers [78], gravity corers [79], and grab corers [80]. Sampling protocols for snow and ice vary and lack standardization [81]. Surface snow is typically collected with a stainless steel spoon and then transferred to clean glass surfaces [82]. Sampling ice from the sea surface involves using steel corers, followed by transportation in pre-cleaned

plastic storage bags for sample preparation. In a recent study, a snow sample was obtained from a depth of 3.9 metres using a steel corer, and the identification of MP and NP was carried out on the sample [83]. MNP air sampling is divided into two categories: (i) Active sampling and (ii) Passive sampling methods. Active sampling employs a vacuum pump, metal ducts, and filters with varying mesh sizes. Air is drawn through the pump, and MNPs are retained on the mesh surface. A cascaded mesh approach is utilised to prevent mesh blockage involving subsequent mesh sizes [84]. On the contrary, the passive sampling process is less complicated. In passive sampling, airborne MNPs settle due to gravitational force and are collected in containers [85]. Outdoor passive sampling is further classified as wet or dry deposition of MNPs in steel or glass containers based on weather conditions. Indoor MNP sampling is more straightforward and requires less expensive equipment than outdoor sampling [86].

1.5 Microplastic Sample Preparation

In the past, various techniques have been employed for sample preparation depending on the specific sample matrices, such as water [87-89] (including drinking water and aquatic environments), soil [90], air [91], biota [92], food [93], etc. Herein, our focus is solely on the preparation of microplastic samples derived from aquatic environments. To avoid contamination during the sample preparation process, a closed workstation, such as a fume hood, is recommended for a clean work environment. Moreover, devices composed of steel or glass are preferred to attain the highest level of contamination-free samples. Plastic equipment like vials and pipette tips should be substituted with non-plastic alternatives, or their usage should be minimised or avoided altogether to reduce plastic contamination. Even in controlled environments like fume hoods, it is essential to minimise airflow to prevent airborne microplastic contamination [94].

Samples extracted from aquatic environments encompass various components, including water, sediments, biota, dissolved organic matter (DOM), and suspended matter [95]. The

preparation methods for sediment and biota samples initially differ from those for water; hence, they are explained separately in sections 1.5.1 and 1.5.2. Subsequent processing of these samples, incorporating other matrices like water, suspended matter, and DOM, is explained in Section 1.5.3.

1.5.1 Sample Preparation of Sediment Samples

The initial stage in processing sediment samples involves separating microplastics (MP) smaller than 1 mm. This separation is accomplished using a specialised device called the microplastic sediment separator (MPSS). MPSS employs density separation via a zinc chloride solution with a volume concentration ranging from 1.6 to 1.7 kg per litre. Microplastics measuring less than 1mm and those within the range of 1 to 1.5 mm are collected in a small detachable chamber, achieving recovery rates of 95.5% and 100%, respectively [96, 97]. However, the recovery rate of sediment samples rich in organic content is comparatively low, ranging from 13% to 39% [98]. The non-plastic content in a large sediment sample can be removed using an electrostatic separator device [99]. This method is cost-effective and offers a short processing time while also eliminating the need for chemicals during initial separation. However, additional processing steps, such as organic digestion and density separation, are required to remove the remaining sediment components from the sample.

1.5.2 Sample Preparation of Biota Sample

Several studies have investigated the presence of microplastics in marine biota, extensively examining both large and small organisms [100-102]. Large animals such as fish, sea turtles, and seabirds have been thoroughly studied [103], while smaller biota, including zooplankton, worms, shrimps, and bivalves, have been comprehensively analysed [104]. Microplastics within biota are typically identified using fluorescent dyes under a fluorescence microscope. The initial step in preparing biota samples involves depuration and thorough cleaning to minimise contamination, apart from microplastics. Additionally, samples should be defrosted before analysis and washed

using non-plastic equipment to prevent external contamination. However, comprehensive guidelines for biota sample preparation have been lacking thus far [105].

1.5.3 Digestion Process

Digestion is the primary step in microplastic sample preparation for most sample matrices, excluding sediment samples, which are processed with MPSS (Section 1.5.1). During this step, the sample undergoes pretreatment involving the use of chemicals or enzymatic digestion to break down any organic matter present within it. However, during digestion, there is a potential risk of microplastic particle degradation stemming from mechanical friction and sample heating [106]. This risk can be averted in drinking or clean water samples, which can be directly filtered for subsequent identification and characterisation. Sample digestion is further divided into four categories.

Enzymatic Digestion: Enzymes are extensively used to eliminate organic matter in tissues and cells [107]. Enzymatic digestion has demonstrated high efficiency, degrading 97% of the organic matter in the study. Compared to chemical digestion, microplastic samples treated with enzymes neither degrade nor dissolve the microplastic particles, and these enzymes pose no hazardous risks. However, enzymes can be costly, especially for larger samples, and the process is time-consuming. Additionally, for some complex matrices, this method may not completely digest all organic matter, necessitating integration with additional processes such as incubation with H_2O_2 to degrade any remaining organic matter.

Oxidising Digestion: This process entails the removal of organic matter using an effective oxidiser (H_2O_2). However, this process can alter the morphology of microplastics, rendering them more transparent, thinner, and smaller when oxidised with a 30% H_2O_2 solution. However, a recovery rate of 70% for microplastics has been achieved with 30% H_2O_2 oxidisation [108]. Another study indicates that using a 35% H_2O_2 solution destroyed 25% of organic matter over 7

days [100]. Optimising the concentration of H_2O_2 presents a challenge, as microplastics exhibit a strong reaction to higher concentrations of H_2O_2. The recommended protocol for oxidative digestion is to use a 10% H_2O_2 solution with an exposure time of 18 hours [109].

Acidic Digestion: This approach employs acids to destroy organic matter, with HNO_3 has been proven to be an efficient solvent, capable of destroying 94-98% of biogenic compounds, surpassing other solvents such as HCl and H_2O_2 in terms of effectiveness [100, 101, 106]. However, these potent acid solvents can cause the dissolution of various microplastics (PE and PS), and particle agglomeration has also been observed. Notably, HCl is not recommended among all solvents due to its low efficiency in eliminating organic matter [100].

Alkaline Digestion: This technique employs alkaline solvents like NaOH and KOH solutions. A destruction efficiency of 90% for organic matter has been attained with a 1 M KOH solution [100]. Furthermore, enhanced digestion effectiveness can be achieved through higher molarity and temperature. However, increased molarity can result in the degradation of microplastics, as evidenced by a study demonstrating the degradation of various microplastics such as polycarbonate (PC), PET, and PVC when exposed to a 10 M KOH solution [110].

1.5.4 Density Separation

This process involves the separation of microplastics from environmental samples based on their respective densities. In many cases, following enzymatic or chemical digestion, density separation is commonly utilised to isolate undamaged microplastics from the sample [109]. The microplastic sample undergoes mixing with highly concentrated solutions, followed by shaking for an appropriate duration. Due to their lower densities, microplastics float atop the mixture and are recovered using a separating funnel [107]. Sodium chloride (NaCl) stands out as the predominant choice for density-based microplastic separation, as recommended by numerous researchers due to its affordability and low toxicity [109, 111]. Another viable option for achieving density

separation is sodium iodide (NaI), although less commonly employed due to its higher cost. Moreover, NaI can be utilised in conjunction with NaCl to attain an efficiency of 80% [112]. Zinc chloride ($ZnCl_2$) emerges as another frequently utilised solution for density separation, often combined with MPSS [96]. The recovery rate of microplastics using this solvent is notably high, and its cost remains relatively inexpensive [109].

1.6 State-of-the-art Reference Microplastic Generation Methods

The identification and characterisation of MNP require standardised analytical techniques such as Raman spectroscopy, Surface-Enhanced Raman Spectroscopy (SERS), and Fourier Transform Infrared (FTIR) spectroscopy. However, most studies have relied on commercially produced spherical microplastic beads [113-115], which do not accurately represent environmental MNP in terms of shape, size, and surface chemistry. Additionally, environmental MNP are challenging to sample, separate, and analyse due to their heterogeneous nature and complex interactions with surrounding matrices, including various biological and chemical species. Therefore, the development and standardisation of analytical techniques necessitate the use of reference MNPs that closely mimic those found in environmental samples.

To address this need, several methods have been employed for generating reference MNPs, including cryogenic milling [116], laser ablation [117], and cryotome [118]. However, each of these methods presents significant limitations in replicating real-world secondary microplastics. Cryo-milling, one of the most commonly used techniques, produces heterogeneous particle sizes (1-200 μm) that do not fully represent the size range of environmental plastic debris, which extends into the nanoscale [119]. Additionally, cryo-milled MPs suffer from low suspensibility and poor dispersion due to static charge, which complicates subsequent processing steps such as filtration, fractionation, and characterisation. A more promising top-down method, laser ablation [120], has been used to generate nanoscale reference particles with irregular morphologies and homogeneous dispersion. However, this technique is restricted to nanoscale plastic production

and cannot generate micron-sized particles, making it unsuitable for studies requiring a broader particle size distribution. The cryotome method efficiently produces standardised microplastic fibres with controlled lengths (40–100 μm) [121], ensuring consistency for laboratory studies. It allows high-throughput production and supports multiple polymers like Nylon, PET, and PP. Additionally, fluorescent labelling confirms its relevance for bioavailability testing. However, it is limited to a maximum fibre length of 100 μm, with potential misalignment issues requiring additional fractionation. Moreover, this method is restricted to producing only fibre-shaped particles and cannot generate fragments, which are commonly found in environmental matrices. In general, each of these methods faces significant challenges in producing reference MNPs that accurately replicate real-world microplastic debris in terms of size, morphology, and suspensibility.

Other approaches have focused on producing nanoscale reference particles through bottom-up synthesis, such as colloidal chemistry [122-124]. While these methods can generate monodisperse spherical nanoparticles (NPs), they often require chemical additives, including solvents, sodium azide residues, and surfactants. These synthetic by-products can interfere with NPs characterisation and introduce misleading results when establishing analytical standards. Furthermore, these NPs typically exhibit smooth surfaces without the physical imperfections found in real environmental NPs, limiting their environmental relevance [125]. To address some of these issues, soap- and metal-free emulsion polymerisation has been developed to produce additive-free NPs with controlled morphology, surface functionality, and stability [126]. However, these particles still differ significantly from environmental nanoplastics, which display irregular shapes and complex surface chemistries developed due to harsh environmental weathering conditions.

Given the challenges posed by existing MNP production techniques, ultra-sonication has emerged as a promising alternative for generating reference MNPs with enhanced suspensibility and structural diversity. The use of high-intensity ultrasound to degrade solid polymers into microscopic fragments was first reported by J. Price [127]. More recently, NPs (200-800 nm) have

been produced via the sonication of polyethylene (PE) dissolved in toluene, demonstrating the potential of sonication for nanoscale plastic particles generation [128]. Moreover, reference secondary MNPs of varying shapes (fragments, spheres, and fibres) and sizes (100 nm-1 mm) were successfully produced using high-power sonication (15 kHz) in strongly basic conditions for 15 hours [129]. However, this method is only applicable to polymers that do not form polyamides in alkaline solutions. Despite the advantages of sonication-based techniques, a major challenge remains in achieving precise size control of the produced MNPs.

Beyond production methods, another critical factor influencing the reliability of reference MNPs is their stability in suspension, as it directly impacts their transport and bioavailability in environmental conditions. The MPs generated through cryo-milling exhibit extremely low suspension in water due to their static charge property. However, these microplastics show adhesion to glass surfaces, and this adhesion increases with a decrease in particle size [130]. The larger microplastic particles of the same material tend to sediment more rapidly compared to the smaller particles due to their cumulative mass. A study on microplastic sedimentation [131] suggests that the residence time of microplastic particles in water columns is highly dependent on particle size and less relevant to density. The settling velocities of environmental microplastics are also dependent on the hydrophobic surface of MPs, which was confirmed through the combination of a semiempirical model [132] and laboratory experiments [133]. To improve suspensibility, two approaches, the use of surfactants and surface oxidation have been explored. In the first approach, surfactants enhance dispersion but alter MPs spectral properties and pose a risk of contaminating samples. Surface oxidation increases hydrophilicity and improves suspensibility but modifies the surface chemistry of MPs, potentially affecting their environmental relevance [129]. Thus, while sonication presents a promising technique for generating reference MNPs, further optimisation is required to control size distribution and improve suspensibility without compromising the integrity of the particles.

1.7 State-of-the-art MNP Detection Techniques

A single technique is insufficient to gather comprehensive information about microplastics (MPs) within complex matrices, including factors like quantity, size, shape, and chemical composition. Therefore, a combination of two or more analytical techniques is commonly employed to completely characterise them. Physical characterisation of MPs involves various microscopic systems such as dissect, SEM, and atomic force microscopes, providing morphological (particle shape) and size-based information on MPs. For chemical identification, spectroscopic techniques such as Raman, FTIR, and mass spectroscopy are commonly used. The combination of spectroscopic systems with microscopes, such as micro-Raman and micro-FTIR, provides comprehensive information, both physical and chemical, about MNP. Table 1.1 includes a list of commonly utilised analytical methods for the detection and characterisation of micro- and nanoplastics (MNPs). However, in this thesis, our primary emphasis is on spectroscopic techniques and the research conducted on MNP identification using these methods.

Table 1.1 List of commonly utilised analytical techniques for the detection and characterisation of micro- and nano-plastics (MNPs).

Analytical Method	Resolution limit	PROS	CONS
Visual detection by microscopes 1. Optical[134] 2. Light and Stereoscopic[135]	>50 µm	Fast, inexpensive, uncomplicated, manageable, less training required, give morphology of MPs	High chances of False-positive or negative and provides no information on the chemical composition.
PY-GC-MS [136-138]	ng-µg	Required less sample preparation, the chemical composition can be determined fast, Highly sensitive, Provides thermal degradation	Destructive, number of MPs and morphological information can not be determined, reproducibility is

		profiling for MPs ageing study	complex, Expensive setup
Fluorescence microscopy [139-141]	µm	Fast, enables to differentiate multiple particles, in-expensive, provides morphological information	High possibility of false-positive, fluorescence background noise, and no information on chemical composition
µ-Raman Spectroscopy [114, 142-146]	> 1 µm	High spatial resolution for small particles, Non-destructive, Sensitive to a wide range of chemical structures, Can analyse opaque and pigmented samples	Fluorescence background issues, expensive instruments, low-intensity signals, and slow measurement can be destructive with high-power lasers
µ-FTIR spectroscopy [147, 148]	>10 µm	Non-destructive, Rapid analysis, Provides detailed chemical composition, Effective for identifying polymer types	Water interference, expensive setup, comparison is difficult, unreliable data of thick, coloured, and opaque plastics in transmission mode
Photlomuniscence & TRPL Spectroscopy [149-151]	Undetermined	Rapid measurement process, Non-destructive, Requires minimal sample preparation, Less expensive, Provides detailed electronic and optical property insights, Can identify plastic types	Not all plastics exhibit intrinsic fluorescence, Susceptible to photobleaching, Potential interference from persistent organic pollutants (POPs)

1.7.1 Pyrolysis-Gas Chromatography-Mass Spectroscopy

Pyrolysis-gas chromatography-mass Spectroscopy (PY-GC-MS) is an analytical technique used to characterise a wide range of materials, including composites and polymers. In this

method, the sample undergoes heating in a vacuum to avoid oxidation or additional reactions, resulting in the breakdown of the sample into smaller, stable fragments for analysis. These fragments, known as pyrolyzates, are then introduced into a conventional gas chromatographic column. This column separates the decomposed particles according to their size and chemical characteristics. Subsequently, the pyrolyzates are directed through a mass spectrometer, generating a spectrum of mass-to-charge ratios. This ratio is utilised to discern the individual components within the sample, enabling the identification of the material and its concentration [152].

The working principle of PY-GC-MS is shown in Figure 1.4. The main advantage of employing this approach for microplastic analysis lies in its ability to identify polymers and provide insights into the organic additives within the sample. Furthermore, this technique can manage microplastic samples of various shapes, sizes, and chemical contamination without the need for any pre-treatment of the samples [153, 154]. While PY-GC-MS is a destructive method, its primary drawback is the inability to provide information on the size, shape, or number of microplastic particles. Additionally, it typically requires longer analysis times (around 30 minutes or more) compared to Raman and FTIR spectroscopies, which can offer faster analysis for single-point measurements but may take longer for complete sample imaging. This approach is predominantly reported as a supplementary technique alongside Raman [155] and FTIR [156] spectroscopies. Another constraint of PY-GC-MS lies in its particle size capability, as it can only analyse particles larger than 50-100 microns. This limitation arises from the manual transport of particles in the pyrolysis tube, and particles exceeding 1.5 mm cannot be measured due to the thermal deposition tube diameter constraints. The detection limit of this method is considered to be between picograms and micrograms [157]. Notably, Hermabessiere reported an exceptionally low limit of 1µg and concluded that the microplastics with higher density exhibit a higher detection limit [158].

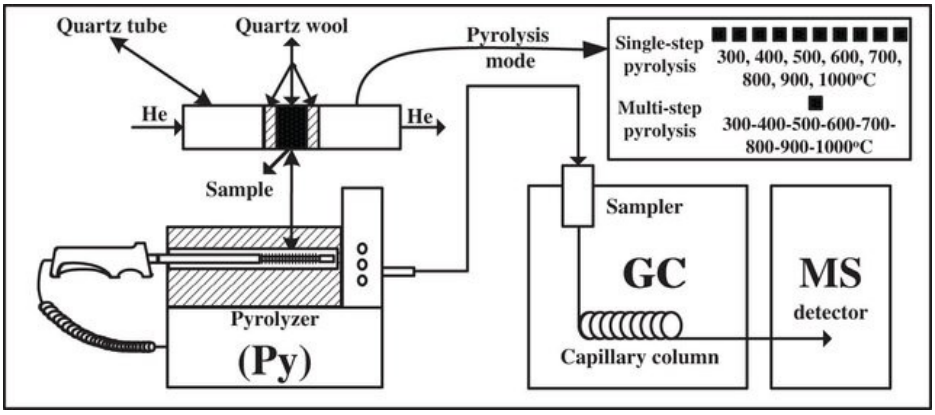

Figure 1.4: Schematic diagram of pyrolysis-gas chromatography-mass spectroscopy (PY-GC-MS). The sample undergoes heating in a pyrolyzer and is subsequently transferred to a gas chromatogram for separation. Finally, it is fed into the mass spectrometer, which provides spectral information about the material [159].

1.7.2 Thermal Analysis

In addition to spectroscopic techniques for MNP analysis, several other methods have been employed to detect, identify, and characterise MNP, such as microscopic (optical, SEM, TEM) and thermal techniques, which mainly include thermogravimetry (TGA) and differential scanning calorimetry (DSC) [136]. These thermal techniques are used primarily to identify and characterise MP in solid environmental samples, such as soil. TGA is utilised to observe the time- or isotherm-dependent mass loss of the sample. This method is well-suited for solid samples, eliminating the need for any sample pretreatment. Recently, a chemometric approach combined with TGA has been employed to qualitatively and quantitatively characterise different common microplastics (PS, PET, PE, and PVC) in soil samples [160]. This method is the preferred choice for characterising microplastics in soil due to its simplicity, lack of sample pretreatment requirements, cost-effectiveness, and efficiency in terms of the time required for measurements.

TGA is integrated with additional methods, referred to as hyphenated TGA, to augment the identification and characterisation capabilities of microplastics. Those hyphenated TGA methods include Thermogravimetry mass spectroscopy (TGA-MS), Thermogravimetric analysis with differential scanning calorimetry (TGA-DSC), Thermogravimetric analysis with thermal

decomposition unit, gas chromatography, and mass spectrometry (TGA-TDU-GC-MS). All these coupled techniques offer additional insights into the sample. For instance, TGA gives data on the mass loss of the sample, while the others provide both qualitative and quantitative information about the sample. The TGA-MS for detecting PET microplastics was utilised to collect mass loss information by heating the sample in an inert environment. Qualitative and quantitative data are then obtained using a mass spectroscopic system [161]. This technique boasts a low detection limit, a cost-effective setup compared to other hyphenated TGA methods, minimal sample preparation requirements, and the ability to handle larger sample volumes to address heterogeneity issues. However, a key challenge in TGA-MS arises from the intricate interpretation of data, especially when the sample contains various contaminants or plastics with similar masses and thermal degradation patterns. To address this complexity, a twist tube method was developed, capturing evolved gases using solid-phase absorbers (SPA) to simplify output data [162]. This addition of SPA introduces an extra chromatographic separation capability, transforming the system into TGA-GC-MS [163].

Furthermore, TGA-DSC has been utilised for microplastic characterisation, capturing additional thermodynamic information about the sample, including phase transition temperature, enthalpies, and heat capacities throughout the process [164]. This study determined the endothermic phase transition temperatures of various microplastics using DSC. Notably, PE and PP exhibited distinct patterns, aiding in their identification. However, other microplastic samples (polyvinyl chloride - PVC, polyester - PES, and polyamide- PA) displayed similar temperatures, introducing complexity in the identification process. To address this data overlap, Chialanza employed a deconvolution process [165]. The overlapping phase transition temperatures were influenced by factors such as the initial particle size, impurities in the sample, and the degree of polymer branching. TGA-DSC emerges as a favourable option for characterising microplastic particles due to its straightforward processing and cost-effectiveness. However, the identification

of microplastics obtained through DSC can be challenging due to shifts in characteristic temperature spikes, especially when dealing with raw and ground particles [166]. Thermal

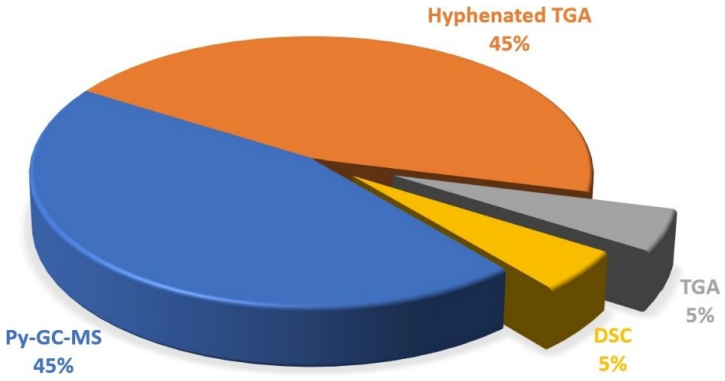

Figure 1.5: Percentage distribution of thermal techniques employed to characterise environmental MP samples [136].

techniques have been widely employed for the characterisation of microplastics, as illustrated in Figure 1.5, which depicts the distribution of various thermal analyses used for microplastic identification and characterisation. Py-GC-MS and hyphenated TGA stand out as the most popular thermal techniques, while TGA and DSC have been explored to a lesser extent for microplastic characterisation.

1.7.3 Raman Spectroscopy

Raman spectroscopy is a vibrational spectroscopic method based on inelastic scattering principle, wherein incident light interacts with matter, leading to characteristic spectral fingerprints. The spectrum provides information about the functional groups within a material, facilitating the identification of the specific materials. An intense monochromatic source, typically at 532 nm or 785 nm, excites the material, leading to the scattering of light in both elastic and inelastic manners. The elastic scattering is known as Rayleigh scattering, while the inelastic scattering is termed Raman scattering. Raman scattering is further divided into two categories: Stokes and anti-Stokes

Raman signals (see Figure 1.6). A laser beam with a frequency υ_0 stimulates electrons, causing them to transition from lower vibrational states to higher vibrational states. Upon relaxation, these

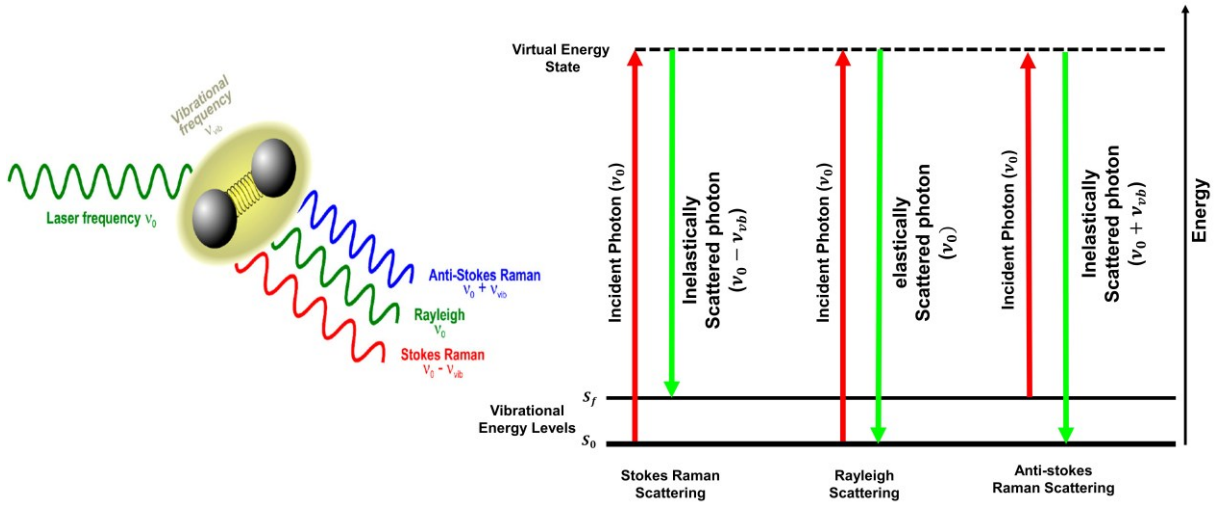

Figure 1.6: The representation of Raman scattering processes, including Stokes, anti-Stokes, and Rayleigh scattering. The left diagram depicts the interaction of an incident laser photon (υ_0) with a molecule, leading to scattered photons of different energy states: Stokes Raman scattering (υ_0- υ_{vib}), Rayleigh scattering (elastic scattering at υ_0), and anti-Stokes Raman scattering (υ_0 + υ_{vib}). The right energy diagram shows the corresponding energy transitions, where Stokes scattering results in energy loss, anti-Stokes scattering involves energy gain, and Rayleigh scattering occurs without a change in energy [167].

electrons emit photons with the same frequency as the initially excited photons (υ_0), a phenomenon known as Rayleigh scattering. The relaxation to lower vibrational states is termed Stokes Raman scattering (υ_0- υ_{vib}), while relaxation to higher vibrational levels is referred to as anti-Stokes Raman scattering (υ_0 + υ_{vib}).

The inelastic scattering from a material can be measured using a Raman spectroscopic setup, as depicted in Figure 1.7. The two most commonly used excitation wavelengths, 532 nm and 785 nm, are used in Raman spectroscopy for microplastic detection [113, 168-170]. These wavelengths offer a balance between signal intensity and fluorescence interference. The shorter wavelength, 532 nm, yields strong Raman signals but can induce fluorescence, while 785 nm reduces fluorescence at the cost of lower signal strength. Additionally, 1064 nm is sometimes used for highly fluorescent samples [171], as it further suppresses fluorescence, though it typically

requires more sensitive detectors due to weaker Raman scattering. The near-infrared wavelength, 785nm, is preferred due to its optimal balance of signal strength, fluorescence suppression, cost-effectiveness, and overall performance [142]. In the Raman spectroscopic setup, the laser beam of one of these wavelengths undergoes splitting and is directed towards the samples, subsequently being focused on the sample through focusing

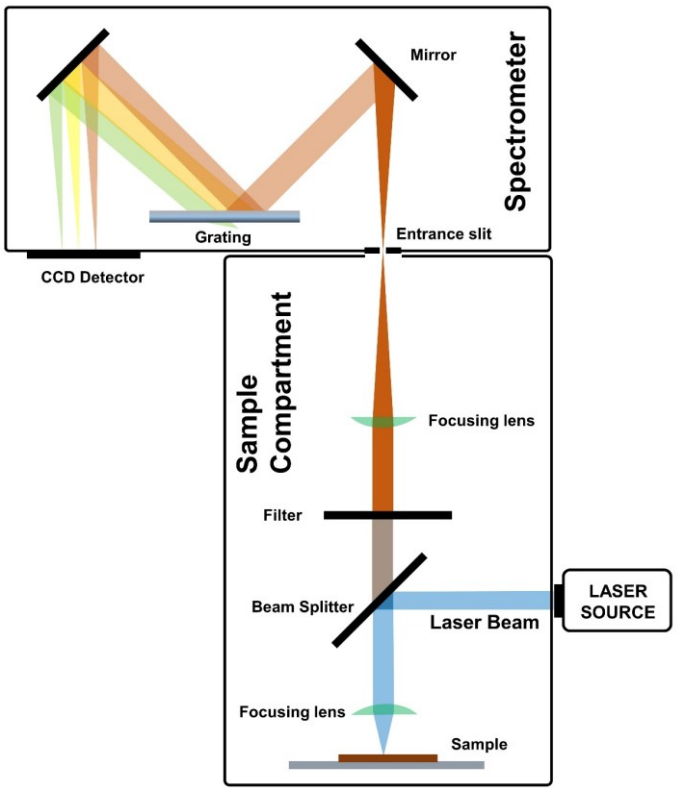

Figure 1.7: Schematic diagram of Raman spectrometer. The blue beam represents the laser, which is subsequently split and directed towards the sample. The scattered light traverses optical components and reaches the detector, where the Raman spectrum is recorded.

optics, typically microscope objectives. The backscattered light from the sample then traverses the same objectives. A filter is employed to block the elastically scattered signal, allowing only the filtered signal, composed of inelastically scattered light, to enter the spectrometer through the entrance slit. Within the spectrometer, this light is reflected onto the grating, which disperses it into individual wavelengths. These wavelengths are then directed onto the charged couple device, facilitating the simultaneous detection of wavenumbers within a specified spectral range. Raman

mapping can also be accomplished through a step-wise movement of the laser focus across the sample, recording the Raman signal for each pixel throughout the entire image.

Over the last decade, this method has been widely employed for identifying microplastics gathered from various environmental sources, such as water [172], soil [173], air [174], blood [175], and food [176]. The prevalence of utilising this method for microplastic identification stems from its non-destructive nature, minimal sample requirements, and the potential for high-throughput measurements. Additionally, when compared to FTIR spectroscopy, this technique provides higher spatial resolution (down to 1μm), better sensitivity to non-polar functional groups, a broader spectral range, and reduced interference from water signals. However, this approach has its drawbacks, including a fluorescence background, a less intense Raman signal, and the potential to cause the burning of microplastic particles with high laser intensity [177, 178]. Raman spectroscopy combined with optical microscopy can provide detailed chemical and physical information on MPs, including the level of degradation, crystallinity, and degree of cross-linking [179]. Moreover, some studies show that the sensitivity of Raman spectroscopy can be increased to detect nanoplastics (NPs) by integrating signal enhancement methods such as surface-enhanced Raman spectroscopy (SERS) [180] and coherent anti-stokes Raman spectroscopy (CARS) [181]. However, each method has its drawbacks, i.e., SERS specifically experiences hetero-aggregation of nano plastics, a plasmonic heating-induced photothermal effect, and time-intensive and cumbersome measurements [182]. In contrast, single-colour CARS has limitations in distinguishing chemically different microplastics, and multiplex CARS has a low imaging rate, which makes it a time-consuming process [183].

1.7.4 Fourier-Transformed Infrared Spectroscopy

Fourier-transformed Infrared (FTIR) spectroscopy is also a promising technique for microplastic identification, and it works by measuring the absorption, transmission, or reflection of infrared radiation by a sample, enabling the detection of microplastics down to 10 μm [184].

Figure 1.8 shows the schematic diagram of a typical FTIR spectrometer with its three modes of signal sample interaction. These modes are referred to as (i) Transmission, (ii) Reflection, and (iii) Total Attenuated Reflection (ATR) for sample characterisation [134]. A time-consuming

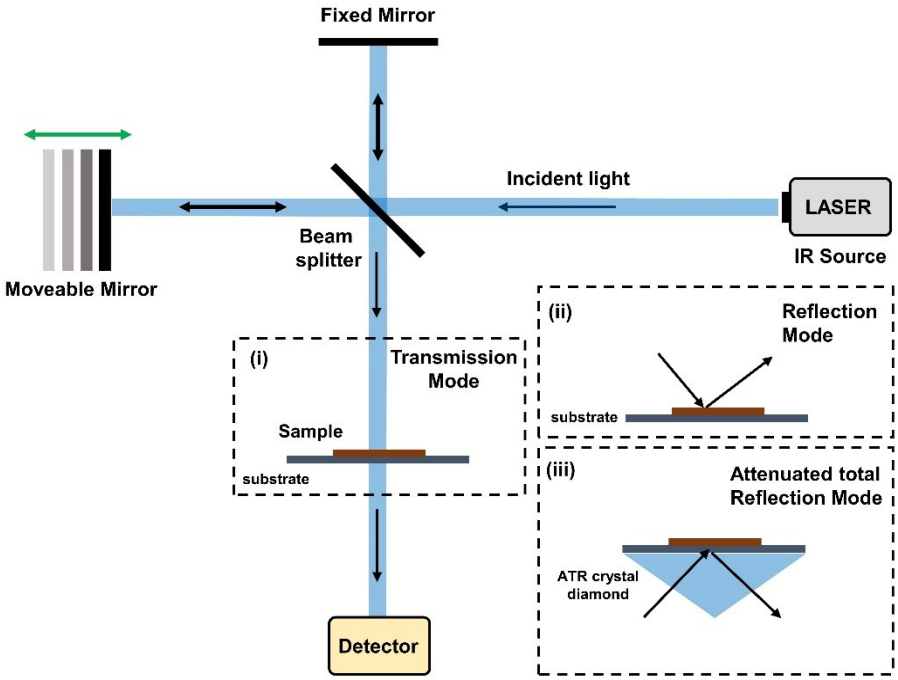

Figure 1.8: Schematic diagram of a Fourier Transformed Infrared (FTIR) spectrometer. The infrared light interacts with the sample in three different modes: (i) Transmission, (ii) Reflection, and (iii) Attenuated total reflection – ATR.

imaging process such as that in Raman spectroscopy, which requires point-by-point scanning, is significantly reduced in FTIR when using focal-plane-array (FPA) detectors in reflection or transmission mode, as FPA enables simultaneous multi-pixel data acquisition. Moreover, micro-FTIR equipment used for microplastic analysis is less expensive than a micro-Raman spectrometer. However, samples need to be dried prior to FTIR analysis. Also, in transmission mode, thicker samples (> 100 µm) cannot be measured due to the high absorbance of light. Light scattering due to irregular shapes of secondary microplastics is another major issue in reflectance mode. [185]. Also, this technique has limitations in detecting MPs up to 10 µm. It cannot identify nanoscale plastic particles because these are typically smaller than the wavelength of mid-

infrared light (approximately 2.5 to 25 µm, corresponding to 4000 to 400 cm^{-1}), making it challenging to detect and characterise them directly. Finally, samples with thicknesses less than 5 µm provide insufficient absorbance for interpretable spectra in FTIR transmission mode [186].

1.8 Photoluminescence Spectroscopy

1.8.1 Theory

Photoluminescence is a phenomenon that characterises light emission from a substance in solid, liquid, or gaseous form after absorbing light. This process is further divided into two main types: fluorescence and phosphorescence. In fluorescence, emissions from the material stop rapidly (from 10^{-9} to 10^{-7} seconds) upon the removal of the excitation source, whereas in phosphorescence, the material continues emitting light (lasting from 10^{-6} to 10^{-3} seconds) even after the excitation source has been removed. The photoluminescence phenomenon is explained using the Jablonski diagram (see Figure 1.9). In the first phase (absorption) of the process, the material absorbs light, providing sufficient energy to transition electrons from the ground electronic state (low energy state – S_0) to the excited electronic state (higher energy states, S_1 and S_2). After residing in the higher excited state for a short duration, electrons undergo relaxation to lower vibrational states, releasing energy in a non-radiative (thermal) manner. This process is referred to as internal conversion, and it typically takes place within a duration of 10^{-12} seconds (picoseconds) or less. In the subsequent stage (luminescence), electrons in the singlet excited state return to the original ground state and pair with electrons of opposite spin. Through this relaxation process, a photon is emitted, and this phenomenon is referred to as fluorescence. Electrons situated in the excited singlet state undergo a spin conversion to an excited triplet state, a phenomenon known as intersystem crossing. The subsequent relaxation of electrons from the triplet state to the ground state generally leads to the emission of longer wavelengths (lower energy), a process referred to as phosphorescence. The transition of electrons from the excited triplet state (T1) to the excited singlet state (S1) is prohibited. Consequently, the rate constant for

triplet emissions is several orders of magnitude lower compared to fluorescence emissions. The Jablonski diagram illustrates that the energy of emitted light (fluorescence or phosphorescence) is typically lower than the absorbed energy. Consequently, this leads to light

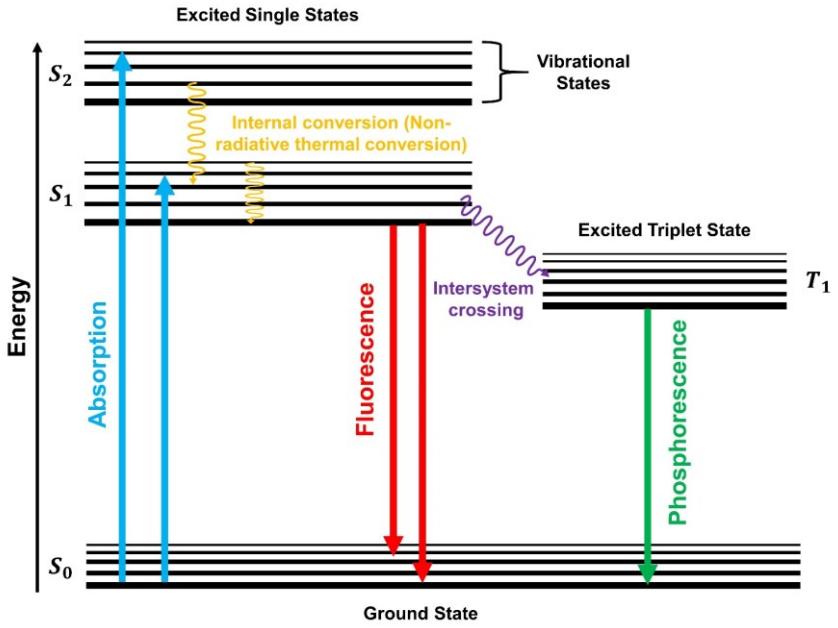

Figure 1.9: The Jablonski diagram illustrates three distinct electronic states (S_0, S_1, S_2) and their associated processes, including absorption, non-radiative internal conversion, fluorescence, intersystem crossing, and phosphorescence.

emission at longer wavelengths compared to the wavelength of the absorbed light. This shift in the wavelength of emitted light was first observed by Sir George Gabriel Stokes [187] at the University of Cambridge in 1852, and it was subsequently named the Stokes shift.

1.8.2 Working Principle

The schematic diagram of the Horiba Nanolog steady-state Excitation-Emission Mapping spectrofluorometer is depicted in Figure 1.10. The system is composed of five different components: (i) Light source, (ii) Excitation Monochromator, (iii) Sample compartment, (iv) Emission Monochromator, and (v) Detector. The light source utilised in this setup is a xenon short-arc lamp (450W) enclosed in a housing with an off-axis ellipsoidal collector. This lamp emits a broad spectrum of light ranging from 270 nm to 800 nm. The light is guided towards the double-

grating excitation monochromator, where it is transformed into a monochromatic beam before being directed into the sample compartment. The monochromatic beam interacts with the sample

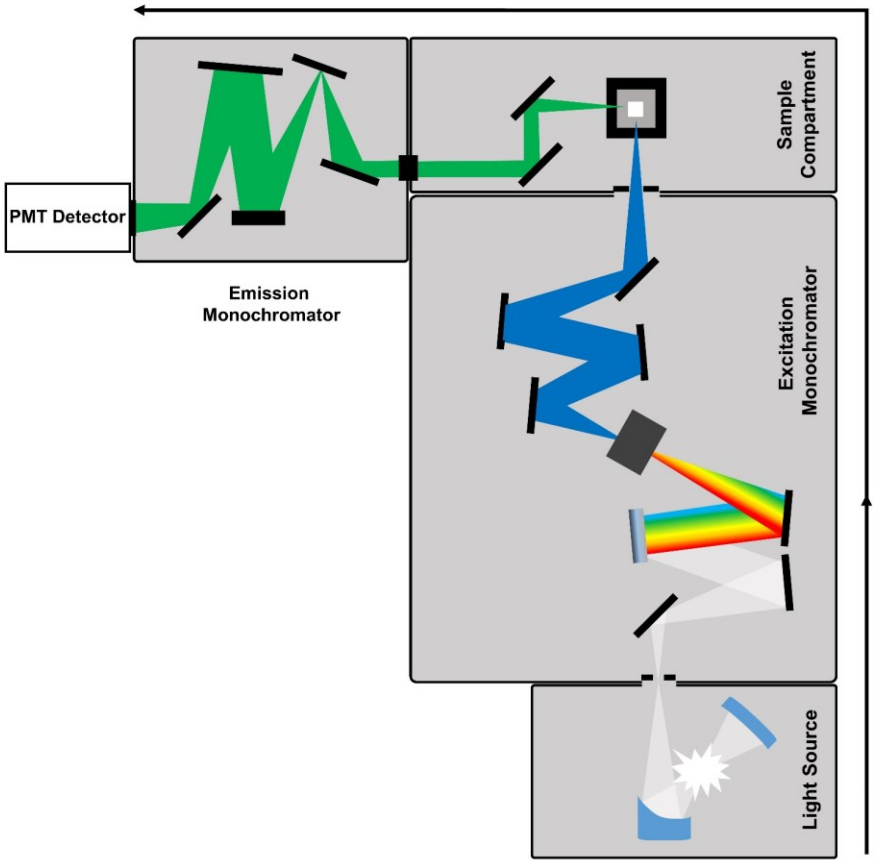

Figure 1.10: A schematic diagram illustrating the operational principle of a photoluminescence spectrometer, highlighting its key components, including the light source, excitation monochromator, sample compartment, emission monochromator, and PMT detector.

housed in a quartz glass cuvette. The sample absorbs the light and then emits radiation at a higher wavelength, which is subsequently directed to the emission monochromator. Finally, the fluorescence emissions are recorded using a photomultiplier tube detector. This setup allows for the excitation of the sample at each individual wavelength of the source and the recording of emissions across a wide spectrum ranging from 280 nm to 1600 nm. This process produces three-dimensional excitation-emission maps (EEM). In an EEM, the x-axis represents emission

wavelengths, the y-axis represents excitation wavelengths, and the z-axis represents fluorescence emissions.

1.8.3 PL Spectroscopy for Microplastic Detection

Photoluminescence (PL) spectroscopy has recently emerged as an alternative method for detecting and identifying microplastics. In comparison to commonly used techniques such as Raman spectroscopy and FTIR, PL spectroscopy is also non-destructive but additionally offers high sensitivity with a detection limit in parts per billion [188] and, like Raman spectroscopy, has low-water interference [189]. The superior sensitivity of photoluminescence (PL) spectroscopy arises from its reliance on radiative electronic transitions, which enable the detection of emitted light upon excitation. Unlike Raman and FTIR spectroscopy, which are based on inelastic scattering and vibrational absorption, respectively, PL directly measures photon emission from excited electronic states. This mechanism allows for inherent signal amplification, facilitating the detection of analytes at ultra-low concentrations. PL spectroscopy has been widely employed to characterise various polymers in the past. The polymers exhibit intrinsic fluorescence (FL) emissions when excited with a specific excitation wavelength, and these emissions correspond to specific compounds present in the material. Torkelson [190] investigated the absorption and intrinsic fluorescence characteristics across various molecular weights (MW) of polystyrene (ranging from 2×10^4 to 9×10^5) in 1,2-dichloroethane. The results revealed an absorption peak at 260 nm, which remained consistent irrespective of the molecular weight of the polystyrene. The fluorescence emission peaks of polystyrene are primarily associated with distinct energy bands corresponding to monomer and excimer states. The monomer fluorescence emission is observed at wavelengths around 283 nm and 286 nm, while the excimer emission appears at approximately 335 nm. These emission peaks arose due to different fluorescence mechanisms within the polymer matrix. The monomer fluorescence resulted from the radiative relaxation of individual styrene units, whereas excimer fluorescence occurred when two aromatic groups within the

polymer chain came into proximity, forming an excited-state dimer. This excimer formation is facilitated by chain mobility and segmental diffusion, which allows interactions between chromophores, leading to characteristic broad and red-shifted emission compared to the monomer fluorescence. The fluorescence behaviour of polystyrene in solution is influenced by polymer concentration, with higher concentrations leading to more excimer formation due to increased inter- and intramolecular interactions. Moreover, solvent polarity and molecular weight can affect the balance between monomer and excimer emissions, which helps better understand the polymer's structural dynamics and aggregation behaviour of styrene units. Healy and Hanson [191] verified these fluorescence emission peaks from polystyrene monomer at approximately 285nm and from excimer emissions at 332nm through front-face PL spectroscopy measurements with 250 nm excitation. They further investigated the critical concentration of polystyrene. The study highlights the role of concentration monitoring in distinguishing between dilute and semi-dilute solution regimes, with the critical concentration (c*) being determined through the ratio of fluorescence intensities of the excimer to monomer emissions. A sudden increase in excimer emission relative to monomer fluorescence indicates the transition from isolated polymer chains to an interconnected network, marking the onset of significant intermolecular interactions. This concentration dependence is crucial for understanding polymer behaviour in solutions and aids in determining key physical properties such as polymer coil dimensions and aggregation tendencies.

Moreover, in a separate investigation by Baibarac [192], where polystyrene was functionalised with single-walled carbon nanotubes (SWCNTs), excitation at 260 nm resulted in a broad fluorescence emission peak spanning from 290 nm to 475 nm, with peak maxima around 313–321 nm. An additional shoulder was observed in the 375–420 nm range. A notable red shift in the emission bands was observed, with the peaks shifting from 313 nm (3.96 eV) to 388 nm (3.19 eV) and further to 412 nm (3.01 eV), depending on the concentration of SWCNTs in the composite. This shift suggests the formation of new luminescent centres, likely arising from

defects induced in the polymer chains due to covalent bonding with the SWCNTs. The fluorescence mechanism involves the excitation of polystyrene molecules, leading to photon emission as the excited states relax. However, in the presence of SWCNTs, the photoluminescence intensity is significantly quenched, which is attributed to interactions such as charge transfer and energy dissipation processes between the polymer and nanotubes.

In addition to PS, polyethylene terephthalate (PET) film was also analysed using UV-Vis spectroscopy [193]. The absorption peaks associated with PET reveal a strong absorption at wavelengths shorter than 325 nm. The absorption spectrum of PET films before UV exposure exhibits a high absorption band in this region, which is primarily attributed to the presence of aromatic ester groups in the polymer backbone. These groups absorb ultraviolet radiation, leading to potential photodegradation effects. Upon exposure to UV radiation, the PET films show an increase in absorption intensity within the range of 310–360 nm, which is attributed to the formation of aromatic hydroxylated species generated during the photodegradation process. These hydroxylated species arise from the scission of hydroxyl radicals on the aromatic rings of the polymer chain, which contribute to the observed changes in the absorption spectrum. The development of new absorption bands, particularly in the range of 370–400 nm, indicates the presence of oxidation by-products, such as carboxyl and hydroxyl groups, which further impact the optical and mechanical properties of PET films. Upon excitation at 340 nm, the fluorescence spectrum of the PET film showed a broad peak covering the range of 350 nm to 500 nm, featuring two prominent peaks at 390 nm and 415 nm.

The first-time collection of excitation and emission spectra for low-density polyethylene (LDPE) revealed two excitation peaks at 240 nm and 290 nm, along with a single emission peak at 360 nm [194]. These peaks correspond to the electronic transitions of the enone functional groups present as impurities in the LDPE. The study also compared the fluorescence spectra of LDPE and polypropylene (PP), revealing similar emission profiles, which indicates the common

presence of enone-type chromophores in both polymers. Moreover, it was also found that including benzoyl-based initiators during polymerisation introduces benzoic acid residues, which predominantly contribute to phosphorescence rather than fluorescence. Furthermore, Osawa and Kuroda [195] extended the research by capturing the fluorescence and phosphorescence spectra of low-density polyethylene (LDPE) and high-density polyethylene (HDPE). The fluorescence spectra revealed that both LDPE and HDPE exhibited similar emission peaks around 460 nm when excited at 285 nm, indicating the presence of common chromophoric impurities in the polymers, primarily enone-type carbonyl compounds. Moreover, when excited at 292 nm, LDPE showed an emission peak at 343 nm, whereas HDPE emitted at 340 nm, demonstrating subtle differences in their luminescence behaviour. These variations can be attributed to structural differences between the two polymers, such as the degree of crystallinity, chain branching, and impurity content. The higher crystallinity of HDPE likely results in a more rigid molecular environment, causing slight blue shifts in its emission, while the amorphous regions in LDPE provide greater chain mobility, leading to red-shifted emissions. Another research on the fluorescence emission spectrum of polypropylene (PP) showed a wide peak centred at 340 nm, featuring two excitation peak maxima at 230 nm and 285 nm [196].

To broaden the investigation for identifying polymers based on their distinctive intrinsic fluorescence spectral features, researchers [150, 151, 197] employed a 405 nm excitation source and recorded observable emissions for specific polymers such as PS, PET, PP, HDPE, and polyamide. However, the fluorescence spectra of most microplastics showcase similar spectral features, making their identification challenging. To address this problem, Benjamin et al. [198] combined machine learning with photoluminescence (PL) data obtained using a single 405 nm excitation source to automate the identification of different microplastics. They analysed 23 different plastic and non-plastic materials, categorised into nine classification groups, using an in-house built PL spectroscopic system (see Figure 1.11). Dimensional reduction (DR) was

performed using Principal Component Analysis (PCA) combined with Signal Dissection by Correlation Maximisation (SDCM). The classification of plastic and non-plastic materials was conducted using machine learning algorithms applied to the processed spectral data. However, despite its advantages, the study presents several limitations and challenges. One key challenge is the variability in spectral data, which arises due to differences in sample composition, environmental degradation, and inconsistencies in measurement setups, such as variations in laser power, alignment, and exposure times. These factors introduce noise and spectral deviations, potentially reducing the accuracy of ML models when applied to real-world samples with diverse characteristics. Another major concern is the reliance on spectral libraries, which are inherently incomplete due to the vast diversity of plastic materials and their varying compositions in environmental conditions. Building a comprehensive spectral database that encompasses all potential plastic types and degradation states remains a considerable challenge. Moreover, while the study utilises PCA and SDCM for dimensional reduction, their effectiveness in capturing subtle spectral features without losing critical information requires further validation. The selection of an optimal combination of dimensional reduction methods and classifiers is crucial, as specific classifiers, such as Gaussian Naïve Bayes (GNB), exhibit significantly lower prediction accuracies compared to more advanced options like Nu-SVM. Furthermore, the approach requires large amounts of training data to achieve robust model generalisation, which can be resource-intensive.

PL spectroscopy is known for high sensitivity, often reaching the detection level of parts per billion (ppb) [199] and, in some cases, even parts per trillion (ppt) [200]. This sensitivity depends on different factors such as instrument setup, the specific fluorescent molecules being analysed, the solvent or matrix, and the wavelength range used. For microplastics, the fluorescence technique has demonstrated the ability to detect concentrations as low as 0.2 μg/g (200 ppb) in natural sea salt samples [201]. This was achieved using pyrene as a fluorescent probe to detect polystyrene microparticles on the salt surface. Another study highlighted the use

of Nile Red as a fluorescent dye, using the Cyclops 7F fluorometer paired with the NR-H, which enabled the detection of MPs in environmental samples at levels from 100 parts per billion (ppb) down to 0.1 ppb [202]. While these studies demonstrated high sensitivity for microplastic detection using external dyes or probe-based surfaces, the sensitivity of fluorescence methods based on the intrinsic fluorescence of microplastics themselves remains unknown. Recent studies [44] employed fluorescence spectroscopy with a 405 nm laser source to acquire fluorescence fingerprints of microplastics, but precise sensitivity levels have not been reported.

The potential of time-resolved photoluminesce (TRPL) as an alternative method for MP detection has also been investigated [203]. This study investigated the potential of time-resolved photoluminescence (TRPL) spectroscopy for detecting and distinguishing plastics from natural materials. The PL emission peaks for plastics were observed predominantly in the spectral range of 420–510 nm, with variations depending on the polymer type. The luminescence is primarily attributed to structural defects within the polymer chains, such as oxidation-induced carbonyl groups and chain breaks, which act as chromophoric sites that absorb excitation energy and subsequently emit light. The TRPL technique allows differentiation between plastics and natural materials based on their distinct decay behaviours, categorised as mono-, bi-, or tri-exponential decay profiles, corresponding to different molecular relaxation processes. Despite its potential, the TRPL technique presents several limitations and challenges. A significant limitation is the inability to distinguish certain plastics with similar decay times, such as polymethyl methacrylate (PMMA) and unplasticised polyvinylchloride (PVC-U), which exhibit identical PL lifetimes, necessitating further spectral data for precise identification. Furthermore, the technique's accuracy is affected by sample conditions, as environmental factors such as weathering, contamination, and surface modifications can alter the fluorescence response, complicating the interpretation of results. Another challenge is the need for a comprehensive spectral database to facilitate accurate identification, as current data is limited to a narrow range of polymers.

Additionally, the detection sensitivity and resolution of the method may be constrained when applied to highly degraded or mixed plastic samples, requiring further refinement of the experimental setup and data processing algorithms.

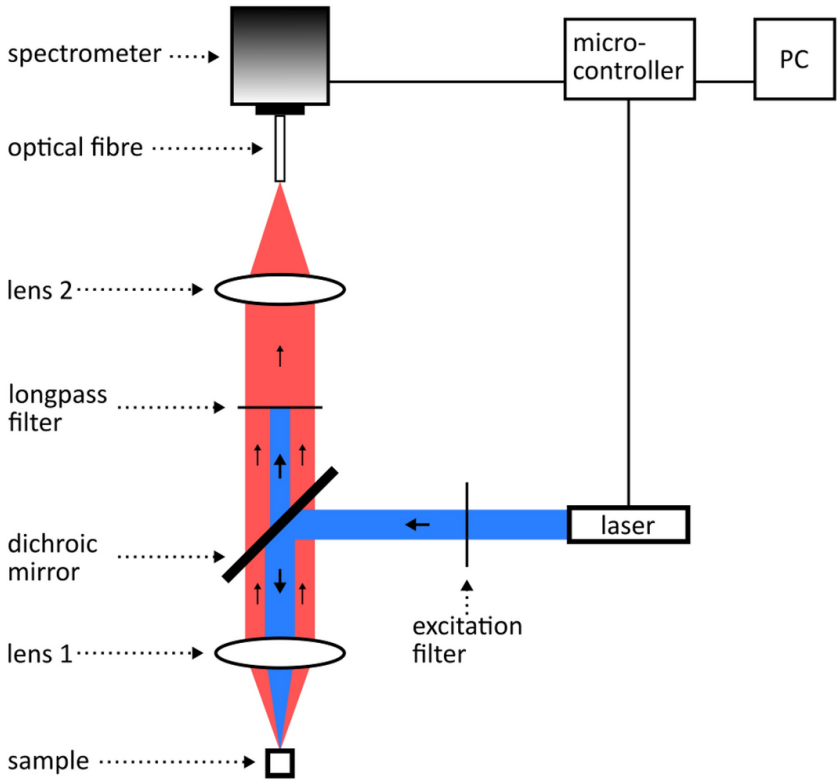

Figure 1.11: The PL spectrometer with excitation source (Laser: 405nm). The laser path is highlighted in blue. The path of PL emission from the sample is highlighted in red [198].

In addition to identifying microplastics (MPs) based on their intrinsic fluorescence, the most commonly used luminescence-based detection method involves staining MPs with dyes for efficient identification through fluorescence microscopy. The most critical property of a dye for microplastic identification is its high affinity for plastics. Nile red is the most commonly used dye for this purpose, though alternatives like Rhodamine B, textile dyes (iDyes), polyhedral oligomeric silsesquioxane (POSS), and perylene-bisimide (PDI) are also employed. The recovery rate of plastic particles has been achieved at 95%–100% using optimised staining protocols. After Nile Red staining, clear fluorescence enables effective identification of various plastics like PE, PP, PS, and nylon-6, though PVC, PET, PA, and tyre rubber exhibit dim or no fluorescence, with PET

and PA sometimes detectable due to intrinsic blue fluorescence [204]. A recent patent [205] demonstrated that nanogels effectively stain MNP with high affinity, enhancing Rhodamine B dye concentration and quantum yield. This results in bright emission spots on plastic surfaces, enabling sensitive detection of nanoplastics down to 100 nm.

Despite significant progress in using fluorescence-based techniques for polymer analysis, most reported studies have relied on a single excitation wavelength to investigate the intrinsic fluorescence emission of plastics [190, 191, 193-196]. While this approach has proven effective for specific polymers that exhibit strong fluorescence, it poses considerable limitations for others that produce weak or undetectable signals. The fluorescence response of polymers is highly dependent on their chemical structure, degree of crystallinity, and the presence of specific chromophoric groups, which may not be effectively excited at a single wavelength. Consequently, plastics with lower luminescence efficiency remain challenging to detect, leading to potential misclassification or incomplete analysis. Furthermore, some plastics exhibit inherent autofluorescence, particularly in the UV range, which can introduce complications such as inner filter effects, reabsorption, and background fluorescence [206]. These factors can reduce the signal-to-noise ratio, affecting the reproducibility and reliability of fluorescence measurements [207]. The influence of additives, fillers, and environmental contaminants further exacerbates these challenges, as they can introduce extraneous luminescent signals that interfere with the polymer's intrinsic fluorescence characteristics. A more comprehensive approach is required to overcome these limitations and improve the robustness of fluorescence-based polymer identification. Multi-probe excitation techniques, which utilise a range of excitation wavelengths, offer the potential to optimise fluorescence detection across different polymer types, enhancing the detection sensitivity of less luminescent plastics. This approach enables a more thorough exploration of the photophysical properties of microplastics, ensuring better discrimination between materials and minimising the influence of interfering factors. The following chapter will

present a detailed investigation into multi-probe excitation-emission mapping analysis of microplastics, demonstrating how this advanced experimental technique can address the limitations of single-wavelength excitation and provide more accurate and comprehensive fluorescence characterisation of plastic materials.

1.9 Portable and Microspectrometers

Over the years, advancements in miniaturisation have facilitated the creation of compact optical instruments through the development of smaller light sources, detectors, and optical components. This progress has also catalysed the emergence of portable and handheld spectrometers. These portable spectrometers have extensively been employed to characterise different materials [208] and monitor system health [209] and environmental pollutants [210]. These handheld devices primarily employ Raman, FTIR, their combination, and hyperspectral imaging techniques. Some popular commercial handheld spectrometers and their spectral acquisition methods are shown in Figure 1.12.

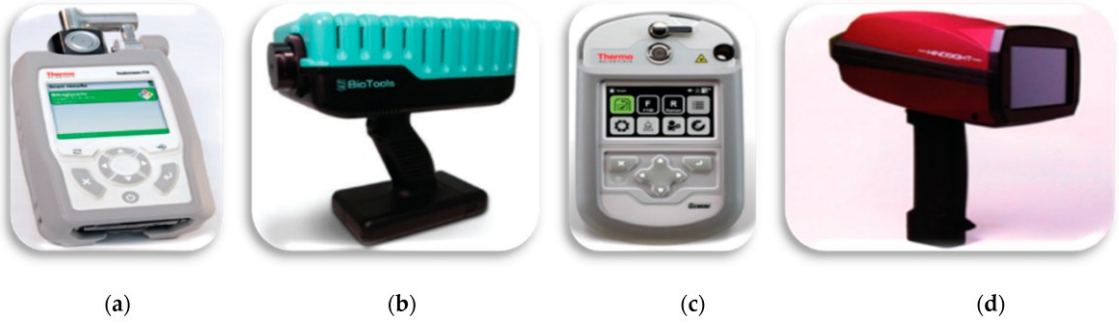

Figure 1.12: Commercial portable spectrometer: (a) Handheld FTIR spectrometer – Thermofisher Scientific (b) Handheld Raman Identifier – RAMTEST-CHE™ (c) Gemini FTIR/Raman analyzer - Thermofisher Scientific (d) Handheld hyperspectral imager GoldenEye™ – Bayspec [211].

These portable Raman and FTIR spectrometers are widely utilised in the pharmaceutical industry to inspect the quality of raw materials and detect counterfeit tablets. Portable FTIR spectrometers are also employed in monitoring pollutants emitted from combustion engines, factories, and chimneys. Additionally, these instruments are utilised for detecting dangerous gas leaks in

buildings [212]. Moreover, a comprehensive quantitative analysis of the alcohol blend can also be performed with a handheld FTIR spectrometer (TruDefenderFT - Thermofisher Scientific) [209]. This handheld device has also been used for quality control in road construction, wherein the quantitative determination of polypropylene maleic anhydride (PPMA) in bitumen was analysed to assess the quality of road construction material using FTIR-ATR based handheld spectrometer [213]. Furthermore, in-situ qualitative and quantitative analysis of hydrocarbon contamination in soil using handheld NIR spectrometers has also been reported [209]. Two different handheld Raman spectrometers with an NIR excitation source of 785nm (Ahura – Wilmington, USA and DeltaNu Inspector Raman – Laramine, USA) have been used for field identification of different minerals [214]. These handheld and portable spectrometers have also been used for biomedical applications. For example, a handheld Raman spectrometer was developed and used for clinical dermatological studies [215]. Another handheld Raman spectrometer (ACCUMAN PR-500) developed by Ocean Optics has also been tested to be a promising portable solution for the rapid and accurate identification of pharmaceutical materials. Ocean Optics offers another handheld Raman spectrometer (HRS-30) for non-technical users to swiftly identify hazardous chemicals and drugs using an in-built comprehensive spectral library [216].

The adoption of handheld spectrometers for identifying microplastic pollutants across different environments is increasingly gaining traction. In recent times, efforts have been made to develop portable solutions for analysing microplastic pollutants. For example, a handheld FTIR spectrometer has been specifically designed and utilised to detect meso- and microscale plastic particles collected from the coastal areas of Greenland [217]. Moreover, a low-cost and portable Raman sensor has been developed for detecting microplastics coated with magnetic particles, with the sample analysed in water using a quartz cuvette [218].

Moreover, recent advances in optical instrumentation and microfabrication have introduced a new generation of spectrometers that are not only compact and cost-efficient but also powerful enough

to support complex analyses [219]. Microspectrometers, which refer to spectrometric systems with miniaturised optical and electronic components, have increasingly become attractive for in situ analysis due to their portability, integration capabilities, and ease of deployment in field conditions [220, 221]. These devices are generally built around four main principles [219]: (i) dispersive optics, which use gratings or prisms to separate wavelengths onto a detector array spatially; (ii) narrowband filters, where either fixed or tunable filters isolate specific wavelength bands; (iii) Fourier transform designs, which rely on interferometry and computational Fourier analysis to achieve high resolution; and (iv) reconstructive approaches, where coded or overlapping filter responses are combined with algorithms to digitally recover the full spectrum.

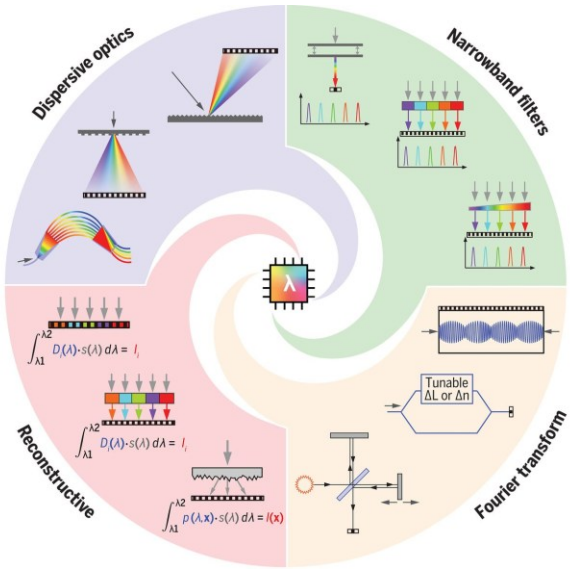

Figure 1.13: Schematic representation of the four main types of microspectrometer architectures. Dispersive optics (gratings/prisms), narrowband filters (fixed or tunable), Fourier transform (interferometry), and reconstructive methods (coded filters with algorithmic recovery) [219].

The optical design of a microspectrometer integrate several key components [222], including a light source, a dispersive or interferometric element (such as a grating [220, 223] or Fabry–Perot cavity [224-226]), focusing optics, and photodetectors into a single, compact package. Their development is closely tied to microelectromechanical systems (MEMS) [220, 227-229] and complementary metal-oxide-semiconductor (CMOS) technologies [230, 231], enabling scalable

manufacturing through standard semiconductor processes. The primary advantage lies in their ultracompact design [223, 232], low power consumption [230], and potential for mass production [233, 234]. These features have made them essential tools across multiple domains, including agriculture [235], aerospace [236], medical diagnostics [237, 238], industrial process control [239], chemical analysis [240, 241], and emerging environmental applications [242-244].

In the medical field, microspectrometers have been applied in non-invasive diagnostics such as pulse oximetry [245], skin cancer detection [246], and biochemical monitoring using near-infrared or visible spectroscopy [247]. Fluorescence-based microspectrometers have been integrated into wearable health monitoring systems, such as wrist-worn or adhesive patch biosensors [248]. Microspectrometers have also been used in point-of-care diagnostic devices for blood glucose monitoring [249], cholesterol assays [250], and COVID-19 antigen detection [251]. Industrial and process control applications involve monitoring gases, liquids, and solids during manufacturing. For instance, miniaturised FTIR spectrometers are deployed for gas sensing [228, 252] and to verify polymer compositions in production lines [253]. In space and aerospace sectors, microspectrometers have been integrated into satellite payloads for earth observation [254], atmospheric composition sensing [255], and mineral analysis on lunar and Martian surfaces [256].

The application of microspectrometers in the field of micro- and nanoplastic (MNP) detection remains rare in the literature. The detection and identification of MNP to date have been achieved using MEMS FTIR modules embedded in handheld systems [257, 258]. For example, a NeoSpectra MEMS Michelson FTIR spectrometer was used to detect sub-20 μm microplastic particles by ATR-FTIR, explicitly noting the MEMS miniaturised spectrometer at the core of the instrument, and comparing against a compact Raman unit for validation [257]. Another related on-site soil study [258] reported that compact instruments, including Bruker ALPHA II N-500 and NeoSpectra Scanner, were the most accurate among miniaturised options for detecting and classifying soil microplastics. Beyond FTIR, micro-optofluidic platforms now concentrate particles

into tiny reservoirs, allowing spectroscopy to be performed rapidly on-chip [259-261]. In a study [262], 100 μm plastics particles were trapped in micro-reservoirs and used Raman and FTIR analysis directly on the chip, demonstrating a clear route to integrated, high-throughput screening, even though the spectrometers themselves were still external to the chip. Research studies [263, 264] on miniturised spectrometers for microplastic detection highlight that while portable/handheld Raman and FTIR are established, chip-scale spectrometers (microspectrometers) are only now becoming technically mature, with integrated designs leading to reduced size and cost while maintaining proper resolution for field classification tasks.

Considering the MP detection capabilities associated with both FTIR and Raman techniques, designing a portable spectrometer that integrates both methods could enhance the efficiency of monitoring MP in the environment. However, in-situ detection of microplastics in the environment can be challenging, considering the low concentration of MP in the large control volume of environmental samples. FTIR measurements necessitate the separation of MP from the matrix prior to analysis, and the absorption of IR light by water renders FTIR-based handheld spectrometers unsuitable for in situ monitoring of MP. Raman spectroscopy, on the other hand, often suffers from fluorescence interference, particularly when analysing weathered plastics or samples containing organic matter, which can obscure the Raman signal. In addition, the relatively weak Raman scattering efficiency demands longer acquisition times or higher laser powers, both of which are less practical for rapid field-based measurements.

Therefore, there arises a necessity for a portable solution capable of detecting and identifying microplastics in water, even at low concentrations. Conventional techniques such as FTIR and Raman, while powerful, face significant challenges in these conditions: FTIR suffers from strong water absorption and requires prior separation of particles, while Raman is hindered by fluorescence interference and weak signal intensity, which limit its effectiveness in rapid field measurements. To address these issues, we conceived the idea of developing a portable PL

spectrometer. PL spectroscopy overcomes both sets of limitations by operating in a spectral region with minimal water interference and by providing high sensitivity through excitation-emission measurements. This enables the detection of particles at extremely low concentrations, down to parts per billion (ppb). The design and construction of the PL spectrometer for MNP detection and identification are detailed in Chapter 5, Sections 5.2 and 5.3.

Chapter 2: Fluorescence Excitation-Emission Mapping Analysis of Microplastics

The work presented in this chapter has been adapted from the following publication [1].
S. A. Iqrar, A. Bibi, R. Chinnambedu Murugesan, D. Hill, and A. Rozhin, "Excitation–Emission Fluorescence Mapping Analysis of Microplastics That Are Typically Pollutants," Photochem, vol. 4, no. 4, pp. 488-500, 2024.

2.1 Introduction

Micro- and nano plastics (MNPs) pose a significant threat to marine and human life due to their immense toxicity. To protect these ecosystems, the development of reliable technologies for MNP detection, characterisation, and removal is vital. While FTIR and Raman spectroscopy are established methods for MNP analysis, fluorescence (FL) spectroscopy has recently emerged as a promising alternative. This is due to its inherently higher sensitivity, lower detection limits, and minimal interference from water in aqueous samples. However, most prior research relies on FL emission probing with a single excitation wavelength for MNP detection. In this study, we introduce a two-dimensional (2D) fluorescence excitation-emission (FLE) mapping method for the detection of commonly found microplastics, namely polystyrene (PS), polyethylene terephthalate (PET), and polypropylene (PP). The FLE mapping technique enables the collective recording of emission spectra across a range of excitation wavelengths, revealing the dominant excitation–emission features of different microplastics. This research advances the field by offering a non-destructive and label-free identification of MNP contamination through the use of FL spectral fingerprints. The graphical representation of this work is shown in Figure 2.1.

2.2 Microplastic Sample Preparation

PS, PET, and PP microplastic samples were measured in aqueous media. The samples, which had been mixed with deionised water at 4.5% *w*/*v*, had previously been prepared by cutting macroscopic source materials into pieces < 1 mm with the use of stainless steel laboratory scissors. Specifically, for the sources, PS millimetre-size beads were purchased from Acros Organics (average 250,000 M.W.), PET plastic was collected from Aqua-Vale

plastic water bottles (London, UK), and PP film was obtained from packaging material (Thermo Fisher Scientific, Horsham, UK).

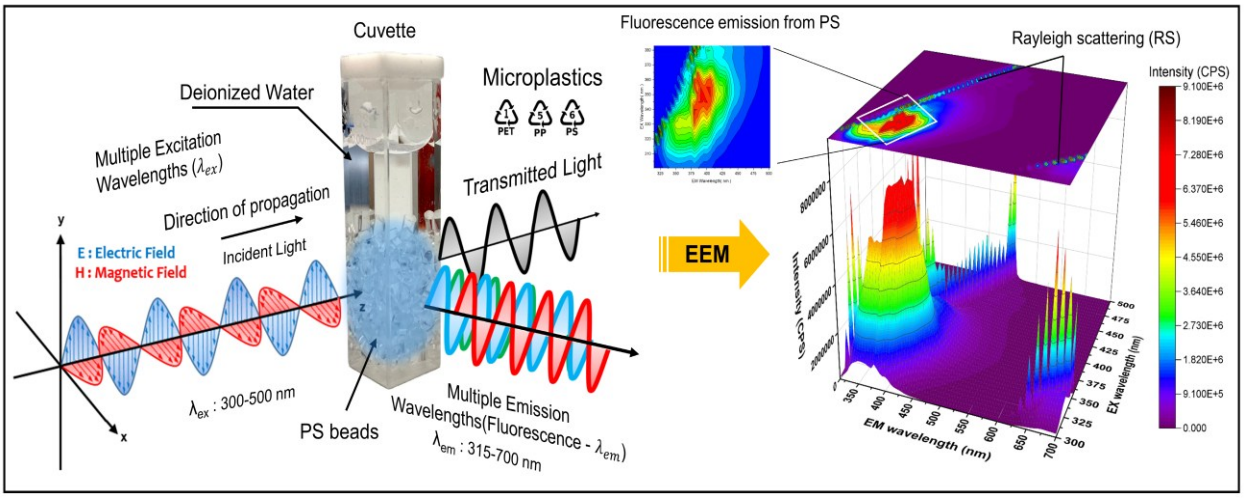

Figure 2.1: Graphical representation of microplastic detection and identification process through Fluorescence Excitation-Emission Mapping technique.

2.3 Methods for Characterising Microplastics

2.3.1 Scanning Electron Microscopy

SEM imaging of the filtered sample was undertaken using a Benchtop SEM JEOL, JCM-6000-plus scanning electron microscope. Scans were recorded in high-vacuum high definition secondary electron diffraction mode (SED) with an accelerating voltage of 15 kV and a magnification of 50x. Prior to imaging, the samples underwent vacuum filtration using an oil-free piston pump (Fisher brand FB70155) through 0.7µm glass fibre membrane filter paper (Merck, Product No. AP4002500) before being transported onto a glass slide and imaged without any metallic coating.

2.3.2 X-Ray Photoelectron Spectroscopy (XPS)

An XPS analysis of the polymer samples was done to determine their chemical constituents and elemental composition of polymer samples (PS, PET, and PP) and to investigate the

presence of impurities and various organic functional groups or elements in the samples with their relative atomic concentration. XPS measurements were obtained using a Thermofisher ESCALAB 250Xi photoelectron spectrometer equipped with a hemispherical sector energy analyser with a standard monochromatic Al Kα X-ray source (1486.6 eV) to enhance the resolution. The samples were analysed using a source excitation energy of 15 KeV and an emission current of 6 mA, an analyser energy of 50 eV with a step size of 0.1 eV, and a dwell time of 50 ms. As XPS measurements require dry samples, dry pieces of microplastics were used, i.e., PS cylindrical microbeads (1±0.2 mm <diameter> 0.4±0.1mm and 3±0.1mm <length> 2.5±0.2mm), PET (from Aqua-Vale plastic water bottles - London, UK), and PP (from packaging material - Thermo Fisher Scientific, Horsham, UK) square sheets (length x width ≈ 2x2mm).

2.3.3 Raman Spectroscopy

A Raman spectroscopy analysis of the fragmented microplastics was performed to confirm the various functional groups of the different plastic materials. These were carried out using a proprietary free space micro-Raman spectroscopic system based on a Horiba MicroHR spectrometer equipped with a Sygnature CCD detector. The spectrometer has a spectral resolution of 0.25 nm and a scanning range of 0 - 1500 nm, while a 40x Melles Griot's microscopic objective with a numerical aperture of 0.65 was used. The excitation source used within the setup was a continuous wave 532 nm Nd: YAG laser (G4 plus 150 Elforlight) with a linewidth of less than 2 MHz. The excitation wavelength (532nm) was chosen to maximise the Raman signal while reducing the fluorescence contributions from samples. Although shifting to longer excitation wavelengths, such as 785 nm or 1064 nm, can further reduce fluorescence interference, this comes at the cost of a significantly reduced Raman signal intensity, since the Raman scattering efficiency scales with $1/\lambda^4$. So, the Raman scattering efficiency decreases sharply with increasing excitation wavelength, following an inverse fourth-power dependence. This means longer wavelengths yield much weaker Raman signals, making detection more challenging. At 1064 nm,

for example, the Raman signal is much weaker, requiring higher laser powers or longer acquisition times, both of which can lead to sample heating or impractical measurement conditions. Moreover, detector sensitivity is another limiting factor; silicon-based detectors used for visible wavelengths perform poorly in the near-infrared. Therefore, moving to higher excitation wavelengths would necessitate the use of InGaAs detectors, which are more expensive and typically noisier. The 532 nm wavelength was therefore chosen as a practical compromise, balancing Raman signal strength, fluorescence suppression, and detector performance. All Raman signals were collected in reflection mode with an integration time of 1 second per pixel, while Raman spectra had manual baseline correction applied to remove contributions from fluorescence and the detector's saturation.

2.3.4 Fluorescence Spectroscopy

The fragmented MPs in an aqueous medium were analysed using a HORIBA Nano-Log spectrofluorometer that contains a 450 W xenon short-arc lamp housing with an off-axis ellipsoidal collector. The Fluorescence excitation-emission (FLE) maps of different microplastics were recorded for a range of excitation wavelengths from 300-500 nm with an emission range of 315-600 nm. The experiment involved exciting the samples with a monochromatic beam, which had a spectral slit width of 2 nm and an excitation wavelength step of $\Delta\lambda = 5$ nm. The emissions produced were then detected within an emission monochromator using the same slit width and wavelength steps integrated with an FL-1073 UV-visible room-temperature photomultiplier tube. Figure 2.2 presents the schematic for the FL measurements of different microplastics, with the incident monochromatic beam interacting with the microplastic sample contained in a cuvette. Some of the light passes through the sample, while the rest is either scattered or absorbed. The absorbed light excites the microplastic (MP) electrons, transitioning them from ground to excited states. As these electrons return to their ground state, they release energy in the form of a photon at a specific wavelength. To investigate the impact of DI water on the fluorescence signal, the FL

measurements of DI water were recorded separately. The auto-fluorescence signal of different microplastics was recorded at θ = 90^0 for a range of excitation (λ_{ex}) and emission (λ_{em}) wavelengths. The instrument was calibrated using both excitation and emission calibration methods before the FL measurements of microplastic samples. For excitation calibration, the system was scanned across a range of 200–600 nm with 1 nm increments, 0.1 s integration time, and a slit width of 1 nm. The xenon lamp source produced a calibration peak at 467 nm, which was used to validate the excitation accuracy of the instrument. For emission calibration, deionised (DI) water was placed in a quartz cuvette and excited at 350 nm, with emission spectra collected from 360–450 nm in 1 nm steps. The characteristic Raman peak of water, corresponding to the O–H stretching vibration, was observed at 397 nm. This confirmed the emission wavelength calibration of the instrument and ensured reliable reference alignment before analysing the microplastic samples. The recorded EEM data were analysed using the Windows-based FluorEssence software (v3.9.0.1), which has integrated Origin software.

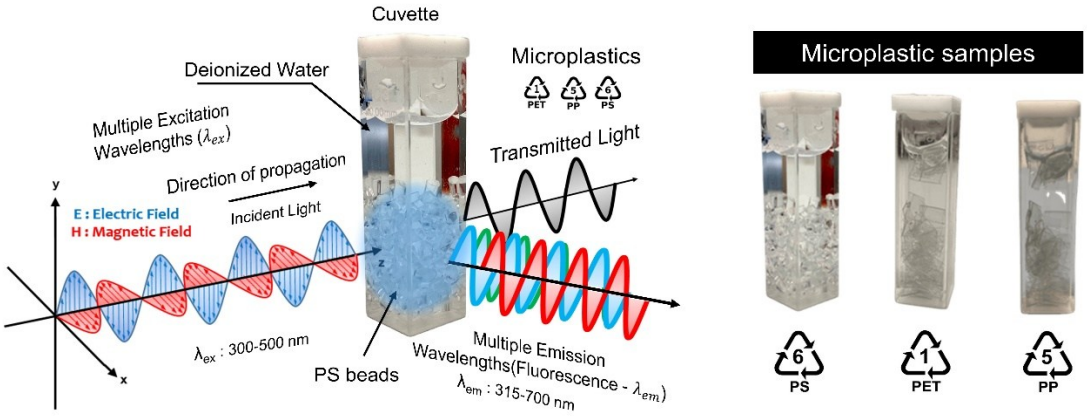

Figure 2.2: A schematic diagram of multiple excitations and multiple fluorescence emissions from the sample of different microplastics, i.e. PS, PET, and PP, in an aqueous medium.

2.4 Results and Discussion

2.4.1 Characterisation of MPs

Scanning Electron Microscopy: Figure 2.3 shows SEM images of PS, PET, and PP microplastic samples, showing their surface morphologies and size distributions estimated to be 250 µm-600 µm, 300 µm-950 µm, and 200 µm-750 µm, respectively. The thicknesses of the PET and PP particles cut from a plastic bottle and food packaging material, respectively, were measured at 250 µm, while the PS sample taken from cylinder beads was comparatively thicker (≥ 350µm). The surfaces of PET and PP pieces were observed to be smooth, whereas PS beads contained rough and uneven surfaces with inhomogeneously distributed holes.

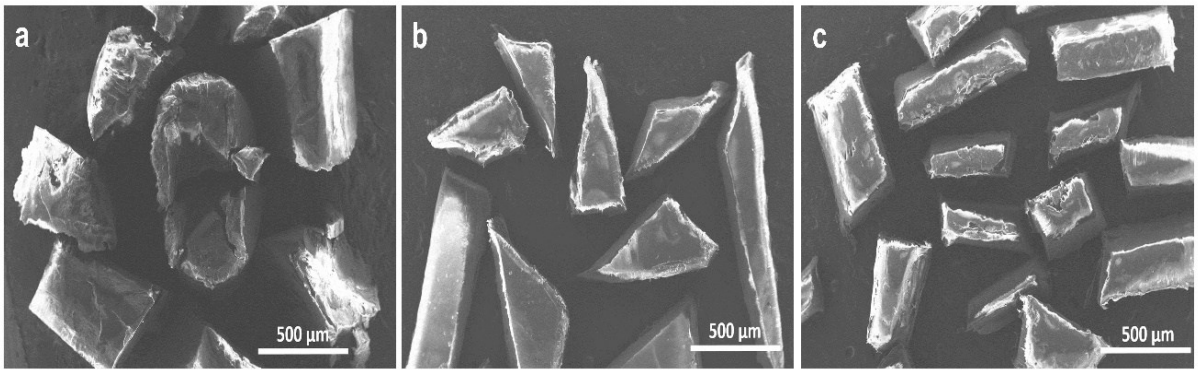

Figure 2.3: SEM images indicating the surface morphologies of (a) polystyrene – PS, (b) polyethylene Terephthalate - PET & (c) polypropylene – PP.

X-ray photoelectron spectroscopy: The relative concentrations of chemical impurities in the samples were confirmed through XPS measurements to be 1.8%, 3.1%, and 5% for PS, PET, and PP, respectively (Table 2.1). In addition to these impurities, our results showed a considerable percentage of C-O bonds in polystyrene (7%) and polypropylene (11.2%) samples. The detected C-O bonds suggest surface-level oxidation, a well-established phenomenon in polymer surface chemistry. Previous studies indicate that PS and PP, though primarily hydrocarbon-based, can undergo oxidation when exposed to ambient air, resulting in oxygenated groups such as C-O and C=O on the polymer surface [265, 266]. This process is often initiated

by prolonged atmospheric oxygen exposure, UV radiation, or handling during sample preparation [266]. Moreover, the PS sample contained a negligible fraction of ZnO with no characteristic intrinsic fluorescence emissions in the analysed mapping range and also has no tendency to overlap in spectroscopic properties with common fluorophores [267-269]. On the other hand, PET and PP samples contain some additional chemical species to ZnO, such as siloxane, C-N, calcium carbonate ($CaCO_3$), and sulphates in minor fractions. These additional components likely stem from common additives and fillers used during plastic manufacturing. For example, siloxane compounds, are frequently incorporated as processing aids or surface modifiers, especially in polyolefins, to improve flow properties and surface finish [270]. Calcium carbonate ($CaCO_3$) is widely used as a low-cost filler that enhances stiffness, printability, and mechanical properties, such as tensile modulus and impact resistance [271]. C-N species likely arise from stabilisers or residual processing chemicals, while sulphate residues may be introduced from inorganic additives or surface treatments during production and handling [272, 273]. Meanwhile, siloxane (Si-O-Si) is intrinsically considered to be non-fluorescent due to its flexibility caused by its bond length (0.164±0.003 nm) and large bond angle (135-180^0) [274]. The bond length refers to the actual atomic distance between silicon and oxygen atoms in the Si-O bond, not a molecular spacing. The relatively long Si–O bond and its wide bond angle create a highly flexible and non-rigid network. This structural flexibility prevents the formation of extended π-conjugated systems that are typically responsible for fluorescence. The large bond angle, in particular, allows the Si–O–Si linkage to rotate and bend easily, enabling rapid non-radiative relaxation of excited states. Together, the bond length and bond angle contribute to an electronically localised and flexible framework, which dissipates excitation energy through vibrations rather than radiative fluorescence [275]. The remaining sample impurities in PET and PP also show no intrinsic fluorescence emissions, including $CaCO_3$ [276], carbon-nitrogen bond [277], and sulphates [278]. Hence, the intrinsic fluorescence emissions reported hereafter in this study for the MPs are purely from their corresponding polymers.

Table 2.1: Elemental composition of PS, PET, and PP samples using XPS spectroscopy.

Element	Relative atomic concentrations (%)		
	Polystyrene (PS)	**Polyethylene terephthalate (PET)**	**Polypropylene (PP)**
C─C/C─H	91.2	74.5	83.8
C─O	7.0	22.5	11.2
Si	─	2.2	3.9
Zn	1.8	0.1	0.1
N	─	0.4	0.7
Ca	─	0.2	0.2
S	─	0.2	0.1

2.4.2 Raman Spectroscopic Analysis

Figures 2.4-2.6 display the obtained Raman spectra for PS, PET, and PP microplastics, with Raman bands assigned based on established standards [279-281]. In Figure 2.4, the predominant Raman band appearing at 1001 cm^{-1} is attributed to the ring breathing mode of polystyrene, while the sharp shoulder observed at 1031 cm^{-1} correlates well with the C-H in-plane deformation mode. Additional bending and stretching modes of PS are observed at 621 cm^{-1} (Ring deformation mode), 1155 cm^{-1} (C-C stretch), 1450 cm^{-1} (CH2 scissoring), 1583 cm^{-1} (C=C stretch), and 1620 cm^{-1} (Ring skeletal stretch), respectively [279].

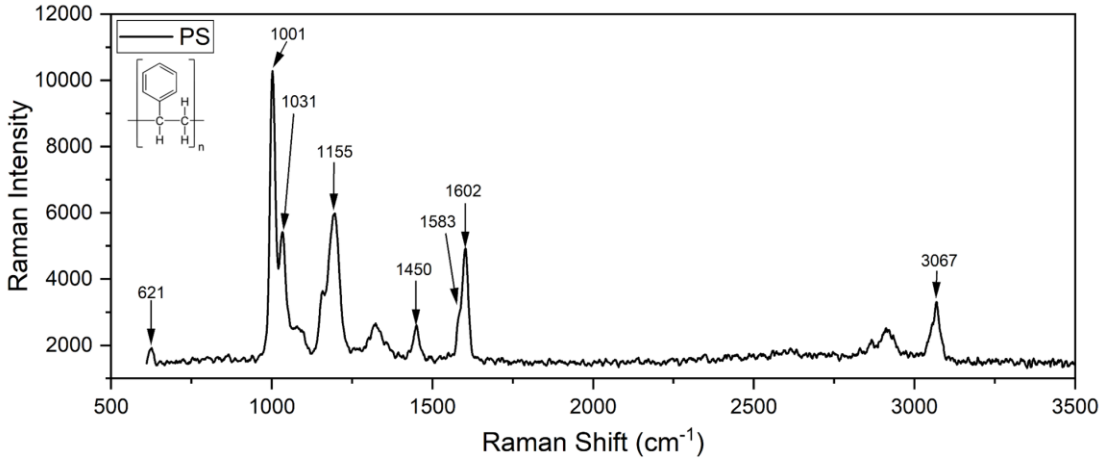

Figure 2.4: Raman spectrum of polystyrene (PS) with corresponding prominent peaks related to the specific vibrational state of the PS.

Figure 2.5 shows the Raman spectrum of PET, in which the intense band at 1594 cm^{-1} is due to the presence of the C─C bond in the aromatic ring. The formations of additional bands at 1100 cm^{-1}, 1165 cm^{-1}, 1276 cm^{-1}, 1402 cm^{-1}, and 1707 cm^{-1} correspond to the -C(O)-O (ester) and C-C bonds, C-H & C-C stretch (ring in-plane vibration), C(O)-O stretching, CCH bending, and OCH bending and stretching C=O vibrations, respectively. The observed results correlated well with those reported elsewhere [280].

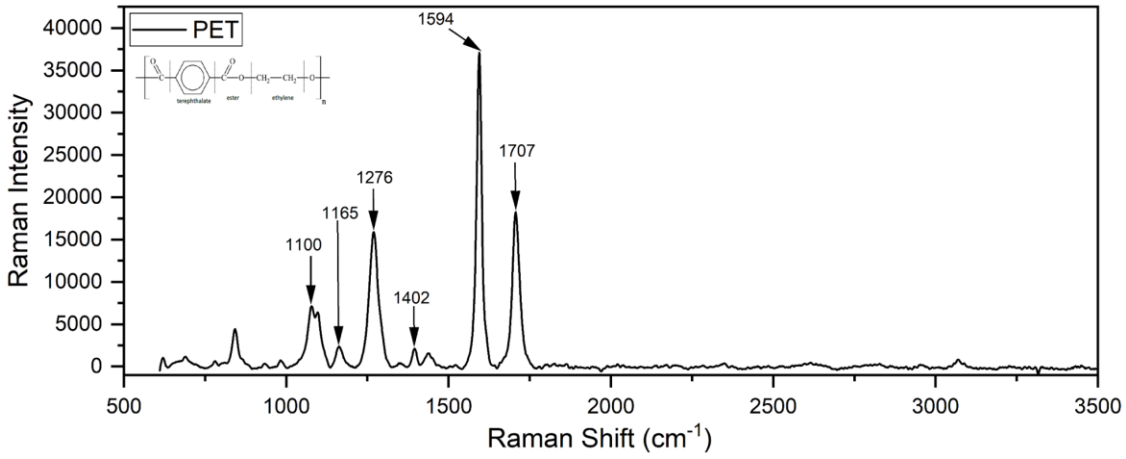

Figure 2.5: Raman spectrum of polyethylene Terephthalate (PET) with corresponding prominent peaks related to the specific vibrational state of the PET.

Figure 2.6 illustrates the spectrum of PP, featuring a broad peak (2800-3000 cm^{-1}) comprising a prominent band at 2892 cm^{-1} and two corresponding shoulders at 2847 cm^{-1} and 2963 cm^{-1}, representing the stretching vibrations of the C-H bond [281]. Other vibrational modes observed include those at 811 cm^{-1} and 977 cm^{-1}, 1155 cm^{-1}, 1331 cm^{-1}, and 1460 cm^{-1}, which can be associated with various stretching and bending motions: C-C stretching and CH_3 bond rocking, C-C stretching and CH bending, CH stretching, CH_2 wagging, and CH_3 bending, CH_2 bending, and CH_3 asymmetric bending, respectively [282].

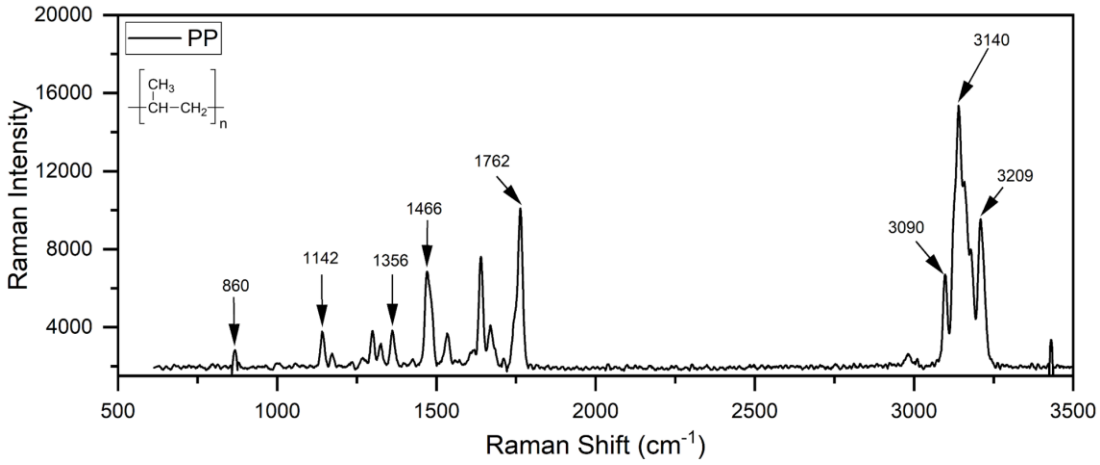

Figure 2.6: Raman spectrum of polypropylene (PP) with corresponding prominent peaks related to the specific vibrational state of the PP.

The Raman vibrational bands associated with the dominant spectral peaks of all measured microplastics, i.e., polystyrene, polyethylene terephthalate, and polypropylene, are shown in Table 2.2.

Table 2.2: The vibrational bands corresponding to prominent Raman peaks of different microplastics (PS, PET, and PP).

Microplastic	Raman peaks (cm^{-1})	Corresponding vibrational band
Polystyrene	621	Ring deformation mode
	1001	Ring breathing mode
	1031	C-H in-plane deformation
	1155	C-C stretch
	1450	CH_2 scissoring
	1583	C=C stretch
	1602	Ring skeletal stretch
	3067	C-H vibrations
Polyethylene Terephthalate	1100	Ester C(O)-O and C-C bond
	1165	Ring in-plane C-H & C-C stretch
	1276	C(O)-O stretching
	1402	CCH bending and OCH bending
	1594	C-C bond in the aromatic ring
	1707	Stretching of C=O vibrations
Polypropylene	860	C-C stretching and CH_3 rocking
	1142	C-C stretching and CH bending
	1356	CH stretching, CH_2 wagging, and CH_3 bending
	1466	CH_2 bending and CH_3 asymmetrical bending
	1762	C=O stretching vibration
	3090-3209	Stretching vibrations of C-H

2.4.3 Fluorescence Mapping Analysis of Microplastics

The FLE maps of all three microplastic samples, PS, PET, and PP, are shown in Figure 2.8. For PS microplastic (Figure 2.8a), the FLE map illustrates a 2D contour map with an intensity scale bar displaying bright emissions in the λ_{em} wavelength range of 350-450 nm when excited within the λ_{ex} range of 300-400 nm. The PET microplastic exhibits a distinctive FLE map (Figure 2.8b) with two separate FL emission regions. The first region demonstrates FL emissions between 370-510 nm when excited between 330-380 nm, while the second region showcases emissions from 400-530 nm when excited between 380-485 nm. Notably, emissions in the first region (λ_{em} = 330-380 nm) are substantially more intense than those in the second region (λ_{em} = 380-485 nm). Polypropylene (PP) displays an FLE map with two prominent FL emission regions similar to those of PET (Figure 2.8c). In the first region, high-intensity FL emissions are observed between 400 and 550 nm when excited between 360 and 380 nm, while the second region shows relatively lower-intensity emissions between 425 and 550 nm when excited between 385 and 430 nm.

The FLE maps (Figures 2.8a-c) offer valuable insights into the optimal excitation wavelengths for each microplastic type, resulting in FL emission spectra of high intensity, as depicted in Figure 2.8d. Our findings indicate the following: The most effective excitation wavelength for PS is observed at 360 nm, yielding two major peaks at 380 nm and 400 nm; PET performs optimally with an excitation wavelength of 360 nm, resulting in three emission peaks, with the primary peak at 390 nm; and PP exhibits the most intense FL with an excitation wavelength of 370 nm and the maximum FL intensity recorded at 450 nm. The measurements reveal Stokes shifts of 40 nm, 30 nm, and 70 nm for PS, PET, and PP, respectively. In the literature, different Stokes shift ranges have been reported for microplastics depending on the excitation wavelength used. For polystyrene (PS), Stokes shifts between 30-50 nm have been observed [197, 283, 284], while polyethylene terephthalate (PET) typically shows shifts in the range of 40-50 nm [285-287]. Polypropylene (PP) has been reported to exhibit larger Stokes

shifts, typically ranging from 80 to 100 nm [288, 289]. The values measured in this work (40 nm for PS, 30 nm for PET, and 70 nm for PP) fall within or closely align with the reported ranges, confirming consistency with previous studies while also reflecting some variation due to differences in excitation conditions and sample characteristics. To ensure the accurate measurement of FL emissions from all the microplastics, we conducted FLE mapping on deionised (DI) water in a cuvette without microplastic particles. The results indicate the absence of FL from DI water (Figure 2.7). This confirms that the recorded emissions from the microplastic samples exclusively originate from the fragmented microplastics themselves.

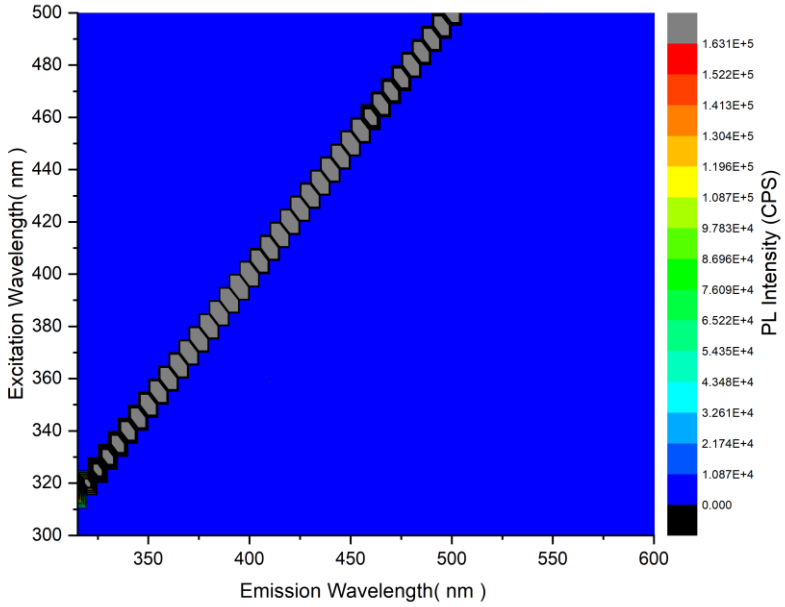

Figure 2.7: Fluorescence Excitation-Emission map of pure deionised water, recorded in a quartz cuvette.

Our results confirm that the spectral characteristics of the examined microplastics (PS, PET, and PP) differ from each other. Therefore, by exciting PL at their respective optimal wavelengths, one can potentially distinguish and identify them based on their distinctive FL spectral fingerprints.

Furthermore, the emissions from microplastics observed in this study are identified as fluorescence rather than phosphorescence. Fluorescence arises from the radiative decay of

singlet excited states ($S_1 \rightarrow S_0$) and typically occurs on the nanosecond timescale, which matches the instant emission recorded here. Phosphorescence, by contrast, involves a spin-forbidden triplet–singlet transition ($T_1 \rightarrow S_0$) and appears on much longer timescales (microseconds to seconds). Additionally, the Horiba Nanolog system used in this work is specifically designed to capture fluorescence signals and does not record long-lived phosphorescence. For these reasons, the observed emissions are attributed exclusively to fluorescence.

In general, the fluorescence emission mechanism from microplastics, including polystyrene (PS), polyethylene terephthalate (PET) and polypropylene (PP), arise from intrinsic photophysical processes associated with the chemical structure of these polymers. Each polymer contains chromophoric groups that, upon excitation, emit characteristic fluorescence signals due to π-conjugated bonds or other reactive functional groups introduced through polymerization and environmental ageing. For example, PS contains aromatic rings that facilitate π-π* transitions, resulting in distinctive fluorescence under UV excitation, whereas PET's carbonyl and ester linkages contribute to strong n-π* and π-π* transitions that result in detectable fluorescence emissions when excited within specific wavelength ranges [286, 290]. In PP, fluorescence is typically weak due to its non-aromatic structure. However, environmental factors such as surface oxidation and UV exposure can induce oxygenated groups (C-O, C=O) on the PP surface, enhancing the fluorescence signal and enabling detection [291]. Moreover, a sharp change observed around 370 nm excitation in Figure 2.8(c) may be due to an instrumental artefact of the Horiba Nanolog system, such as a changeover point in the excitation monochromator optics or correction algorithm in this wavelength region. These artefacts can occasionally appear as discontinuities in excitation-emission maps. The fact that such a step is seen in PP but not in PS or PET may be related to the much weaker fluorescence response of PP. Because its emission is weaker, even small instrumental irregularities in excitation intensity or detector response

become more noticeable in the FLE map, whereas in strongly fluorescent polymers like PS and PET, the signal dominates and masks such effects.

To gain further insight into identifying different microplastics based on their optimised single-probe excitation wavelength, the spectral fingerprints of all microplastics were extracted from their respective FLE maps. The extracted spectral fingerprints from 2D excitation-emission maps of all microplastics (PS, PET, and PP) are presented in Figure 2.9 (a-c). Figure 2.9a displays three distinct spectra for polystyrene, recorded at excitation wavelengths (λ_{ex}) of

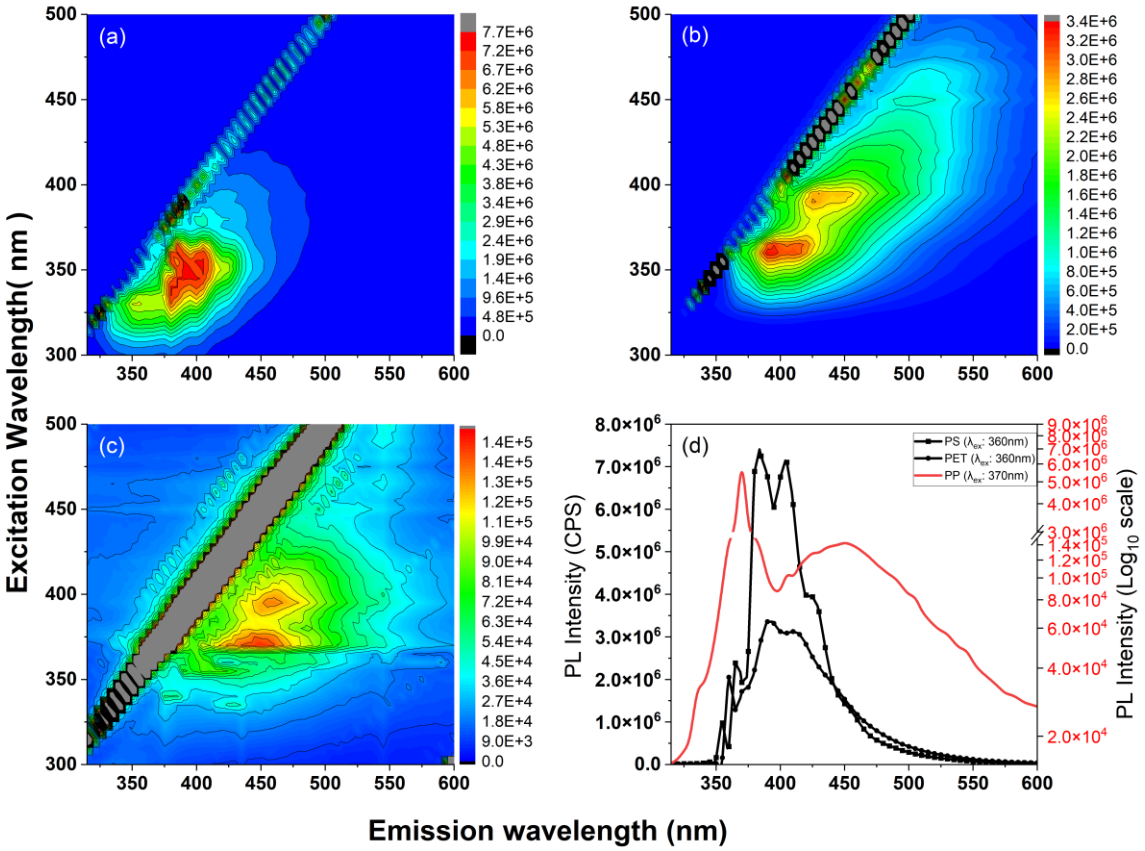

Figure 2.8: Two-dimensional FL excitation-emission (FLE) maps of (a) polystyrene-PS microbeads, (b) polyethylene terephthalate-PET (c) polypropylene-PP & (d) FL spectra of PS (solid black line with squares), PET (solid black line with circles), and PP (solid red line), recorded at optimized excitation wavelengths 360nm, 360nm, and 370nm, respectively. The scale bar for (a-c) represents fluorescence emission intensity in counts per second (CPS).

310 nm, 360 nm, and 405 nm. The figure shows that when excited at λ_{ex} =310 nm, the FL spectrum of PS exhibits a peak centred at 355 nm, accompanied by weak shoulder peaks at 380 nm, 400 nm, and 425 nm. Increasing the excitation wavelength to 360 nm significantly (~3.3 times) enhanced the FL intensity compared to that from the excitation at 310 nm. Within this region, the FL emission peak splits into two maxima at 380 nm and 405 nm, indicating characteristic FL originating from conjugated styrene units [292]. Moreover, a broad shoulder is recorded at λ_{em} 425 nm and λ_{em} 455 nm, indicating that the FL emissions originate from π-conjugated bonds [293]. Thereafter, at the excitation wavelength of 405 nm, another broad emission spectrum centred at 435 nm, with a shoulder at 460 nm, is observed, aligning well with previously published results for a single-wavelength excitation at 405 nm for PS microplastics [197]. The sharp peak in the FL spectrum for λex 405nm (Figure 2.9a) may be attributed to the Rayleigh scattering of the PS microplastics. Finally, it is notable that while prior studies have reported FL emissions from polystyrene in the range of 300-330 nm when excited at λ_{ex} 253-265 [290, 294, 295], our FLE mapping study indicates that the dominant FL emission for PS microplastic detection occurs at λ_{ex} 360 nm, which is approximately 3.3 times higher than that at λ_{ex} 310 nm and roughly 7 times higher than that at λ_{ex} 405 nm.

Figure 2.9b shows three distinct spectral fingerprints extracted from the FLE map of PET microplastic. The two spectra recorded at excitation wavelengths λ_{ex} 330 nm and 360 nm correspond to the first bright emission zone of the 2D FLE map of PET in Fig. 2.8b, while the spectrum recorded at λ_{ex} 405 nm belongs to the second emission region of the same figure. The first spectrum in Figure 2.9b shows that when excited at 330 nm, there is a broad peak with emission maxima centred at 390 nm, along with a weak shoulder at 410 nm, while the second spectrum at 360 nm shows a significant increase in emission intensity (approximately 5.6 times), resulting in prominent FL emission maxima at 390 nm and 410 nm. All the above fluorescence emissions for the excitation wavelengths 330 nm and 360 nm occurred due to the π*←n electronic

transition associated with the carbonyl group of the conjugated phenylene ring. These emissions are quite likely due to the interaction of the carbonyl group with the π-electrons of the phenylene ring, which reduces coplanarity and speeds up the π*←n transition of the non-coplanar C=O group [296]. Similarly, the FL emission bands at 390 and 410 nm from PET polymer were previously reported by Days and Wales [297] at an excitation wavelength of 340 nm, and they were associated with the ground state monomer, dimer, and excimers of polyethylene terephthalate [286, 287, 298-301]. Further increasing the excitation to 405 nm causes consecutive redshifts with the observation of FL emissions with broad maxima at 460 nm (Figure 2.9b). However, among all acquired FL spectra from PET, the most intense fluorescent emission was observed at λ_{ex} 360nm, which is ~1.8 times higher than that at λ_{ex} 405nm.

Figure 2.9c displays the dominant FL features of polypropylene (PP), with the first spectrum corresponding to an excitation of 350 nm exhibiting a broad FL emission with maxima centred at 435 nm. Increasing the excitation wavelength to 370 nm, the second spectrum shows that the FL emission intensity is significantly enhanced (approximately 2.7 times higher than that at 350 nm) and results in a 20 nm redshift in the emission maxima. The FL emission at 455 nm is associated with the presence of polyenone, and as the polyene length increases, it implies the formation of complexes such as excimers or exciplexes [289]. Increasing the excitation wavelength to 405nm leads to additional redshifts, as seen in the third spectrum, resulting in an emission at 465 nm and additional shoulder humps, different from those seen previously, at 445 nm (shoulder), 465 nm (main peak), 550 nm (shoulder), and 665 nm (shoulder). The emissions at 455 nm and the broadening of the spectrum are indicative of a higher degree of oxidation [301]. Based on the analysis conducted through FLE mapping, it was determined that polypropylene exhibits the highest FL emission when excited at 370 nm, resulting in an emission peak at 460 nm.

Based on the extracted spectra of all three microplastics (MPs) shown in Figure 2.9, the spectra selected as fingerprints were those exhibiting the highest fluorescence emission intensity when

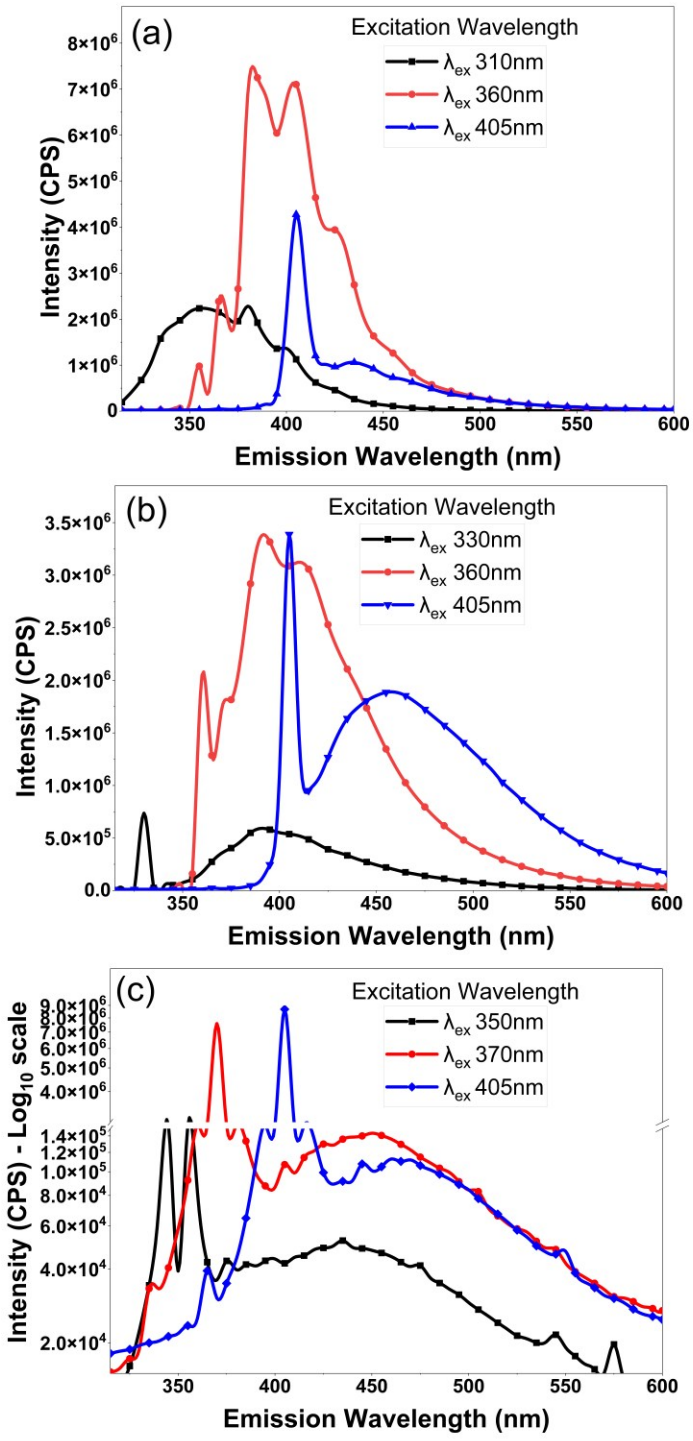

Figure 2.9: Fluorescence spectra acquired from (a) polystyrene at excitation wavelengths λ_{ex} 310nm (solid black line), λ_{ex} 360nm (solid red line), and λ_{ex} 405nm (solid blue line), (b) polyethylene terephthalate at excitation wavelengths λ_{ex} 330nm (solid black line), λ_{ex} 360nm (solid red line), and λ_{ex} 405nm (solid blue line) (c) polypropylene at excitation wavelengths λ_{ex} 350nm (solid black line), λ_{ex} 370nm (solid red line), and λ_{ex} 405nm (solid blue line).

excited at their respective optimal wavelengths. These unique intrinsic emissions from each type of MP can serve as reference spectral fingerprints for real-time analysis of environmental microplastic samples. Researchers can more accurately identify and quantify microplastics using these reference spectra in various environmental contexts, even with a suitable small-scale excitation light source and portable USB-type spectrometer. The novelty of our approach lies in optimising excitation wavelengths, as conventional methods typically use a single excitation wavelength, yielding a weaker emission signal. Our study achieves a significantly enhanced emission signal by using optimised wavelengths, thereby improving the sensitivity and applicability of this method for detecting microplastics in real aquatic samples. Furthermore, This technique enables the rapid and label-free identification of microplastics with minimal sample preparation, offering a non-destructive approach for accurately detecting and characterising microplastics in aqueous environments. Moreover, environmental factors such as surface oxidation can further enhance fluorescence signals, offering spectral fingerprints unique to each polymer type [302].

The challenge of distinguishing microplastics (MPs) from other organic materials in real aqueous environments can be catered to using the unique excitation-emission characteristics of MPs observed in this study. MPs exhibit distinct spectral profiles due to their polymeric structures and specific additives, differentiating them from natural organic matter that are commonly present in aquatic samples [303]. However, in some cases, the fluorescence spectra of microplastics overlap with the spectra obtained from organic matter, which can complicate the detection and identification process [150, 197]. By carefully selecting an optimised excitation wavelength, the intrinsic fluorescence of MPs can be enhanced while minimising interference from other organic compounds, a strategy also highlighted in a recent fluorescence-based detection study [304]. In our work, the “optimal” excitation wavelengths were not chosen solely based on producing the strongest or maximum emission intensity. It was also observed that at these wavelengths, the

emission spectra of different microplastics exhibited distinctive and non-overlapping features. This spectral uniqueness makes the technique practically useful for environmental applications, where microplastics can be distinguished from one another and from other organic materials based on their characteristic fluorescence fingerprints. Furthermore, studies have also suggested that integrating machine learning or spectral pattern recognition could significantly improve this method's ability to distinguish MPs from organic materials present in the aquatic sample [305, 306]. These methodological considerations will allow our approach to distinguish MPs better in real aqueous environmental matrices.

2.5 Chapter Conclusion

In this study, we employed Fluorescence Excitation-Emission (FLE) mapping analysis to investigate microplastic contaminants extracted from polystyrene, polyethylene terephthalate, and polypropylene macroscopic materials to gain insights into their dominant intrinsic FL excitation and emission features. Through our analysis, we determined the most intense fluorescence emissions against the optimal excitation wavelengths for each type of microplastic.

- For polystyrene, peak emissions occurred at 380 nm and 405 nm when excited at 360 nm.
- Polyethylene terephthalate exhibited its most intense emissions at 390 nm when excited at 360 nm.
- Polypropylene displayed its dominant emissions at 455 nm when excited at 370 nm.

These distinct fluorescence emissions originated from different molecular properties: Polystyrene's emissions were tied to its conjugated styrene units; for polyethylene terephthalate, emissions were linked to dimerisation and phenylene-carbonyl transitions; Polypropylene's emissions were associated with polyenone excimers. The unique fluorescence spectra and optimal excitation wavelengths identified for each microplastic type can be invaluable for precise, label-free identification and detection. Our study provides a foundation for the development of a

non-destructive and label-free fluorescence spectroscopic method for analysing microplastics across various environmental settings, including plants, food, and aquatic ecosystems. This research holds promise for improving our ability to monitor and address the impact of microplastics in diverse environmental matrices.

Chapter 3: Efficient Generation of Suspensible Secondary Reference Micro-and Nanoplastic Particles by Direct Ultrasound Treatment

The work presented in this chapter was carried out in collaboration with a colleague, Jordi Valls-Conesa, from Aalborg University, Denmark. His contribution focused specifically on the characterisation of ultrasonicated microplastics using QCL-based FTIR spectroscopy combined with machine learning classification (section 3.3.2).

3.1 Introduction

Acquiring secondary environmental MNP is a challenging, labour-intensive, and time-consuming task. Therefore, the development of laboratory-scale methods for generating reference MNP that replicate the characteristics of environmental MNP is essential. This chapter presents a simple and rapid direct ultra-sonication technique for producing MNP from polystyrene, polymethyl methacrylate, polypropylene, and polyvinyl chloride. Compared to other reported methods, the direct ultrasonication technique presented in this work offers several advantages. Cryogenic milling produces a wide particle size range (1-200 μm) with poor suspensibility and requires additional treatments to aid dispersion [116, 130]. Laser ablation can generate nanoscale particles with good dispersion, but is limited to the sub-micron range and cannot produce larger fragments [117]. The cryotome method yields uniform fibres but cannot produce fragments or spheres, which are more representative of environmental debris [121]. Bottom-up chemical synthesis produces smooth, spherical particles that lack the irregular morphologies of environmental MNPs and often involve residual chemical contaminants [122, 124, 126, 307, 308]. In contrast, the direct sonication method used here yields environmentally relevant secondary MNPs spanning nano- to microscale sizes (100 nm-150 μm), with diverse morphologies (fragments, fibres, and spheres) and stable suspensibility in water without the need for chemical additives. The morphological characteristics of the ultrasonicated MNPs were examined using SEM, which revealed that fragments constitute the dominant shape across all polymers, with fibres appearing only rarely. Importantly, the ultrasound treatment preserves the chemical composition of the generated MNPs, as confirmed

by Raman spectroscopic analysis conducted on particles ranging in size from 5 to 150 μm. Furthermore, the generated MNP were classified using a random forest machine learning model applied to images captured by a quantum cascade laser infrared (QCL-IR) microscope. The stability of the ultrasonicated MNP suspension was assessed through ultraviolet-visible transmission spectroscopy, which demonstrated that the produced microplastics maintain high suspensibility (>2 hours) in an aqueous medium. These attributes make the MNP generated via direct sonication highly suitable as reference materials for research purposes.

3.2 Methodology for Secondary Microplastic Generation

3.2.1 Sample Preparation

We used four different types of plastics, i.e., polystyrene (PS), polypropylene (PP), polyvinyl chloride (PVC), and polymethyl methacrylate (PMMA). The cylindrical-shaped millimetre-sized PS beads (average M.W. 250,000) were purchased from Acros Organics; PP sheets were obtained from a packaging material (Thermo Fisher Scientific); PVC (high molecular weight beads) were purchased from Sigma-Aldrich (81387-250G); and PMMA beads (average M.W. 35,000) were purchased from Acros Organics (9011-14-7). Each plastic sample was prepared separately in 6 mL of deionised water in a glass vial. Cylindrical PS beads (diameter between 1±0.2 mm and 0.4±0.1 mm; length between 3±0.1 mm and 2.5±0.2 mm) were added to one vial, with approximately 1500 μg of PS. In separate vials, 650 μg each of PVC and PMMA were prepared in 6mL of DI water. Additionally, a large PP sheet (~1×1 cm^2, ~530 μg each) was cut into 3×3 mm^2 pieces and placed in a glass vial (6 mL DI) for ultrasound treatment (Figure 3.1 - Fragmentation).

3.2.2 Direct Ultrasound Treatment

The homogenous dispersion and disintegration of larger plastic pieces (PS, PP, PVC, and PMMA) in DI water were achieved using high-power (P_{max} ≈ 400 watts) pulsed ultrasound waves

with a laboratory-grade Hielscher ultra-sonicator (UP400S). The plastics were exposed to high-power (0.75 P_{max}) and high-frequency (24 kHz) cyclic ultrasound waves continuously for 7 hours. The titanium sonotrode (H3-tip, 3 mm diameter, 100 mm full length) was partially immersed (15% of its total length) into the sample, as shown in Figure 3.1. The power and cycles of ultrasound waves were controlled with a digital ultrasonic processor (Ultrasonicator, UP400S, Hielscher Ultrasonics GmbH, Germany). Prior to the disintegration of plastics, the samples (PVC and PMMA) were mixed in DI water for 120 seconds at 500 rpm using a Topmix Vortex mixer (Fisher Scientific FB15012). The sonotrode tip was cleaned before each experiment with DI water and wiper sheets (Kleenex - 07432010) to avoid cross-contamination of microplastic samples.

The ultrasound method was selected as the fragmentation technique because it overcomes many of the limitations of existing methods, such as cryo-milling, laser ablation, cryotome, and bottom-up synthesis (see chapter 1, section 1.6), and produces micro- and nanoplastics that more closely resemble environmentally weathered particles in terms of shape, size diversity, and suspensibility. Previous studies [127, 128, 309] have also demonstrated the potential of ultrasound for generating MNPs. For example, a 15 kHz ultrasonic bath treatment successfully produced micro- and nanoplastics after 15 hours of processing [309]. In contrast, we employed a direct sonication approach, which is more efficient and achieved the disintegration of larger plastic pieces into microplastics within 7 hours.

The chosen frequency of 24 kHz corresponds closely to the cavitation threshold described by the Blake threshold formulation [310], where bubble formation and collapse generate the high shear forces required for polymer fragmentation. Frequencies significantly higher than this reduce cavitation efficiency, while lower frequencies risk incomplete dispersion [311]. Thus, 24 kHz represents an effective compromise between strong cavitation and stable, reproducible processing. The operating power of ultrasound waves was optimised experimentally. Initially, the sonotrode was operated at full output (400 W, 100% power), but this resulted in cracking of the glass vial and sample leakage due to excessive energy input and heat generation. The power

was then gradually reduced in steps (95%, 90%, 85%) until stable operation was achieved at 75% of maximum power (≈300 W), which was sufficient to generate cavitation and produce MNPs without damaging the vials.

The ultrasonication process to generate MNPs consisted of three key steps. In the first step (fragmentation), PP sheets (1 cm^2) were cut down to smaller square sheets (3 mm^2) to facilitate further processing. In the second step (ultra-sonication), these smaller sheets were placed in a 10 mL glass vial with DI water and subjected to ultrasound treatment. Finally, in the third step (sample collection), the generated MNPs were collected from the sonicated sample into a separate vial using a laboratory pipette (SciQuip SP1000A) and a plastic pipette tip (Sigma-Aldrich CLS4821).

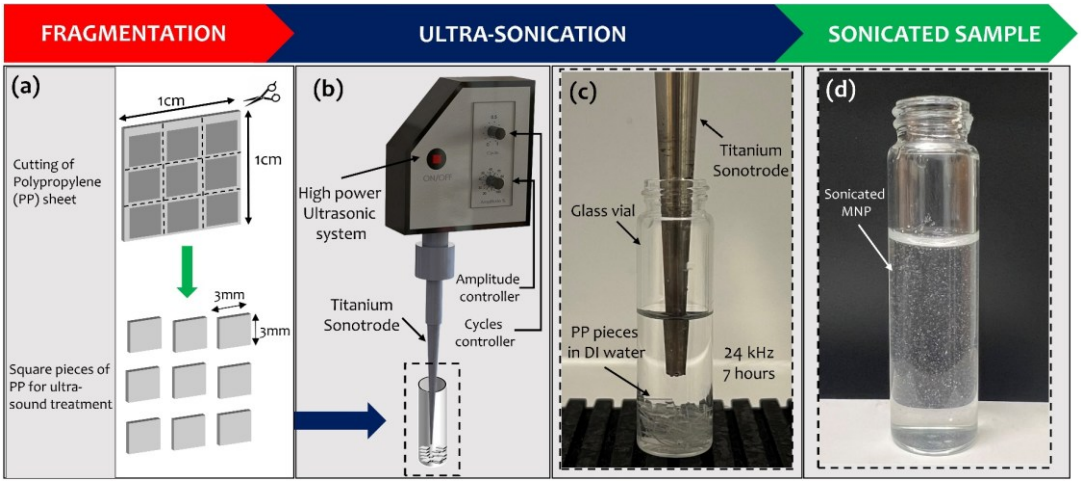

Figure 3.1: Process flow of MNP bulk generation using high-power direct ultra-sonication treatment. (a) Fragmentation shows the cut-down of large plastic sheets of PP, PS (cylindrical pallets), PMMA, and PVC (granular powder). (b) and (c) The ultrasonication step shows the cyclic ultrasound treatment of cut-down plastic pieces of PP with titanium sonotrode of 24kHz for 7 hours. (d) Finally, the sonicated sample step shows the generated suspensible reference secondary MNP.

3.2.3 Vacuum Filtration of US-MNPs

Following ultrasound treatment, the sonicated samples were transferred to 10 mL transparent glass vials. The samples then underwent sequential filtration using a vacuum filtration system powered by an oil-free piston pump (Fisherbrand FB70155), as illustrated in Figure 3.2. Polycarbonate membrane filters (PCMF) with varying pore sizes were used for this process.

Initially, the samples were filtered through 1.2 µm pore size PCMF (RTTP02500, Merck UK). The residue from this filtration was transferred to a 15 mL glass vial containing deionised water (DI) and agitated in a topmix vortex mixer at 1500 rpm for 10 minutes, effectively releasing microplastics larger than 1.2 µm into the DI water. The filtrate from this step was collected in a Buchner flask.

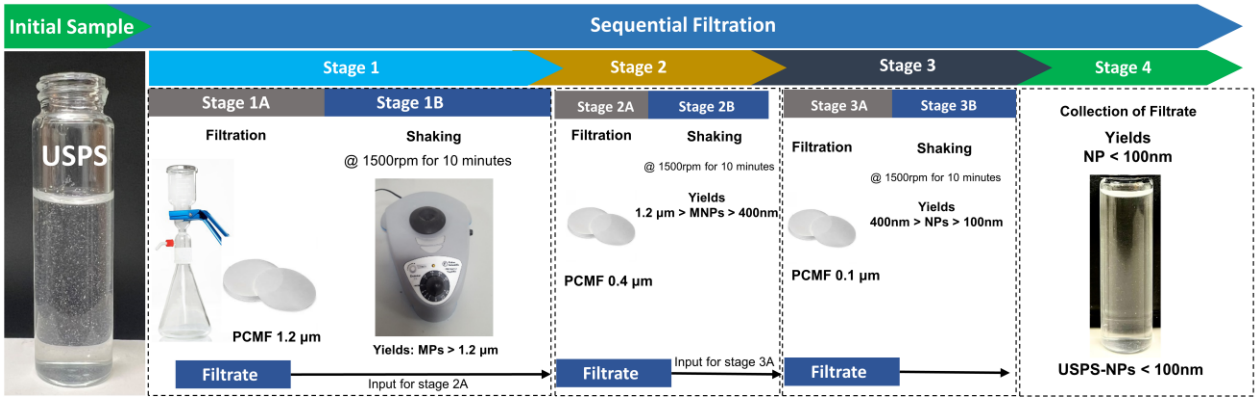

Figure 3.2: Schematic diagram of sequential filtration process for ultrasonicated micro- and nanoplastics using standard vacuum filtration and shaking process.

In the second step, the filtrate was filtered through 0.4 µm pore size PCMF (HTBP02500). The residue collected was similarly agitated to isolate microplastics ranging from 400 nm to 1.2 µm. In the final step, the remaining filtrate was filtered through 0.1 µm pore size PCMF (VCTP02500) to isolate nanoplastics between 100 nm and 400 nm, while the filtrate containing particles smaller than 100 nm was collected separately. This sequential filtration process was applied to all four types of sonicated plastics (PS, PP, PVC, and PMMA). The resulting filtered samples were then transferred to individual 10 mL glass vials for further characterisation.

3.3 Results and Discussion

3.3.1 Morphological Analysis of US-MNPs

The morphological characteristics of US-MNP samples were analysed using an ultrahigh-resolution field emission scanning electron microscope (FESEM, JEOL IT-800). The samples were deposited onto copper tape (75 × 25 mm) to provide a conductive surface, minimising

charging effects during electron microscopy. To prevent any sample distortion or alteration of surface features, the drying conditions were optimised by placing the samples in a universal oven (MEMMERT UN30) at 40 °C for 4 hours. The imaging process was conducted under high vacuum conditions, using high-definition secondary electron diffraction (SED) mode to capture detailed surface morphology. A range of magnifications was employed to ensure a comprehensive analysis of the particle features: 270× and 1700× to examine larger particle structures (field of view at 10 μm) and 4000× to resolve finer details (field of view at 5 μm). An accelerating voltage of 15 kV was used to achieve optimal resolution while minimising electron beam damage to the samples.

The application of high-power and periodic ultrasound waves induced strong vortices due to cavitation in the water medium, which rigorously displaced and degraded the parent polymer beads and sheets. The changes in surface morphology of different plastics before and after ultra-sonication were examined using SEM analysis (Figure 3.3). The SEM data show that the direct ultrasound treatment significantly damaged the surface of raw PS and PP plastic sheets and beads. After continuous and intense ultrasonication, the PP sheets remained transparent, whereas the PS beads turned opaque. The opacity change in PS beads is likely due to a combination of surface roughening, increased microcracks, loss of homogeneity, and enhanced light scattering [312, 313] caused by cavitation. In contrast, PP remains transparent due to its semi-crystalline structure, higher resistance to surface damage, and better elasticity [314], which helps it withstand ultrasound-induced stresses. When subjected to direct sonication, the edges of PS and PP plastics underwent more deformation compared to their central surfaces (Figures 3.3b and 3.3d). Additionally, surface irregularities such as holes and cracks were also observed on the deformed plastic sheets and beads.

After the sonication process, the initially transparent deionised water became partially cloudy due to the presence of suspended US-MNPs. Among the sonicated liquid samples, PP

and PVC remained relatively transparent compared to PS, which exhibited more significant cloudiness. In contrast, the PMMA sample became completely opaque, displaying considerable cloudiness. This change in PMMA was due to its higher brittleness and lower resistance to mechanical stress [315], which made it more susceptible to fragmentation under intense and repeated sonication, resulting in greater dispersion of micro- and nanoplastic particles.

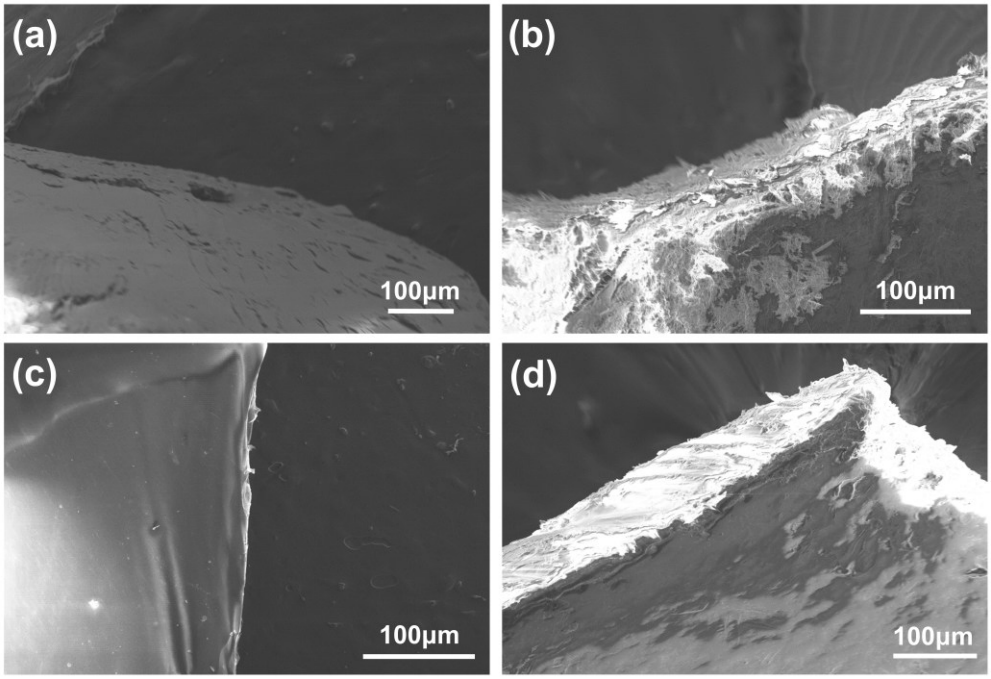

Figure 3.3: The surface morphology of plastic beads and sheets before and after the ultrasound treatment. PS: (a) before (b) after ultrasonication; PP: (c) before (d) after ultrasonication.

Figure 3.4 shows SEM images of ultra-sonicated MNP plastics (PS, PP, PVC, and PMMA) recorded before sequential filtration. The images reveal particles of varying sizes (200 nm-100µm) and diverse morphologies, including fragments, fibres, and semi-spheres. The ultra-sonicated PS particles are observed to be random in shapes with a wide distribution of sizes (Figure 3.4a). Some nanoscale (below 1 µm) PS particles are also observed (Figure 3.4b). After sonication, the PP sample shows homogenously distributed MNPs with different shapes. Most of the generated microplastics are irregularly shaped, with sizes varying between 2 -15 µm. However, some larger fragments (30-50 µm) and fibres (100-150 µm) are also found in the sample (Figure 3.4 c-d). The

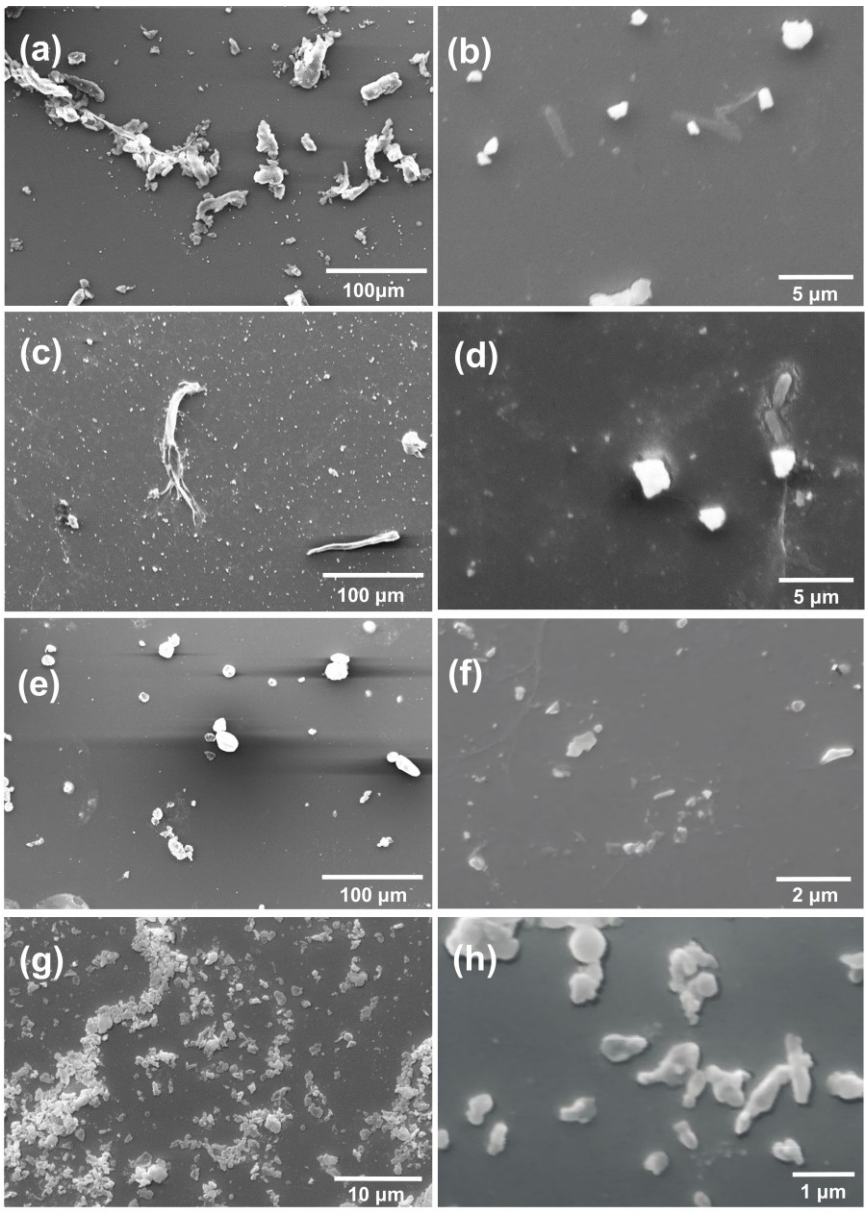

Figure 3.4: The surface morphology of ultrasonicated MNPs recorded before filtration using scanning electron microscopy (a-b) polystyrene –PS (c-d) polypropylene- PP (e-f) polyvinyl chloride - PVC (g-h) polymethyl methacrylate – PMMA.

PVC sonicated sample shows numerous fragments, with the most particles having a size below 100 µm. Several nanoscale PVC particles are also observed (Figure 3.4e-f). Compared to all sonicated polymers, PMMA produced the most uniformly distributed and highly concentrated MNPs, which can be attributed to its material properties. PMMA is an amorphous polymer with relatively low crystallinity and a glassy structure, making it more brittle under mechanical stress

[316] compared to semi-crystalline polymers such as PP or PVC. Under ultrasound-induced cavitation, this brittleness promotes more efficient fragmentation into smaller and more uniformly sized particles [317]. In addition, PMMA surfaces tend to become more hydrophilic after mechanical breakdown, which enhances dispersion and prevents aggregation [318], contributing to the higher concentration and stable suspensibility of the generated MNPs. Most of the particles were observed to be in the same size range, and several particles were found in the submicron range (Figure 3.4 g-h).

Figure 3.5 presents SEM images of ultra-sonicated PS, PVC, and PMMA MNPs recorded after sequential filtration, recording different size ranges of the generated US-MNPs. The images reveal a broad size distribution from 100 nm to 10 μm, along with various morphologies, including fragments, fibres, and semi-spheres. The ultra-sonicated PS particles exhibit random shapes and a wide size range from microns to submicrons (Figures 3.5 a-c). Larger PS microplastics (>1.2 μm) are shown in Figure 3.5a, while submicron PS nanoplastics are depicted in Figures 3.5b and 3.5c. The sonicated PVC sample displays randomly shaped fragments and agglomerated micro- and nanoplastic particles (size range from 500 nm to 1μm), with most particles in the micron range (Figure 3.5d) and some nanoplastics rarely distributed (Figures 3.5e and 3.5f). PMMA produced the most uniformly distributed and highly concentrated micro- and nanoparticles, with particles densely agglomerated into clusters, resulting in a higher concentration of micron-scale particles (Figure 3.5g) and low-concentration nanoplastics, primarily in the form of fragments (Figures 3.5h and 3.5i). The sonicated PP sample shows homogenously distributed micro- and nanoplastic particles of randomly shaped fragments, with a rare distribution of MNP particles compared to other samples and extremely low concentrations in the submicron range (Figures 3.5k and 3.5l).

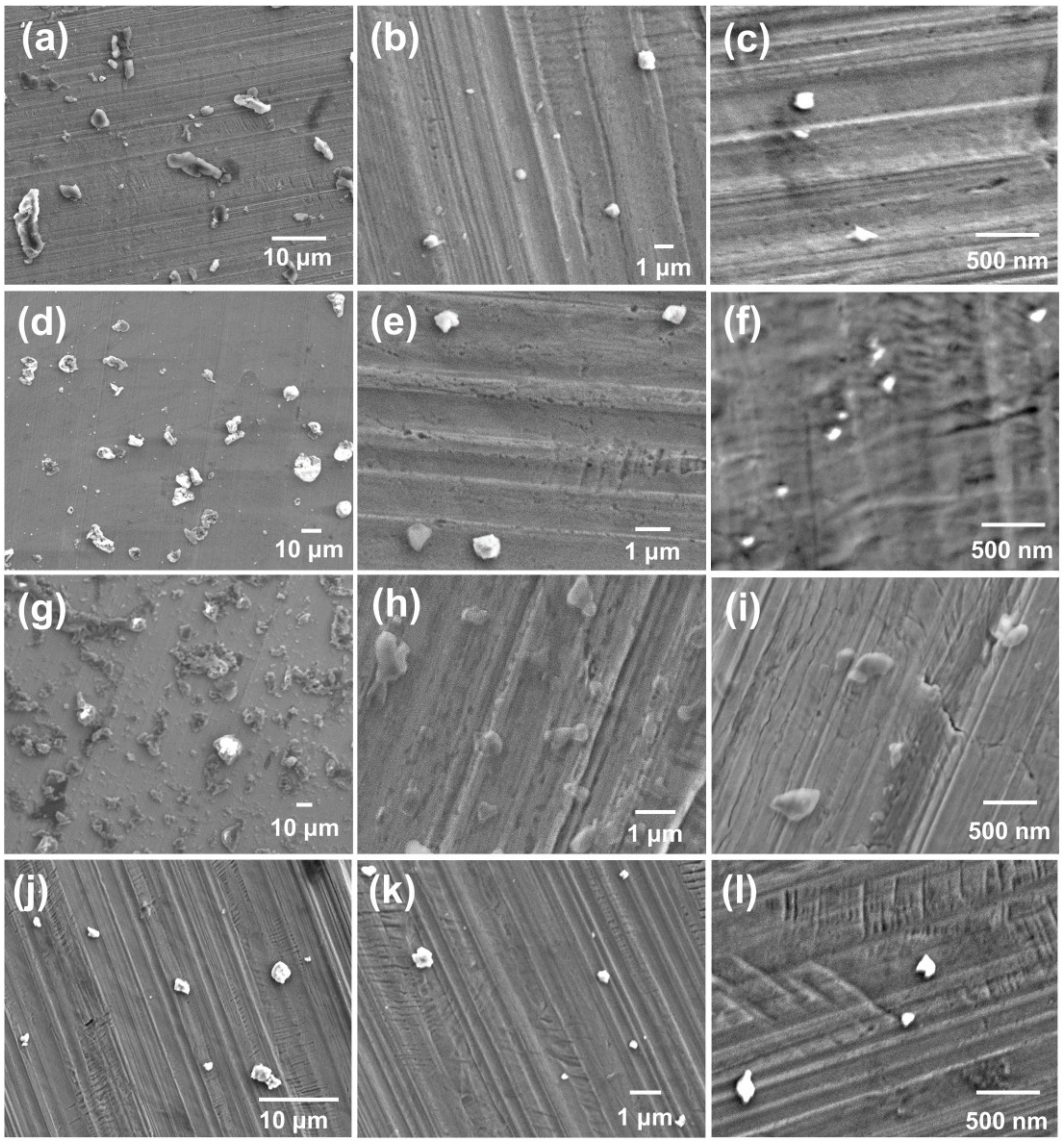

Figure 3.5: The surface morphology of different classes of ultrasonicated MNPs recorded using scanning electron microscopy (a-c) polystyrene –PS (d-f) polyvinyl chloride- PVC, (g-i) polymethyl methacrylate – PMMA (j-l), and polypropylene – PP.

3.3.2 Size Distribution and Sample Composition of Generated US-MNPs

The US-MNP samples were characterised using an advanced infrared (IR) spectrometer equipped with a prototype quantum cascade laser (QCL) microscope developed by Bruker [319]. This advanced instrument was employed to examine the chemical composition of MNP particles. Prior to analysis, the MNP particles were filtered onto aluminium oxide anodiscs (25 mm diameter, 0.2 µm pore size) via vacuum filtration. The detection limit for the QCL microscope was

constrained to particles larger than 5 μm due to the physical limitations of IR light transmission. Following the scanning of samples using the QCL-based FTIR spectrometer, the acquired data was processed for automated classification and identification. This process utilised two complementary approaches, Fast Background Correction and Identification (FBCI) and Machine Learning Classification (MLC), enabling efficient and precise analysis of MP particles. The FBCI method [320] automatically generates binary segmentations to isolate particles of specific polymer types from the spectral data. By eliminating the need for manual data processing, FBCI efficiently extracts valuable information about the targeted particles. In MLC, a Random Forest (RF) classification model was implemented [321] to accurately and rapidly identify up to 10 different types of MP polymers present in the samples. This approach not only allowed for precise particle identification but also enabled the detection of impurities or the presence of other polymer types within the samples. The RF model utilised the IR spectral fingerprints of different MNPs as a basis for extracting features from the IR data, ensuring accurate classification results.

The calibration of the QCL-based hyperspectral imaging system was performed through spectral alignment, background correction, noise reduction, and validation steps [321]. Wavenumber calibration was conducted using reference spectra from pure microplastic samples to ensure accurate spectral alignment. Background and baseline correction were applied using Fast Background Correction and Identification (FBCI) to remove distortions from environmental factors. Signal-to-noise ratio thresholding was used to filter out low-quality spectra, improving overall accuracy. The classification performance of the system was validated using ground truth samples (reference microplastic samples with known composition and IR characteristics), with a Random Forest model trained on high-fidelity reference spectra. Additionally, a single optimal baseline channel around 1840 cm^{-1} was selected to correct baseline offsets and maintain spectral consistency. These calibration steps ensured the system provided reliable and reproducible microplastic classification.

The classification of US-MNP samples using FTIR imaging and the RF Method provided valuable insights into the composition and contamination levels of ultrasonicated samples (Figure 3.6). This approach employed a winner-takes-all (WTA) representation [321], where classification predictions are encoded at varying brightness levels. The machine learning-processed IR hyperspectral image of USMNPs-PS (Figure 3.6a) shows a significant presence of sonicated PS

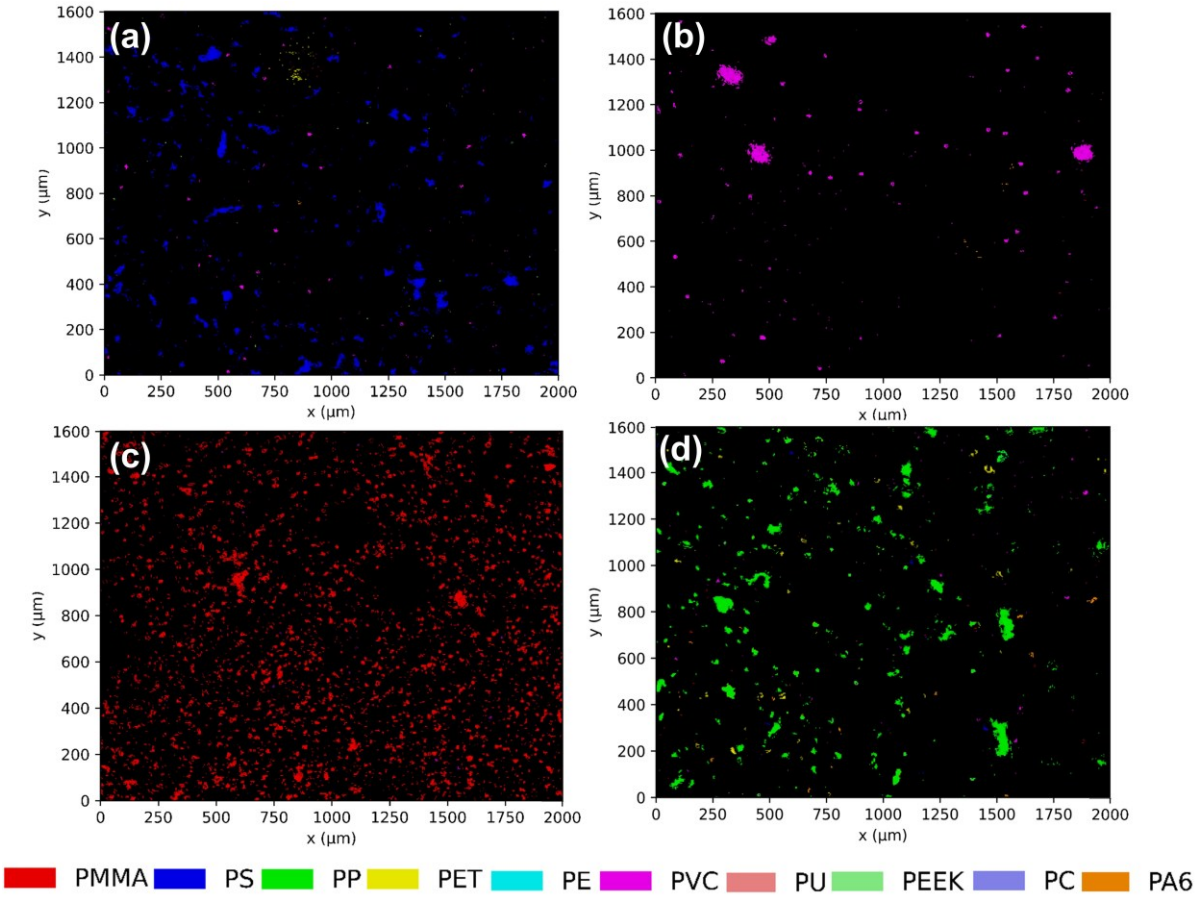

Figure 3.6: Simulated test image data of ultra-sonicated MNP samples and environmental background data from the data set. Visualisation of output for MP classification applied to the IR hyperspectral image. The size distribution of (a) polystyrene-PS, (b) polyvinyl chloride (PVC), (c) polymethyl methacrylate (PMMA), and (d) polypropylene (PP) is presented in the colour bar.

particles (96.63%), represented by blue particles of varying sizes and shapes. Minor impurities, primarily PVC and PMMA, are also detected in the USPS sample. The classification outputs for USPMMA (red particles) and USPVC (pink particles), shown in Figures 3.6b and 3.6c, respectively, exhibit high purity, with particle concentrations exceeding 98%. Similarly, Figure 3.6d

shows the USPP sample (green particles), which maintains a high purity of 97.32%, with only minor traces of PS, PVC, PMMA, and other polymers, each contributing less than 1.2% of the composition. These findings align with previous studies employing RF classifiers for microplastic identification [321-324], which have demonstrated high accuracy in distinguishing polymer types based on IR spectral signatures. The effectiveness of the RF classification method is because of its ability to handle spectral similarities among different polymers while minimising noise and background interference. This is achieved through selective feature extraction, using only highly discriminative wavenumbers to improve differentiation. The ensemble learning approach increases generalisation by mitigating misclassifications due to spectral overlap. FBCI isolates polymer-specific spectral signals, reducing the effect of background interference. Moreover, the model compensates for spectral variability and Mie scattering effects through baseline corrections. Finally, the WTA approach ensures accurate classification of US-MNP particles.

The size distribution of all US-MNP samples was estimated through statistical analysis of data obtained from FTIR hyperspectral imaging combined with Random Forest Machine Learning (RFML) analysis. The results indicate a homogeneous distribution of MNPs across the six samples of each sonicated polymer, suggesting consistency in the fragmentation process. This is further supported by Figure 3.7, which illustrates the percentage distribution of different size ranges for PMMA, PP, PVC, and PS across multiple samples, demonstrating reproducibility in particle size distribution. Six samples of ultra-sonicated PMMA exhibited a homogeneous size distribution with a slight variation of 4-5 % (Figure 3.7a). The majority of USPMMA particles (55%) fall within the 10-30 μm range, with 30% below 10 μm, 9-10% between 30-60 μm, 4-4.5% within 60-100 μm, and less than 0.5% exceeding 100 μm. Ultra-sonicated PP (USPP) samples show a slightly larger deviation of 6-7% but remain primarily homogeneous, with approximately 45-50% of particles in the 10-30 μm range, 25-30% below 10 μm, 14-16% in the 30-60 μm range, 4-5% between 60-100 μm, and 1-2% exceeding 100 μm (Figure 3.7b).

The size distribution of ultra-sonicated PVC (USPVC) is similar to that of USPP but with a higher proportion (55-60%) of particles in the 10-30 µm range. The quantity of particles below 10 µm (~28-30%) is comparable to that of PMMA and PP (Figure 3.7c). However, the proportion of 30-60 µm particles is lower (~2-3%) than in other samples, while the percentage of 60-100 µm particles is ~5-6%. Particles exceeding 100 µm show a higher proportion (~7-8%), likely due to PVC's greater strength and resistance to breakage compared to PMMA, which is more brittle in

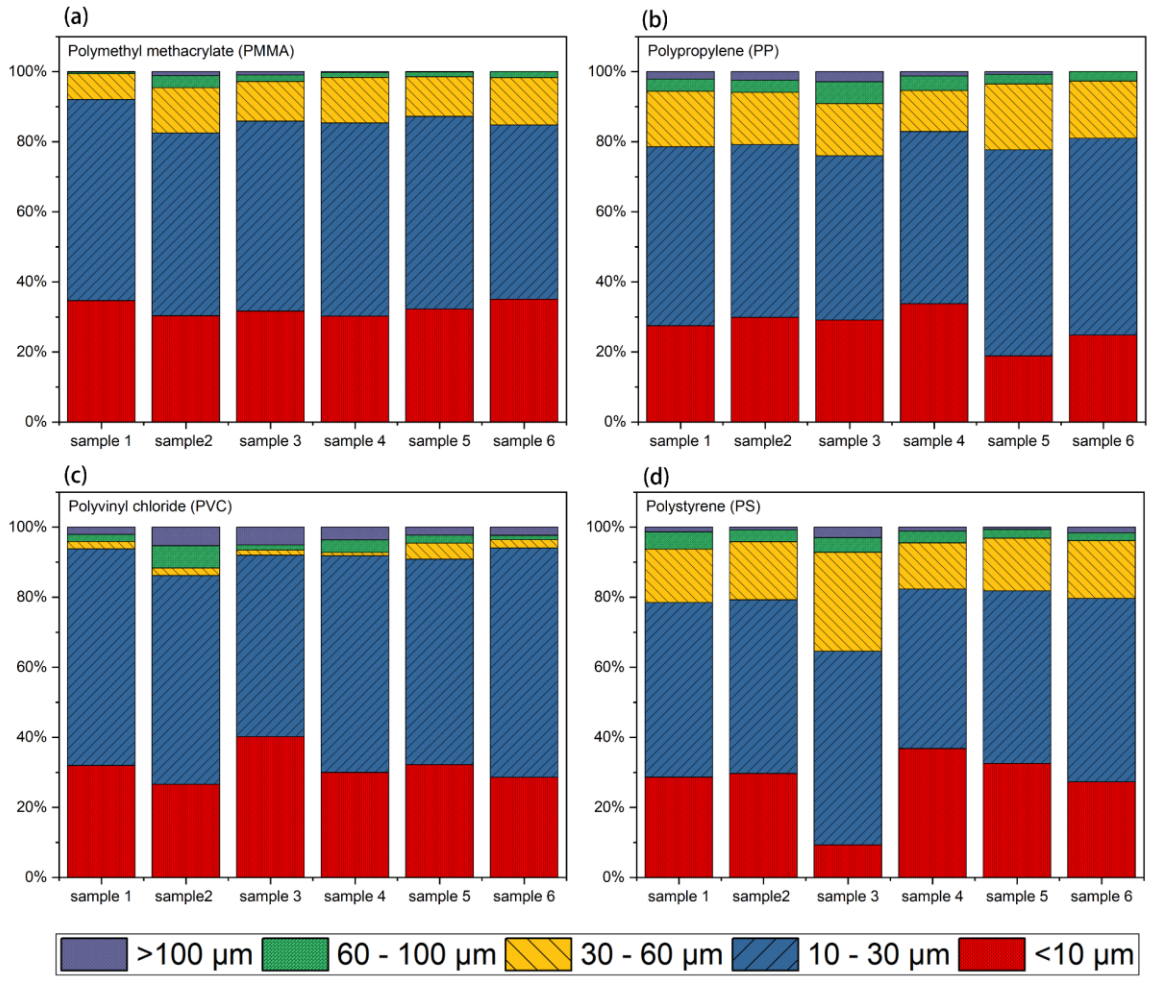

Figure 3.7: Size distribution of six ultra-sonicated microplastic samples of (a) Polymethyl methacrylate (PMMA), (b) Polypropylene (PP), (c) Polyvinyl chloride (PVC), (d) Polystyrene (PS).

nature [325]. Ultra-sonicated PS (USPS) samples exhibit greater variation, indicating more inhomogeneity. Around 27-29% of USPS particles are below 10 µm, while 50-52% fall within the 10-30 µm range, similar to other sonicated polymers (Figure 3.7d). However, USPS has the

highest proportion (19-20%) of 30-60 μm particles among all sonicated polymers, while those in the 60-100 μm and above 100 μm ranges are 2-3% and 1-2%, respectively, comparable to PP.

Figure 3.8 shows the particle size distributions of USMPs generated from PMMA, PP, PVC, and PS following direct ultrasonication. The bar charts represent the percentage of particles in each size category, while the overlaid Gaussian curves describe the overall distribution shape. In all polymers, the most frequent particle sizes (modes) fall within the 10-30 μm range, indicating that this is the dominant fragment size produced by ultrasound. The calculated weighted mean particle sizes were 21.6 μm for PMMA, 28.0 μm for PP, 26.6 μm for PVC, and 24.4 μm for PS. The distributions are positively skewed (γ = 1.62 to 2.48), indicating that the mean lies to the right of the mode, due to the influence of larger particles. PMMA and PS show relatively narrower distributions ($\sigma \approx 20$ μm), whereas PP and PVC display broader spreads ($\sigma \approx$ 27-29 μm), reflecting more variability in fragment sizes. These results confirm that ultrasonication effectively produces micron-sized fragments across all polymers, while also highlighting polymer-specific differences in fragmentation behaviour.

Investigating impurities in ultrasonicated MNP samples is crucial, as these contaminants may originate from the manufacturing process of the raw materials. Identifying and quantifying these impurities helps assess the purity of each polymer sample and provides insights into potential cross-contamination during production. To investigate this, a statistical analysis was conducted on FTIR combined RFML produced data to determine the concentration of impurities in US-MNP samples, as presented in Table 3.1. The table details the composition of different materials in each ultrasonicated sample. Among the ultra-sonicated samples, USPMMA exhibits the highest purity, with 99.04% PMMA particles and only 0.96% impurities (mainly PVC particles).

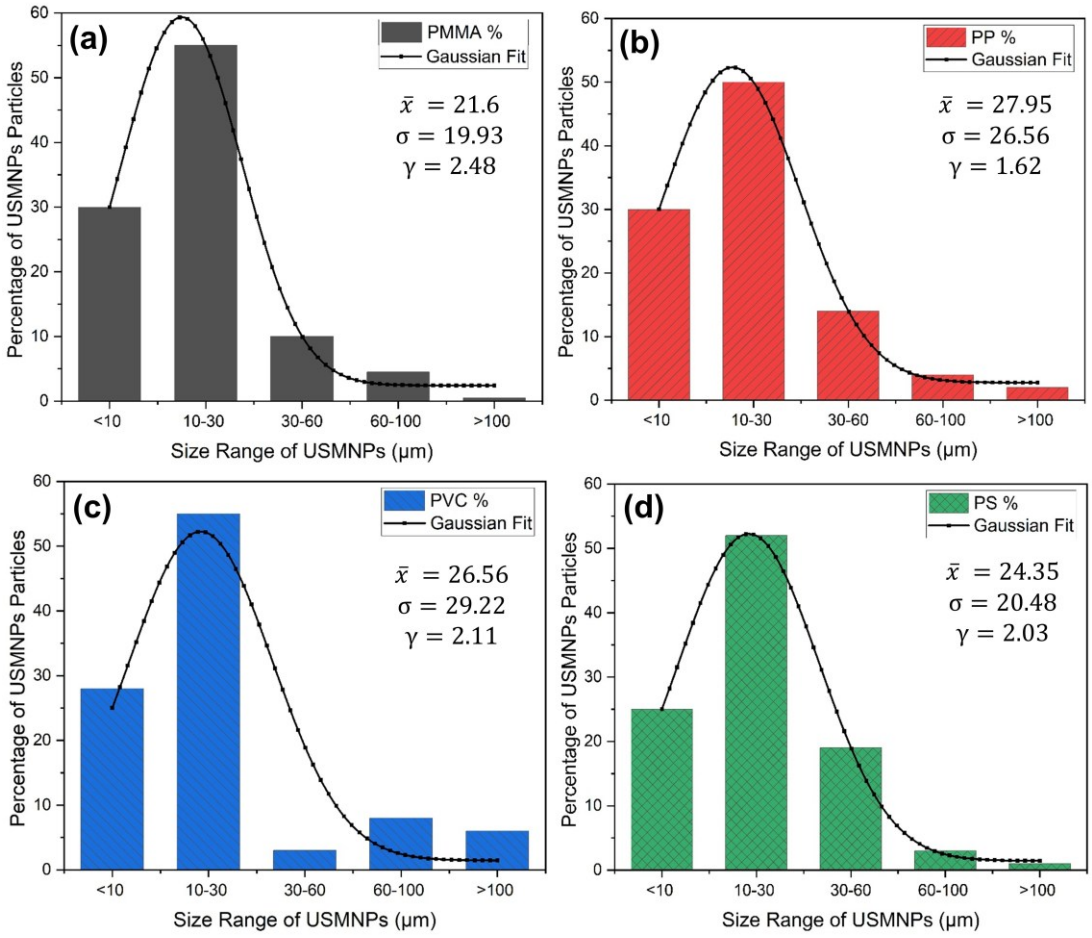

Figure 3.8: The size distribution of ultra-sonicated microplastics (USMPs) for different polymers (a) PMMA, (b) PP, (c) PVC, and (d) PS. The bar chart represents the percentage of particles in five size ranges (<10 μm, 10-30 μm, 30-60 μm, 60-100 μm, and >100 μm) for each polymer. The black lines indicate the Gaussian fit, highlighting the predominant size range of USMPs.

Similarly, USPVC maintains a high purity of 98.69%, with minor impurities of PMMA (0.83%) and other polymer debris (0.48%). The USPP sample follows closely, with 97.32% PP purity, small amounts of PS (0.34%), PVC (1.19%), PMMA (0.74%), and other polymer particles (0.41%). The USPS sample shows a slightly lower purity of 96.63%, with impurities including PP (0.74%), PVC (1.83%), PMMA (0.49%), and other polymers (0.31%). This demonstrates that the ultra-sonication method is a promising technique capable of producing MNPs with purity levels exceeding 95%.

Table 3.1: Percentage concentration of different constituents in ultra-sonicated microplastic samples.

Concentration of different constituents (%)					
Ultra-sonicated Samples	**PS**	**PP**	**PVC**	**PMMA**	**Others**
Polystyrene	96.63	0.74	1.83	0.49	0.31
Polypropylene	0.34	97.32	1.19	0.74	0.41
Polyvinyl chloride	0	0	98.69	0.83	0.48
Polymethyl methacrylate	0	0	0.96	99.04	0

3.3.3 Raman Analysis of US-MNPs

The Raman analysis of USMPs was performed using the Renishaw inVia Basis™ and inVia™ Qontor Raman microscope. The laser source with wavelength 785nm, operating at ~50 mW, was used. The Raman measurements of raw microplastic debris were collected at 5x magnification, whereas 50x magnification was used for ultrasonicated MNP samples with a numerical aperture of 0.5 (long working distance). The laser power on each type of US-MNP sample was manually optimised to prevent sample burning or distortion during measurements. Prior to measurements, the setup was calibrated by taking a reading of the silicon peak (520.5±1 cm^{-1}) from a standard reference. Random multi-point measurements were acquired to confirm the type of plastic present in the USMP samples.

Raman spectroscopy is essential for analysing polymers before and after sonication, as it provides detailed molecular fingerprints that help determine potential structural or chemical alterations caused by high-power ultrasound treatment. By detecting vibrational modes specific to polymer bonds, Raman spectra can confirm whether the chemical composition of microplastics remains unchanged or undergoes degradation due to external factors such as mechanical stress or oxidation. To investigate this, Raman spectra of four ultrasonicated MNP samples and their pre-sonicated raw plastics (PP, PVC, PMMA, and PS) were recorded and presented in Figure

3.9. The unaltered spectral features of all US-MNP confirm that ultrasound treatment has not affected the chemical structure of these polymers. This stability is critical in ensuring that the sonication process effectively reduces particle size without inducing chemical degradation or modifying the molecular composition. Moreover, the Raman vibrational bands corresponding to the characteristic peaks of US-MNPs (USPP, USPVC, USPMMA, and USPS) are presented in Table 3.2. The Raman spectra of both the original and ultrasonicated PP samples (Figures 3.9a and 3.9b) exhibit strong agreement with the standard reference spectrum [326], indicating that the polymer backbone remains intact. PP and USPP exhibit several vibrational peaks, with a primary broad peak in the 2800-3000 cm^{-1} region, comprising a prominent band at 2892 cm^{-1} and two corresponding shoulders at 2847 cm^{-1} and 2963 cm^{-1}, representing the stretching vibrations of the C-H bond [281, 327]. Other observed vibrational modes include peaks at 811 cm^{-1}, 977 cm^{-1}, 1155 cm^{-1}, 1331 cm^{-1}, 1460 cm^{-1}, and 1762 cm^{-1} which correspond to various stretching and bending motions: C-C stretching and CH_3 bond rocking, C-C stretching and CH bending, CH stretching, CH_2 wagging and CH_3 bending, CH_2 bending, CH_3 asymmetric bending, and C=O stretching vibration, respectively [282, 328-330]. Figures 3.9c and 3.9d illustrate the recorded Raman spectra of PVC before and after sonication, respectively, showing a strong correlation with the reference spectrum of PVC [142, 326]. The characteristic Raman peaks associated with PVC and USPVC are observed at 636 cm^{-1} (C-Cl stretching), 696 cm^{-1}, 1431 cm^{-1}, and 2914 cm^{-1} (C-H stretching) [331, 332]. The obtained Raman spectra of PMMA and PS are likewise comparable to their reference fingerprints [142, 333, 334], as shown in Figures 3.9f and 3.9h (before sonication) and Figures 3.9e and 3.9g (after sonication), respectively. The Raman spectra of both PMMA and USPMMA (Figures 3.9e and 3.9f) exhibit a prominent band at 2957 cm^{-1}, corresponding to the C-H stretching vibration [335]. Additional vibrational modes are observed at

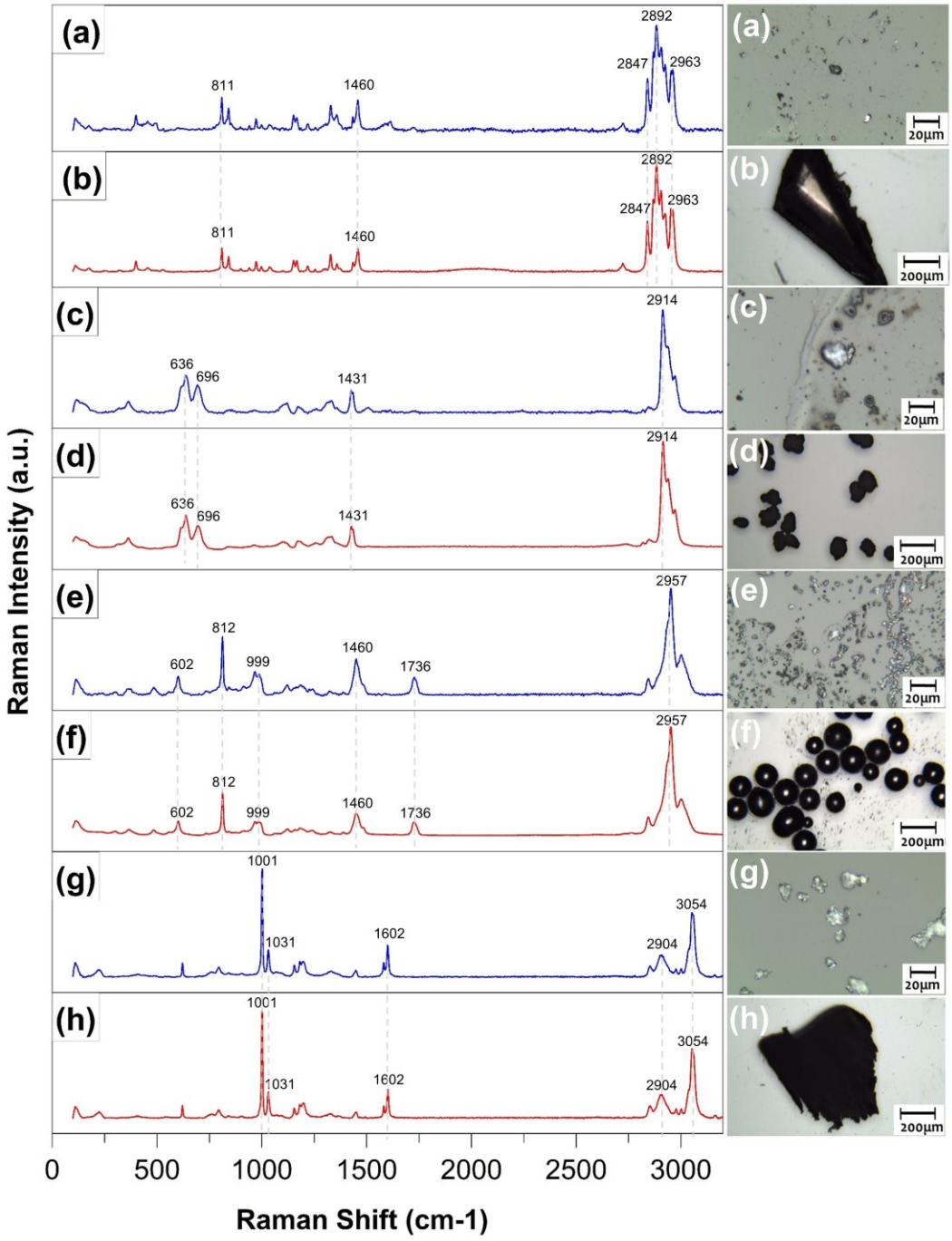

Figure 3.9: Raman microscopy of ultra-sonicated micro and Nanoplastic. Microscopic images (right side) show the morphology of pre- and post-ultrasound treatment of plastics (a and b) PP, (c and d) PVC, (e and f) PMMA, and (g and h) PS. The Raman spectra acquired through point measurements are shown on the right side (a, c, e, and g) USPP, USPVC, USPMMA, and USPS after ultra-sonication, and (b, d, f, and h) PP, PVC, PMMA, and PS before ultra-sonication.

602, 812, 925, 999, 1081, 1264, 1460, 1648, 1736, 2848, and 3001 cm^{-1}. The band at 1648 cm^{-1}

Table 3.2: The Raman vibrational bands corresponding to the characteristic peaks of different ultrasonicated micro- and nanoplastics (USPP, USPVC, USPMMA, and USPS).

US-MNPs	Raman Peaks (cm^{-1})	Corresponding Vibrational Band
Ultrasonicated Polypropylene (USPP)	811	C-C stretching and CH3 rocking
	977	C-C stretching and CH bending
	1155	C-H stretching
	1331	CH2 wagging, and CH3 bending
	1460	CH_2 bending and CH_3 asymmetrical bending
	1762	C=O stretching vibration
	2800-3000	Stretching vibrations of C-H
Ultrasonicated Polyvinyl Chloride (USPVC)	636	C-Cl stretching
	696	C-H stretching
	1431	
	2914	
Ultrasonicated Poly(methyl methacrylate) (USPMMA)	602	(C-C-O)
	812	CH_2 rock
	925	α-CH_3 rock
	999	O-CH3 rock
	1081	(C-C-O)
	1264	C-O stretching
	1460	δ_a(C-H) of α-CH_3
	1648	C=C stretching and C–COO vibrations
	1736	C=O
	2848	O-CH_3
	2957	C-H stretching
	3001	(C-H) of O-CH_3
Ultrasonicated Polystyrene (USPS)	621	Ring deformation
	795	CH deformation out-of-plane
	1001	Breathing mode of the aromatic carbon ring
	1031	CH deformation in-plane
	1155	C-C stretching
	1450	CH_2 scissoring
	1583	C=C stretch
	1602	Skeletal stretching
	2850	symmetric aliphatic CH_2 stretching
	2904	Antisymmetric aliphatic CH_2 stretching
	3054	C-H bond stretching

is attributed to a combination of C=C stretching and C–COO vibrations [336]. The Raman spectra of PS and USPS (Figures 3.9g and 3.9h) exhibit a strong band at 1001 cm^{-1}, corresponding to the breathing mode of the aromatic carbon ring. Additional vibrational modes are observed at 621, 795, 1031, 1155, 1450, 1583, 1602, 2850, 2904, and 3054 cm^{-1} [337, 338]. These bands are associated with various molecular motions, including ring deformation (621 cm^{-1}), CH deformation out-of-plane (795 cm^{-1}) and in-plane (1031 cm^{-1}), C-C stretching (1155 cm^{-1}), CH_2 scissoring (1450 cm^{-1}), C=C stretch (1502 cm^{-1}), skeletal stretching (1602 cm^{-1}), symmetric (2852 cm^{-1}) and antisymmetric (2904 cm^{-1}) aliphatic CH_2 stretching modes. Additionally, PS exhibits a band at 3054 cm^{-1}, attributed to C-H bond stretching in the benzene ring [337, 338]. To validate the chemical stability of the polymers, the Raman spectra of both the original and ultrasonicated samples were compared with standard reference spectra reported in the literature [142, 326, 335-338]. The characteristic peaks for each polymer (PP, PVC, PMMA, and PS) were carefully matched in terms of their positions with a tolerance of ±2-3 cm^{-1}. The diagnostic vibrational bands, such as the stretching vibration of C–H at (2847,2892, and 2963) cm^{-1} for PP, the C–Cl stretching at 636 cm^{-1} for PVC, the C=O stretching at 1736 cm^{-1} for PMMA, and the aromatic ring breathing mode at 1001 cm^{-1} for PS, were all observed at their expected locations. These reference peak positions are also highlighted in Figure 3.9 to provide direct visual confirmation. The strong agreement between pre- and post-sonicated spectra with the literature values confirms that the sonication process did not alter the molecular structure of the polymers.

3.3.4 Suspensibility Analysis of US-MNPs Using Transmission Spectroscopy

The suspensibility of the synthesised US-MNP in an aqueous medium was evaluated using a UV-Vis-NIR spectrophotometer (PerkinElmer Lambda 1050). Transmission measurements were recorded for all ultrasonicated samples (3 mL) over a 2-hour period, with 12 measurements

taken at 10-minute intervals. The analysis was conducted using incident light spanning a broad wavelength range λ_{in} (200–1200 nm) with a scan interval of $\delta\lambda$ = 1 nm. These measurements provide valuable insights into the sedimentation rate of various US-MNP types.

The stability of suspended MNP in water is essential for their characterisation and subsequent optical analysis. In particular, the fluorescence excitation–emission (FLE) measurements described in Chapter 4, Section 4.2.3, require the microplastic suspensions to be held in a quartz cuvette for durations ranging from 45 minutes to 1.5 hours. During this time, it is critical that the particles remain suspended so that incident light can continuously interact with them and generate detectable fluorescence signals. To ensure this condition was satisfied, the suspensibility of the ultrasonicated samples was tested for up to 2 hours.

Figure 3.10 demonstrates the high suspensibility of the ultrasonicated micro- and nanoplastics through the gradual change in transmission over time. In all samples, the transmission remains significantly lower than that of pure DI water (100%) throughout the measurement period, indicating that a substantial fraction of particles remained suspended and continued to scatter and absorb incident light. The relatively small transmission differences observed for USPMMA (~0.5–0.6%) and USPP (~1.4–1.5%) confirm that these particles remain well-dispersed with minimal sedimentation. In contrast, USPS and USPVC show larger increases in transmission (~4.7–5% and ~5.8–6.1%, respectively), reflecting faster sedimentation rates but still maintaining measurable suspensions within the 2-hour window. Thus, the limited rise in transmission over time, combined with transmission values that remain well below the DI water baseline, confirms the high suspensibility of the US-MNPs produced by direct ultrasonication. The observed differences in suspensibility across the four polymers can be attributed to variations in particle size distribution, surface chemistry, and polymer properties [339]. USPMMA exhibited the highest suspensibility, likely due to its smaller particle size and increased surface hydrophilicity resulting from fragmentation-induced surface modifications [340]. USPP also showed good

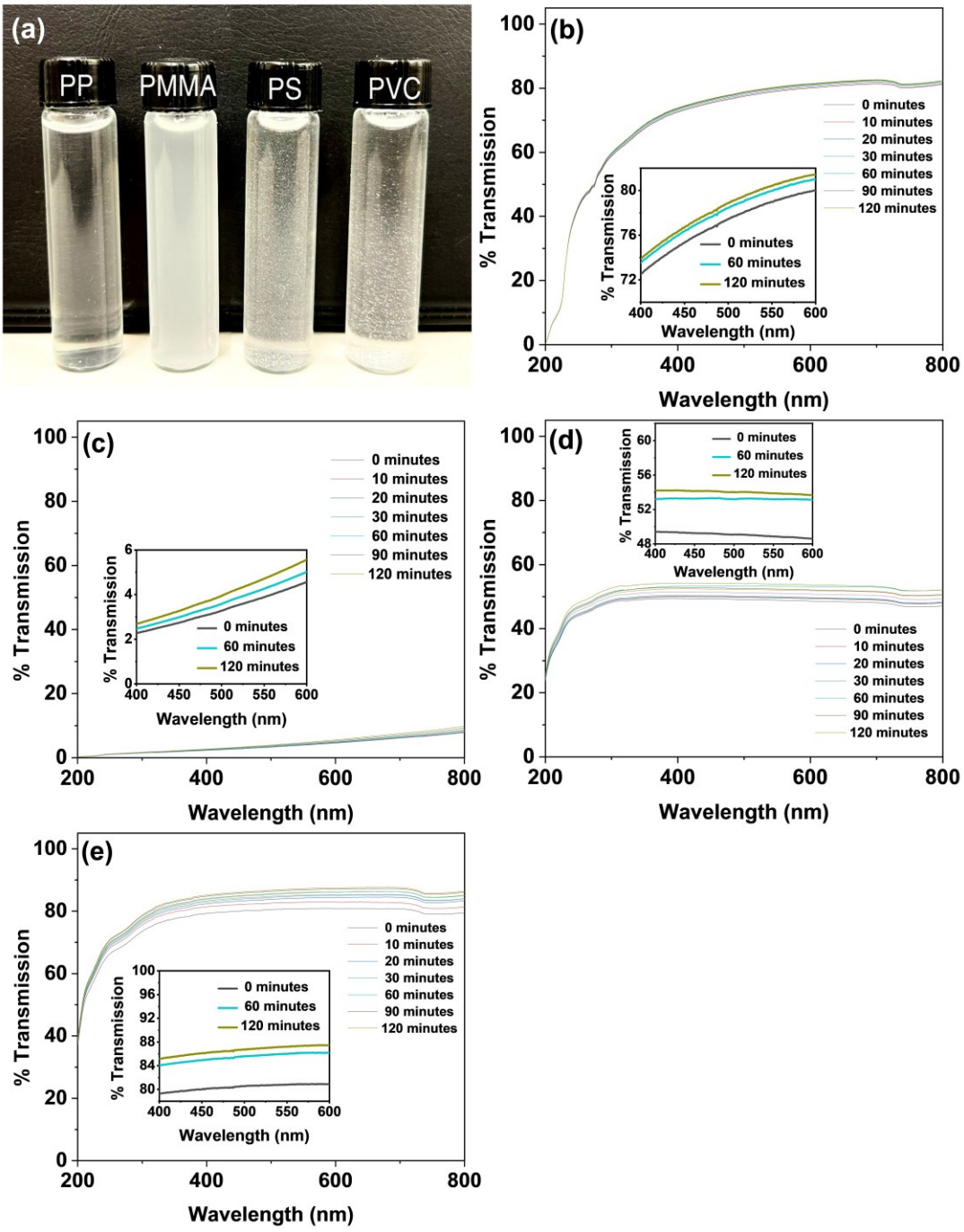

Figure 3.10: Ultrasonicated MNP particles of PP, PMMA, PS, and PVC suspended in DI water (a), UV-Vis transmission spectra recorded for the time period of 2 hours (b) PP (c) PMMA (d) PS, and (e) PVC.

suspensibility, but slightly lower than PMMA, possibly reflecting the formation of somewhat larger fragments during sonication [341]. USPS displayed higher sedimentation than both PMMA and PP, which may be linked to the intrinsic hydrophobic nature of polystyrene surfaces, reducing

water–particle interactions and leading to faster settling [342]. USPVC showed the highest sedimentation rate of all four polymers. Although PVC has a higher density (1260 kg/m³) [343] than PS (1050 kg/m³) [344], previous studies confirm that sedimentation is primarily size-dependent rather than density-dependent [132, 133]. Therefore, the greater sedimentation observed for PVC is more likely due to broader particle size distribution and aggregation tendencies rather than density alone.

Unlike cryo-milled MPs, which often require surfactants or oxidation treatments to achieve stable suspensions due to static charge [130], the ultrasound treatment directly fragments polymer particles, likely introducing surface modifications that enhance dispersibility [129]. Furthermore studies [132, 133] have shown that MP sedimentation is primarily size-dependent rather than density-dependent, with smaller particles remaining suspended for longer. By generating ultrafine particles in DI water, our method overcomes the limitations of cryo-milling and indirect sonication. For instance, in previous work where indirect sonication was employed, the suspensibility of MNPs was reported to be very low, with particles sedimenting within 25 minutes [309]. In contrast, the direct ultrasonication method applied here produced suspensions that remained stable for over 2 hours, which is sufficient for subsequent optical analyses such as FLE. This demonstrates that direct sonication not only yields environmentally relevant particle morphologies but also ensures stable aqueous suspensions suitable for extended spectroscopic measurements.

3.4 Chapter Conclusion

This study demonstrated a novel method for generating secondary reference micro- and nanoplastics (US-MNPs) in water using high-power direct ultrasound treatment. Unlike the conventional indirect ultrasonication method using an ultrasonic bath, which requires around 15 hours of treatment to produce MNPs [309], our direct sonication approach reduces the processing time to 7 hours, representing a reduction of more than 53%. It also eliminates the need for alkaline

solutions or surfactants to achieve sufficient suspensibility. The direct sonication method produced highly stable suspensions, with US-MNPs remaining dispersed in water for over two hours.

The generated US-MNPs exhibit a broad particle size distribution, ranging from 100 nm to 150 µm, with the potential for even smaller fragments below 100 nm. These particles predominantly display irregular shapes, resembling microplastic pollutants in real environmental matrices. Different analytical techniques were employed to comprehensively characterise and quantify the reference MNP particles, each serving a distinct purpose. Raman spectroscopy was used for precise chemical identification, providing molecular vibrational information to confirm that the polymer composition remained unaltered after the ultrasound treatment. The µ-QCL-based IR spectral acquisition, combined with machine learning classification, enabled efficient and accurate identification, impurity analysis, and size distribution assessment of MNPs. UV-Vis transmission spectroscopy was utilised to assess the suspensibility of US-MNPs in water, monitoring their sedimentation behaviour over time. SEM imaging provided detailed morphological analysis, revealing particle size, surface texture, and shape, which are critical for understanding the environmental relevance of the generated microplastics. Finally, vacuum filtration was used to fractionate the ultrasonicated MNP samples into four distinct size ranges for subsequent detection and analysis. Future work can focus on refining size separation techniques to achieve even more precise and controlled particle distributions. The Implementation of rate-zonal density gradient centrifugation may further enhance fractionation efficiency, enabling targeted investigations into the environmental behaviour and impacts of specific US-MNP size ranges.

Chapter 4: Fluorescence Excitation-Emission Mapping Analysis of Ultra-sonicated Micro- and Nanoplastics

4.1 Introduction

Fluorescence (FL) spectroscopy has emerged as a promising technique for detecting and characterising microplastics (MP) in water [1, 150, 197, 201], offering a rapid and non-destructive detection tool alongside conventional spectroscopic methods. While FTIR and Raman spectroscopy are widely used for MNP analysis, their detection threshold presents limitations. Standard FTIR spectroscopy typically detects particles no smaller than 10 μm [186, 257, 345, 346], while Raman spectroscopy can extend detection down to 1 μm [184, 347-349]. However, detecting nanoplastics remains a significant challenge due to background fluorescence and weak Raman signal at the nanoscale. This challenge has led to the exploration of fluorescence excitation-emission (FLE) mapping as an alternative technique for assessing its detection capabilities at the nanoscale. Moreover, the detection limit of FL spectroscopy for MNPs is not yet well established in the literature, which also makes it an active research area.

Building on the findings from Chapter 3, where a laboratory-scale ultrasonication technique was used to generate reference MNPs, this chapter investigates the FL properties of these US-MNPs and extends the previous work (Chapter 2) by evaluating the potential of FL spectroscopy to detect and differentiate MNPs in water. Specifically, FLE maps are recorded for US-MNPs, including polystyrene (PS), polyethylene terephthalate (PET), and polypropylene (PP), to identify their distinct FL signatures. Moreover, this study explores the intrinsic FL characteristics of nanoplastics (NPs < 1000nm) to assess the capability of FL spectroscopy as a rapid and non-destructive technique for NP detection in water. The findings are expected to contribute to the advancement of FL spectroscopy as a reliable tool for detecting and characterising MNPs in aqueous environments, offering a potential alternative to traditional spectroscopic methods while addressing their inherent limitations.

It is important to note that the definition of nanoplastics varies in the literature. Some studies classify them as particles smaller than 100 nm, while others extend the upper limit to 1000 nm, as discussed in Chapter 1 (Introduction section). In this study, we classify particles smaller than 1000 nm as nanoplastics, ensuring consistency in analysis and alignment with the detection limits of existing spectroscopic methods.

4.2 Methodology

4.2.1 Sample Preparation

MNP particles in deionised (DI) water were produced using laboratory-scale high-power ultrasound treatment. Plastic beads (PS) and sheets (PET and PP) were cut down and processed using a direct ultrasonication system, as described in Sections 3.2.1 and 3.2.2, respectively. Following the sonication, vacuum filtration was employed to fractionate US-MNPs into four different size ranges (Range 1: MPs > 1.2 μm, Range 2: 1.2 μm > MNPs > 400 nm, Range 3: 400 nm > NPs > 100 nm, Range 4: NPs < 100 nm), as detailed in Section 3.2.3. Twelve samples were prepared, with each US-MNP type (PS, PET, and PP) fractionated into four distinct size ranges. For each US-MNP, four samples were obtained corresponding to the defined size ranges (R1 to R4). This ensured the availability of all size fractions, with each cuvette containing 3 mL of the sample for subsequent absorption and FLE mapping analysis.

4.2.2 Absorption Spectroscopy of US-MNPs

The ultra-sonicated MNPs in an aqueous medium (DI water) were analysed using a UV-Vis-NIR spectrophotometer (PerkinElmer Lambda 1050) to assess their absorption characteristics. Absorption spectra were recorded for all three ultrasonicated samples, including PS, PET, and PP, across size ranges (Range 1 to 4), each with a volume of 3 mL. The measurements were conducted in absorption mode, utilising incident light across a broad wavelength range of 200-700 nm (UV-Vis) with a scanning interval of 1 nm. The Lambda 1050 spectrophotometer is equipped with deuterium and tungsten-halogen lamps, providing an

extended operating range of 175-3300 nm (UV-Vis-NIR), which makes it suitable for analysing a broad spectrum of materials. According to its technical specifications, the instrument offers a wavelength accuracy of ±0.08 nm in the ultraviolet (UV) and visible (Vis) regions, enabling precise spectral detection within these ranges. The wavelength accuracy in the near-infrared (NIR) region is ±0.3 nm, ensuring reliable performance for longer wavelengths. This analysis was conducted to determine the specific wavelengths at which MNPs absorb light, helping to identify the most suitable excitation wavelength range for subsequent FLE mapping analysis. Understanding the absorption properties of MNPs allows for optimised selection of excitation wavelengths in fluorescence spectroscopy, ensuring improved detection and characterisation of their intrinsic fluorescence emissions.

The raw absorption spectra collected from the US-MNPs were processed in two stages to enhance data accuracy and facilitate the identification of key spectral features. In the first stage, baseline correction was performed using the Asymmetric Least Squares (ALS) method [350] to eliminate noise and background interference. This method was chosen because it effectively corrects spectral baselines without distorting the original signal, ensuring more reliable absorption measurements. ALS is particularly advantageous for absorption data as it adapts to asymmetric baselines [351], which are commonly observed in spectroscopic measurements due to instrumental or sample-related variations.

In the second stage, spectral deconvolution was carried out using a multi-peak fitting approach based on the Gaussian function [352] in Origin Pro software. The Gaussian method was employed because it provides an accurate representation of overlapping absorption peaks by modelling them as symmetric curves [353], which is commonly observed in molecular absorption spectra. This technique allows for the precise resolution of individual spectral components, facilitating the identification of characteristic absorption bands associated with different US-MPs.

4.2.3 Fluorescence Mapping Analysis of US-MNPs

The FLE mapping analysis of US-MNPs in water was conducted using the HORIBA Nano-Log spectrofluorometer, following the same methodology detailed in Chapter 2, Section 2.3.4. The procedure involved recording FLE maps to assess the fluorescence characteristics of all three US-MNPs across four size ranges (see Section 3.2.3). The excitation and emission wavelength ranges used in this study were 300-500 nm and 315-600 nm, respectively, consistent with the approach previously applied for larger microplastics (>500 µm) in Chapter 2.

While the core methodology remained unchanged, a key difference in this analysis was the selection of slit width. In contrast to the 2 nm spectral slit width used for larger microplastics in Chapter 2, a 5 nm slit width was employed for the FLE mapping of US-MNPs. This adjustment was made to enhance the fluorescence signal for smaller particles, ensuring improved detection sensitivity for US-MNPs.

The raw FLE maps of US-MNPs were processed in multiple stages to improve data accuracy and facilitate the identification of key FL spectral features. The methodology applied for post-processing was based on the approach detailed in section 4.2.4, where R code in the R statistics software was used to remove Rayleigh and Raman scattering interferences, ensuring that the extracted fluorescence signals accurately represent the intrinsic emissions of MNPs. In the first stage, Rayleigh and Raman scattering artefacts were removed using R-code, as described in the next section 4.2.4. In the second stage, spectral deconvolution was performed on the processed fluorescence spectra using the same approach applied to the absorption spectra (see Section 4.2.2).

4.2.4 Post-processing of FLE maps Using R-Language

The recorded FLE maps were utilised to evaluate the intrinsic fluorescence of US-MNPs across a range of excitation and emission wavelengths. However, a major challenge in fluorescence spectroscopy is the presence of scattering artefacts such as Rayleigh and Raman

scattering. These artefacts can obscure original fluorescence signals, complicating data interpretation and reducing accuracy. Therefore, before conducting any further data analysis, it is essential to remove these scattering artefacts to ensure an accurate representation of the underlying fluorescence features from the US-MNP particles.

This was achieved using the staRdom package in R, a well-established tool for processing excitation-emission matrix (EEM) data [354-356]. The staRdom facilitates the removal of scattering artefacts and applies linear interpolation, enhancing the clarity and reliability of the fluorescence emission signals from the sample. Figure 4.2 illustrates the workflow for EEM data processing, outlining the main steps from data loading, scatter removal, and data interpolation to data export. The following sections provide a detailed breakdown of the procedures and code used for this analysis.

EEM Data Preparation: The raw EEM three-way data of US-MNPs for this study was collected using the Horiba NanoLog spectrofluorometer. This instrument records emission wavelengths in rows and excitation wavelengths in columns. However, the staRdom package in R-studio requires the data to be structured with excitation wavelengths as rows and emission wavelengths as columns for efficient processing. Therefore, restructuring the raw data was a necessary pre-processing step. The EEM data matrix was transposed to achieve restructuring so that excitation wavelengths were placed in rows and emission wavelengths in columns. This transformation was performed in Microsoft Excel before importing the data into R-studio, ensuring compatibility with the staRdom package. Proper dataset formatting is crucial to prevent errors during data import and processing, enabling seamless analysis in subsequent steps. Data Import and Initial Visualisation: Following data restructuring, the EEM dataset was imported into R-Studio. The FLE maps were stored in a designated folder and imported using the eem_read() function from the

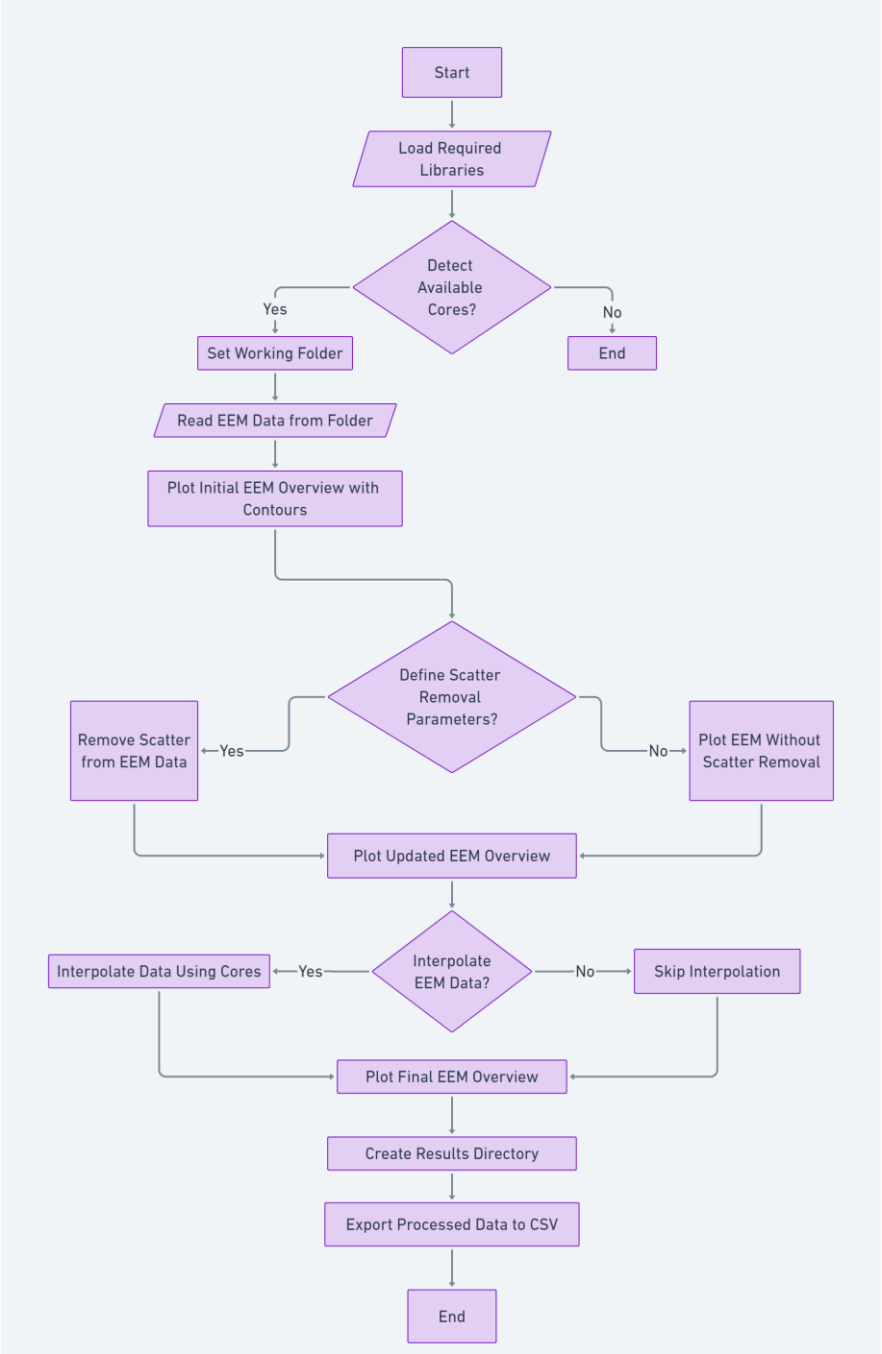

Figure 4.1: This flowchart shows the workflow for FLE mapping data processing using R-code. It outlines the step-by-step procedure for handling EEM data, including data loading, scatter removal, interpolation, and data export.

staRdom package. This function reads and organises the EEM data into a structured list format, allowing for smooth manipulation and visualisation in subsequent analyses. For data visualisation, the eem_overview_plot() function was used to generate contour plots (FLE maps) of the EEMs

under the graphical window in R-studio. These plots provide an overview of the fluorescence emissions, highlighting bright FL emission zones. At this stage, scattering artefacts were observed as diagonal features across the excitation-emission plane (Figure 4.2). The broad grey diagonal corresponded to Rayleigh scattering, while the offset diagonal with higher red intensity

R-Code:

```
library("staRdom")
library(magrittr)
library("dplyr")

cores <- detectCores(logical=FALSE)
folder <- "file-path"
eem_list <- eem_read(folder, recursive = TRUE, import_function = "aqualog")
eem_overview_plot(eem_list,spp=9, contour=TRUE)
```

represented Raman scattering. These artefacts were masked during data processing to avoid interference with the fluorescence signals of interest.

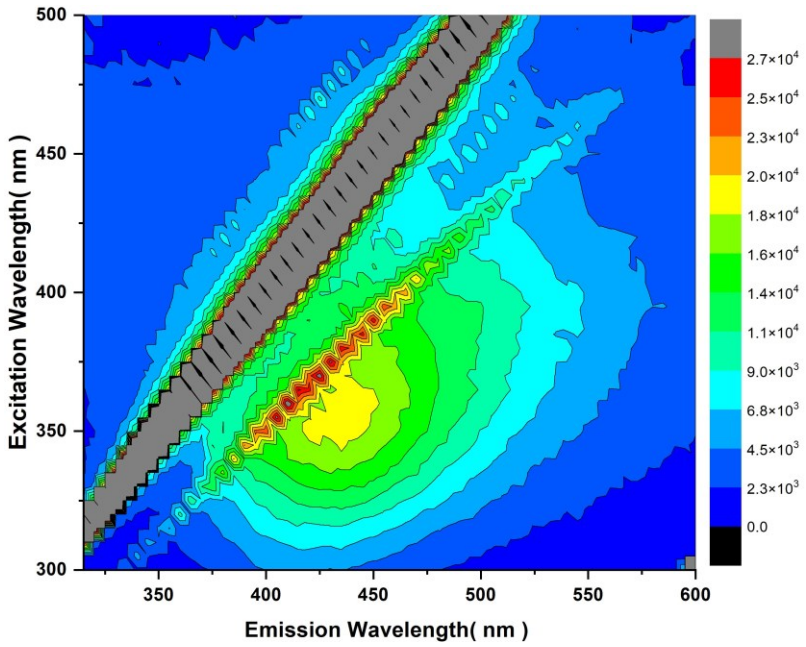

Figure 4.2: Unprocessed fluorescence exictation-emission (FLE) map of USNPs (<100nm) sample of Polypropylene (PP).

Rayleigh and Raman Scattering Removal: Rayleigh scattering is an elastic scattering process that occurs when light interacts with a material and is re-emitted at the same wavelength as the absorbed light, resulting in both first- and second-order scattering effects. First-order elastic scattering occurs when the emitted wavelength is identical to the incident wavelength ($\lambda_{ex} = \lambda_{em}$). In contrast, second-order elastic scattering results from a diffraction grating effect, where incident photons can also appear in the emission spectrum at twice the incident wavelength ($2\lambda_{ex} = \lambda_{em}$). The Raman scattering is inelastic, occurring when incident light interacts with molecular vibrational modes, causing a shift in the wavelength of the scattered light. In FLE analysis, these effects typically appear as horizontal or diagonal bands in the FLE map, which can obscure correct FL signals. To eliminate these scattering artefacts, the `eem_rem_scat()` function from the staRdom package was used. This function allows for the selective removal of both first- and second-order Rayleigh scattering as well as Raman scattering. In the R script, the `remove_scatter` vector was configured to remove these scattering components, with the first two `TRUE` values corresponding to the Raman scattering and the next two for first- and second-order Rayleigh scattering, ensuring a more cleaned dataset. The remove_scatter_width parameter defines the thickness of the regions removed around each scattering band; larger values remove broader regions, whereas smaller values retain more of the surrounding data. Here, a width of 10 nm was selected, ensuring effective elimination of scattering artefacts while preserving the underlying fluorescence features. After removal, the masked regions were interpolated during later processing, and the dataset was re-visualised with the eem_overview_plot() function to confirm that the scatter bands had been successfully eliminated.

R-Code:

```
remove_scatter <- c(TRUE, TRUE, TRUE, TRUE)
remove_scatter_width <- c(10, 10, 10, 10)
eem_list <- eem_rem_scat(eem_list, remove_scatter = remove_scatter, remove_scatter_width = remove_scatter_width)
```

Interpolation of Missing Data: The removal of Rayleigh and Raman scattering often leaves gaps in the EEM data where these artefacts were previously located. To restore continuity in the dataset, interpolation is applied to estimate missing values. The staRdom package offers the `eem_interp()` function, which efficiently interpolates missing data points in EEM matrices.

For this analysis, linear interpolation was applied across the dataset using the following steps:

Step 1: The `cores` parameter was set to utilise multiple processor cores, optimising computational efficiency.

Step 2: The `type = 1` argument specified linear interpolation, chosen for its balance between accuracy and computational speed, making it well-suited for filling gaps left by scattering removal.

Step 3: The `extend = FALSE` parameter ensured that interpolation was confined within the existing data range, preventing the introduction of artificial fluorescence peaks in areas where no data was originally recorded. After performing the interpolation, contour plots were generated again to visualise the results.

Export of Processed EEM Data: After removing scattering artefacts and applying interpolation, the next step was to export the processed EEM data for further analysis. The cleaned EEM data set was saved in CSV format using the `eem_export()` function. The exported CSV files contained the fully processed EEM data, free from scattering artefacts and with interpolated values seamlessly integrated. The CSV format was chosen for its broad compatibility with various analytical software, ensuring efficient downstream processing.

4.3 Results and Discussion

4.3.1 Absorption Spectroscopic Analysis of US-MNPs

The raw absorption spectra recorded for all three US-MNPs, PS, PET, and PP, across their four different size ranges, are provided in the appendices (A1, A2, and A3), respectively. The absorption spectra of all three sonicated plastic samples for size ranges Range 2 to 4 did not

exhibit significant or observable absorption peaks. However, Range 1 (MPs > 1.2 μm) showed a strong absorption signal in the 200-400 nm range. Therefore, the processed absorption spectra (using the ALS and Gaussian approach) for USMPs, PS, PET, and PP, specifically for MPs > 1.2 μm, have been selected and presented in Figures 4.3, 4.4, and 4.5, respectively. The absorption spectrum of USMPs-PS (black line), shown in Figure 4.3, reveals a strong absorption peak at 264 nm. This peak corresponds to the absorption by the pendant phenyl group (C_6H_5), a six-carbon ring structure characteristic of polystyrene. This structure is essentially a benzene ring with one hydrogen removed, which contributes to the distinctive absorption at 264nm [190, 357, 358]. Additionally, the spectrum displays a broad absorption band extending from 320 nm to 375 nm, with a shoulder around 402 nm. This broad absorption feature has been attributed to the triplet state of polystyrene [359], as it closely resembles the absorption observed in benzene [360]. The spectrum was further deconvoluted to identify the contributing peaks mainly within the broad absorption band (325-402 nm). The deconvoluted spectrum exhibited five distinct peaks at P1: 261 nm, P2: 324 nm, P3: 343 nm, P4: 370 nm, and P5: 402 nm. The last four peaks (P2-P5) correspond to the broad absorption band (325-402 nm), providing further insights into the optical characteristics of polystyrene and its electronic transitions, which are influenced by its aromatic structure. The first three individual peaks at 324 nm, 343 nm, and 370 nm correspond to regions of high optical density in polystyrene when exposed to UV irradiation. These peaks play a significant role in the yellowish discolouration observed in transparent polystyrene [361-363]. The shoulder at 402nm is associated with the lowest triplet state ($T_n \leftarrow T_1$) within the absorption band, which was previously identified using a microsecond flash photolysis method [364]. The absorption spectrum of USMPs-PET, as shown in Figure 4.4, exhibits a major peak accompanied by a shoulder and another distinct but weaker absorption peak. Upon deconvolution, three distinct peaks were identified. The first peak appears at P1: 245 nm, the shoulder is observed at P2: 259 nm, and the third peak is located at P3: 303 nm. The latter has comparatively lower absorption than the primary peaks (P1 and P2). These three absorption peaks from PET have previously

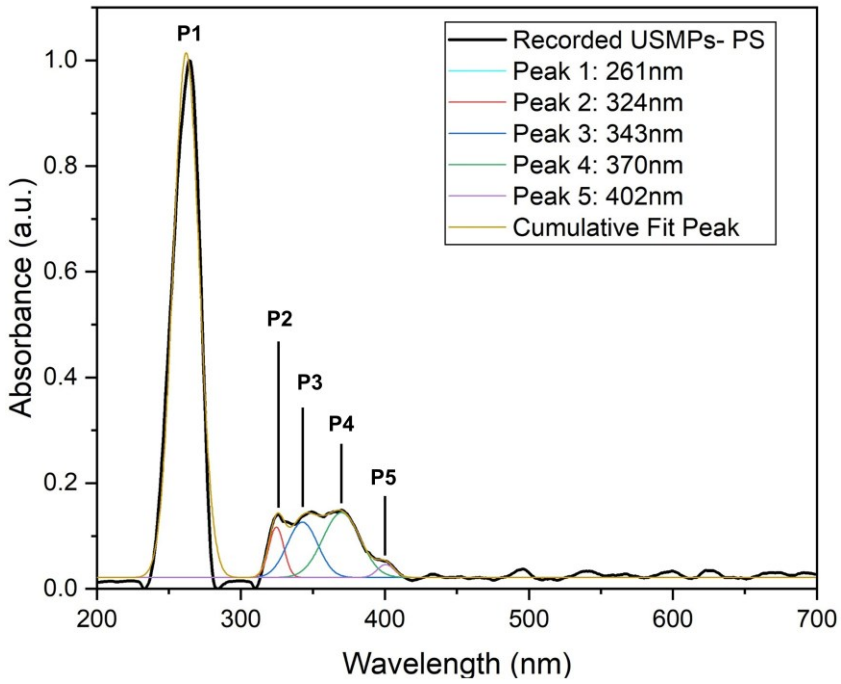

Figure 4.3: The processed absorption spectrum of USMPs-PS (Range 1: MPs > 1.2 µm). The recorded spectrum (black line) is shown alongside its deconvoluted components. The spectrum was fitted using multiple Gaussian peaks to resolve individual absorption features. Five distinct peaks were identified at P1: 261 nm (cyan), P2: 324 nm (red), P3: 343 nm (blue), P4: 370 nm (green), and P5: 402 nm (violet), each represented by different coloured curves. The cumulative fit peak (gold line) closely follows the recorded spectrum, confirming the presence of multiple overlapping absorption components contributing to the overall spectral profile.

been reported [365]. The main functional groups in PET that influence its electronic transitions include aromatic benzene rings (originating from terephthalic acid), carbonyl (C=O) groups (present in the ester linkages), and ester (-COO-) [366]. The strong absorption peak at 245 nm and its associated shoulder at 259 nm corresponds to $\pi \rightarrow \pi^*$ transitions, primarily originating from the benzene rings and ester functional groups within PET [367]. These transitions occur due to the excitation of electrons from the bonding π-orbital to the antibonding π* orbital. The weaker absorption peak at 303 nm is likely attributed to extended conjugation or interactions between polymer chains [368]. This absorption band may also be associated with structural modifications in PET, such as degradation or oxidation [285]. The presence of conjugated structures, which can develop under rigorous ultrasound treatment, may result in absorption at longer wavelengths.

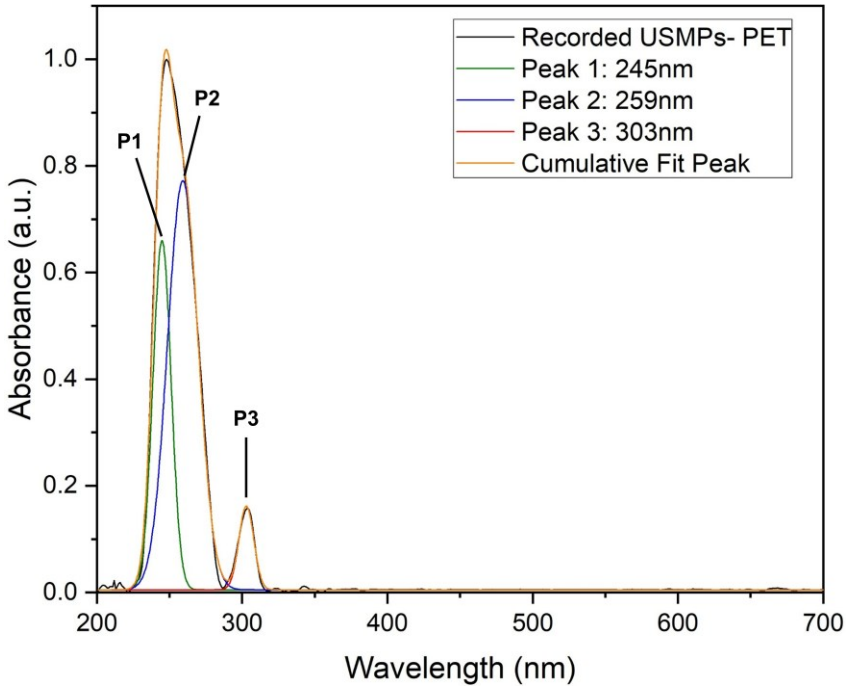

Figure 4.4: The processed absorption spectrum of USMPs-PET (Range 1: MPs > 1.2 µm) recorded using UV-Vis-NIR spectrophotometry is shown with deconvoluted spectra. The recorded spectrum (black line) was fitted using multiple Gaussian peaks to resolve individual absorption features. Three distinct peaks were identified at P1: 245 nm (green), P2: 259 nm (blue), and P3: 303 nm (red). The cumulative fit peak (orange line) closely follows the recorded spectrum, confirming the presence of multiple overlapping absorption components contributing to the overall spectral profile.

Over time, these structural changes can contribute to the yellowing of aged PET materials, as conjugated chromophores absorb visible light, altering the optical properties of the material [369].

The absorption spectrum of USMPs-PP, as shown in Figure 4.5, exhibits a major peak followed by a broad absorption band. The latter has a comparatively lower absorption than the major peak. Upon deconvolution, five distinct peaks were identified. The first peak (major peak) appears at P1: 221 nm, followed by an additional peak at P2: 270 nm, and three consecutive peaks, P3: 289 nm, P4: 311nm, and P5: 332 nm, from the broad absorption band. The strong absorption peak at P1: 221 nm is associated with conjugated ethylenic bonds (C=C) and α,β-unsaturated carbonyl group [288, 370]. These functional groups can form in the PP due to oxidation during ultrasonication or environmental exposure [371]. The second absorption peak at 270 nm, which

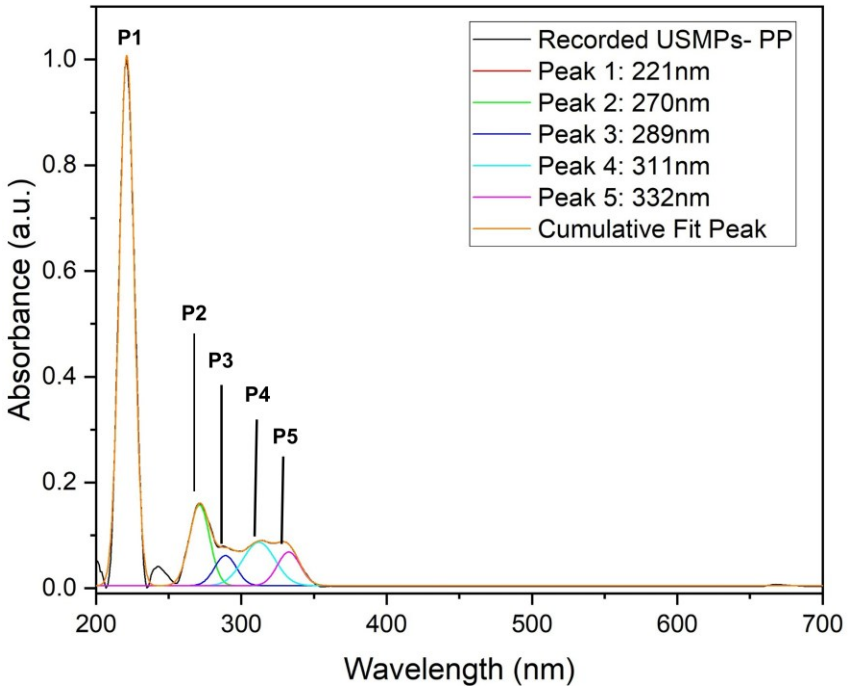

Figure 4.5: The processed absorption spectrum of USMPs-PP (Range 1: MPs > 1.2 µm) is shown, with the recorded spectrum (black line) displayed alongside its deconvoluted components. The spectrum was analysed using Gaussian peak fitting to resolve individual absorption features. Five distinct peaks were identified at P1: 221 nm (red), P2: 270 nm (green), P3: 289 nm (blue), P4: 311 nm (cyan), and P5: 332 nm (violet). The cumulative fit peak (orange line) closely follows the recorded spectrum, confirming the presence of multiple overlapping absorption components contributing to the overall spectral profile.

is weaker compared to P1, is likely attributed to n → π* transitions of carbonyl-containing species present as minor impurities or degradation byproducts [370]. Additionally, the broad absorption band spanning 285 nm to 335 nm can be associated with n→π* transitions of conjugated carbonyl groups, which have been identified in previous studies of polypropylene degradation [370, 372]. The peak at 289 nm is associated with the presence of extended conjugation in the polymer structure [373]. The peaks at 311 nm and 332 nm likely correspond to higher-order n → π* transitions of conjugated carbonyl groups, which have been previously observed in UV studies of degraded polypropylene [372]. The cumulative fit peak closely follows the recorded spectrum, validating the presence of multiple overlapping electronic transitions. This deconvolution provides a better understanding of how oxidative modifications and molecular interactions influence the optical properties of polypropylene, particularly under ultrasonication-induced structural changes.

4.3.2 FLE Mapping Analysis of US-MNPs

The FLE maps of all three US-MNPs, PS, PET, and PP, were recorded across all four size ranges (R1 to R4) and are provided in the appendices (B1, B2, and B3), respectively. All sonicated MNPs exhibited strong fluorescence emissions with varying emission intensities across different size ranges. However, the position of the fluorescence emission zone remained consistent for each polymer type, regardless of size range. Rayleigh scattering artefacts were observed in the FLE maps of all US-MNPs, while Raman scattering was additionally present in the FLE maps of USMNPs-PP. To enhance data accuracy and ensure reliable spectral interpretation, the raw FLE maps were processed using a multi-stage post-processing approach, as detailed in section 4.2.4. These processing steps allowed for the precise identification of fluorescence peaks, facilitating a better understanding of the FL properties of each US-MNP type.

The processed FLE maps, along with their extracted and deconvoluted fluorescence spectra, are presented in Figures 4.6, 4.7, and 4.8 for USMNPs, including PS, PET, and PP, respectively. The FLE maps presented in the abovementioned figures correspond to Range 4 (NPs < 100nm), as this study aims to demonstrate the detection capability of the FLE technique in identifying the smallest particle sizes that can be detected using FL spectroscopy. By selecting Range 4, this analysis provides insights into the feasibility of fluorescence spectroscopy for detecting and characterising nanoplastics, ensuring an accurate evaluation of the method's sensitivity in the lower particle size range.

For each processed FLE map, two deconvoluted spectra were selected. The first corresponds to the optimised excitation wavelength identified within the FLE map, which exhibited the highest FL emission intensity. The second corresponds to the optimised excitation wavelength reported in Chapter 2, Section 2.4.3. These selections provide a comparative analysis of the fluorescence fingerprints of US-MNPs before and after sonication.

The processed FLE map with extracted and deconvoluted spectra of USMNPs-PS (for Range 4) are presented in Figure 4.6. The processed FLE map (Figure 4.6a) exhibits a strong intrinsic FL emission zone in the 370-465 nm range, corresponding to excitation wavelengths between 310 nm and 380 nm. This excitation range aligns well with the broad absorption peak (320-375nm) observed in Figure 4.3, indicating that the USMNPs-PS absorb light in the same spectral region where excitation in the FLE map is observed. Within this region, two dominant fluorescence emission spots are observed at 375 nm and 395 nm, indicating the key FL emission peaks of USMNPs-PS.

Two FL spectra, extracted from the processed FLE map at excitation wavelengths of 345 nm and 360 nm, along with their deconvoluted components, are illustrated in Figures 4.6b and 4.6c, respectively. The FL spectrum recorded at 345 nm excitation (Figure 4.6b) exhibits two major emission peaks at 373 nm and 395 nm, along with a weaker fluorescence signal at 410 nm. The higher FL intensities at this excitation suggest a strong fluorescence response at this excitation wavelength (345nm). At an excitation of 360 nm (Figure 4.6c), which is an optimised excitation wavelength reported in Chapter 2 (Section 2.4.3), four distinct fluorescence emission peaks were observed. Two dominant peaks with high PL intensities appear at 370 nm and 407 nm, while two additional peaks with relatively lower FL intensities are observed at 395 nm and 451 nm. When excited at 345 nm, the observed fluorescence emission peaks align well with findings from previous research [374]. The FL emission peak at 373 nm is attributed to the fluorescence of excited phenyl trimers, which arise due to the aggregation of three aromatic rings in close proximity, leading to enhanced π-π interactions [375]. The emission peaks at 395 nm and 410 nm are associated with excited phenyl tetramers, where four aromatic rings interact through extended conjugation and intermolecular forces. These higher-order aggregates exhibit slightly red-shifted emissions compared to trimers due to the increased delocalisation of π-electrons

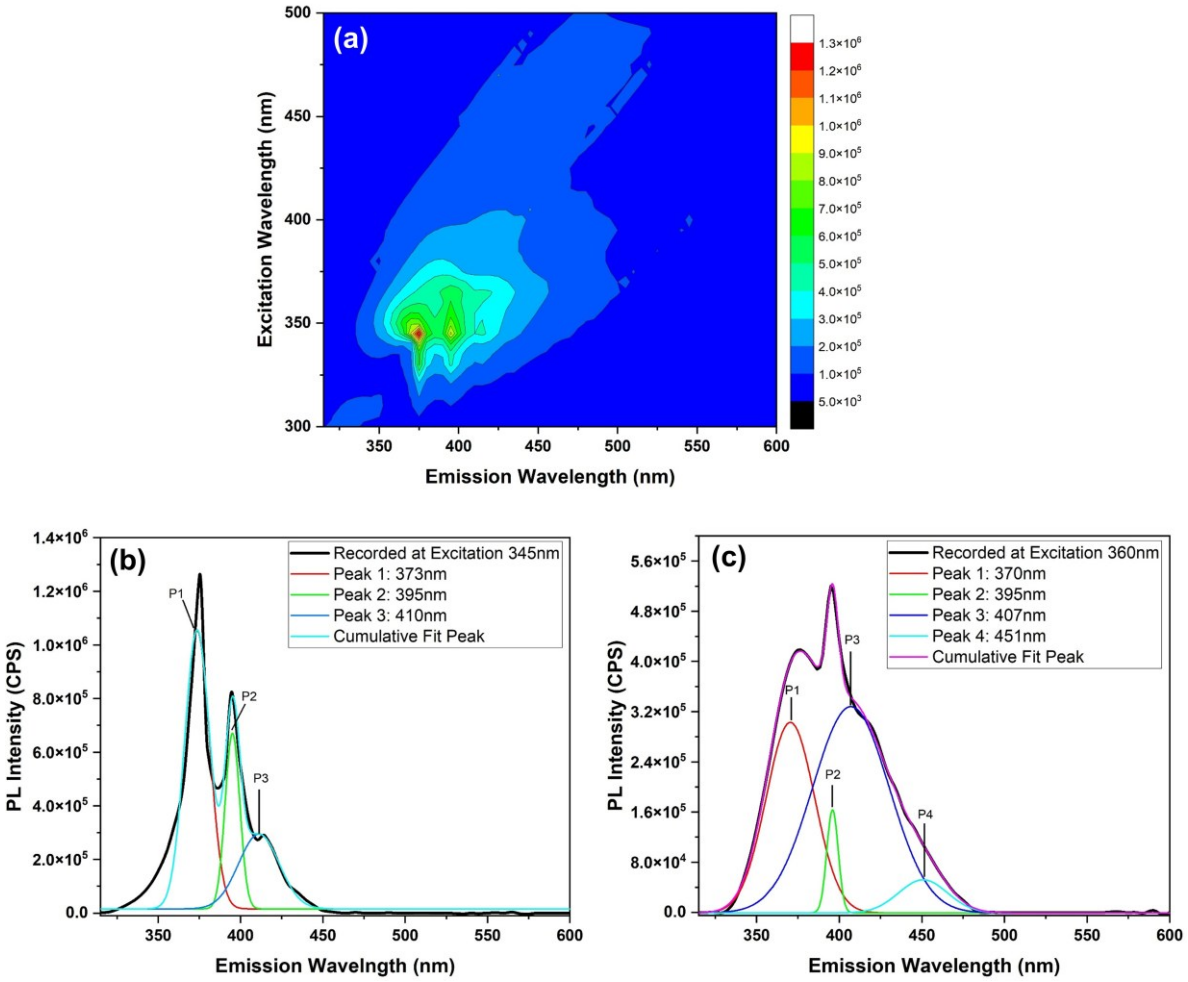

Figure 4.6: FLE analysis of ultra-sonicated micro- and nanoplastic polystyrene (USMNPs-PS). (a) The processed FLE map after scatter removal using R-code, revealing a refined fluorescence emissioon profile. (b) The fluorescence emission spectrum extracted from the processed FLE map at an excitation wavelength of λ_{ex} = 345 nm, with deconvoluted peaks at 373 nm (red), 395 nm (green), and 410 nm (blue), alongside the cumulative fit peak (cyan). (c) The fluorescence emission spectrum at λ_{ex} = 360 nm, displaying deconvoluted peaks at 370 nm (orange), 395 nm (green), 407 nm (blue), and 451 nm (cyan), along with a comulative spectrum (pink).

across the structure, lowering the energy gap between electronic states [376]. This aggregation-induced fluorescence behaviour is a characteristic feature of polystyrene-based materials and contributes to the optical properties of ultrasonicated MNPs. The deconvoluted emission spectrum recorded at an excitation wavelength of 360 nm (Figure 4.6c) exhibits very slight variations in the first three fluorescence peaks compared to those observed at 345 nm. While the primary emission features remain similar, an additional fluorescence emission peak appears at 451 nm, which is

attributed to π-conjugated bonds within the polystyrene structure [293]. In polystyrene, the benzene rings are capable of forming extended π-conjugation through interactions between adjacent phenyl groups. Under excitation at 360 nm, this additional peak at 451 nm suggests that ultrasonication-induced modifications or intermolecular interactions between neighbouring phenyl rings enhance π-electron delocalisation, extending the conjugation length and lowering the energy gap between the ground and excited states. Such extended π-conjugation results in a red-shifted emission, as observed in many aromatic polymers [377], where increased overlap between π-orbitals enables more stabilised excited-state transitions. Comparing these results with the FL spectrum recorded before sonication at 360 nm (section 2.4.3), a shift in fluorescence behaviour is observed. Before sonication, excitation at 360 nm resulted in two major emission peaks at 380 nm and 405 nm, which are similar to FL peaks (P1-P3) of Figure 4.5c, characteristic of fluorescence from conjugated styrene units [283]. Additionally, a broad shoulder was present at 425 nm and 455 nm, indicating fluorescence originating from π-conjugated bonds [293]. After sonication, a more broad shoulder at 451 nm, which resembles the shoulders (425nm and 455nm) observed before sonicated samples, suggests that the ultrasonication has extended the π-conjugation.

The FLE map of USMNPs-PET was recorded in a manner similar to USMNPs-PS, and the corresponding processed FLE map (for Range 4), along with extracted and deconvoluted spectra, are presented in Figure 4.7. The processed FLE map of USMNPs-PET (Figure 4.7a) exhibits a strong bright fluorescence emission from the sample. Within the emission region, two high-intensity FL zones are observed, each containing distinct bright spots representing the key FL emissions. To further investigate the fluorescence behaviour, two spectra were extracted from the processed FLE map at excitation wavelengths of 380 nm and 360 nm, with their respective deconvoluted spectra shown in Figures 4.7b and 4.7c. The extracted FL spectrum at 380 nm excitation (Figure 4.7b) shows two major emission peaks at 415 nm and 437 nm. Upon

deconvolution, three distinct emission peaks were identified at 415 nm, 437 nm, and 443 nm, suggesting multiple overlapping fluorescence contributions. Similarly, the FL spectrum recorded at 360 nm excitation (Figure 4.7c) exhibits two prominent peaks at 412 nm and 434 nm, along with a shoulder at 457 nm, indicating an extended fluorescence response.

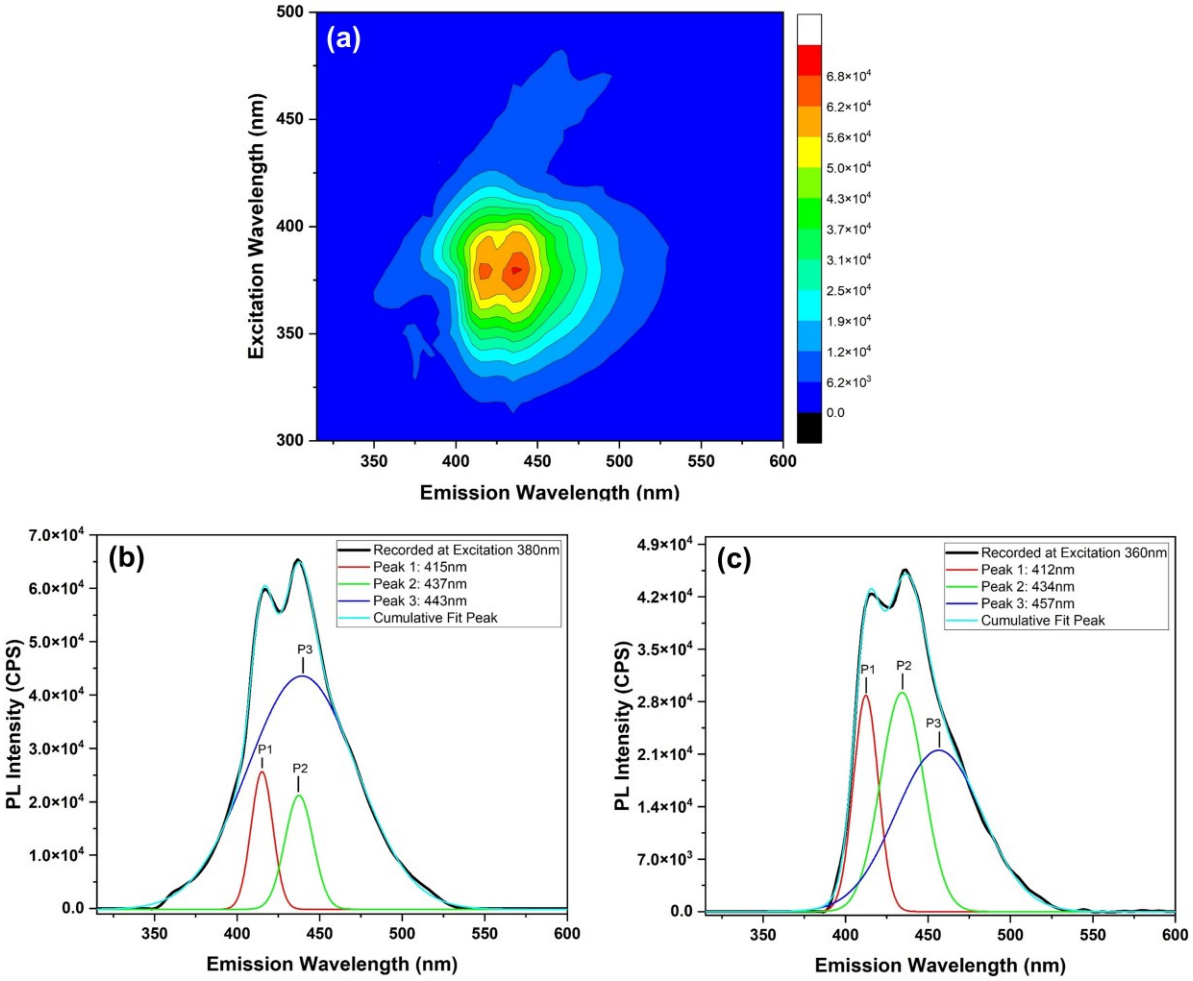

Figure 4.7: FLE analysis of ultra-sonicated micro- and nanoplastic polyethylene terephthalate (USMNPs-PET). (a) The processed FLE map after scatter removal using R code, revealing a refined fluorescence emission profile. (b) The fluorescence emission spectrum extracted from the processed FLE map at an excitation wavelength of λex = 380 nm, with deconvoluted peaks at 415 nm (red), 437 nm (green), and 443 nm (blue), alongside the cumulative spectrum (cyan). (c) The fluorescence emission spectrum at λex = 360 nm, displaying deconvoluted peaks at 412 nm (red), 434 nm (green), and 457 nm (blue), along with the cumulative spectrum (cyan).

The observed FLE spectral fingerprints of USMNPs-PET correlate well with the literature [365, 378, 379], with emission peaks attributed to intrinsic chromophoric structures within the PET,

particularly from aromatic rings present in the terephthalate group and π-conjugation within the polymer chains. According to Lionetto [378], PET exhibits intrinsic fluorescence due to the presence of fluorescent phenylene moieties within its polymer backbone, with emission peaks typically appearing in the 370–450 nm range, depending on polymer morphology and processing conditions. In the present study, the extracted fluorescence spectra from USMNPs-PET reveal a broad emission region ranging from 375nm to 457 nm (see Figure 4.7a), which is consistent with previously reported PET fluorescence characteristics. The FL spectrum recorded at an excitation of 380 nm (Figure 4.7b) shows two major peaks at 415 nm and 437 nm, while deconvolution further resolves to an additional peak at 443 nm. These emission bands suggest the presence of multiple overlapping fluorescence contributions, which may arise from various excited-state conformations of PET macromolecules [287, 380]. Previous studies have also demonstrated that PET fluorescence can be influenced by polymer crystallinity, molecular chain interactions, and processing conditions, all of which impact the relative distribution of emissive states within the polymer matrix [381-383]. The presence of multiple overlapping emission bands is because of a complex interaction between monomeric and excimeric fluorescence states, wherein excimers are formed due to the interaction between adjacent aromatic rings in the polymer backbone [286]. A notable shift in fluorescence emission is observed when PET is excited at 360 nm (Figure 4.7c), where two primary emission peaks appear at 412 nm and 434 nm, with an additional shoulder at 457 nm. The emergence of this shoulder suggests that higher-order interactions or aggregation-induced effects may be influencing the fluorescence properties of PET [384]. Such effects are commonly observed in polymers undergoing mechanical fragmentation, where ultrasonication-induced modifications enhance fluorescence by altering the polymer's chain packing, conjugation length, and local energy states [385]. The extended conjugation that results from these modifications lowers the energy gap between the excited and ground states, leading to a red-shifted emission. The presence of emission bands extending up to 457 nm suggests that PET

fluorescence is not solely due to localised π-π* transitions but also includes delocalised electronic transitions across conjugated molecular structures [367].

The FL spectral comparison of USMNPs-PET before and after sonication at 360 nm excitation reveals significant variations in spectral peak distribution, highlighting the effects of ultrasonication on the polymer's electronic transitions. Before sonication, excitation at 360 nm resulted in fluorescence maxima appearing at 390 nm and 410 nm. These emissions were attributed to π*←n electronic transitions associated with the carbonyl group of the conjugated phenylene ring, indicating that fluorescence primarily originated from localised electronic transitions (see section 2.4.3). After sonication, The FL emission spectrum showed a notable shift, with two dominant peaks appearing at 412 nm and 434 nm, along with a broad shoulder at 457 nm. The red shift in FL peaks and the emergence of this shoulder suggest that higher-order interactions, aggregation effects, or extended conjugation have altered the fluorescence response. Such changes are characteristic of polymers subjected to mechanical fragmentations.

The FLE map of USMNPs-PP was recorded following the same approach used for USMNPs-PS and USMNPs-PET. The corresponding processed FLE maps (for Range 4), along with extracted spectra and deconvoluted peaks, are presented in Figure 4.8. The processed FLE map of USMNPs-PP (Figure 4.8a) shows a strong FL emission zone within the emission region, which highlights characteristic FL features from USMNPs-PP. To further investigate the fluorescence behaviour, two spectra were extracted from the processed FLE map at excitation wavelengths of 355 nm and 370 nm, with their respective deconvoluted spectra shown in Figures 4.8b and 4.8c, respectively. The extracted FL spectrum at 355 nm excitation (Figure 4.8b) shows a major emission peak at 435 nm with a weak shoulder at 520 nm. Similarly, the FL spectrum recorded at 370 nm excitation (Figure 4.8c) exhibits a slightly red-shited major peak at 440 nm along with shoulder at 535 nm.

The emission spectra recorded at various excitation wavelengths of 355 nm and 370 nm (Figure 4.7b and c) exhibited a broad FL peak. The FL emission maxima in the spectrum (Figure 4.8b

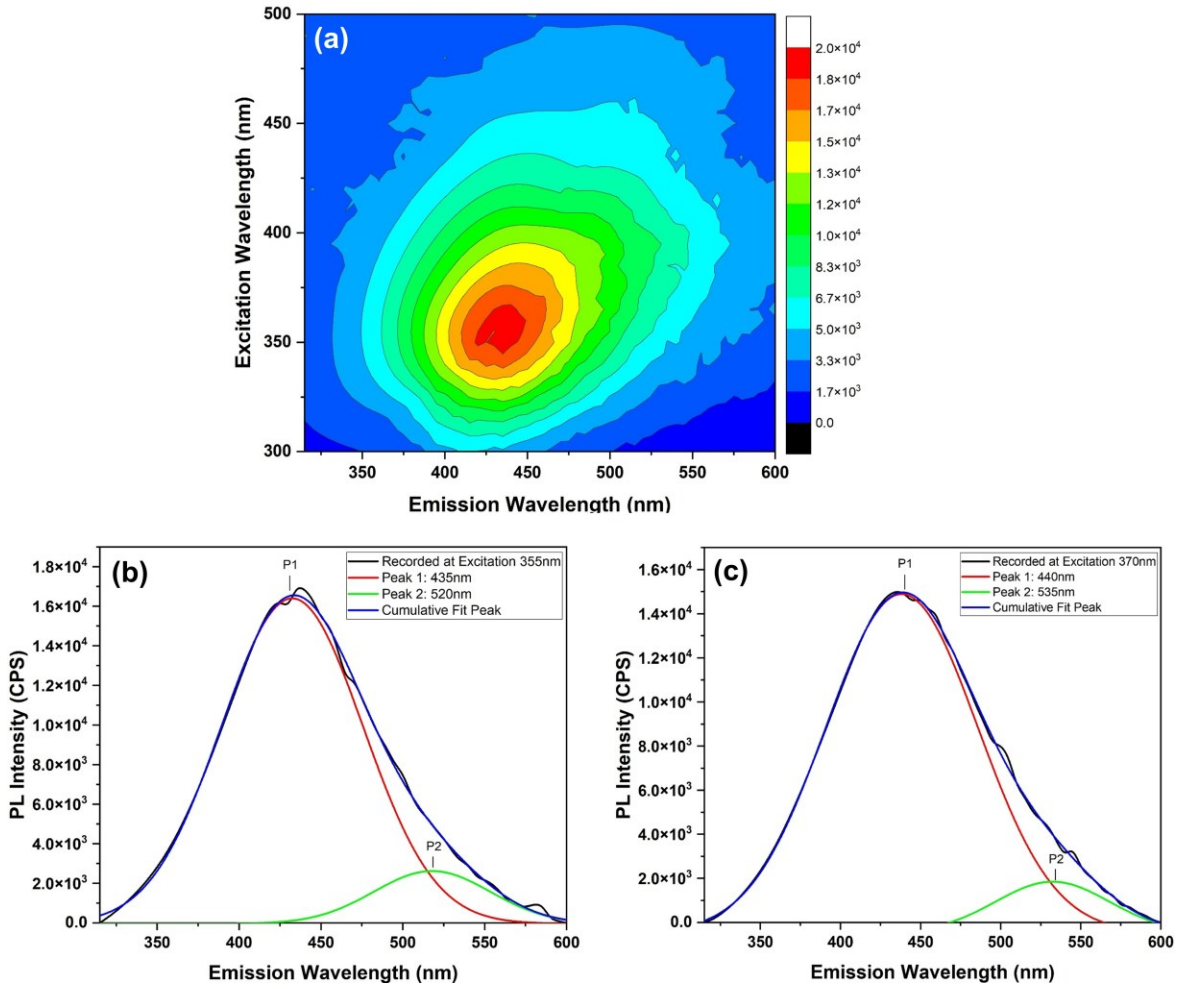

Figure 4.8: FLE analysis of ultra-sonicated micro- and nanoplastic polypropylene (USMPs-PP). (a) The processed FLE map after scatter removal (Rayleigh and Raman) using R code, revealing a refined fluorescence emission profile. (b) The fluorescence emission spectrum extracted from the processed FLE map at an excitation wavelength of λex = 355 nm, with deconvoluted peaks at 435 nm (red) and 520 nm (green), alongside the cumulative spectrum (blue). (c) The fluorescence emission spectrum at λex = 370 nm, displaying deconvoluted peaks at 440 nm (red) and 535 nm (green) along with the cumulative spectrum (blue).

and c) is centred around 435-440 nm, which closely matches the emission maxima observed in 18 polypropylene (PP) samples collected from different packaging materials [386]. These previously analysed PP samples consistently displayed an emission peak at 432 nm, supporting the characteristic fluorescence signature of polypropylene. The FL emission from USMNPs-PP,

observed in the range of 435 nm to 440 nm, is primarily attributed to the presence of polyenone structures that might be formed due to oxidation or degradation (ultrasonication) processes. Polyenones contain conjugated carbonyl (-C=O) and alkene (-C=C) groups, which create localised π-electron delocalisation, enabling fluorescence emission. As the length of the polyene chain increases, it suggests the growth of extended conjugation within the polymer matrix, which can facilitate lower energy electronic transitions. This extension of conjugation is commonly associated with the formation of fluorescent complexes, including excimers and exciplexes [289]. Moreover, the additional shoulder observed in both FL spectra at 520nm-535nm can be attributed to oxidative ageing, where ultrasonication or environmental exposure could have induced carbonyl chromophores that extend the effective conjugation length, lowering the energy gap and shifting emission to a longer wavelength [387].

The FL spectral comparison of USMNPs-PP before and after ultra-sonication at 370 nm excitation reveals distinct variations in spectral characteristics. For instance, before ultra-sonication, excitation at 370 nm resulted in a prominent FL emission peak at 455 nm, attributed to polyenone structures and the formation of excimers or exciplexes due to increasing polyene chain length (see section 2.4.3). However, after sonication, the fluorescence spectrum exhibited a major peak at 435nm-440nm range with an additional shoulder at 520nm-535nm, suggesting oxidative ageing and ultrasonication-induced structural modifications.

The FLE method successfully identified MNP particles of all fractional size ranges (R1-R4) and, most notably, nanoplastics below 100nm. This study enhances FL emission signal strength by utilising optimised excitation wavelengths, thereby improving both the sensitivity and applicability of this method for detecting MNPs in real environmental samples. Moreover, this technique enables rapid, label-free identification of both micro- and nanoplastics, providing a non-destructive and highly effective approach for detecting and characterising MNP contaminants in aqueous media.

4.4 Chapter Conclusion

This chapter investigated the potential of fluorescence (FL) spectroscopy as an effective technique for detecting and characterising micro- and nanoplastics (MNPs) in aqueous media. The study demonstrated that each type of US-MNPs, including polystyrene (PS), polyethylene terephthalate (PET), and polypropylene (PP), exhibits distinct FL excitation-emission zones. The extracted FL spectra confirmed that these MNPs have unique spectral signatures, enabling their detection across various size fractions, including the nanoscale range.

Furthermore, the following dominant fluorescence emission features for these US-MNPs were identified based on the optimised excitation wavelengths:

- USMNPs-PS exhibited the most intense emission at 373 nm and 395 nm when excited at 345 nm.
- USMNPs-PET displayed the fluorescence emission maxima at 415 nm, 437 nm, and 443 nm with an excitation wavelength of 380 nm.
- USMNPs-PP showed the most intense fluorescence emission at 435 nm when excited at 355 nm.

The selection of optimised excitation wavelengths can significantly enhance the fluorescence intensity, improving the adaptability of this technique for real-time environmental MNP monitoring. Moreover, the FL emission peak maxima of USMNPs-PS closely match those recorded for microplastics before sonication, as presented in Chapter 2 (Section 2.4.3). However, USMNPs-PET and USMNPs-PP exhibited additional emission peaks that were not present before sonication. These additional peaks suggest structural modifications induced by ultrasound treatment, resulting in emissions at longer wavelengths due to alterations in molecular arrangement and extended conjugation effects.

Another notable finding was that fluorescence intensity varied across different size fractions of USMNPs, with larger MPs (>1.2 μm) exhibiting stronger signals, whereas smaller NPs (<100 nm) displayed reduced emission intensities. However, this decrease in fluorescence intensity is likely influenced by lower particle concentration, resulting from the sequential filtration process used during US-MNPs preparation, rather than being solely a size-dependent fluorescence effect. Despite this decrease in concentration, the fluorescence peak positions remained consistent across all size fractions, confirming the capability of fluorescence spectroscopy to detect and differentiate plastic types even at the nanoscale.

In conclusion, this chapter establishes fluorescence spectroscopy as a powerful and adaptable tool for detecting and differentiating MNPs in aqueous environments. The ability to extract reliable fluorescence fingerprints from MNP samples underscores the potential of this method for real-world applications, including environmental monitoring and pollution assessment. The findings of this study provide a foundation for further investigations into the fluorescence properties of aged and environmentally degraded plastics, contributing to the advancement of fluorescence-based MNP detection.

Chapter 5: Design and Development of Semi-Portable Spectrometer for Microplastic Detection

5.1 Introduction

The development of the SPPL spectrometer was guided by the limitations observed in existing portable and microspectrometer technologies discussed in Chapter 1, section 1.9. While Raman- and FTIR-based systems have demonstrated portability and chemical specificity, their application in aquatic environments is restricted by fluorescence interference, weak scattering signals, and strong water absorption. In contrast, PL spectroscopy offers a route to overcome these barriers, operating in a spectral region with minimal water interference while achieving high sensitivity for MPs in aqueous media. The growing demand for portable spectrometers originates from the need to conduct on-site and real-time analysis at low cost across various environmental and industrial applications. Portable systems offer flexibility, rapid response, and reduced reliance on bulk laboratory equipment, which makes them particularly valuable for field-based monitoring. In recent years, their potential has gained increasing attention in environmental pollution, particularly in detecting micro- and nano-plastics (MNPs). This chapter builds upon the EEM (Excitation-Emission Mapping) data of microplastics (MP) presented in Chapter 2 (Figure 2.8) and proposes an innovative approach for MP detection using portable PL spectroscopy. We introduce the design and development of a semi-portable photoluminescence (SPPL) spectrometer, a compact yet not entirely portable system that bridges the gap between laboratory-grade and field-deployable spectroscopic instruments. The construction and operational protocols of the SPPL system are detailed, along with considerations for its practical implementation in MP analysis. To validate the efficiency of the SPPL spectrometer, we conducted a proof-of-concept study wherein two commonly encountered microplastics, polystyrene (PS) and polyethylene terephthalate (PET), were analysed in deionised (DI) water. The photoluminescence spectra obtained from the SPPL system were then compared with reference spectral fingerprints obtained using a high-

precision bulk spectrometer (Horiba Nanolog PL spectrometer). The strong correlation between the emission spectra of PS and PET across both systems unequivocally confirms the successful detection and identification of these MPs. This study paves the way for the future development of fully portable spectroscopic systems for robust, rapid, and in-situ detection of microplastics in real-time environmental settings.

5.2 Design of Portable PL Spectroscopic System

5.2.1 Limitations and Challenges for Fully Portable PL spectrometer

The initial conceptualisation of a fully portable photoluminescence (FPPL) spectrometer for microplastic (MP) detection focused on developing a compact design. It aimed to incorporate a small-scale, automated excitation source composed of various laser diodes, each optimised for a specific excitation wavelength to obtain strong FL emission signals from individual microplastic types. These optimised wavelengths were identified through excitation-emission fluorescence mapping analysis (Chapter 2, Section 2.4.3) and presented in Figure 5.1. The figure confirms that the optimal excitation wavelengths for dominant FL emissions from different microplastics predominantly fall within the ultraviolet (UV) region of the electromagnetic spectrum. The FLE maps of PS and PET microplastics (Figures 5.1a and 5.1c) provide valuable insight into the most suitable (optimised) excitation wavelengths for each polymer material. From these maps, high-intensity FL emission spectra were extracted for optimised excitation wavelengths, as shown in Figures 5.1b and 5.1d for PS and PET, respectively. Specifically, PS showed optimal excitation at 360 nm, resulting in two prominent emission peaks at 380 nm and 400 nm. Similarly, PET also exhibited its strongest FL response at 360 nm, with strong emission peaks at approximately 390 nm and 410nm. Based on this information, we planned to integrate UV laser diodes of these specific optimised wavelengths in the FPPL design to achieve portability and enhance detection sensitivity. However, a major limitation was the unavailability of compact commercial UV laser diodes suitable for portable spectrometer system. This posed a significant challenge in the

practical implementation of the FFPL spectrometer, leading to the development of a modified, semi-portable spectrometer.

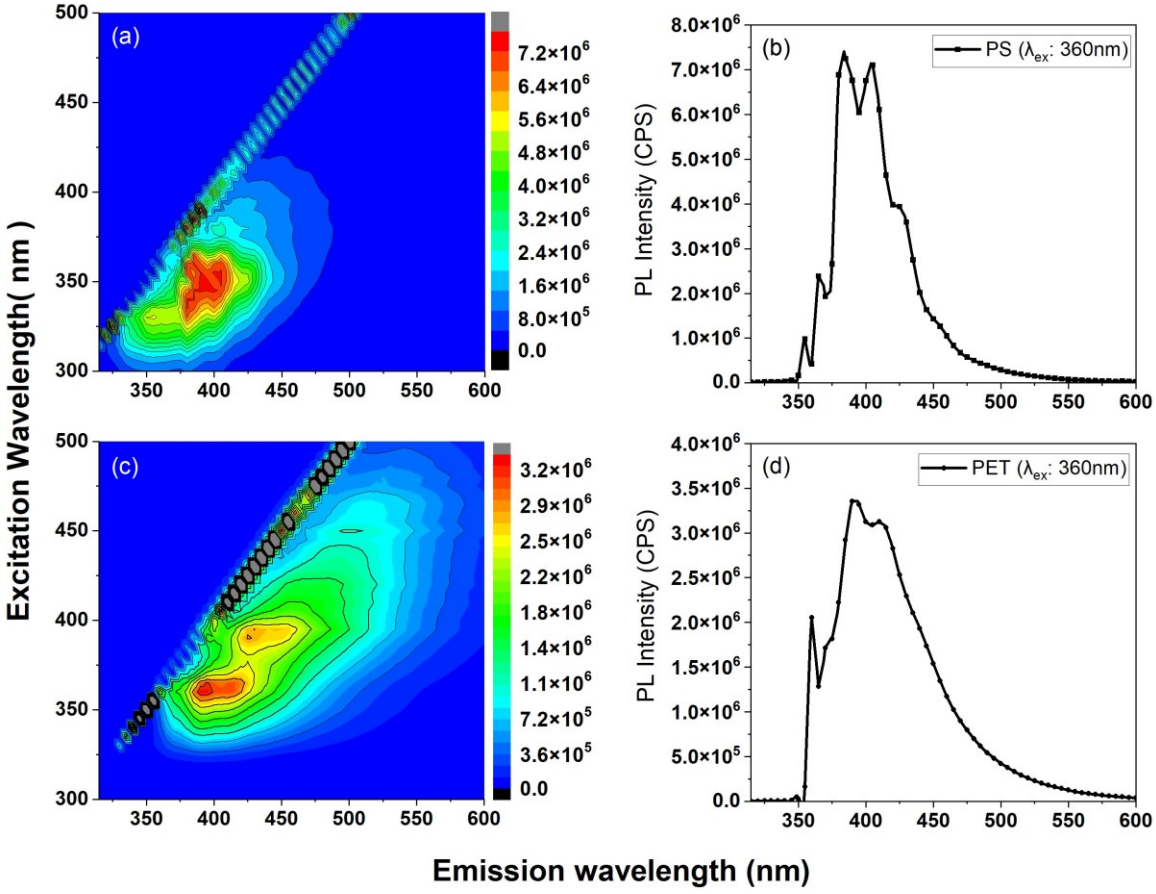

Figure 5.1: Fluorescence excitation-emission (FLE) maps and corresponding photoluminescence (PL) emission spectra of microplastics. (a) FLE map of polystyrene (PS); (b) PL emission spectrum of PS at an excitation wavelength of 360 nm; (c) FLE map of polyethylene terephthalate (PET); (d) PL emission spectrum of PET at an excitation wavelength of 360 nm.

Another challenge was detecting weak fluorescence signals, even when using UV laser diodes, due to their low power and the naturally low emission intensity of smaller MP particles. To address this, two possible strategies can be considered: (i) increasing particle concentration in the sample to improve fluorescence intensity, and (ii) amplifying the emission signal through adjusting the optical path length, using more sensitive detectors, applying fluorescence filters, and employing signal amplification methods.

These challenges underscore the technical hurdles in developing an FFPL spectrometer for MP detection. The insights gained have led to the development of a semi-portable alternative, balancing performance with feasibility while paving the way for future advancements in real-time environmental monitoring of microplastics.

5.2.2 Semi-Portable PL System

Due to current technological limitations, compact and small-scale UV laser diodes are not commercially available for a fully portable spectrometer. To address this, a new spectrometer design, referred to as the Semi-Portable PL (SPPL) Spectrometer, is proposed to serve as a proof-of-concept for MP detection. The SPPL spectrometer integrates essential optical components while maintaining a relatively compact design. The complete description of the SPPL spectrometer design, including a schematic diagram, is presented in Appendix C, Section C.2. This semi-portable setup serves as an intermediate step toward achieving full portability while ensuring accurate and reliable detection of microplastics. The integration of appropriate optical components and collection of strong fluorescence signals enhances detection sensitivity, providing a strong foundation for future developments in portable MP spectrometry.

5.3 Construction of Semi-Portable PL Spectrometer

Based on the design presented in Appendix C.2, the SPPL spectrometer was constructed using a combination of optical, mechanical, and electronic components to ensure precise excitation and detection of strong intrinsic fluorescence from MPs. The system consists of three main sections: (i) the excitation source and optical components, (ii) the sample compartment, and (iii) the fluorescence measurement system. A detailed list of the components used in its construction is provided in Table 5.1, while Figure 5.2 shows the components utilised for constructing the SPPL system.

Table 5.1: A list of components used for the construction of semi-portable PL spectrometer

Excitation Source and optical components	**Sample compartment**	**Fluorescence measurement system**
1x IK series He-Cd Laser (IK3252R-E) (wavelength range 315-360nm with peak λ=325nm (30mW))	CVH100-CV - Light-Tight Cover for CVH100(/M) Cuvette Holder	Compact CCD Czerny-Turne Spectrometers (CSS200) (200-1000nm), 3648 Pixel, spectral resolution of 2nm, CCD Line Array
1x He-Cd Laser power supply (KR1801C)	CVH100 - Cuvette Holder for Micro & Macro Cuvettes with SMA905 Fibre Adapter, 30 mm Cage Cube Compatible	SMA905-connectorised fibres
1x Laser shutter (UNIBLITZ Elec.) (VMM-D1)	CVH100-COL SMA905 Fibre Adapter with Lens Mount, Spacers, and Retaining Ring	0.22 NA TECS Double-Clad Silica Step Index Multimode Optical Fibre
1x Kinematic mount (KM100CP/M) and mirror (KM100-E01)	Additional Ø1" Mounted Filter Holder (CVH100-FH)	USB connecting cable
2x Mirror mount (New focus 9807)	Bi-directional vertical stand/mount for cuvette holder	THORLAB software
2x 45-degree mirror holder (New focus 9920)		

5.3.1 Excitation Source and Optical Pathway

The SPPL system used an IK series Helium-Cadmium (He-Cd) laser as the excitation source. It operates in the 315–360 nm UV wavelength range, with a peak emission at 325 nm and a power output of 30 mW. The laser was powered by a KR1801C He-Cd power supply, ensuring a stable and consistent beam for excitation. To regulate laser exposure on the sample, a semi-automated laser shutter (UNIBLITZ VMM-D1) was installed at the output of the laser source. This shutter allowed precise control over the laser beam, preventing unnecessary exposure and

improving measurement accuracy. The laser beam was then directed through a carefully aligned optical pathway consisting of kinematic mounts, mirrors, and 45-degree mirror holders. The first kinematic mount (KM100CP/M) held a mirror positioned at a 45-degree angle, reflecting the laser beam toward the next optical component. A second mirror, mounted on a New Focus 9807 mirror holder, further redirected the beam at 90 degrees upwards. A third 45-degree mirror (New Focus 9920) ensured the beam was adjusted to a horizontal position, making it parallel to the optical axis, before reaching the sample. A black optical block was placed to eliminate unwanted transmitted light, ensuring minimal background noise in the fluorescence signal.

Figure 5.2: The components used for the construction of the PL spectrometer (Design II) for microplastic detection. (a) He-Cd laser power supply, (b-c) semi-automated laser shutter-VMM-D1, (d) cuvette holder and accessories, (e) compact USB spectrometer, (f) new focus mirror mount, (g) new focus 45-degree mirror holder, (h) kinematic mount and mirror.

5.3.2 Sample Compartment and Fluorescence Collection

The laser beam enters the CVH100 cuvette holder, which securely holds a macro- or micro-cuvette containing the MP sample. The sample holder was integrated with a bi-directional vertical stage featuring Y-Z adjustments, allowing precise positioning of the sample for optimal excitation. Upon interaction with the UV laser beam, the microplastic particles absorbed the excitation energy

and subsequently emitted fluorescence at a longer wavelength. The fluorescence emission was collected at a 90-degree angle from the incident beam to avoid direct laser interference. The emitted fluorescence was captured using a step-index multimode optical fibre (0.22 NA TECS Double-Clad Silica Fibre) with a SMA905 connector, which efficiently transmits the signal to the spectrometer for spectral analysis.

5.3.3 Fluorescence Detection and Data Acquisition

The collected fluorescence signal from the MP sample is directed to a compact CCD Czerny-Turner THORLAB USB Spectrometer (CSS200), which operates in the 200–1000 nm spectral range high-precision detection. The spectrometer was connected to a computer via a

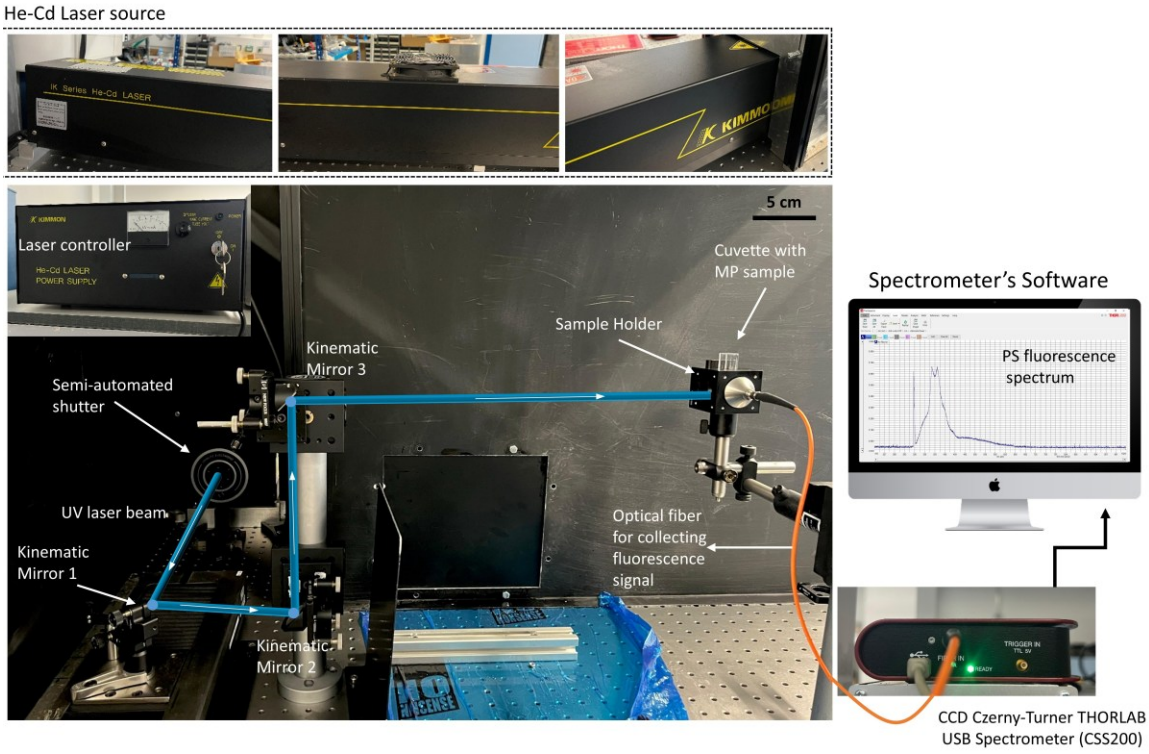

Figure 5.3: Photoluminescence-based SPPL spectrometer for microplastic detection. He-Cd UV laser (excitation source) with a continuous wavelength range of 315-360nm and a maximum output power of 30 mW at λ 325 nm. CCD Czerny-Turner THORLAB USB Spectrometer (CSS200) with in-built software.

USB interface, where data acquisition and analysis were carried out using Thorlabs software. To improve measurement accuracy, the system recorded an average of 10 fluorescence spectra per

sample, ensuring reliable and reproducible results. The final fluorescence fingerprints of the microplastic sample were then generated and analysed. The entire setup was carefully aligned and optimised to ensure high-quality intrinsic fluorescence detection of microplastics. The final assembled PL spectrometer (based on Design-II) is shown in Figure 5.3.

5.4 Microplastic Sample Preparation

Microplastic samples of PS and PET were analysed in an aqueous medium to ensure consistency in fluorescence measurements. The samples were prepared by mixing PS and PET with deionised water at a concentration of 4.5% w/v. Prior to measurement, the raw source materials, PS and PP, were cut into fragments approximately 1 mm in size using stainless steel laboratory scissors to achieve uniform sample sizes. For sample sourcing, PS microplastics were obtained in the form of millimetre-sized cylindrical beads purchased from Acros Organics (average molecular weight: 250,000 M.W.). The PET plastic fragments were obtained from Aqua-Vale plastic water bottles (London, UK). This preparation method ensured that the samples were adequately sized for efficient interaction with the excitation source, facilitating reliable fluorescence detection using the SPPL spectrometer. The preparation steps followed here were consistent with the methodology described in Chapter 2, Section 2.2.

5.5 Microplastic Analysis using SPPL Spectrometer

After assembling the SPPL spectrometer, the system was tested to evaluate its capability to detect and analyse MP samples. The primary objective was to validate the spectrometer's ability to reliably capture fluorescence signals from different microplastic types, ensuring that the collected spectra were reproducible and distinct. The analysis involved exposing microplastic samples, such as PS and PET, to a UV laser source (325 nm, 30 mW), which provided sufficient excitation energy to induce fluorescence. The emitted photoluminescence was then collected orthogonal to the incident laser beam, ensuring minimal interference from scattered light. To

optimise fluorescence signal collection, careful attention was given to sample positioning, optical alignment, and external noise reduction. The emitted fluorescence spectra were recorded using the Thorlabs compact USB spectrometer, and the resulting spectral fingerprints were analysed to confirm the presence of microplastics. The spectrometer's capability to differentiate between various plastic types was assessed based on excitation-emission matrix (EEM) data and spectral comparisons with reference samples.

Following the successful implementation of the SPPL system, a standard measurement protocol was established (Appendix C.1) to ensure consistent and accurate data acquisition.

5.5.1 Data Acquisition

The PL spectra of two microplastic samples, PS and PET, were recorded using the custom-designed SPPL spectrometer following the measurement protocol outlined in Section 5.4.1. The acquired spectra provide valuable insights into the fluorescence characteristics of microplastics under UV excitation. The PL spectra of PS and PET microplastics were obtained using a broad-range excitation source (315-360 nm), with a peak excitation wavelength at 325 nm [388]. The PL spectrum of PS (Figure 5.4a) highlights several key features, including Rayleigh Scattering at 325 nm, a strong elastic scattering signal detected at the excitation wavelength, a commonly observed phenomenon in PL measurements. The primary PL emissions were detected at 383 nm and 402 nm, corresponding to the intrinsic fluorescence response of polystyrene. In addition to these dominant peaks, a strong shoulder peak at 420 nm was also observed, which may be linked to structural variations or energy transfer processes within the polymer matrix (see Chapter 2, section 2.4.3). Aside from the intrinsic fluorescence of PS, an unwanted background noise (see Section A) appeared as a broad hump between 460–650 nm. This interference is likely caused by external light sources or system misalignment, leading to unwanted fluorescence artefacts. Two corrective measures are recommended to improve spectral accuracy and minimise background interference: (i) Using a fully enclosed sample compartment to block stray light from

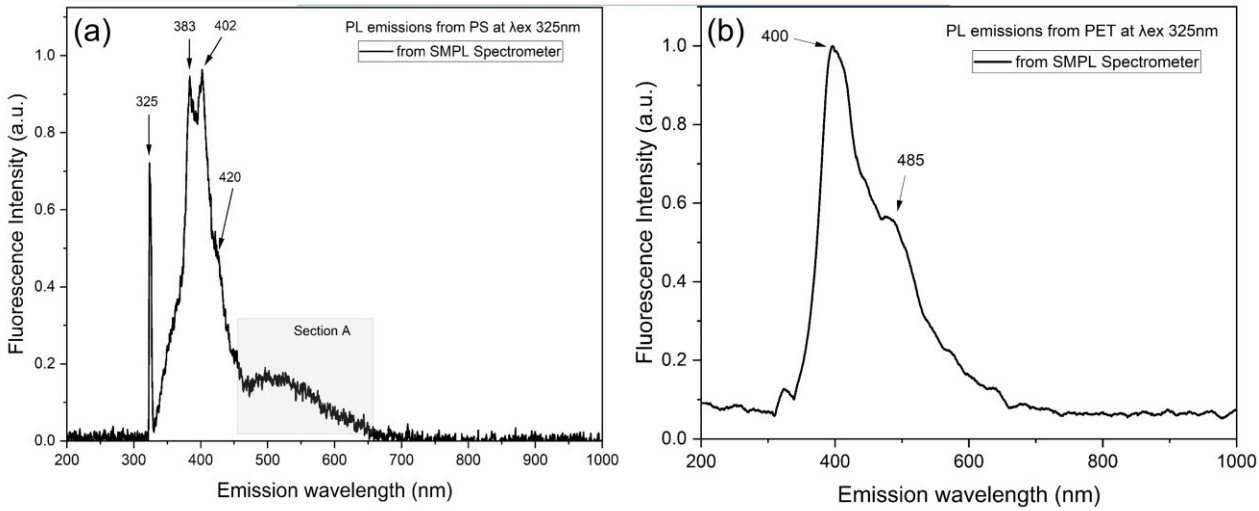

Figure 5.4: The PL emission spectrum of polystyrene beads in water was recorded using Design-II USB spectrometer. The excitation wavelength is 325 nm, with two emission peaks at 383 nm and 402 nm and a shoulder at 420 nm. Section-A shows additional noise in the signal.

external sources and (ii) Ensuring precise laser beam alignment to minimise unintended scattering effects. By implementing these adjustments, the signal-to-noise ratio (SNR) of the acquired spectra can be improved, leading to more reliable fluorescence detection of microplastics. The PET squared sheets (length < 500 µm) were analysed using the same system parameters as those configured for PS, ensuring consistency in excitation conditions. The resulting PL spectrum of PET is presented in Figure 5.4b, highlighting its fluorescence emission characteristics. In the PL spectrum of PET, two distinct fluorescence emission peaks are observed at 400 nm and 485 nm. The peak at 400 nm represents the primary intrinsic fluorescence emission, while the secondary peak at 485 nm indicates an extended fluorescence response. Compared to PS, the fluorescence emissions from PET exhibit significantly higher intensity, effectively suppressing both the Rayleigh scattering signal and any additional background noise. This strong emission signal enhances the clarity of the spectral fingerprint, making PET identification more straightforward.

The fluorescence behaviour of PET under UV excitation can be attributed to its molecular structure, having a greater stokes shift, which allows efficient absorption and subsequent

emission at longer wavelengths. The origin of the PL emissions from both PS and PET, including the mechanisms governing their fluorescence properties, has been discussed in detail in Chapter 2, Section 2.4.3. Overall, the high-intensity fluorescence emissions observed in the PET spectrum confirm the sensitivity of the SPPL spectrometer in detecting microplastic samples.

5.5.2 Comparison of SPPL Data with Bulk Spectrometer Measurements

To validate the performance of the SPPL spectrometer, the fluorescence spectra of PS and PET acquired using the SPPL system were compared with those obtained from a conventional bulk spectrometer (Nanolog Horiba spectrofluorometer). This comparison aimed to assess the accuracy, spectral resolution, and noise levels associated with the SPPL system in relation to a well-established bulk fluorescence measurement system. The PL spectra of PS, measured using both the SPPL spectrometer and the Nanolog EEM spectrofluorometer, are presented in Figure 5.5.

The spectrum obtained from the SPPL spectrometer is represented by the black line, while the blue line corresponds to the spectrum recorded using the Nanolog system. Both spectrometers successfully captured the two primary PL emission peaks of PS at 383 nm, 402 nm, and a shoulder at 420 nm, demonstrating the ability of the SPPL spectrometer to detect the intrinsic fluorescence signature of PS. However, some notable differences between the two spectra were observed. The SPPL spectrum exhibits a strong elastic scattering signal originating from the excitation source (325 nm), which is less prominent in the Nanolog spectrum. A broad noise peak appears in the SPPL spectrum, which is absent in the Nanolog spectrum. This discrepancy is likely due to the open configuration of the SPPL system, which allows external light interference, whereas the Nanolog system operates within a closed setup, minimising background noise.

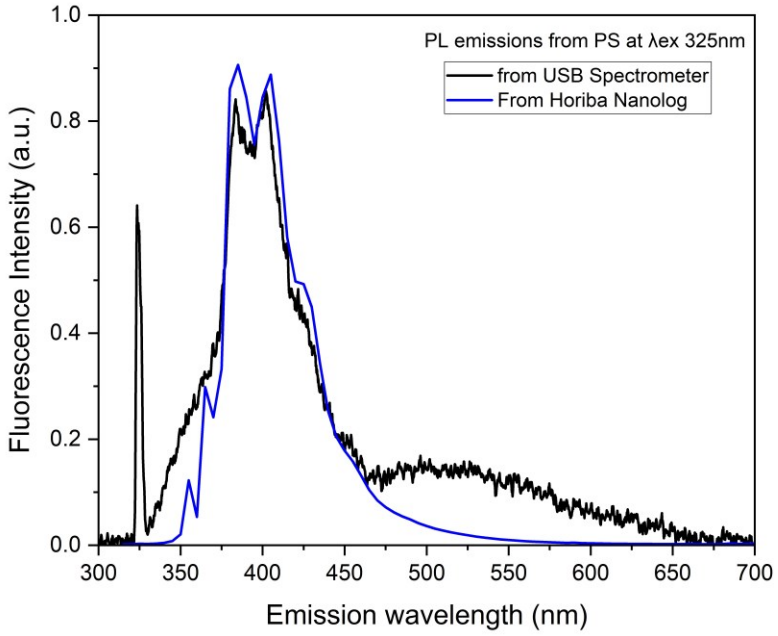

Figure 5.5: The PL emission spectra from polystyrene microplastic beads, The PL spectrum recorded with an advanced bulk Nanolog Horiba spectrometer (blue), and the spectrum recorded with a designed semi-portable USB PL spectrometer (black).

The PL spectra of PET measured using both spectrometers are shown in Figure 5.6. The black line represents the spectrum recorded with the SPPL spectrometer, while the red line corresponds to the Nanolog EEM spectrofluorometer. Both systems display the primary PL emission peak of PET between 395–400 nm, confirming that the SPPL spectrometer effectively detects the fluorescence signature of PET. However, differences between the two spectra include an additional shoulder at 485 nm, which is not present in the Nanolog spectrum. This additional peak is likely caused by background noise from the open configuration of the SPPL system. Rayleigh scattering at 325 nm, originating from the excitation source, is visible in both spectra. An extra elastic scattering peak at 650 nm appears in the Nanolog spectrum, which is absent in the SPPL spectrum. This peak is likely due to the first overtone or second harmonic generation from the short-arc xenon lamp used in the Nanolog system.

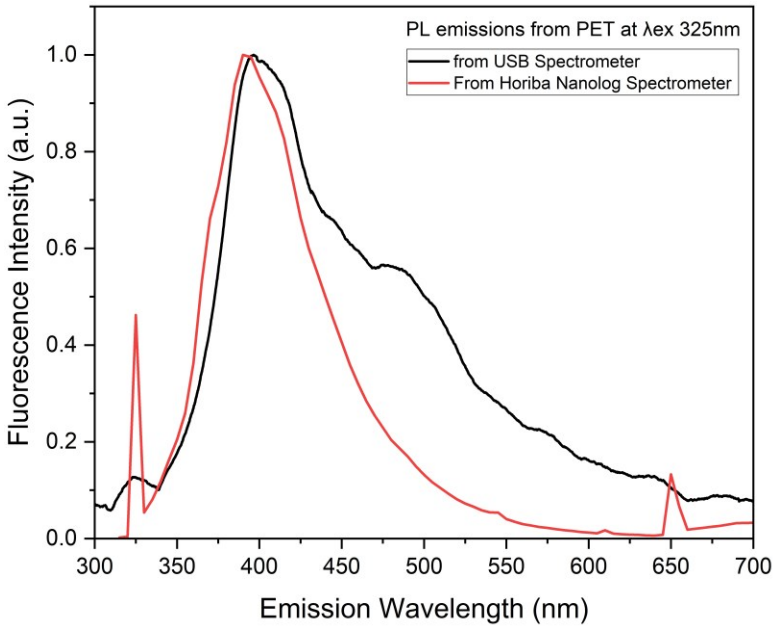

Figure 5.6: PL emission spectra from polyethylene terephthalate microplastic sheets, The PL spectrum was recorded with an advanced bulk Nanolog Horiba spectrometer (red), and the spectrum was recorded with a USB SPPL spectrometer (black).

5.6 Chapter Conclusion

This chapter focused on the design and development of a semi-portable photoluminescence (SPPL) spectrometer for detecting microplastics (MPs). The initial design was intended to be fully portable for on-site detection of microplastics (Appendix C: section C.3). However, due to the unavailability of compact UV laser diodes, the initial design was modified into a semi-portable spectrometer. This design featured a semi-portable PL spectrometer incorporating a Helium-Cadmium (He-Cd) laser source for rapid and label-free detection of MPs based on their intrinsic fluorescence. The fluorescence signatures of polystyrene (PS) and polyethylene terephthalate (PET) were recorded using this system and validated against a commercial bulk PL spectrometer (Horiba Nanolog EEM spectrofluorometer). The comparative analysis demonstrated that the SPPL spectrometer successfully captured the characteristic fluorescence emissions of PS and PET, confirming its effectiveness in detecting MPs. However, it exhibited higher background noise

levels due to its open optical configuration, in contrast to the Nanolog system, which operates within a closed configuration, minimising external interference. Despite these limitations, the SPPL system demonstrated rapid spectral acquisition of MPs in less than a second for particles exceeding 500 μm in diameter.

This proof-of-concept study underscores the potential of a semi-portable PL spectrometer for non-destructive, rapid, and label-free detection of MNP contamination in aqueous media. While further optimisation is required to enhance its signal-to-noise ratio (SNR) and portability, these findings represent a significant step toward developing a field-deployable platform for real-time MNP analysis in water bodies using PL spectroscopy. In terms of performance, the desired SNR is >100, as this provides sufficient sensitivity to reliably distinguish polymer-specific emission features from background noise, even at low concentrations representative of environmental levels (ppb range). For comparison, commercial portable Raman spectrometers [389, 390] designed for laboratory-quality performance have reported SNR values exceeding 1000 under optimised conditions, but such levels are typically achieved with strong reference samples. Future improvements to our system, such as optimising optical alignment, integrating higher-efficiency detectors, and applying digital signal processing, will be aimed at reaching the >100 SNR threshold required for reliable microplastic detection in the field while maintaining compactness and portability.

Chapter 6: Conclusion and Future Work

This thesis aims to explore the potential of photoluminescence spectroscopy for the detection, identification, and characterisation of micro- and nanoplastic (MNPs) in aqueous media. The aim has been achieved through a systematic investigation in the following areas:

- Microplastic detection and identification using fluorescence spectroscopy.
- Generation of model secondary micro- and nanoplastics for research purposes
- Exploring the capability of the FLE mapping approach in detecting and identifying micro- to nanoscale plastic particles.
- Assessing the feasibility of developing portable PL spectrometers for MNP detection.

The main achievements of this research can be summarised in three key areas:

1. **Identification and Characterisation of Microplastics through Fluorescence Spectroscopy:** In Chapter 2, a systematic fluorescence excitation-emission (FLE) mapping approach was employed to determine the intrinsic fluorescence characteristics of polystyrene (PS), polyethene terephthalate (PET), and polypropylene (PP) microplastics. The analysis revealed distinct fluorescence excitation and emission features for each polymer, establishing an effective method for non-destructive and label-free identification. The optimal excitation wavelengths for each type of microplastic were determined through FLE analysis, with PS and PET best excited at 360 nm and PP at 370 nm. These strong excitation-emission features of MP provide a foundation for the development of fluorescence-based spectroscopic methods applicable in environmental, food, and aquatic studies. These findings underscore the potential of fluorescence spectroscopy as a rapid and non-destructive technique for microplastic identification.
2. **Development of a Systematic Protocol for Producing Model Micro- and Nanoplastics through Direct Sonication:** In Chapter 3, a direct ultrasonication-based

protocol was successfully developed to generate reference micro- and nanoplastics (US-MNPs) in aqueous media. This approach significantly accelerated (~ 53%) the process compared to conventional ultrasonication methods. Moreover, our approach eliminated the need for additional chemical treatments. The generated US-MNPs exhibited high suspension stability (USPMMA showing the highest stability (~0.5–0.6% transmission change) and USPVC the lowest (~5.8–6.1% transmission change) over 2 hours) and a broad size distribution (100nm to 150 μm), closely resembling environmental MNP pollutants. Advanced analytical techniques were employed to comprehensively characterise the particles, including Raman spectroscopy to assess chemical structure changes after ultrasonication; μ-QCL-based infrared spectroscopy combined with machine learning for MP classification; UV-Vis spectroscopy to quantify the suspensibility of USMNPs; and SEM imaging to observe particle size and surface morphology. The outcomes of this study provide a reproducible and efficient protocol for generating micro- and nanoplastics, offering a valuable tool for future research on their environmental behaviour and impact.

3. **Application of Fluorescence Spectroscopy for Nanoplastic Detection and the Development of a Semi-Portable PL Spectrometer:**

   The feasibility of FLE mapping as a detection technique for micro- and nanoplastics was demonstrated through FLE mapping analysis of US-MNPs in aqueous media. The findings of Chapter 4 confirmed that each ultrasonicated polymer (PS, PET, and PP) exhibited distinct spectral fingerprints, facilitating their identification. The dominant FL emissions for each USMNPs were determined using optimised excitation wavelengths: USMNPs-PS showed intense emissions at 373 nm and 395 nm (excitation at 345 nm); USMNPs-PET exhibited maxima at 415 nm, 437 nm, and 443 nm (excitation at 380 nm); and USMNPs-PP displayed a strong peak at 435 nm (excitation at 355 nm). While these results confirm the effectiveness of FLE mapping in detecting nanoscale plastics, some spectral overlap,

particularly between PET and PP, may be observed, indicating the need for advanced statistical tools such as Parallel Factor Analysis (PARAFAC) to resolve complex fluorescence signals. This study establishes FLE mapping as a powerful alternative for MNP detection and characterisation.

Further advancements were made by designing and developing a semi-portable photoluminescence (PL) spectrometer for real-time microplastic detection, as shown in Chapter 5. The prototype successfully captured the fluorescence emissions of PS and PET microplastics, validating its capability as an alternative to conventional bulk spectrometers. Despite challenges such as background noise and the need for further optimisation, this proof-of-concept study demonstrates the potential for a compact, field-deployable PL spectrometer, paving the way for real-world applications in environmental monitoring.

In conclusion, this research provides a significant contribution to the field of micro- and nanoplastic detection, offering novel methodologies (Ultrasoincation and FL spectroscopy) for sample preparation and optical characterisation. The integration of FL spectroscopy for MNP detection, coupled with the development of a semi-portable spectrometer, represents a step forward in establishing efficient, label-free, and real-time monitoring techniques. The findings of this study not only enhance the understanding of the intrinsic fluorescence properties of micro- and nanoplastics but also provide a practical foundation for the development of more accessible and field-deployable detection systems.

Future research should aim to build on the current findings by addressing key gaps in quantification, applicability to real-world samples, and integration with advanced analytical and computational tools. The following are some potential directions for future research:

Quantification of Particle Concentration and Mass Yield: Most current studies remain qualitative, focusing on the presence or absence of nanoplastic signals. Moving towards absolute quantification is crucial if photoluminescence (PL) spectroscopy is to become a reliable monitoring tool. Techniques such as nanoparticle tracking analysis (NTA), gravimetric analysis, dynamic light scattering (DLS), or UV-Vis calibration standards can be employed to provide concentration and mass-based data. Establishing quantitative relationships between fluorescence intensity and particle concentration would allow to compare datasets across collected in laboratories and real environments. This would also facilitate the development of standard protocols and reference libraries for nanoplastic detection. Incorporating such quantification would bridge the gap between laboratory-based demonstrations and regulatory or environmental monitoring requirements.

Integration of Quantum Yield Measurements: The fluorescence quantum yield (QY) of ultrasonically generated micro- and nanoplastics (US-MNPs) remains under characterised, yet it is fundamental for comparing the fluorescence response across polymer types and environmental conditions. Measuring QY under controlled conditions would support the establishment of standardised optical sensing platforms and could improve reproducibility in fluorescence-based monitoring studies. It would also help reveal how polymer properties, such as crystallinity, ageing, or surface oxidation, affect photophysical behaviour. By systematically mapping QY values across polymer types and sizes, future research could provide a database that enhances the predictive power of PL-based detection.

Expanding to Mixed-Polymer and Real-World Samples: The vast majority of studies to date have been conducted on single polymer types in controlled laboratory environments. However, environmental samples are inherently complex, containing heterogeneous mixtures of polymers, organic matter, and other interfering materials. Testing PL spectroscopy in these conditions will be essential to demonstrate its robustness. Advanced spectral decomposition methods, such as Parallel Factor Analysis (PARAFAC), should be further applied to separate overlapping

fluorescence signatures within mixed-polymer matrices. Expanding the technique to sediment, soil, food, and biological tissue samples would greatly increase its environmental relevance.

Integration of PL with Lab-on-a-Chip Platforms: Miniaturisation and automation are critical for translating laboratory-based spectroscopy into portable field-deployable systems. Future work should therefore focus on integrating PL spectroscopy with microfluidic lab-on-a-chip devices. Acoustic manipulation within microfluidic channels could allow for efficient sample handling, concentration, and sorting of MNPs particles prior to detection through PL system. Such platforms could enable high-throughput analysis with reduced sample preparation times, making them more practical for real-world monitoring of MNPs.

Machine Learning-Based Classification and Automated Data Processing: The volume and complexity of fluorescence spectral data will continue to increase as PL spectroscopy is applied to mixed and environmental samples. Integrating machine learning (ML) algorithms for automated classification of polymer types offers a promising solution. Supervised learning approaches could be trained on large datasets of labelled spectra, while unsupervised learning could assist in recognising new or unknown polymer signatures. Combining ML with FLE mapping would improve both accuracy and efficiency, while reducing human error in interpretation. Beyond classification, artificial intelligence could be employed for automated spectral decomposition, noise reduction, and anomaly detection, enabling real-time decision-making in field applications.

Application Across Environmental and Biological Matrices: To establish PL spectroscopy as a comprehensive monitoring tool, its applicability should be demonstrated across a broad range of matrices, including freshwater, marine systems, soils, sediments, food, and biota. Particular emphasis should be placed on testing biota samples to evaluate uptake, accumulation, and potential toxicity of MNPs.

References

[1] S. A. Iqrar, A. Bibi, R. Chinnambedu Murugesan, D. Hill, and A. Rozhin, "Excitation–Emission Fluorescence Mapping Analysis of Microplastics That Are Typically Pollutants," *Photochem,* vol. 4, no. 4, pp. 488-500, 2024.

[2] S. Al-Thawadi, "Microplastics and nanoplastics in aquatic environments: challenges and threats to aquatic organisms," *Arabian Journal for Science and Engineering,* vol. 45, no. 6, pp. 4419-4440, 2020.

[3] J. C. Anderson, B. J. Park, and V. P. Palace, "Microplastics in aquatic environments: implications for Canadian ecosystems," *Environmental Pollution,* vol. 218, pp. 269-280, 2016.

[4] J. Gigault *et al.*, "Current opinion: What is a nanoplastic?," *Environmental Pollution,* vol. 235, pp. 1030-1034, 2018/04/01/ 2018.

[5] A. Ter Halle *et al.*, "Nanoplastic in the North Atlantic subtropical gyre," *Environmental science & technology,* vol. 51, no. 23, pp. 13689-13697, 2017.

[6] M. Cole and T. S. Galloway, "Ingestion of nanoplastics and microplastics by Pacific oyster larvae," *Environmental science & technology,* vol. 49, no. 24, pp. 14625-14632, 2015.

[7] Z. Sobhani, X. Zhang, C. Gibson, R. Naidu, M. Megharaj, and C. Fang, "Identification and visualisation of microplastics/nanoplastics by Raman imaging (i): Down to 100 nm," *Water research,* vol. 174, p. 115658, 2020.

[8] J. P. Da Costa, P. S. Santos, A. C. Duarte, and T. Rocha-Santos, "(Nano) plastics in the environment–sources, fates and effects," *Science of the total environment,* vol. 566, pp. 15-26, 2016.

[9] A. A. Koelmans, E. Besseling, and W. J. Shim, "Nanoplastics in the aquatic environment. Critical review," *Marine anthropogenic litter,* pp. 325-340, 2015.

[10] E. J. Petersen *et al.*, "Adapting OECD aquatic toxicity tests for use with manufactured nanomaterials: key issues and consensus recommendations," *Environmental science & technology,* vol. 49, no. 16, pp. 9532-9547, 2015.

[11] K. Aquleema, N. Ahmed, D. Deepshikha, A. Kumari, and R. Dev, "Plastic Pollution and Public Health: A Systematic Review of Degradation Pathways and Health Risks," *International Journal of Pharmaceutical Sciences,* 2024.

[12] K. Boyle and B. Örmeci, "Microplastics and nanoplastics in the freshwater and terrestrial environment: A review," *Water,* vol. 12, no. 9, p. 2633, 2020.

[13] D. M. Mitrano, P. Wick, and B. Nowack, "Placing nanoplastics in the context of global plastic pollution," *Nature Nanotechnology,* vol. 16, no. 5, pp. 491-500, 2021.

[14] S. Ghosh, J. K. Sinha, S. Ghosh, K. Vashisth, S. Han, and R. Bhaskar, "Microplastics as an emerging threat to the global environment and human health," *Sustainability,* vol. 15, no. 14, p. 10821, 2023.

[15] S. Adhikari, V. Kelkar, R. Kumar, and R. U. Halden, "Methods and challenges in the detection of microplastics and nanoplastics: a mini-review," *Polymer international,* vol. 71, no. 5, pp. 543-551, 2022.

[16] E. C. Ebere and V. E. Ngozi, "Microplastics, an emerging concern: a review of analytical techniques for detecting and quantifying microplatics," *Analytical methods in environmental chemistry journal,* vol. 2, no. 2, pp. 13-30, 2019.

[17] S. Primpke *et al.*, "Critical assessment of analytical methods for the harmonized and cost-efficient analysis of microplastics," *Applied Spectroscopy,* vol. 74, no. 9, pp. 1012-1047, 2020.

[18] K. Nirmala, G. Rangasamy, M. Ramya, V. U. Shankar, and G. Rajesh, "A critical review on recent research progress on microplastic pollutants in drinking water," *Environmental Research,* vol. 222, p. 115312, 2023.

[19] K. Nirmala, G. Rangasamy, M. Ramya, V. U. Shankar, and G. Rajesh, "A critical review on recent research progress on microplastic pollutants in drinking water," *Environmental Research,* p. 115312, 2023.

[20] P. Europe, "Plastics Europe association of plastics manufacturers plastics—the facts 2021 an analysis of European plastics production, demand and waste data," *Plastic-Facts,* vol. 2021, p. 34, 2021.

[21] M. Enfrin, L. F. Dumée, and J. Lee, "Nano/microplastics in water and wastewater treatment processes–origin, impact and potential solutions," *Water research,* vol. 161, pp. 621-638, 2019.

[22] A. G. Rellán, D. V. Ares, C. V. Brea, A. F. López, and P. M. B. Bugallo, "Sources, sinks and transformations of plastics in our oceans: Review, management strategies and modelling," *Science of the Total Environment,* vol. 854, p. 158745, 2023.

[23] J. Boucher and D. Friot, *Primary microplastics in the oceans: a global evaluation of sources*. Iucn Gland, Switzerland, 2017.

[24] C. Guerranti, T. Martellini, G. Perra, C. Scopetani, and A. Cincinelli, "Microplastics in cosmetics: Environmental issues and needs for global bans," *Environmental toxicology and pharmacology,* vol. 68, pp. 75-79, 2019.

[25] F. Belzagui, M. Crespi, A. Álvarez, C. Gutiérrez-Bouzán, and M. Vilaseca, "Microplastics' emissions: Microfibers' detachment from textile garments," *Environmental Pollution,* vol. 248, pp. 1028-1035, 2019.

[26] A. van Wezel, I. Caris, and S. A. Kools, "Release of primary microplastics from consumer products to wastewater in the Netherlands," *Environmental toxicology and chemistry,* vol. 35, no. 7, pp. 1627-1631, 2016.

[27] I. Efimova, M. Bagaeva, A. Bagaev, A. Kileso, and I. P. Chubarenko, "Secondary microplastics generation in the sea swash zone with coarse bottom sediments: laboratory experiments," *Frontiers in Marine Science,* vol. 5, p. 313, 2018.

[28] B. Pandey *et al.*, "Microplastics in the Ecosystem: An Overview on Detection, Removal, Toxicity Assessment, and Control Release," *Water,* vol. 15, no. 1, p. 51, 2023.

[29] S. Vijayaraman, P. Mondal, A. Nandan, and N. A. Siddiqui, "Presence of microplastic in water bodies and its impact on human health," in *Advances in Air Pollution Profiling and Control: Select Proceedings of HSFEA 2018*, 2020: Springer, pp. 57-65.

[30] L. Yang, Y. Zhang, S. Kang, Z. Wang, and C. Wu, "Microplastics in soil: A review on methods, occurrence, sources, and potential risk," *Science of the Total Environment,* vol. 780, p. 146546, 2021.

[31] J. Gasperi *et al.*, "Microplastics in air: are we breathing it in?," *Current Opinion in Environmental Science & Health,* vol. 1, pp. 1-5, 2018.

[32] L. Van Cauwenberghe, L. Devriese, F. Galgani, J. Robbens, and C. R. Janssen, "Microplastics in sediments: a review of techniques, occurrence and effects," *Marine environmental research,* vol. 111, pp. 5-17, 2015.

[33] K. Ugwu, A. Herrera, and M. Gómez, "Microplastics in marine biota: A review," *Marine pollution bulletin,* vol. 169, p. 112540, 2021.

[34] M. Jin, X. Wang, T. Ren, J. Wang, and J. Shan, "Microplastics contamination in food and beverages: Direct exposure to humans," *Journal of Food Science,* vol. 86, no. 7, pp. 2816-2837, 2021.

[35] D. Eerkes-Medrano, H. A. Leslie, and B. Quinn, "Microplastics in drinking water: A review and assessment," *Current Opinion in Environmental Science & Health,* vol. 7, pp. 69-75, 2019.

[36] H. A. Leslie, M. J. Van Velzen, S. H. Brandsma, A. D. Vethaak, J. J. Garcia-Vallejo, and M. H. Lamoree, "Discovery and quantification of plastic particle pollution in human blood," *Environment international,* vol. 163, p. 107199, 2022.

[37] Y. Wang *et al.*, "Airborne hydrophilic microplastics in cloud water at high altitudes and their role in cloud formation," *Environmental Chemistry Letters,* vol. 21, no. 6, pp. 3055-3062, 2023.

[38] D. An, J. Na, J. Song, and J. Jung, "Size-dependent chronic toxicity of fragmented polyethylene microplastics to Daphnia magna," *Chemosphere,* vol. 271, p. 129591, 2021.

[39] W. Liu, H. Liao, M. Wei, M. Junaid, G. Chen, and J. Wang, "Biological uptake, distribution and toxicity of micro (nano) plastics in the aquatic biota: A special emphasis on size-dependent impacts," *TrAC Trends in Analytical Chemistry,* p. 117477, 2023.

[40] Y. Wang *et al.*, "Size-dependent effects of nanoplastics on structure and function of superoxide dismutase," *Chemosphere,* vol. 309, p. 136768, 2022.

[41] Z. Yang, G. M. DeLoid, J. Baw, H. Zarbl, and P. Demokritou, "Assessment of ingested micro-and nanoplastic (MNP)-mediated genotoxicity in an in vitro model of the small intestinal epithelium (SIE)," *Nanomaterials,* vol. 14, no. 9, p. 807, 2024.

[42] O. Pikuda *et al.*, "Toxicity of microplastics and nanoplastics to Daphnia magna: current status, knowledge gaps and future directions," *TrAC Trends in Analytical Chemistry,* p. 117208, 2023.

[43] Y. K. Song *et al.*, "Large accumulation of micro-sized synthetic polymer particles in the sea surface microlayer," *Environmental science & technology,* vol. 48, no. 16, pp. 9014-9021, 2014.

[44] S. Naidu, V. Ranga Rao, and K. Ramu, "Microplastics in the benthic invertebrates from the coastal waters of Kochi, Southeastern Arabian Sea," *Environmental geochemistry and health,* vol. 40, pp. 1377-1383, 2018.

[45] W. Courtene-Jones, B. Quinn, S. F. Gary, A. O. Mogg, and B. E. Narayanaswamy, "Microplastic pollution identified in deep-sea water and ingested by benthic invertebrates in the Rockall Trough, North Atlantic Ocean," *Environmental pollution,* vol. 231, pp. 271-280, 2017.

[46] N. C. Ory, P. Sobral, J. L. Ferreira, and M. Thiel, "Amberstripe scad Decapterus muroadsi (Carangidae) fish ingest blue microplastics resembling their copepod prey along the coast

of Rapa Nui (Easter Island) in the South Pacific subtropical gyre," *Science of the Total Environment,* vol. 586, pp. 430-437, 2017.

[47] L. Fu, J. Li, G. Wang, Y. Luan, and W. Dai, "Adsorption behavior of organic pollutants on microplastics," *Ecotoxicology and Environmental Safety,* vol. 217, p. 112207, 2021.

[48] G. Obersteiner *et al.*, "Assessment of Different Sampling, Sample Preparation and Analysis Methods Addressing Microplastic Concentration and Transport in Medium and Large Rivers Based on Research in the Danube River Basin," *Sustainability,* vol. 17, no. 13, p. 5836, 2025.

[49] I. A. Kane *et al.*, "Seafloor microplastic hotspots controlled by deep-sea circulation," *Science,* vol. 368, no. 6495, pp. 1140-1145, 2020.

[50] M. Liedermann, P. Gmeiner, S. Pessenlehner, M. Haimann, P. Hohenblum, and H. Habersack, "A Methodology for Measuring Microplastic Transport in Large or Medium Rivers. Water, 10 (4): 414," ed, 2018.

[51] C. Sun, J. Ding, and F. Gao, "Methods for microplastic sampling and analysis in the seawater and fresh water environment," in *Methods in Enzymology*, vol. 648: Elsevier, 2021, pp. 27-45.

[52] M. Jian, Y. Zhang, W. Yang, L. Zhou, S. Liu, and E. G. Xu, "Occurrence and distribution of microplastics in China's largest freshwater lake system," *Chemosphere,* vol. 261, p. 128186, 2020/12/01/ 2020.

[53] X. Xiong, S. Xie, K. Feng, and Q. Wang, "Occurrence of microplastics in a pond-river-lake connection water system: How does the aquaculture process affect microplastics in natural water bodies," *Journal of Cleaner Production,* vol. 352, p. 131632, 2022.

[54] B. K. Pramanik, S. K. Pramanik, and S. Monira, "Understanding the fragmentation of microplastics into nano-plastics and removal of nano/microplastics from wastewater using membrane, air flotation and nano-ferrofluid processes," *Chemosphere,* vol. 282, p. 131053, 2021.

[55] Y. Lai, L. Dong, Q. Li, P. Li, and J. Liu, "Sampling of micro-and nano-plastics in environmental matrixes," *TrAC Trends in Analytical Chemistry,* vol. 145, p. 116461, 2021.

[56] D. Li *et al.*, "Profiling the Vertical Transport of Microplastics in the West Pacific Ocean and the East Indian Ocean with a Novel in Situ Filtration Technique," *Environmental Science & Technology,* vol. 54, no. 20, pp. 12979-12988, 2020/10/20 2020.

[57] R. Di Mauro, M. J. Kupchik, and M. C. Benfield, "Abundant plankton-sized microplastic particles in shelf waters of the northern Gulf of Mexico," *Environmental Pollution,* vol. 230, pp. 798-809, 2017/11/01/ 2017.

[58] C. B. Crawford and B. Quinn, "8 - Microplastic collection techniques," in *Microplastic Pollutants*, C. B. Crawford and B. Quinn Eds.: Elsevier, 2017, pp. 179-202.

[59] Z. L. Botterell *et al.*, "Microplastic ingestion in zooplankton from the Fram Strait in the Arctic," *Science of the Total Environment,* vol. 831, p. 154886, 2022.

[60] S. S. Sadri, "Investigation of microplastic debris in marine surface waters using different sampling methods," 2015.

[61] M. Liedermann, P. Gmeiner, S. Pessenlehner, M. Haimann, P. Hohenblum, and H. Habersack, "A methodology for measuring microplastic transport in large or medium rivers," *Water,* vol. 10, no. 4, p. 414, 2018.

[62] A. A. Koelmans, N. H. Mohamed Nor, E. Hermsen, M. Kooi, S. M. Mintenig, and J. De France, "Microplastics in freshwaters and drinking water: Critical review and assessment of data quality," *Water Research,* vol. 155, pp. 410-422, 2019/05/15/ 2019.

[63] Z. Dai *et al.*, "Occurrence of microplastics in the water column and sediment in an inland sea affected by intensive anthropogenic activities," *Environmental Pollution,* vol. 242, pp. 1557-1565, 2018/11/01/ 2018.

[64] C. Wang *et al.*, "Microplastics profile in a typical urban river in Beijing," *Science of The Total Environment,* vol. 743, p. 140708, 2020/11/15/ 2020.

[65] B. Rios-Fuster *et al.*, "Ubiquitous vertical distribution of microfibers within the upper epipelagic layer of the western Mediterranean Sea," *Estuarine, Coastal and Shelf Science,* vol. 266, p. 107741, 2022/03/05/ 2022.

[66] K. Liu, W. Courtene-Jones, X. Wang, Z. Song, N. Wei, and D. Li, "Elucidating the vertical transport of microplastics in the water column: a review of sampling methodologies and distributions," *Water Research,* vol. 186, p. 116403, 2020.

[67] L. D. K. Kanhai, K. Gårdfeldt, O. Lyashevska, M. Hassellöv, R. C. Thompson, and I. O'Connor, "Microplastics in sub-surface waters of the Arctic Central Basin," *Marine Pollution Bulletin,* Article vol. 130, pp. 8-18, 2018.

[68] C. G. Bannick *et al.*, "Development and testing of a fractionated filtration for sampling of microplastics in water," *Water Research,* vol. 149, pp. 650-658, 2019/02/01/ 2019.

[69] S. M. Mintenig, P. S. Bäuerlein, A. A. Koelmans, S. C. Dekker, and A. P. Van Wezel, "Closing the gap between small and smaller: towards a framework to analyse nano- and microplastics in aqueous environmental samples," *Environmental Science: Nano,* Article vol. 5, no. 7, pp. 1640-1649, 2018.

[70] L. Hildebrandt, D. M. Mitrano, T. Zimmermann, and D. Pröfrock, "A nanoplastic sampling and enrichment approach by continuous flow centrifugation," *Frontiers in Environmental Science,* vol. 8, p. 89, 2020.

[71] X. Guo, Y. Yin, Z. Tan, Z. Zhang, Y. Chen, and J. Liu, "Significant Enrichment of Engineered Nanoparticles in Water Surface Microlayer," *Environmental Science & Technology Letters,* vol. 3, no. 10, pp. 381-385, 2016/10/11 2016.

[72] P. Ren, S. Luo, L. Wang, Y. Chi, and Y. Tang, "A method for efficient separation of polystyrene nanoplastics and its application in natural freshwater," *RSC Advances,* vol. 15, no. 36, pp. 29217-29229, 2025.

[73] L. Zhang *et al.*, "Distribution of microplastics in surface water and sediments of Qin river in Beibu Gulf, China," *Science of The Total Environment,* vol. 708, p. 135176, 2020/03/15/ 2020.

[74] T. M. Karlsson, A. Kärrman, A. Rotander, and M. Hassellöv, "Comparison between manta trawl and in situ pump filtration methods, and guidance for visual identification of microplastics in surface waters," *Environmental science and pollution research,* vol. 27, pp. 5559-5571, 2020.

[75] Y. Huang, Q. Liu, W. Jia, C. Yan, and J. Wang, "Agricultural plastic mulching as a source of microplastics in the terrestrial environment," *Environmental Pollution,* vol. 260, p. 114096, 2020/05/01/ 2020.

[76] B. Zhou *et al.*, "Microplastics in agricultural soils on the coastal plain of Hangzhou Bay, east China: Multiple sources other than plastic mulching film," *Journal of Hazardous Materials,* vol. 388, p. 121814, 2020/04/15/ 2020.

[77] L. A. Amaral-Zettler, E. R. Zettler, T. J. Mincer, M. A. Klaassen, and S. M. Gallager, "Biofouling impacts on polyethylene density and sinking in coastal waters: a macro/micro tipping point?," *Water Research,* vol. 201, p. 117289, 2021.

[78] G. Peng, B. Zhu, D. Yang, L. Su, H. Shi, and D. Li, "Microplastics in sediments of the Changjiang Estuary, China," *Environmental Pollution,* vol. 225, pp. 283-290, 2017/06/01/ 2017.

[79] L. Niu *et al.*, "New insights into the vertical distribution and microbial degradation of microplastics in urban river sediments," *Water Research,* vol. 188, p. 116449, 2021/01/01/ 2021.

[80] J. A. Baptista Neto *et al.*, "The impact of sediment dumping sites on the concentrations of microplastic in the inner continental shelf of Rio de Janeiro/Brazil," *Marine Pollution Bulletin,* vol. 149, p. 110558, 2019/12/01/ 2019.

[81] M. Bergmann, S. Mützel, S. Primpke, M. B. Tekman, J. Trachsel, and G. Gerdts, "White and wonderful? Microplastics prevail in snow from the Alps to the Arctic," *Science advances,* vol. 5, no. 8, p. eaax1157, 2019.

[82] M. Bergmann, S. Mützel, S. Primpke, M. Tekman, J. Trachsel, and G. Gerdts, "White and wonderful? Microplastics prevail in snow from the Alps to the Arctic. Sci. Adv. 5, eaax1157," ed, 2019.

[83] D. Materić *et al.*, "Micro- and Nanoplastics in Alpine Snow: A New Method for Chemical Identification and (Semi)Quantification in the Nanogram Range," *Environmental Science & Technology,* vol. 54, no. 4, pp. 2353-2359, 2020/02/18 2020.

[84] K. Liu, X. Wang, T. Fang, P. Xu, L. Zhu, and D. Li, "Source and potential risk assessment of suspended atmospheric microplastics in Shanghai," *Science of The Total Environment,* vol. 675, pp. 462-471, 2019/07/20/ 2019.

[85] S. Allen *et al.*, "Atmospheric transport and deposition of microplastics in a remote mountain catchment," *Nature Geoscience,* vol. 12, no. 5, pp. 339-344, 2019/05/01 2019.

[86] A. Torres-Agullo, A. Karanasiou, T. Moreno, and S. Lacorte, "Airborne microplastic particle concentrations and characterization in indoor urban microenvironments," *Environmental Pollution,* vol. 308, p. 119707, 2022.

[87] Á. Mári *et al.*, "Validation of microplastic sample preparation method for freshwater samples," *Water Research,* vol. 202, p. 117409, 2021.

[88] F. Stock, C. Kochleus, B. Bänsch-Baltruschat, N. Brennholt, and G. Reifferscheid, "Sampling techniques and preparation methods for microplastic analyses in the aquatic environment–A review," *TrAC Trends in Analytical Chemistry,* vol. 113, pp. 84-92, 2019.

[89] N. Razeghi *et al.*, "Sample preparation methods for the analysis of microplastics in freshwater ecosystems: a review," *Environmental Chemistry Letters,* pp. 1-27, 2022.

[90] D. Thomas, B. Schütze, W. M. Heinze, and Z. Steinmetz, "Sample preparation techniques for the analysis of microplastics in soil—a review," *Sustainability,* vol. 12, no. 21, p. 9074, 2020.

[91] K. S. Din, M. F. Khokhar, S. I. Butt, A. Qadir, and F. Younas, "Exploration of microplastic concentration in indoor and outdoor air samples: Morphological, polymeric, and elemental analysis," *Science of the Total Environment,* vol. 908, p. 168398, 2024.

[92] S. S. Monteiro and J. P. da Costa, "Methods for the extraction of microplastics in complex solid, water and biota samples," *Trends in Environmental Analytical Chemistry,* vol. 33, p. e00151, 2022.

[93] K. Kadac-Czapska, P. J. Trzebiatowska, E. Knez, A. Zaleska-Medynska, and M. Grembecka, "Microplastics in food-a critical approach to definition, sample preparation, and characterisation," *Food Chemistry,* vol. 418, p. 135985, 2023.

[94] Z. Song *et al.*, "To what extent are we really free from airborne microplastics?," *Science of the Total Environment,* vol. 754, p. 142118, 2021.

[95] V. Artifon, E. Zanardi-Lamardo, and G. Fillmann, "Aquatic organic matter: Classification and interaction with organic microcontaminants," *Science of the Total Environment,* vol. 649, pp. 1620-1635, 2019.

[96] H. K. Imhof, J. Schmid, R. Niessner, N. P. Ivleva, and C. Laforsch, "A novel, highly efficient method for the separation and quantification of plastic particles in sediments of aquatic environments," *Limnology and oceanography: methods,* vol. 10, no. 7, pp. 524-537, 2012.

[97] R. Dris *et al.*, "Beyond the ocean: contamination of freshwater ecosystems with (micro-) plastic particles," *Environmental chemistry,* vol. 12, no. 5, pp. 539-550, 2015.

[98] M. B. Zobkov and E. E. Esiukova, "Evaluation of the Munich Plastic Sediment Separator efficiency in extraction of microplastics from natural marine bottom sediments," *Limnology and Oceanography: Methods,* vol. 15, no. 11, pp. 967-978, 2017.

[99] S. Felsing, C. Kochleus, S. Buchinger, N. Brennholt, F. Stock, and G. Reifferscheid, "A new approach in separating microplastics from environmental samples based on their electrostatic behavior," *Environmental Pollution,* vol. 234, pp. 20-28, 2018.

[100] M. Cole, P. Lindeque, C. Halsband, and T. S. Galloway, "Microplastics as contaminants in the marine environment: a review," *Marine pollution bulletin,* vol. 62, no. 12, pp. 2588-2597, 2011.

[101] E. M. Foekema, C. De Gruijter, M. T. Mergia, J. A. van Franeker, A. J. Murk, and A. A. Koelmans, "Plastic in north sea fish," *Environmental science & technology,* vol. 47, no. 15, pp. 8818-8824, 2013.

[102] E. Hermsen, S. M. Mintenig, E. Besseling, and A. A. Koelmans, "Quality criteria for the analysis of microplastic in biota samples: a critical review," *Environmental science & technology,* vol. 52, no. 18, pp. 10230-10240, 2018.

[103] L. Mai, L.-J. Bao, L. Shi, C. S. Wong, and E. Y. Zeng, "A review of methods for measuring microplastics in aquatic environments," *Environmental Science and Pollution Research,* vol. 25, pp. 11319-11332, 2018.

[104] L. Van Cauwenberghe and C. R. Janssen, "Microplastics in bivalves cultured for human consumption," *Environmental pollution,* vol. 193, pp. 65-70, 2014.

[105] F. Stock, C. Kochleus, B. Bänsch-Baltruschat, N. Brennholt, and G. Reifferscheid, "Sampling techniques and preparation methods for microplastic analyses in the aquatic environment – A review," *TrAC Trends in Analytical Chemistry,* vol. 113, pp. 84-92, 2019/04/01/ 2019.

[106] M. Claessens, L. Van Cauwenberghe, M. B. Vandegehuchte, and C. R. Janssen, "New techniques for the detection of microplastics in sediments and field collected organisms," *Marine pollution bulletin,* vol. 70, no. 1-2, pp. 227-233, 2013.

[107] M. G. Löder and G. Gerdts, "Methodology used for the detection and identification of microplastics—a critical appraisal," *Marine anthropogenic litter,* pp. 201-227, 2015.

[108] M.-T. Nuelle, J. H. Dekiff, D. Remy, and E. Fries, "A new analytical approach for monitoring microplastics in marine sediments," *Environmental pollution,* vol. 184, pp. 161-169, 2014.

[109] J. Frias *et al.*, "Standardised protocol for monitoring microplastics in sediments. Deliverable 4.2," 2018.

[110] A. Dehaut *et al.*, "Microplastics in seafood: Benchmark protocol for their extraction and characterization," *Environmental pollution,* vol. 215, pp. 223-233, 2016.

[111] F. Galgani *et al.*, *Guidance on the monitoring of marine litter in European seas*. European Commission, Joint Research Centre, 2023.

[112] M. Kedzierski, V. Le Tilly, G. César, O. Sire, and S. Bruzaud, "Efficient microplastics extraction from sand. A cost effective methodology based on sodium iodide recycling," *Marine pollution bulletin,* vol. 115, no. 1-2, pp. 120-129, 2017.

[113] A.-K. Kniggendorf, C. Wetzel, and B. Roth, "Microplastics detection in streaming tap water with Raman spectroscopy," *Sensors,* vol. 19, no. 8, p. 1839, 2019.

[114] C. F. Araujo, M. M. Nolasco, A. M. P. Ribeiro, and P. J. A. Ribeiro-Claro, "Identification of microplastics using Raman spectroscopy: Latest developments and future prospects," *Water Research,* vol. 142, pp. 426-440, 2018/10/01/ 2018.

[115] L. Mikac, I. Rigó, L. Himics, A. Tolić, M. Ivanda, and M. Veres, "Surface-enhanced Raman spectroscopy for the detection of microplastics," *Applied Surface Science,* vol. 608, p. 155239, 2023/01/15/ 2023.

[116] S. Kühn, A. Van Oyen, A. M. Booth, A. Meijboom, and J. A. Van Franeker, "Marine microplastic: Preparation of relevant test materials for laboratory assessment of ecosystem impacts," *Chemosphere,* vol. 213, pp. 103-113, 2018.

[117] D. Magrì *et al.*, "Laser ablation as a versatile tool to mimic polyethylene terephthalate nanoplastic pollutants: characterization and toxicology assessment," *ACS nano,* vol. 12, no. 8, pp. 7690-7700, 2018.

[118] M. Cole, "A novel method for preparing microplastic fibers," *Scientific Reports,* vol. 6, no. 1, p. 34519, 2016/10/03 2016.

[119] L. Eitzen, S. Paul, U. Braun, K. Altmann, M. Jekel, and A. S. Ruhl, "The challenge in preparing particle suspensions for aquatic microplastic research," (in eng), *Environ Res,* vol. 168, pp. 490-495, Jan 2019.

[120] D. Magrì *et al.*, "Laser Ablation as a Versatile Tool To Mimic Polyethylene Terephthalate Nanoplastic Pollutants: Characterization and Toxicology Assessment," *ACS Nano,* vol. 12, no. 8, pp. 7690-7700, 2018/08/28 2018.

[121] M. Cole, "A novel method for preparing microplastic fibers," *Scientific reports,* vol. 6, no. 1, pp. 1-7, 2016.

[122] O. Pikuda, E. G. Xu, D. Berk, and N. Tufenkji, "Toxicity assessments of micro-and nanoplastics can be confounded by preservatives in commercial formulations," *Environmental Science & Technology Letters,* vol. 6, no. 1, pp. 21-25, 2018.

[123] J.-K. Wan, W.-L. Chu, Y.-Y. Kok, and C.-S. Lee, "Distribution of microplastics and nanoplastics in aquatic ecosystems and their impacts on aquatic organisms, with emphasis on microalgae," *Reviews of Environmental Contamination and Toxicology Volume 246,* pp. 133-158, 2019.

[124] R. Lehner, C. Weder, A. Petri-Fink, and B. Rothen-Rutishauser, "Emergence of nanoplastic in the environment and possible impact on human health," *Environmental science & technology,* vol. 53, no. 4, pp. 1748-1765, 2019.

[125] L. Manfra, A. Rotini, E. Bergami, G. Grassi, C. Faleri, and I. Corsi, "Comparative ecotoxicity of polystyrene nanoparticles in natural seawater and reconstituted seawater using the rotifer Brachionus plicatilis," (in eng), *Ecotoxicol Environ Saf,* vol. 145, pp. 557-563, Nov 2017.

[126] L. Pessoni *et al.*, "Soap-and metal-free polystyrene latex particles as a nanoplastic model," *Environmental Science: Nano,* vol. 6, no. 7, pp. 2253-2258, 2019.

[127] G. J. Price, A. J. White, and A. A. Clifton, "The effect of high-intensity ultrasound on solid polymers," *Polymer,* vol. 36, no. 26, pp. 4919-4925, 1995/01/01/ 1995.

[128] G. Balakrishnan, M. Déniel, T. Nicolai, C. Chassenieux, and F. Lagarde, "Towards more realistic reference microplastics and nanoplastics: preparation of polyethylene micro/nanoparticles with a biosurfactant," *Environmental Science: Nano,* vol. 6, no. 1, pp. 315-324, 2019.

[129] E. Von der Esch *et al.*, "Simple generation of suspensible secondary microplastic reference particles via ultrasound treatment," *Frontiers in Chemistry,* p. 169, 2020.

[130] L. Eitzen, S. Paul, U. Braun, K. Altmann, M. Jekel, and A. S. Ruhl, "The challenge in preparing particle suspensions for aquatic microplastic research," *Environmental research,* vol. 168, pp. 490-495, 2019.

[131] W. Li, G. Brunetti, C. Zafiu, M. Kunaschk, M. Debreczeby, and C. Stumpp, "Experimental and simulated microplastics transport in saturated natural sediments: impact of grain size and particle size," *Journal of Hazardous Materials,* vol. 468, p. 133772, 2024.

[132] W. E. Dietrich, "Settling velocity of natural particles," *Water Resources Research,* vol. 18, no. 6, pp. 1615-1626, 1982.

[133] H. Elagami *et al.*, "Measurement of microplastic settling velocities and implications for residence times in thermally stratified lakes," *Limnology and Oceanography,* vol. 67, no. 4, pp. 934-945, 2022.

[134] W. J. Shim, S. H. Hong, and S. E. Eo, "Identification methods in microplastic analysis: a review," *Analytical Methods,* 10.1039/C6AY02558G vol. 9, no. 9, pp. 1384-1391, 2017.

[135] V. Hidalgo-Ruz, L. Gutow, R. C. Thompson, and M. Thiel, "Microplastics in the Marine Environment: A Review of the Methods Used for Identification and Quantification," *Environmental Science & Technology,* vol. 46, no. 6, pp. 3060-3075, 2012/03/20 2012.

[136] R. Peñalver, N. Arroyo-Manzanares, I. López-García, and M. Hernández-Córdoba, "An overview of microplastics characterization by thermal analysis," *Chemosphere,* vol. 242, p. 125170, 2020/03/01/ 2020.

[137] F. Akoueson *et al.*, "Identification and quantification of plastic additives using pyrolysis-GC/MS: A review," (in eng), *Sci Total Environ,* vol. 773, p. 145073, Jun 15 2021.

[138] Y. Picó and D. Barceló, "Analysis of microplastics and nanoplastics: How green are the methodologies used?," *Current Opinion in Green and Sustainable Chemistry,* vol. 31, p. 100503, 2021/10/01/ 2021.

[139] W. J. Shim, Y. K. Song, S. H. Hong, and M. Jang, "Identification and quantification of microplastics using Nile Red staining," (in eng), *Mar Pollut Bull,* vol. 113, no. 1-2, pp. 469-476, Dec 15 2016.

[140] T. Maes, R. Jessop, N. Wellner, K. Haupt, and A. G. Mayes, "A rapid-screening approach to detect and quantify microplastics based on fluorescent tagging with Nile Red," (in eng), *Sci Rep,* vol. 7, p. 44501, Mar 16 2017.

[141] J. C. Prata, V. Reis, J. T. V. Matos, J. P. da Costa, A. C. Duarte, and T. Rocha-Santos, "A new approach for routine quantification of microplastics using Nile Red and automated software (MP-VAT)," (in eng), *Sci Total Environ,* vol. 690, pp. 1277-1283, Nov 10 2019.

[142] V. Nava, M. L. Frezzotti, and B. Leoni, "Raman Spectroscopy for the Analysis of Microplastics in Aquatic Systems," *Applied Spectroscopy,* vol. 75, no. 11, pp. 1341-1357, 2021.

[143] P. M. Anger, E. von der Esch, T. Baumann, M. Elsner, R. Niessner, and N. P. Ivleva, "Raman microspectroscopy as a tool for microplastic particle analysis," *TrAC Trends in Analytical Chemistry,* vol. 109, pp. 214-226, 2018/12/01/ 2018.

[144] Z. Sobhani, X. Zhang, C. Gibson, R. Naidu, M. Megharaj, and C. Fang, "Identification and visualisation of microplastics/nanoplastics by Raman imaging (i): Down to 100 nm," *Water Research,* vol. 174, p. 115658, 2020/05/01/ 2020.

[145] C. Fang, Z. Sobhani, X. Zhang, C. T. Gibson, Y. Tang, and R. Naidu, "Identification and visualisation of microplastics/ nanoplastics by Raman imaging (ii): Smaller than the diffraction limit of laser?," *Water Research,* vol. 183, p. 116046, 2020/09/15/ 2020.

[146] C. Fang *et al.*, "Identification and visualisation of microplastics / nanoplastics by Raman imaging (iii): algorithm to cross-check multi-images," *Water Research,* vol. 194, p. 116913, 2021/04/15/ 2021.

[147] J.-L. Xu, K. V. Thomas, Z. Luo, and A. A. Gowen, "FTIR and Raman imaging for microplastics analysis: State of the art, challenges and prospects," *TrAC Trends in Analytical Chemistry,* vol. 119, p. 115629, 2019/10/01/ 2019.

[148] J. P. Harrison, J. J. Ojeda, and M. E. Romero-González, "The applicability of reflectance micro-Fourier-transform infrared spectroscopy for the detection of synthetic microplastics in marine sediments," *Science of The Total Environment,* vol. 416, pp. 455-463, 2012/02/01/ 2012.

[149] J. Ornik *et al.*, "Could photoluminescence spectroscopy be an alternative technique for the detection of microplastics? First experiments using a 405 nm laser for excitation," *Applied Physics B,* vol. 126, no. 1, pp. 1-7, 2020.

[150] S. Konde, J. Ornik, J. A. Prume, J. Taiber, and M. Koch, "Exploring the potential of photoluminescence spectroscopy in combination with Nile Red staining for microplastic detection," *Marine Pollution Bulletin,* vol. 159, p. 111475, 2020.

[151] S. Gies, E.-M. Schömann, J. A. Prume, and M. Koch, "Exploring the potential of time-resolved photoluminescence spectroscopy for the detection of plastics," *Applied Spectroscopy,* vol. 74, no. 9, pp. 1161-1166, 2020.

[152] S. Tsuge, H. Ohtani, and C. Watanabe, *Pyrolysis-GC/MS data book of synthetic polymers: pyrograms, thermograms and MS of pyrolyzates*. Elsevier, 2011.

[153] M. Fischer and B. M. Scholz-Böttcher, "Simultaneous trace identification and quantification of common types of microplastics in environmental samples by pyrolysis-gas chromatography–mass spectrometry," *Environmental science & technology,* vol. 51, no. 9, pp. 5052-5060, 2017.

[154] E. Fries, J. H. Dekiff, J. Willmeyer, M.-T. Nuelle, M. Ebert, and D. Remy, "Identification of polymer types and additives in marine microplastic particles using pyrolysis-GC/MS and scanning electron microscopy," *Environmental science: processes & impacts,* vol. 15, no. 10, pp. 1949-1956, 2013.

[155] L. Hermabessiere *et al.*, "Occurrence and effects of plastic additives on marine environments and organisms: A review," *Chemosphere,* vol. 182, pp. 781-793, 2017/09/01/ 2017.

[156] A. Käppler *et al.*, "Comparison of μ-ATR-FTIR spectroscopy and py-GCMS as identification tools for microplastic particles and fibers isolated from river sediments," *Analytical and Bioanalytical Chemistry,* vol. 410, pp. 5313-5327, 2018.

[157] L. Hermabessiere *et al.*, "Optimization, performance, and application of a pyrolysis-GC/MS method for the identification of microplastics," *Analytical and bioanalytical chemistry,* vol. 410, no. 25, pp. 6663-6676, 2018.

[158] L. Hermabessiere *et al.*, "Optimization, performance, and application of a pyrolysis-GC/MS method for the identification of microplastics," *Analytical and Bioanalytical Chemistry,* vol. 410, no. 25, pp. 6663-6676, 2018/10/01 2018.

[159] X. Su *et al.*, "Investigating pyrolysis characteristics of Shengdong coal through Py-GC/MS," *Open Chemistry,* vol. 21, no. 1, p. 20230112, 2023.

[160] J. David *et al.*, "Introducing a soil universal model method (SUMM) and its application for qualitative and quantitative determination of poly(ethylene), poly(styrene), poly(vinyl chloride) and poly(ethylene terephthalate) microplastics in a model soil," *Chemosphere,* vol. 225, pp. 810-819, 2019/06/01/ 2019.

[161] J. David, Z. Steinmetz, J. Kučerík, and G. E. Schaumann, "Quantitative Analysis of Poly(ethylene terephthalate) Microplastics in Soil via Thermogravimetry–Mass Spectrometry," *Analytical Chemistry,* vol. 90, no. 15, pp. 8793-8799, 2018/08/07 2018.

[162] U. Braun *et al.*, "Accelerated determination of microplastics in environmental samples using thermal extraction desorption-gas chromatography/mass spectrometry (TED-GC/MS)," 2020.

[163] E. Dümichen *et al.*, "Analysis of polyethylene microplastics in environmental samples, using a thermal decomposition method," *Water Research,* vol. 85, pp. 451-457, 2015/11/15/ 2015.

[164] M. Majewsky, H. Bitter, E. Eiche, and H. Horn, "Determination of microplastic polyethylene (PE) and polypropylene (PP) in environmental samples using thermal analysis (TGA-DSC)," *Science of the Total Environment,* vol. 568, pp. 507-511, 2016.

[165] M. Rodríguez Chialanza, I. Sierra, A. Pérez Parada, and L. Fornaro, "Identification and quantitation of semi-crystalline microplastics using image analysis and differential scanning calorimetry," *Environmental Science and Pollution Research,* vol. 25, pp. 16767-16775, 2018.

[166] P. Sun and D. W. Armstrong, "Ionic liquids in analytical chemistry," *Analytica Chimica Acta,* vol. 661, no. 1, pp. 1-16, 2010/02/19/ 2010.

[167] T. Schmid and P. Dariz, "Raman Microspectroscopic Imaging of Binder Remnants in Historical Mortars Reveals Processing Conditions," *Heritage,* vol. 2, no. 2, pp. 1662-1683, 2019.

[168] Q. Xue, N. Wang, H. Yang, J. Yang, and H. Bai, "Detection of microplastics based on spatial heterodyne Raman spectroscopy," *Spectrochimica Acta Part A: Molecular and Biomolecular Spectroscopy,* vol. 283, p. 121712, 2022.

[169] J. S. Böke, J. Popp, and C. Krafft, "Optical photothermal infrared spectroscopy with simultaneously acquired Raman spectroscopy for two-dimensional microplastic identification," *Scientific Reports,* vol. 12, no. 1, p. 18785, 2022.

[170] S. L. Wright, J. M. Levermore, and F. J. Kelly, "Raman spectral imaging for the detection of inhalable microplastics in ambient particulate matter samples," *Environmental science & technology,* vol. 53, no. 15, pp. 8947-8956, 2019.

[171] J.-T. Lin *et al.*, "Emerging analytical frontiers in microplastic detection: From spectroscopy to smart sensor technologies," *Talanta Open,* vol. 12, p. 100514, 2025/12/01/ 2025.

[172] D. Schymanski, C. Goldbeck, H.-U. Humpf, and P. Fürst, "Analysis of microplastics in water by micro-Raman spectroscopy: Release of plastic particles from different packaging into mineral water," *Water research,* vol. 129, pp. 154-162, 2018.

[173] Z. Sobhani, M. Al Amin, R. Naidu, M. Megharaj, and C. Fang, "Identification and visualisation of microplastics by Raman mapping," *Analytica chimica acta,* vol. 1077, pp. 191-199, 2019.

[174] C. Fang, O. S. Awoyemi, G. Saianand, L. Xu, J. Niu, and R. Naidu, "Characterising microplastics in indoor air: Insights from Raman imaging analysis of air filter samples," *Journal of Hazardous Materials,* vol. 464, p. 132969, 2024.

[175] D. Wu *et al.*, "Pigment microparticles and microplastics found in human thrombi based on Raman spectral evidence," *Journal of advanced research,* vol. 49, pp. 141-150, 2023.

[176] X. Guo, H. Lin, S. Xu, and L. He, "Recent advances in spectroscopic techniques for the analysis of microplastics in food," *Journal of Agricultural and Food Chemistry,* vol. 70, no. 5, pp. 1410-1422, 2022.

[177] P. Ribeiro-Claro, M. M. Nolasco, and C. Araújo, "Chapter 5 - Characterization of Microplastics by Raman Spectroscopy," in *Comprehensive Analytical Chemistry*, vol. 75, T. A. P. Rocha-Santos and A. C. Duarte Eds.: Elsevier, 2017, pp. 119-151.

[178] A. B. Silva, A. S. Bastos, C. I. L. Justino, J. P. da Costa, A. C. Duarte, and T. A. P. Rocha-Santos, "Microplastics in the environment: Challenges in analytical chemistry - A review," *Analytica Chimica Acta,* vol. 1017, pp. 1-19, 2018/08/09/ 2018.

[179] S. Phan, J. L. Padilla-Gamiño, and C. K. Luscombe, "The effect of weathering environments on microplastic chemical identification with Raman and IR spectroscopy: Part I. polyethylene and polypropylene," *Polymer Testing,* vol. 116, p. 107752, 2022/12/01/ 2022.

[180] T. Dey, "Microplastic pollutant detection by surface enhanced Raman spectroscopy (SERS): a mini-review," *Nanotechnology for Environmental Engineering,* vol. 8, no. 1, pp. 41-48, 2023.

[181] M. Cole *et al.*, "Microplastic ingestion by zooplankton," *Environmental science & technology,* vol. 47, no. 12, pp. 6646-6655, 2013.

[182] N. K. Mogha and D. Shin, "Nanoplastic detection with surface enhanced Raman spectroscopy: Present and future," *TrAC Trends in Analytical Chemistry,* vol. 158, p. 116885, 2023/01/01/ 2023.

[183] D. S. Choi, S. Lim, J.-S. Park, C.-H. Kim, H. Rhee, and M. Cho, "Label-Free Live-Cell Imaging of Internalized Microplastics and Cytoplasmic Organelles with Multicolor CARS Microscopy," *Environmental Science & Technology,* vol. 56, no. 5, pp. 3045-3055, 2022/03/01 2022.

[184] S. Fortin, B. Song, and C. Burbage, "Quantifying and identifying microplastics in the effluent of advanced wastewater treatment systems using Raman microspectroscopy," *Marine Pollution Bulletin,* vol. 149, p. 110579, 2019/12/01/ 2019.

[185] A. Käppler *et al.*, "Identification of microplastics by FTIR and Raman microscopy: a novel silicon filter substrate opens the important spectral range below 1300 cm− 1 for FTIR transmission measurements," *Analytical and bioanalytical chemistry,* vol. 407, no. 22, pp. 6791-6801, 2015.

[186] Y. Chen *et al.*, "Identification and quantification of microplastics using Fourier-transform infrared spectroscopy: Current status and future prospects," *Current Opinion in Environmental Science & Health,* vol. 18, pp. 14-19, 2020/12/01/ 2020.

[187] G. G. Stokes, "On the change of refrangibility of light," in *Abstracts of the Papers Communicated to the Royal Society of London*, 1854, no. 6: The Royal Society London, pp. 195-200.

[188] M. L. Nahorniak and K. S. Booksh, "Excitation-emission matrix fluorescence spectroscopy in conjunction with multiway analysis for PAH detection in complex matrices," *Analyst,* vol. 131, no. 12, pp. 1308-1315, 2006.

[189] G. M. Strasburg and R. D. Ludescher, "Theory and applications of fluorescence spectroscopy in food research," *Trends in Food Science & Technology,* vol. 6, no. 3, pp. 69-75, 1995.

[190] J. M. Torkelson, S. Lipsky, M. Tirrell, and D. A. Tirrell, "Fluorescence and absorbance of polystyrene in dilute and semidilute solutions," *Macromolecules,* vol. 16, no. 2, pp. 326-330, 1983/02/01 1983.

[191] M. S. Healy and J. E. Hanson, "Fluorescence excitation spectroscopy of polystyrene near the critical concentration c*," *Journal of Applied Polymer Science,* vol. 104, no. 1, pp. 360-364, 2007.

[192] M. Baibarac, I. Baltog, S. Lefrant, J. Y. Mevellec, and C. Bucur, "Vibrational and photoluminescence properties of the polystyrene functionalized single-walled carbon nanotubes," *Diamond and Related Materials,* vol. 17, no. 7, pp. 1380-1388, 2008/07/01/ 2008.

[193] G. J. M. Fechine, R. M. Souto-Maior, and M. S. Rabello, "Photodegradation of multilayer films based on PET copolymers," *Journal of Applied Polymer Science,* vol. 104, no. 1, pp. 51-57, 2007.

[194] N. S. Allen, J. Homer, J. F. McKellar, and D. G. M. Wood, "Identification of the luminescent species in low-density polyethylene," *Journal of Applied Polymer Science,* vol. 21, no. 11, pp. 3147-3152, 1977.

[195] Z. Osawa and H. Kuroda, "Luminescence emission of high-density polyethylene," *Journal of Polymer Science: Polymer Letters Edition,* vol. 20, no. 11, pp. 577-581, 1982.

[196] N. S. Allen, J. Homer, and J. F. McKellar, "Origin and role of the luminescent species in the photo-oxidation of commercial polypropylene," *Journal of Applied Polymer Science,* vol. 21, no. 8, pp. 2261-2267, 1977.

[197] J. Ornik *et al.*, "Could photoluminescence spectroscopy be an alternative technique for the detection of microplastics? First experiments using a 405 nm laser for excitation," *Applied Physics B,* vol. 126, pp. 1-7, 2020.

[198] B. Lotter, S. Konde, J. Nguyen, M. Grau, M. Koch, and P. Lenz, "Identifying plastics with photoluminescence spectroscopy and machine learning," *Scientific Reports,* vol. 12, no. 1, p. 18840, 2022/11/06 2022.

[199] L. C. LM, "Ratiometric Fluorescence Detection of Mercury Ions in Water by Conjugated Polymer Nanoparticles," 2012.

[200] Y. Oki, K. Furukawa, and M. Maeda, "Extremely sensitive Na detection in pure water by laser ablation atomic fluorescence spectroscopy," *Optics communications,* vol. 133, no. 1-6, pp. 123-128, 1997.

[201] C. Q. Costa *et al.*, "Fluorescence sensing of microplastics on surfaces," *Environmental Chemistry Letters,* vol. 19, pp. 1797-1802, 2021.

[202] R. Peinador, P. T. HP, and J. I. Calvo, "Innovative application of Nile Red (NR)-based dye for direct detection of micro and nanoplastics (MNPs) in diverse aquatic environments," *Chemosphere,* p. 142609, 2024.

[203] S. Gies, E.-M. Schömann, J. Anna Prume, and M. Koch, "Exploring the Potential of Time-Resolved Photoluminescence Spectroscopy for the Detection of Plastics," *Applied Spectroscopy,* vol. 74, no. 9, pp. 1161-1166, 2020.

[204] T. Maes, R. Jessop, N. Wellner, K. Haupt, and A. Mayes, "A rapid-screening approach to detect and quantify microplastics based on fluorescent tagging with Nile Red. Sci Rep 7: 44501," ed, 2017.

[205] D. Genovese, L. Prodi, E. Rampazzo, and N. Zaccheroni, "Luminescent sensor for nano/microplastics," ed: Google Patents, 2023.

[206] C. Capolungo, D. Genovese, M. Montalti, E. Rampazzo, N. Zaccheroni, and L. Prodi, "Photoluminescence-Based Techniques for the Detection of Micro- and Nanoplastics," *Chemistry – A European Journal,* vol. 27, no. 70, pp. 17529-17541, 2021.

[207] A. Piruska *et al.*, "The autofluorescence of plastic materials and chips measured under laser irradiation," *Lab on a Chip,* vol. 5, no. 12, pp. 1348-1354, 2005.

[208] S. Bottura-Scardina, P. Vandenabeele, C. Miguel, and A. Candeias, "Comparative assessment of two portable Raman spectrometers for the characterisation of historical natural dye lakes," *Journal of Raman Spectroscopy,* vol. 54, no. 11, pp. 1303-1313, 2023.

[209] D. Sorak, L. Herberholz, S. Iwascek, S. Altinpinar, F. Pfeifer, and H. W. Siesler, "New developments and applications of handheld Raman, mid-infrared, and near-infrared spectrometers," *Applied Spectroscopy Reviews,* vol. 47, no. 2, pp. 83-115, 2012.

[210] B. R. Wood, P. Heraud, S. Stojkovic, D. Morrison, J. Beardall, and D. McNaughton, "A portable Raman acoustic levitation spectroscopic system for the identification and environmental monitoring of algal cells," *Analytical chemistry,* vol. 77, no. 15, pp. 4955-4961, 2005.

[211] B. O. Asamoah, E. Uurasjärvi, J. Räty, A. Koistinen, M. Roussey, and K.-E. Peiponen, "Towards the Development of Portable and In Situ Optical Devices for Detection of Micro- and Nanoplastics in Water: A Review on the Current Status," *Polymers,* vol. 13, no. 5, p. 730, 2021.

[212] S. Wartewig and R. H. Neubert, "Pharmaceutical applications of Mid-IR and Raman spectroscopy," *Advanced drug delivery reviews,* vol. 57, no. 8, pp. 1144-1170, 2005.

[213] J.-F. Masson, L. Pelletier, and P. Collins, "Rapid FTIR method for quantification of styrene-butadiene type copolymers in bitumen," *Journal of Applied Polymer Science,* vol. 79, no. 6, pp. 1034-1041, 2001.

[214] J. Jehlička, A. Culka, P. Vandenabeele, and H. G. M. Edwards, "Critical evaluation of a handheld Raman spectrometer with near infrared (785nm) excitation for field identification of minerals," *Spectrochimica Acta Part A: Molecular and Biomolecular Spectroscopy,* vol. 80, no. 1, pp. 36-40, 2011/10/01/ 2011.

[215] C. A. Lieber and A. Mahadevan-Jansen, "Development of a handheld Raman microspectrometer for clinical dermatologic applications," *Optics Express,* vol. 15, no. 19, pp. 11874-11882, 2007/09/17 2007.

[216] B. Joseph, A. Bryan, R. John, and O. Ty, "Miniature Raman spectrometer development," in *Proc.SPIE*, 2018, vol. 10490, p. 104900W.

[217] P. Tang, R. Forster, R. McCumskay, M. Rogerson, and C. Waller, "Handheld FT-IR spectroscopy for the triage of micro-and meso-sized plastics in the marine environment incorporating an accelerated weathering study and an aging estimation," 2019.

[218] A. H. Iri *et al.*, "Optical detection of microplastics in water," *Environmental Science and Pollution Research,* pp. 1-7, 2021.

[219] Z. Yang, T. Albrow-Owen, W. Cai, and T. Hasan, "Miniaturization of optical spectrometers," *Science,* vol. 371, no. 6528, p. eabe0722, 2021.

[220] R. F. Wolffenbuttel, "MEMS-based optical mini-and microspectrometers for the visible and infrared spectral range," *Journal of Micromechanics and Microengineering,* vol. 15, no. 7, p. S145, 2005.

[221] J. Malinen *et al.*, "Advances in miniature spectrometer and sensor development," in *Next-generation spectroscopic technologies VII*, 2014, vol. 9101: SPIE, pp. 83-97.

[222] D. Xu, C. Sui, J. Tong, and H. Yang, "Optical design of micro spectrometer," in *2012 Second International Conference on Instrumentation, Measurement, Computer, Communication and Control*, 2012: IEEE, pp. 339-341.

[223] T. Yokino *et al.*, "Grating-based ultra-compact SWNIR spectral sensor head developed through MOEMS technology," in *MOEMS and Miniaturized Systems XVIII*, 2019, vol. 10931: SPIE, pp. 55-68.

[224] S. Mallinson and J. Jerman, "Miniature micromachined Fabry-Perot interferometers in silicon," *Electronics letters,* vol. 23, no. 20, pp. 1041-1043, 1987.

[225] N. Neumann, M. Ebermann, S. Kurth, and K. Hiller, "Tunable infrared detector with integrated micromachined Fabry-Perot filter," *Journal of Micro/Nanolithography, MEMS and MOEMS,* vol. 7, no. 2, pp. 021004-021004-9, 2008.

[226] R. Mannila, R. Hyypiö, M. Korkalainen, M. Blomberg, H. Kattelus, and A. Rissanen, "Gas detection with microelectromechanical Fabry-Perot interferometer technology in cell

phone," in *Next-Generation Spectroscopic Technologies VIII*, 2015, vol. 9482: SPIE, pp. 133-141.

[227] L. P. Schuler, J. S. Milne, J. M. Dell, and L. Faraone, "MEMS-based microspectrometer technologies for NIR and MIR wavelengths," *Journal of Physics D: Applied Physics,* vol. 42, no. 13, p. 133001, 2009.

[228] M. Erfan, Y. M. Sabry, M. Sakr, B. Mortada, M. Medhat, and D. Khalil, "On-chip micro–electro–mechanical system Fourier transform infrared (MEMS FT-IR) spectrometer-based gas sensing," *Applied spectroscopy,* vol. 70, no. 5, pp. 897-904, 2016.

[229] T. Sandner, A. Kenda, C. Drabe, H. Schenk, and W. Scherf, "Miniaturized FTIR-spectrometer based on an optical MEMS translatory actuator," in *MOEMS and miniaturized systems VI*, 2007, vol. 6466: SPIE, pp. 9-20.

[230] J. Correia, G. De Graaf, S. Kong, M. Bartek, and R. Wolffenbuttel, "Single-chip CMOS optical microspectrometer," *Sensors and Actuators A: Physical,* vol. 82, no. 1-3, pp. 191-197, 2000.

[231] X. Nie, E. Ryckeboer, G. Roelkens, and R. Baets, "CMOS-compatible broadband co-propagative stationary Fourier transform spectrometer integrated on a silicon nitride photonics platform," *Optics express,* vol. 25, no. 8, pp. A409-A418, 2017.

[232] A. Y. Zhu *et al.*, "Ultra-compact visible chiral spectrometer with meta-lenses," *Apl Photonics,* vol. 2, no. 3, 2017.

[233] M. Ebermann, N. Neumann, K. Hiller, M. Seifert, M. Meinig, and S. Kurth, "Tunable MEMS Fabry-Pérot filters for infrared microspectrometers: a review," *MOEMS and miniaturized systems XV,* vol. 9760, pp. 64-83, 2016.

[234] J. P. Carmo, R. P. Rocha, M. Bartek, G. de Graaf, R. F. Wolffenbuttel, and J. H. Correia, "A review of visible-range Fabry–Perot microspectrometers in silicon for the industry," *Optics & Laser Technology,* vol. 44, no. 7, pp. 2312-2320, 2012.

[235] J. M. Dell, J. S. Milne, J. Antoszewski, A. J. Keating, L. P. Schuler, and L. Faraone, "MEMS-based Fabry-Perot microspectrometers for agriculture," in *Next-Generation Spectroscopic Technologies II*, 2009, vol. 7319: SPIE, pp. 165-173.

[236] A. Näsilä and T. Kohout, "Miniaturized spectral imaging instrumentation for planetary exploration," in *2020 IEEE Aerospace Conference*, 2020: IEEE, pp. 1-7.

[237] H. Zeng, C. E. MacAulay, D. I. McLean, and B. Palcic, "Novel microspectrophotometer and its biomedical applications," *Optical Engineering,* vol. 32, no. 8, pp. 1809-1814, 1993.

[238] R. F. Wolffenbuttel and T. M. Wolffenbuttel Hosli, "Medical apps in need of optical microspectrometers," *Microsystem Technologies,* vol. 22, no. 7, pp. 1549-1555, 2016.

[239] D. Brennan *et al.*, "Development of a micro-spectrometer system for process control application," *Infrared physics & technology,* vol. 43, no. 2, pp. 69-76, 2002.

[240] G. Chen, Z.-y. Wen, Y. Xu, Z.-p. Jiang, and B. Zhang, "Miniature biochemical analytical system based on micro-spectrometer," in *MOEMS and Miniaturized Systems V*, 2005, vol. 5719: SPIE, pp. 95-101.

[241] C. P. Bacon, Y. Mattley, and R. DeFrece, "Miniature spectroscopic instrumentation: applications to biology and chemistry," *Review of Scientific instruments,* vol. 75, no. 1, pp. 1-16, 2004.

[242] X. Mengyuan, Y. Yongai, J. Meng, and Y. Fu, "Development of a Micro-Spectrophotometer and Its Application in Water Quality Testing," *Journal of Donghua University (English Edition),* vol. 42, no. 3, 2025.

[243] C.-M. Tsai, Y.-C. Hsu, C.-T. Yang, W.-Y. Kong, C. Hong, and C.-H. Ko, "Micro-Spectrometer-Based Interferometric Spectroscopy and Environmental Sensing with Zinc Oxide Thin Film," in *Micro*, 2024, vol. 4, no. 2: MDPI, pp. 305-317.

[244] Z. Li, M. J. Deen, Q. Fang, and P. Selvaganapathy, "Design of a flat field concave-grating-based micro-Raman spectrometer for environmental applications," *Applied Optics,* vol. 51, no. 28, pp. 6855-6863, 2012.

[245] Q. Milner and G. Mathews, "An assessment of the accuracy of pulse oximeters," *Anaesthesia,* vol. 67, no. 4, pp. 396-401, 2012.

[246] C. L. Arrasmith, C. A. Patil, D. L. Dickensheets, and A. Mahadevan-Jansen, "A MEMS based handheld confocal microscope with Raman spectroscopy for in-vivo skin cancer diagnosis," in *Advanced Biomedical and Clinical Diagnostic Systems VII*, 2009, vol. 7169: SPIE, pp. 114-121.

[247] G. M. Yee, N. I. Maluf, P. A. Hing, M. Albin, and G. T. Kovacs, "Miniature spectrometers for biochemical analysis," *Sensors and Actuators A: Physical,* vol. 58, no. 1, pp. 61-66, 1997.

[248] V. P. Rachim and W.-Y. Chung, "Wearable-band type visible-near infrared optical biosensor for non-invasive blood glucose monitoring," *Sensors and Actuators B: Chemical,* vol. 286, pp. 173-180, 2019.

[249] C. Bouyé, H. Kolb, and B. d'Humières, "Mini and micro spectrometers pave the way to on-field advanced analytics," in *Photonic Instrumentation Engineering III*, 2016, vol. 9754: SPIE, pp. 28-36.

[250] H. J. van Manen and C. Otto, "Cholesterol esters are detected by Raman microspectroscopy in HeLa cells," *Journal of Raman Spectroscopy: An International Journal for Original Work in all Aspects of Raman Spectroscopy, Including Higher Order Processes, and also Brillouin and Rayleigh Scattering,* vol. 40, no. 2, pp. 117-118, 2009.

[251] C. C. S. Bandeira *et al.*, "Micro-Fourier-transform infrared reflectance spectroscopy as tool for probing IgG glycosylation in COVID-19 patients," *Scientific reports,* vol. 12, no. 1, p. 4269, 2022.

[252] J. Meng, S. Balendhran, Y. Sabri, S. K. Bhargava, and K. B. Crozier, "Smart mid-infrared metasurface microspectrometer gas sensing system," *Microsystems & Nanoengineering,* vol. 10, no. 1, p. 74, 2024.

[253] R. Bhargava, S.-Q. Wang, and J. L. Koenig, "FTIR microspectroscopy of polymeric systems," in *Liquid chromatography/FTIR microspectroscopy/microwave assisted synthesis*: Springer, 2003, pp. 137-191.

[254] E. Martellato *et al.*, "A new orbiting deployable system for small satellite observations for ecology and Earth observation," *Remote Sensing,* vol. 14, no. 9, p. 2066, 2022.

[255] J. M. Boehmler *et al.*, "Development of a multispectral albedometer and deployment on an unmanned aircraft for evaluating satellite retrieved surface reflectance over Nevada's Black Rock Desert," *Sensors,* vol. 18, no. 10, p. 3504, 2018.

[256] S. H. Choi, R. W. Moses, C. Park, C. C. Fay, and D. R. Komar, "Implementation Concept of Operation for a Multi-Purpose Cassegrain Solar Concentrator, Micro-Spectrometers,

and Electrostatic Neutralizers to Enable In Situ Construction Activities plus Lunar, Planetary, and Deep Space Science Exploration on the Moon," 2020.

[257] A. M. Othman, A. A. Elsayed, Y. M. Sabry, D. Khalil, and T. Bourouina, "Detection of Sub-20 μm microplastic particles by attenuated total reflection fourier transform infrared spectroscopy and comparison with raman spectroscopy," *ACS omega,* vol. 8, no. 11, pp. 10335-10341, 2023.

[258] K. B. Bec, J. Grabska, F. Pfeifer, H. W. Siesler, and C. W. Huck, "Rapid on-site analysis of soil microplastics using miniaturized NIR spectrometers: Key aspect of instrumental variation," *Journal of Hazardous Materials,* vol. 480, p. 135967, 2024/12/05/ 2024.

[259] Kathleen E. Bates and H. Lu, "Optics-Integrated Microfluidic Platforms for Biomolecular Analyses," *Biophysical Journal,* vol. 110, no. 8, pp. 1684-1697, 2016.

[260] A. Kayani, "Study of particle suspensions in microfluidics for the development of optical devices," RMIT University, 2024.

[261] H. Gai, Y. Li, and E. S. Yeung, "Optical detection systems on microfluidic chips," *Microfluidics: Technologies and Applications,* pp. 171-201, 2011.

[262] A. A. Elsayed *et al.*, "A microfluidic chip enables fast analysis of water microplastics by optical spectroscopy," *Scientific Reports,* vol. 11, no. 1, p. 10533, 2021/05/18 2021.

[263] M. G. Blevins *et al.*, "Field-Portable Microplastic Sensing in Aqueous Environments: A Perspective on Emerging Techniques," *Sensors,* vol. 21, no. 10, p. 3532, 2021.

[264] A. Li *et al.*, "Advances in cost-effective integrated spectrometers," *Light: Science & Applications,* vol. 11, no. 1, p. 174, 2022/06/07 2022.

[265] E. A. Bartis, P. Luan, A. J. Knoll, C. Hart, J. Seog, and G. S. Oehrlein, "Polystyrene as a model system to probe the impact of ambient gas chemistry on polymer surface modifications using remote atmospheric pressure plasma under well-controlled conditions," *Biointerphases,* vol. 10, no. 2, 2015.

[266] H. Du, A. Komuro, and R. Ono, "Quantitative and selective study of the effect of O radicals on polypropylene surface treatment," *Plasma Sources Science and Technology,* vol. 32, no. 7, p. 075013, 2023.

[267] V. Adalsteinsson, O. Parajuli, S. Kepics, A. Gupta, W. B. Reeves, and J.-i. Hahm, "Ultrasensitive detection of cytokines enabled by nanoscale ZnO arrays," *Analytical chemistry,* vol. 80, no. 17, pp. 6594-6601, 2008.

[268] A. Dorfman, N. Kumar, and J.-i. Hahm, "Highly sensitive biomolecular fluorescence detection using nanoscale ZnO platforms," *Langmuir,* vol. 22, no. 11, pp. 4890-4895, 2006.

[269] A. Dorfman, O. Parajuli, N. Kumar, and J.-i. Hahm, "Novel telomeric repeat elongation assay performed on zinc oxide nanorod array supports," *Journal of nanoscience and nanotechnology,* vol. 8, no. 1, pp. 410-415, 2008.

[270] S. Stadtmüller, "Siloxanes as Additives for Plastics," *Polymers and Polymer Composites,* vol. 10, no. 1, pp. 49-62, 2002.

[271] Y. Peng, M. Musah, B. Via, and X. Wang, "Calcium Carbonate Particles Filled Homopolymer Polypropylene at Different Loading Levels: Mechanical Properties Characterization and Materials Failure Analysis," *Journal of Composites Science,* vol. 5, no. 11, p. 302, 2021.

[272] A. Turner and M. Filella, "The influence of additives on the fate of plastics in the marine environment, exemplified with barium sulphate," *Marine Pollution Bulletin,* vol. 158, p. 111352, 2020/09/01/ 2020.

[273] W. Brostow, X. Lu, O. Gencel, and A. T. Osmanson, "Effects of UV Stabilizers on Polypropylene Outdoors," *Materials,* vol. 13, no. 7, p. 1626, 2020.

[274] H. Lu, Z. Hu, and S. Feng, "Nonconventional Luminescence Enhanced by Silicone-Induced Aggregation," *Chemistry – An Asian Journal,* vol. 12, no. 11, pp. 1213-1217, 2017.

[275] N. Prigyai, S. Chanmungkalakul, S. Thanyalax, M. Sukwattanasinitt, and V. Ervithayasuporn, "Cyclic siloxanes conjugated with fluorescent aromatic compounds as fluoride sensors," *Materials Advances,* 10.1039/D0MA00476F vol. 1, no. 9, pp. 3358-3368, 2020.

[276] M. Gaft, L. Nagli, G. Panczer, G. Waychunas, and N. Porat, "The nature of unusual luminescence in natural calcite CaCO3," *American Mineralogist,* vol. 93, no. 1, pp. 158-167, 2008.

[277] A. Padwa, "Photochemistry of the carbon-nitrogen double bond," *Chemical Reviews,* vol. 77, no. 1, pp. 37-68, 1977/02/01 1977.

[278] Z. Kaszowska, K. Malek, E. Staniszewska-Slezak, and K. Niedzielska, "Raman scattering or fluorescence emission? Raman spectroscopy study on lime-based building and conservation materials," *Spectrochimica Acta Part A: Molecular and Biomolecular Spectroscopy,* vol. 169, pp. 7-15, 2016.

[279] M. Mazilu, A. C. De Luca, A. Riches, C. S. Herrington, and K. Dholakia, "Optimal algorithm for fluorescence suppression of modulated Raman spectroscopy," *Optics express,* vol. 18, no. 11, pp. 11382-11395, 2010.

[280] E. Rebollar *et al.*, "Physicochemical modifications accompanying UV laser induced surface structures on poly (ethylene terephthalate) and their effect on adhesion of mesenchymal cells," *Physical Chemistry Chemical Physics,* vol. 16, no. 33, pp. 17551-17559, 2014.

[281] M. Meng, Y. Feng, Y. Liu, X. Dai, J. Pan, and Y. Yan, "Fabrication of submicrosized imprinted spheres attached polypropylene membrane using “two-dimensional” molecular imprinting method for targeted separation," *Adsorption Science & Technology,* vol. 35, no. 1-2, pp. 162-177, 2017.

[282] X. Guo, Z. Lin, Y. Wang, Z. He, M. Wang, and G. Jin, "In-line monitoring the degradation of polypropylene under multiple extrusions based on Raman spectroscopy," *Polymers,* vol. 11, no. 10, p. 1698, 2019.

[283] L. J. Basile, "Effect of styrene monomer on the fluorescence properties of polystyrene," *Journal of Chemical Physics,* vol. 36, no. 8, pp. 2204-2210, 1962.

[284] R. K. Swank and W. L. Buck, "The Scintillation Process in Plastic Solid Solutions," *Physical Review,* vol. 91, no. 4, pp. 927-933, 08/15/ 1953.

[285] M. Day and D. Wiles, "Photochemical degradation of poly (ethylene terephthalate). II. Effect of wavelength and environment on the decomposition process," *Journal of Applied Polymer Science,* vol. 16, no. 1, pp. 191-202, 1972.

[286] N. S. Allen and J. F. McKellar, "Luminescent species in poly (ethylene terephthalate)," *Die Makromolekulare Chemie,* vol. 179, no. 2, pp. 523-526, 1978.

[287] D. J. Hemker, C. W. Frank, and J. W. Thomas, "Photophysical studies of amorphous orientation in poly (ethylene terephthalate) films," *Polymer,* vol. 29, no. 3, pp. 437-447, 1988.

[288] N. Allen, J. Homer, and J. McKellar, "Origin and role of the luminescent species in the photo-oxidation of commercial polypropylene," *Journal of Applied Polymer Science,* vol. 21, no. 8, pp. 2261-2267, 1977.

[289] F. Massines, P. Tiemblo, G. Teyssedre, and C. Laurent, "On the nature of the luminescence emitted by a polypropylene film after interaction with a cold plasma at low temperature," *Journal of applied physics,* vol. 81, no. 2, pp. 937-943, 1997.

[290] L. Pichat, P. Pesteil, and J. Clément, "Solides fluorescents non cristallins pour mesures de radiactivité," *Journal de Chimie Physique,* vol. 50, pp. 26-41, 1953.

[291] F. Saudrais *et al.*, "The Impact of Virgin and Aged Microstructured Plastics on Proteins: The Case of Hemoglobin Adsorption and Oxygenation," *International Journal of Molecular Sciences,* vol. 25, no. 13, p. 7047, 2024.

[292] L. J. Basile, "Effect of Styrene Monomer on the Fluorescence Properties of Polystyrene," *The Journal of Chemical Physics,* vol. 36, no. 8, pp. 2204-2210, 1962.

[293] R. Nurmukhametov, L. Volkova, and S. Kabanov, "Fluorescence and absorption of polystyrene exposed to UV laser radiation," *Journal of Applied Spectroscopy,* vol. 73, no. 1, pp. 55-60, 2006.

[294] L. J. Basile, "Effect of Styrene Monomer on the Fluorescence Properties of Polystyrene," *The Journal of Chemical Physics,* vol. 36, no. 8, pp. 2204-2210, 2004.

[295] R. K. Swank and W. L. Buck, "The scintillation process in plastic solid solutions," *Physical Review,* vol. 91, no. 4, p. 927, 1953.

[296] L. Chen, X. Jin, J. Du, and R. Qian, "On the origin of the fluorescence emission of poly (ethylene terephthalate) by excitation at 340 nm," *Die Makromolekulare Chemie: Macromolecular Chemistry and Physics,* vol. 192, no. 6, pp. 1399-1408, 1991.

[297] M. Day and D. Wiles, "Photochemical degradation of poly (ethylene terephthalate). III. Determination of decomposition products and reaction mechanism," *Journal of Applied Polymer Science,* vol. 16, no. 1, pp. 203-215, 1972.

[298] N. S. Allen and J. F. McKellar, "Luminescent species in poly (ethylene terephthalate)," *Die Makromolekulare Chemie: Macromolecular Chemistry and Physics,* vol. 179, no. 2, pp. 523-526, 1978.

[299] J. P. LaFemina, D. R. Carter, and M. B. Bass, "Photophysical properties, intermolecular interactions, and molecular dynamics of poly (ethylene terephthalate)," *The Journal of Physical Chemistry,* vol. 96, no. 6, pp. 2767-2772, 1992.

[300] R. G. Merrill and C. W. Roberts, "Photophysical processes and interactions between poly (ethylene terephthalate) and 1-amino-2-(2-methoxyethoxy)-4-hydroxy-9, 10-anthraquinone," *Journal of Applied Polymer Science,* vol. 21, no. 10, pp. 2745-2768, 1977.

[301] M. Sonnenschein and C. Roland, "Absorption and fluorescence spectra of poly (ethylene terephthalate) dimers," *Polymer,* vol. 31, no. 11, pp. 2023-2026, 1990.

[302] D. Ho, S. Liu, H. Wei, and K. Karthikeyan, "The glowing potential of Nile red for microplastics Identification: Science and mechanism of fluorescence staining," *Microchemical Journal,* vol. 197, p. 109708, 2024.

[303] Y. K. Lee, S. Hong, and J. Hur, "A fluorescence indicator for source discrimination between microplastic-derived dissolved organic matter and aquatic natural organic matter," *Water Research,* vol. 207, p. 117833, 2021.

[304] A. Motalebizadeh, S. Fardindoost, and M. Hoorfar, "Selective on-site detection and quantification of polystyrene microplastics in water using fluorescence-tagged peptides and electrochemical impedance spectroscopy," *Journal of Hazardous Materials,* vol. 480, p. 136004, 2024.

[305] B. Hu *et al.*, "Using artificial intelligence to rapidly identify microplastics pollution and predict microplastics environmental behaviors," *Journal of Hazardous Materials,* p. 134865, 2024.

[306] N. Merlemis, E. Drakaki, E. Zekou, G. Ninos, and A. L. Kesidis, "Laser induced fluorescence and machine learning: A novel approach to microplastic identification," *Applied Physics B,* vol. 130, no. 9, p. 168, 2024.

[307] J.-K. Wan, W.-L. Chu, Y.-Y. Kok, and C.-S. Lee, "Distribution of microplastics and nanoplastics in aquatic ecosystems and their impacts on aquatic organisms, with emphasis on microalgae," *Reviews of environmental contamination and toxicology,* vol. 246, pp. 133-158, 2018.

[308] L. Manfra, A. Rotini, E. Bergami, G. Grassi, C. Faleri, and I. Corsi, "Comparative ecotoxicity of polystyrene nanoparticles in natural seawater and reconstituted seawater using the rotifer Brachionus plicatilis," *Ecotoxicology and environmental safety,* vol. 145, pp. 557-563, 2017.

[309] E. von der Esch *et al.*, "Simple Generation of Suspensible Secondary Microplastic Reference Particles via Ultrasound Treatment," (in English), *Frontiers in Chemistry,* Original Research vol. Volume 8 - 2020, 2020-March-18 2020.

[310] R. Apfel, "Acoustic cavitation prediction," *The Journal of the Acoustical Society of America,* vol. 69, no. 6, pp. 1624-1633, 1981.

[311] R. Feng, Y. Zhao, C. Zhu, and T. Mason, "Enhancement of ultrasonic cavitation yield by multi-frequency sonication," *Ultrasonics sonochemistry,* vol. 9, no. 5, pp. 231-236, 2002.

[312] J. Ritter, J. Stevens, and K. Jakus, "Failure of amorphous polystyrene," *Journal of Materials Science,* vol. 14, pp. 2446-2452, 1979.

[313] S. Sikka, "Molecular behavior of amorphous polystyrene under tensile stress," *Polymer Bulletin,* vol. 3, pp. 123-127, 1980.

[314] H. A. Maddah, "Polypropylene as a promising plastic: A review," *Am. J. Polym. Sci,* vol. 6, no. 1, pp. 1-11, 2016.

[315] H. Kuleyin, R. Gümrük, and S. Çalışkan, "Fatigue behavior of polymethyl methacrylate/acrylonitrile butadiene styrene blends including blend composition, stress ratio, frequency, and holding pressure effects," *International Journal of Fatigue,* vol. 187, p. 108483, 2024.

[316] L. Ben Said, H. Hentati, M. Wali, B. Ayadi, and M. Alhadri, "Damage Investigation in PMMA Polymer: Experimental and Phase-Field Approaches," *Polymers,* vol. 16, no. 23, p. 3304, 2024.

[317] F. Farbod and B. Pourabbas, "Ultrasonic wave effect on PMMA surface, silica nanoparticles assisted erosion," *Wear,* vol. 300, no. 1, pp. 105-113, 2013/03/15/ 2013.

[318] J. J. Shah, J. Geist, L. E. Locascio, M. Gaitan, M. V. Rao, and W. N. Vreeland, "Surface modification of poly(methyl methacrylate) for improved adsorption of wall coating polymers for microchip electrophoresis," *ELECTROPHORESIS,* vol. 27, no. 19, pp. 3788-3796, 2006.

[319] N. Kröger-Lui *et al.*, "Rapid identification of goblet cells in unstained colon thin sections by means of quantum cascade laser-based infrared microspectroscopy," *Analyst,* vol. 140, no. 7, pp. 2086-2092, 2015.

[320] R. Harig and G. Matz, "Toxic cloud imaging by infrared spectrometry: A scanning FTIR system for identification and visualization," *Field Analytical Chemistry & Technology,* vol. 5, no. 1-2, pp. 75-90, 2001.

[321] J. Valls-Conesa *et al.*, "Random forest microplastic classification using spectral subsamples of FT-IR hyperspectral images," *Analytical Methods,* vol. 15, no. 18, pp. 2226-2233, 2023.

[322] B. Hufnagl, D. Steiner, E. Renner, M. G. Löder, C. Laforsch, and H. Lohninger, "A methodology for the fast identification and monitoring of microplastics in environmental samples using random decision forest classifiers," *Analytical Methods,* vol. 11, no. 17, pp. 2277-2285, 2019.

[323] X. Yan, Z. Cao, A. Murphy, and Y. Qiao, "An ensemble machine learning method for microplastics identification with FTIR spectrum," *Journal of Environmental Chemical Engineering,* vol. 10, no. 4, p. 108130, 2022.

[324] A. Walter, "Tall trees and small plastics: Using random forest classification to identify microplastic pollution in surface soil samples," Wien, 2021.

[325] R. Chakrabarti, M. Das, and D. Chakraborty, "Physical, mechanical, and thermal properties of PVC/PMMA blends in relation to their morphologies," *Journal of applied polymer science,* vol. 93, no. 6, pp. 2721-2730, 2004.

[326] N. Jin, Y. Song, R. Ma, J. Li, G. Li, and D. Zhang, "Characterization and identification of microplastics using Raman spectroscopy coupled with multivariate analysis," *Analytica Chimica Acta,* vol. 1197, p. 339519, 2022/03/08/ 2022.

[327] B. Stuart, "Temperature studies of polycarbonate using Fourier transform Raman spectroscopy," *Polymer bulletin,* vol. 36, pp. 341-346, 1996.

[328] A. Gopanna, R. N. Mandapati, S. P. Thomas, K. Rajan, and M. Chavali, "Fourier transform infrared spectroscopy (FTIR), Raman spectroscopy and wide-angle X-ray scattering (WAXS) of polypropylene (PP)/cyclic olefin copolymer (COC) blends for qualitative and quantitative analysis," *Polymer Bulletin,* vol. 76, no. 8, pp. 4259-4274, 2019.

[329] A. S. Nielsen, D. N. Batchelder, and R. Pyrz, "Estimation of crystallinity of isotactic polypropylene using Raman spectroscopy," *Polymer,* vol. 43, no. 9, pp. 2671-2676, 2002/04/01/ 2002.

[330] U. Schmidt, J. Müller, and J. Koenen, "Confocal Raman Imaging of Polymeric Materials," in *Confocal Raman Microscopy*, J. Toporski, T. Dieing, and O. Hollricher Eds. Cham: Springer International Publishing, 2018, pp. 485-507.

[331] M. E. R. Robinson, D. I. Bower, and W. F. Maddams, "A study of the C・Cl stretching region of the Raman spectrum of PVC," *Polymer,* vol. 19, no. 7, pp. 773-784, 1978/07/01/ 1978.

[332] M. Bowden, P. Donaldson, D. J. Gardiner, J. Birnie, and D. L. Gerrard, "Monitoring polyvinyl chloride degradation using Raman microline focus spectrometry," *Analytical Chemistry,* vol. 63, no. 24, pp. 2915-2918, 1991.

[333] K. J. Thomas, M. Sheeba, V. P. N. Nampoori, C. P. G. Vallabhan, and P. Radhakrishnan, "Raman spectra of polymethyl methacrylate optical fibres excited by a 532 nm diode pumped solid state laser," *Journal of Optics A: Pure and Applied Optics,* vol. 10, no. 5, p. 055303, 2008/03/27 2008.

[334] X. Xu, "Stimulated Raman spectrum threshold in poly (methyl methacrylate) optical fibers," *Optics communications,* vol. 199, no. 1-4, pp. 89-93, 2001.

[335] H. A. Willis, V. J. Zichy, and P. J. Hendra, "The laser-Raman and infra-red spectra of poly (methyl methacrylate)," *Polymer,* vol. 10, pp. 737-746, 1969.

[336] X. Xingsheng, M. Hai, Z. Qijing, and Z. Yunsheng, "Properties of Raman spectra and laser-induced birefringence in polymethylmethacrylate optical fibres," *Journal of Optics A: Pure and Applied Optics,* vol. 4, no. 3, p. 237, 2002.

[337] M. Mazilu, A. C. D. Luca, A. Riches, C. S. Herrington, and K. Dholakia, "Optimal algorithm for fluorescence suppression of modulated Raman spectroscopy," *Optics express,* vol. 18, no. 11, pp. 11382-11395, 2010.

[338] X. Yan *et al.*, "A Raman spectroscopy study on single-wall carbon nanotube/polystyrene nanocomposites: mechanical compression transferred from the polymer to single-wall carbon nanotubes," *The Journal of Physical Chemistry C,* vol. 116, no. 33, pp. 17897-17903, 2012.

[339] D. Shaniv, I. Dror, and B. Berkowitz, "Effects of particle size and surface chemistry on plastic nanoparticle transport in saturated natural porous media," *Chemosphere,* vol. 262, p. 127854, 2021/01/01/ 2021.

[340] L. Baissac *et al.*, "Synthesis of sub-micronic and nanometric PMMA particles via emulsion polymerization assisted by ultrasound: Process flow sheet and characterization," *Ultrasonics Sonochemistry,* vol. 40, pp. 183-192, 2018/01/01/ 2018.

[341] K. Haremaki, T. Kida, Y. Koide, T. Uneyama, Y. Masubuchi, and T. Ishida, "Effects of Stirring Time on Formation of Microplastics Fragmented from Photo-aged Polypropylene," *arXiv preprint arXiv:2503.21373,* 2025.

[342] A. Faghihnejad and H. Zeng, "Interaction Mechanism between Hydrophobic and Hydrophilic Surfaces: Using Polystyrene and Mica as a Model System," *Langmuir,* vol. 29, no. 40, pp. 12443-12451, 2013/10/08 2013.

[343] N. H. Al Hasan, "Molecular dynamic simulation of the density and mechanical properties of polyvinyl chloride (PVC)/high density polyethylene (HDPE) composites based on materials studio," in *Journal of Physics: Conference Series*, 2019, vol. 1294, no. 5: IOP Publishing, p. 052062.

[344] W. Patnode and W. Scheiber, "The density, thermal expansion, vapor pressure, and refractive index of styrene, and the density and thermal expansion of polystyrene," *Journal of the American Chemical Society,* vol. 61, no. 12, pp. 3449-3451, 1939.

[345] A. H. Kamel, A. Hefnawy, L. J. Hazeem, S. A. Rashdan, and H. S. Abd-Rabboh, "Current perspectives, challenges, and future directions in the electrochemical detection of microplastics," *RSC advances,* vol. 14, no. 3, pp. 2134-2158, 2024.

[346] S. Cunsolo, J. Williams, M. Hale, D. S. Read, and F. Couceiro, "Optimising sample preparation for FTIR-based microplastic analysis in wastewater and sludge samples: multiple digestions," *Analytical and Bioanalytical Chemistry,* vol. 413, no. 14, pp. 3789-3799, 2021.

[347] A. Azari, S. Ronsmans, J. A. J. Vanoirbeek, P. H. M. Hoet, and M. Ghosh, "Challenges in Raman spectroscopy of (micro)Plastics: The interfering role of colourants," *Environmental Pollution,* vol. 363, p. 125250, 2024/12/15/ 2024.

[348] P. Vandenabeele, *Practical Raman spectroscopy: an introduction*. John Wiley & Sons, 2013.

[349] A. Käppler *et al.*, "Analysis of environmental microplastics by vibrational microspectroscopy: FTIR, Raman or both?," *Analytical and bioanalytical chemistry,* vol. 408, pp. 8377-8391, 2016.

[350] Q. Yao and H. Tong, "Asymmetric least squares regression estimation: a nonparametric approach," *Journal of nonparametric statistics,* vol. 6, no. 2-3, pp. 273-292, 1996.

[351] Z.-y. Dong and J.-l. Xu, "Baseline estimation using optimized asymmetric least squares (O-ALS)," *Measurement,* vol. 233, p. 114731, 2024.

[352] D. Mukherjee, L. Miao, G. Stone, and N. Alem, "mpfit: a robust method for fitting atomic resolution images with multiple Gaussian peaks," *Advanced Structural and Chemical Imaging,* vol. 6, no. 1, p. 1, 2020/01/27 2020.

[353] R. C. Eanes and R. K. Marcus, "Peakfitter—an integrated Excel-based Visual Basic program for processing multiple skewed and shifting Gaussian-like spectral peaks simultaneously: application to radio frequency glow discharge ion trap mass spectrometry," *Spectrochimica Acta Part B: Atomic Spectroscopy,* vol. 55, no. 4, pp. 403-428, 2000.

[354] M. Pucher, U. Wünsch, G. Weigelhofer, K. Murphy, T. Hein, and D. Graeber, "staRdom: versatile software for analyzing spectroscopic data of dissolved organic matter in R," *Water,* vol. 11, no. 11, p. 2366, 2019.

[355] M. Pucher, D. Graeber, and G. Weigelhofer, "Spectroscopic data analysis of dissolved organic matter in R-staRdom," in *EGU General Assembly Conference Abstracts*, 2018, p. 19642.

[356] B. E. Ifon *et al.*, "Effects of bisphenols and perfluoroalkylated substances on fluorescence properties of humic and amino acids substances of dissolved organic matter: EEM-PARAFAC and ATR-FTIR analysis," *Journal of Environmental Chemical Engineering,* vol. 10, no. 4, p. 108186, 2022.

[357] T. Li, C. Zhou, and M. Jiang, "UV absorption spectra of polystyrene," *Polymer Bulletin,* vol. 25, pp. 211-216, 1991.

[358] M. M. Radhi, A. J. Haider, Z. N. Jameel, T. W. Tee, M. Z. B. Ab Rahman, and A. B. Kassim, "Synthesis and characterization of grafted acrylonitrile on polystyrene modified with carbon nanotubes using gamma-irradiation," *Research Journal of Chemical Sciences,* vol. 2231, p. 606X, 2012.

[359] S. Tagawa, N. Nakashima, and K. Yoshihara, "Absorption spectrum of the triplet state and the dynamics of intramolecular motion of polystyrene," *Macromolecules,* vol. 17, no. 6, pp. 1167-1169, 1984.

[360] N. Nakashima and M. Sumitani, "1. Ohmine and K. Yoshihara," *J. Chem. Phys,* vol. 72, p. 2226, 1980.

[361] B. Randy and J. Rabek, "Photodegradation, Photo-oxidation, and Photostabilization of Polymers," *Ed. Wiley interscience publication,* 1975.

[362] N. Grassie and G. Scott, *Polymer degradation and stabilisation*. CUP Archive, 1988.

[363] J. Lucki, J. Rabek, B. Rånby, and Y. Jiang, "Spectral differences in photodegraded polystyrene in various solvents," *Polymer,* vol. 27, no. 8, pp. 1193-1200, 1986.

[364] R. Astier and Y. Meyer, "First allowed triplet-triplet transition in benzene," *Chemical Physics Letters,* vol. 3, no. 6, pp. 399-401, 1969.

[365] R. Lettieri *et al.*, "Control of Nanoparticle Size of Intrinsically Fluorescent PET (Polyethylene Terephthalate) Particles Produced Through Nanoprecipitation," *Molecules,* vol. 30, no. 2, p. 282, 2025.

[366] P. Schmidt, "Polyethylene terephthalate structural studies," *Journal of Polymer Science Part A: General Papers,* vol. 1, no. 4, pp. 1271-1292, 1963.

[367] I. Ouchi, I. Nakai, M. Ono, and S.-i. Kimura, "Features of fluorescence spectra of polyethylene terephthalate films," *Japanese journal of applied physics,* vol. 43, no. 12R, p. 8107, 2004.

[368] I. Ouchi, "Anisotropic absorption and reflection spectra of poly (ethylene terephthalate) films in ultraviolet region," *Polymer Journal,* vol. 15, no. 3, pp. 225-243, 1983.

[369] I. Christensen, "Developments in colorants for plastics," 2003.

[370] N. S. Allen, "A study of the light absorption properties of polymer films using UV-visible derivative spectroscopy," *Polymer Photochemistry,* vol. 1, no. 1, pp. 43-55, 1981.

[371] A. Charlesby and R. Partridge, "The identification of luminescence centres in polyethylene and other polymers," *Proceedings of the Royal Society of London. Series A. Mathematical and Physical Sciences,* vol. 283, no. 1394, pp. 312-328, 1965.

[372] N. Allen, J. Homer, and J. McKellar, "Luminescence from thermally oxidized polypropylene in relation to its light stability," *Journal of Applied Polymer Science,* vol. 20, no. 9, pp. 2553-2556, 1976.

[373] N. Allen, J. McKellar, G. Phillips, and D. Wood, "Effect of photochemical oxidation on polypropylene phosphorescence," *Journal of Polymer Science: Polymer Chemistry Edition,* vol. 12, no. 11, pp. 2647-2650, 1974.

[374] A. Kuo, "Fluorescence resulting from π-stacking in polystyrene solutions," *CheM,* vol. 1, no. 1, pp. 80-86, 2011.

[375] R. M. Masegosa, I. Hernández-Fuentes, I. F. de Piérola, and A. Horta, "Polystyrene fluorescence in cosolvent mixtures," *Polymer,* vol. 28, no. 2, pp. 231-235, 1987/02/01/ 1987.

[376] I. Teraoka and P. Solutions, "An introduction to physical properties," *Polymer Solutions,* 2002.

[377] A. Sánchez-Ruiz, A. Sousa-Herves, J. Tolosa, A. Navarro, and J. C. García-Martínez, "Aggregation-induced emission properties in fully π-conjugated polymers, dendrimers, and oligomers," *Polymers,* vol. 13, no. 2, p. 213, 2021.

[378] F. Lionetto *et al.*, "Autofluorescence of model polyethylene terephthalate nanoplastics for cell interaction studies," *Nanomaterials,* vol. 12, no. 9, p. 1560, 2022.

[379] N. Allen, J. Homer, and J. McKellar, "The use of luminescence spectroscopy in aiding the identification of commercial polymers," *Analyst,* vol. 101, no. 1201, pp. 260-264, 1976.

[380] M. Hennecke, K. Kurz, and J. Fuhrmann, "Orientation of hot-drawn poly (butylene terephthalate) films as determined from the intrinsic polarized fluorescence," *Macromolecules,* vol. 25, no. 23, pp. 6190-6194, 1992.

[381] T. Corrales, C. Peinado, P. Bosch, and F. Catalina, "Study of secondary relaxations of poly (ethylene terephthalate) by photoluminescence technique," *Polymer,* vol. 45, no. 5, pp. 1545-1554, 2004.

[382] M. Auer, J. Schmidt, and J. Woidasky, "Effects of Fluorescent Tracer Additives on PET During Material Recycling," *Journal of Applied Polymer Science,* vol. 142, no. 10, p. e56574, 2025.

[383] S. Doose, H. Neuweiler, and M. Sauer, "Fluorescence quenching by photoinduced electron transfer: a reporter for conformational dynamics of macromolecules," *ChemPhysChem,* vol. 10, no. 9-10, pp. 1389-1398, 2009.

[384] X. Zhai, R. Chen, and W. Shen, "Aggregation-induced emission active luminescent polymeric nanofibers: From design, synthesis, fluorescent mechanism to applications," *TrAC Trends in Analytical Chemistry,* vol. 146, p. 116502, 2022/01/01/ 2022.

[385] M. M. Caruso *et al.*, "Mechanically-Induced Chemical Changes in Polymeric Materials," *Chemical Reviews,* vol. 109, no. 11, pp. 5755-5798, 2009/11/11 2009.

[386] N. Maslov and V. Dulin, "Investigation of fluorescence spectra of various types of plastics for the purpose of sorting and further processing," in *Journal of Physics: Conference Series*, 2020, vol. 1677, no. 1: IOP Publishing, p. 012186.

[387] D. J. Lacey and V. Dudler, "Chemiluminescence from polypropylene. Part 2: The emission wavelengths during prolonged oxidation," *Polymer Degradation and Stability,* vol. 51, no. 2, pp. 109-113, 1996/02/01/ 1996.

[388] Kimmon. "He-Cd (IK3252R-E) Wavelength : 325nm Power : 30mW - Lasers Specifications." https://www.kimmon.com/english/products/hecd.html (accessed.

[389] L. Aps. "The miniRaman 785 nm handheld spectrometer achieved an SNR of 1256:1 when measuring a polystyrene reference sample under optimized conditions." Lightnovo. https://lightnovo.com/technical-notes/miniraman-785-nm-spectrometer-signal-to-noise-ratio-determinationnew/ (accessed 10 September 2025.

[390] Laboao. "LATR2500 portable Raman spectrometer achieves an SNR >1300:1 at 918 cm^{-1} , measured using acetonitrile, 4 s integration time, 130 mW laser power. ." Laboao. https://www.laboao.com/products/raman-spectrometer/portable-mini-raman-spectrometer?utm_source=chatgpt.com (accessed 10 September 2025.

Appendices

Appendix A: UV-Vis Absorption Spectroscopy Analysis of Ultrasonicated Micro- and Nanoplastic (US-MNP) Samples

This appendix presents the UV-Vis absorption spectroscopy analysis of ultrasonicated micro- and nanoplastics (US-MNPs) obtained from three different polymer types: polystyrene (PS), polyethylene terephthalate (PET), and polypropylene (PP). Each sample was fractionated into four distinct size ranges: Range 1: MPs > 1.2 µm, Range 2: 1.2 µm > MNPs > 400 nm, Range 3: 400 nm > NPs > 100 nm, Range 4: NPs < 100 nm.

The absorption spectra of all sonicated plastics and their different size ranges are presented in the following sections.

A.1 Absoprtion Spectroscopic Analysis of USMNP-PS

Figure A.1.1 presents the absorbance spectra of US-MNPs classified into four distinct size ranges (Range 1 to 4), measured across a wavelength range of 200 nm to 1200 nm. The absorbance is plotted against the wavelength (in nm) to analyse the optical properties of the samples.

The UV-Vis absorption spectra of ultrasonicated PS samples show that distinct prominent absorption peaks (260nm and region 320-375nm) are observed only for the MPs (>1.2 µm) fraction, while the smaller-sized fractions (Range 2-4) show no significant absorption. This absence of absorption features in smaller fractions might be due to their smaller particle size and lower concentration in aqueous media.

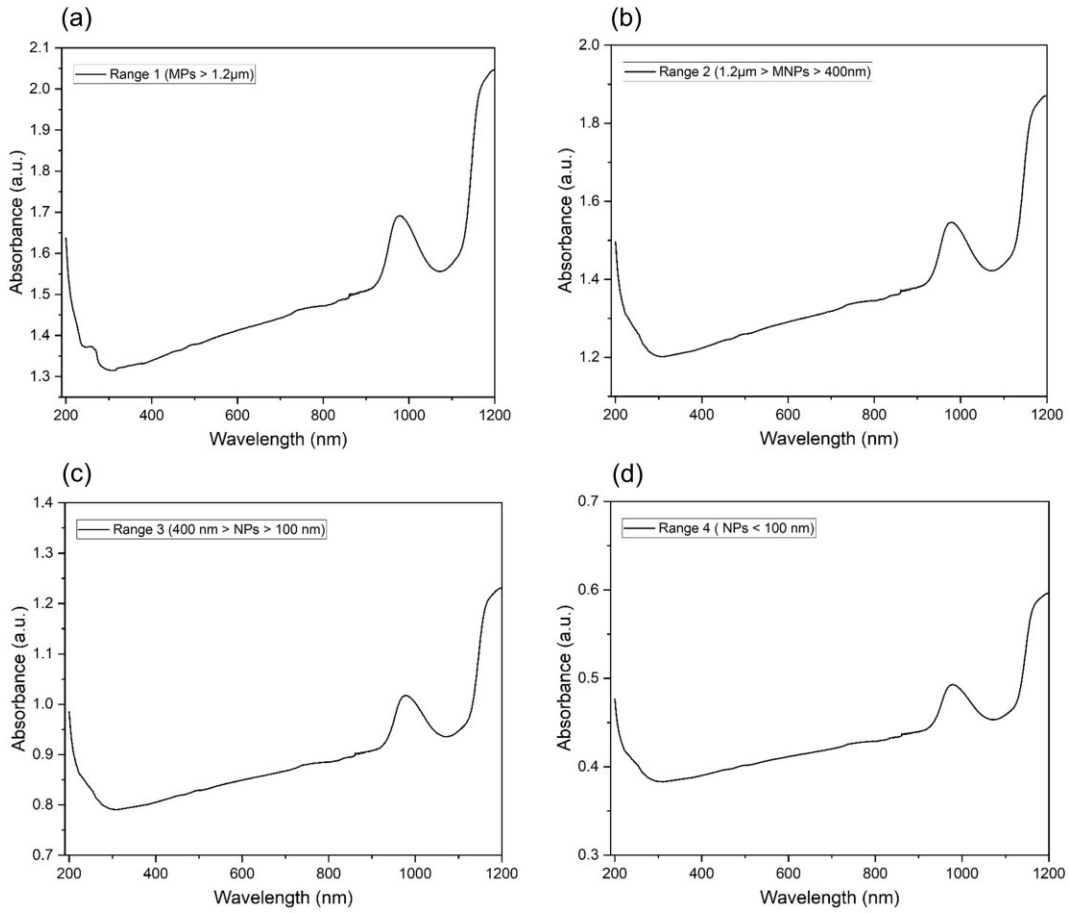

Figure A.1.1. UV-Vis Absorbance spectra of USMNPs-PS in different size ranges. (a) Range 1: MPs larger than 1.2 μm, (b) Range 2: MNPs between 1.2 μm and 400 nm, (c) Range 3: NPs between 400 nm and 100 nm, and (d) Range 4: NPs smaller than 100 nm.

A.2 Absoprtion Spectroscopic Analysis of USMNP-PET

Figure A.2.1 illustrates the absorbance spectra of USMNPs-PET, categorised into four size ranges (Range 1 to 4), measured over a wavelength range of 200 nm to 1200 nm. The absorbance is plotted against the wavelength (in nm) to evaluate the optical characteristics of the PET-based samples.

The UV-Vis absorption spectra of USMNPs-PET reveal that distinct absorption peaks appear exclusively in the MPs fraction (>1.2 μm), specifically at 245nm, 259nm, and 303nm. In contrast, the smaller-sized fractions (Range 2-4) do not exhibit any significant absorption peaks, particularly in the 200-350 nm range. This absence of clear absorption features for the smaller particles may

be attributed to their reduced particle size and lower concentration in solution, which minimises light absorption within this spectral region.

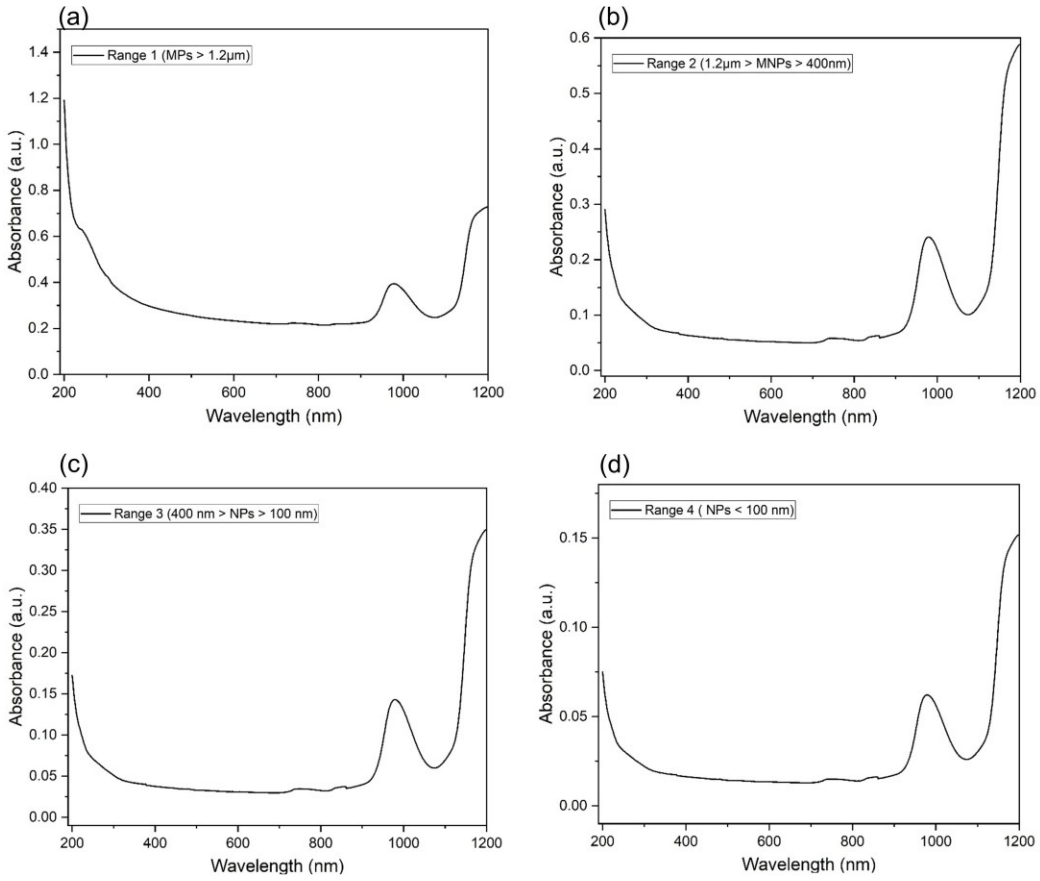

Figure A.2.1 : UV-Vis Absorbance spectra of USMNPs-PET in different size ranges. (a) Range 1: MPs larger than 1.2 μm, (b) Range 2: MNPs between 1.2 μm and 400 nm, (c) Range 3: NPs between 400 nm and 100 nm, and (d) Range 4: NPs smaller than 100 nm.

A.3 Absoprtion Spectroscopic Analysis of USMNP-PP

The absorbance spectra of USMNPs-PP are shown in Figure A.3.1, where the particles are further classified into four size fractions (Range 1 to 4) and measured over a wavelength range of 200 nm to 1200 nm.

Similar to USMNPs-PS and USMNPs-PET, the absorption spectra of USMNPs-PP indicate that only the MPs fraction (>1.2 μm) exhibits distinct absorption peaks, primarily at 221 nm, 270 nm, and within the 285-335 nm range. In contrast, the smaller-sized fractions (Range 2-4) show no significant absorption peaks within these spectral regions. This absence of absorption features

for smaller PP particles is likely attributed to the same factors observed for USMNPs-PS and USMNPs-PET, namely their smaller particle size and lower sample concentration in solution.

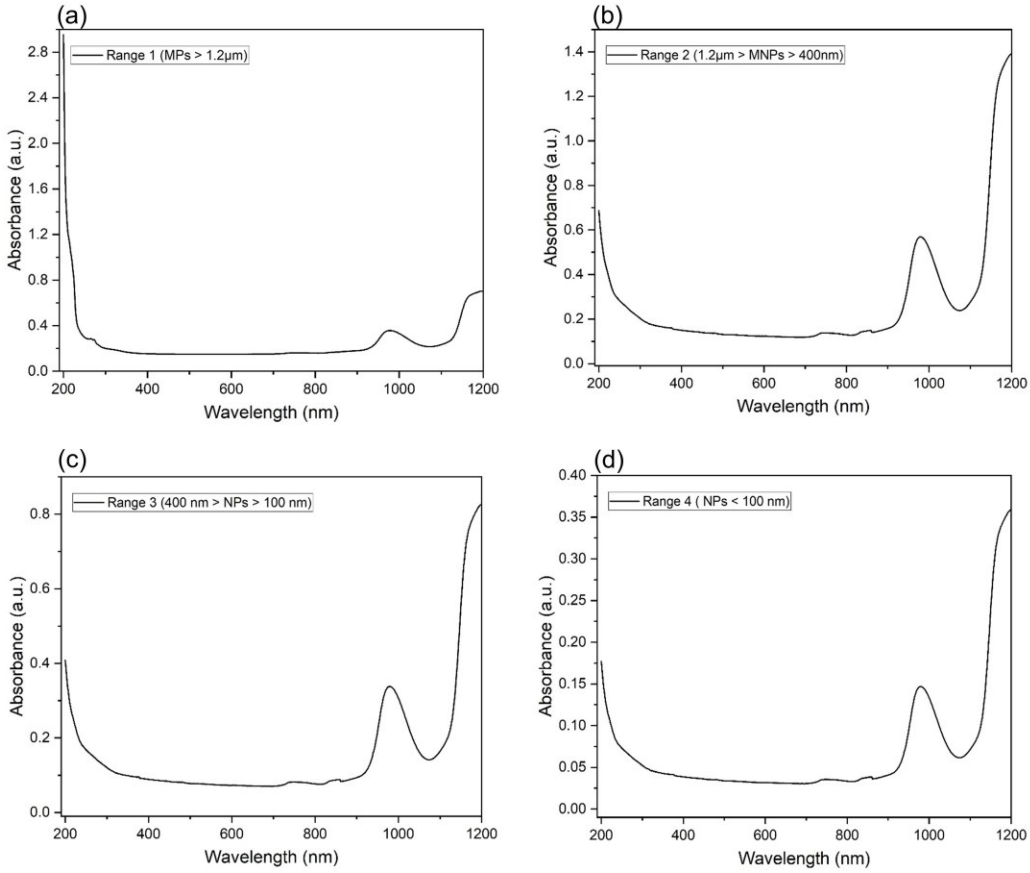

Figure A.3.1: UV-Vis Absorbance spectra of USMNPs-PP of different size ranges. (a) Range 1: MPs larger than 1.2 μm, (b) Range 2: MNPs between 1.2 μm and 400 nm, (c) Range 3: NPs between 400 nm and 100 nm, and (d) Range 4: NPs smaller than 100 nm.

Appendix B: FLE mapping analysis of Ultrasonicated Micro- and Nanoplastic Samples

The FLE mapping analysis was performed for USMNPs-PS, PET, and PP across four distinct size fractions (R1 to R4) over an excitation wavelength range of 300–500 nm and an emission wavelength range of 315–600 nm. The recorded fluorescence responses offer insights into the FL properties of the selected polymers and their behaviour at varying particle sizes.

The following sections present the FLE maps for USMNPs-PS (B.1), PET (B.2), and PP (B.3), highlighting the fluorescence emission zones, intensity variations, and potential factors influencing the observed spectral differences across four different size ranges.

B.1 FLE Mapping Analysis of USMNP-PS

The fluorescence excitation-emission (FLE) maps of ultrasonicated micro- and nanoplastics polystyrene (USMNPs-PS) are presented in Figure B.1.1, and classified into four distinct size fractions: (a) Range 1: MPs larger than 1.2 µm, (b) Range 2: MNPs between 1.2 µm and 400 nm, (c) Range 3: NPs between 400 nm and 100 nm, and (d) Range 4: NPs smaller than 100 nm. These FLE maps illustrate the fluorescence response of PS particles under different excitation and emission wavelengths, measured over an excitation wavelength range of 300-500 nm and an emission wavelength range of 315-600 nm, providing insights into their intrinsic fluorescence properties.

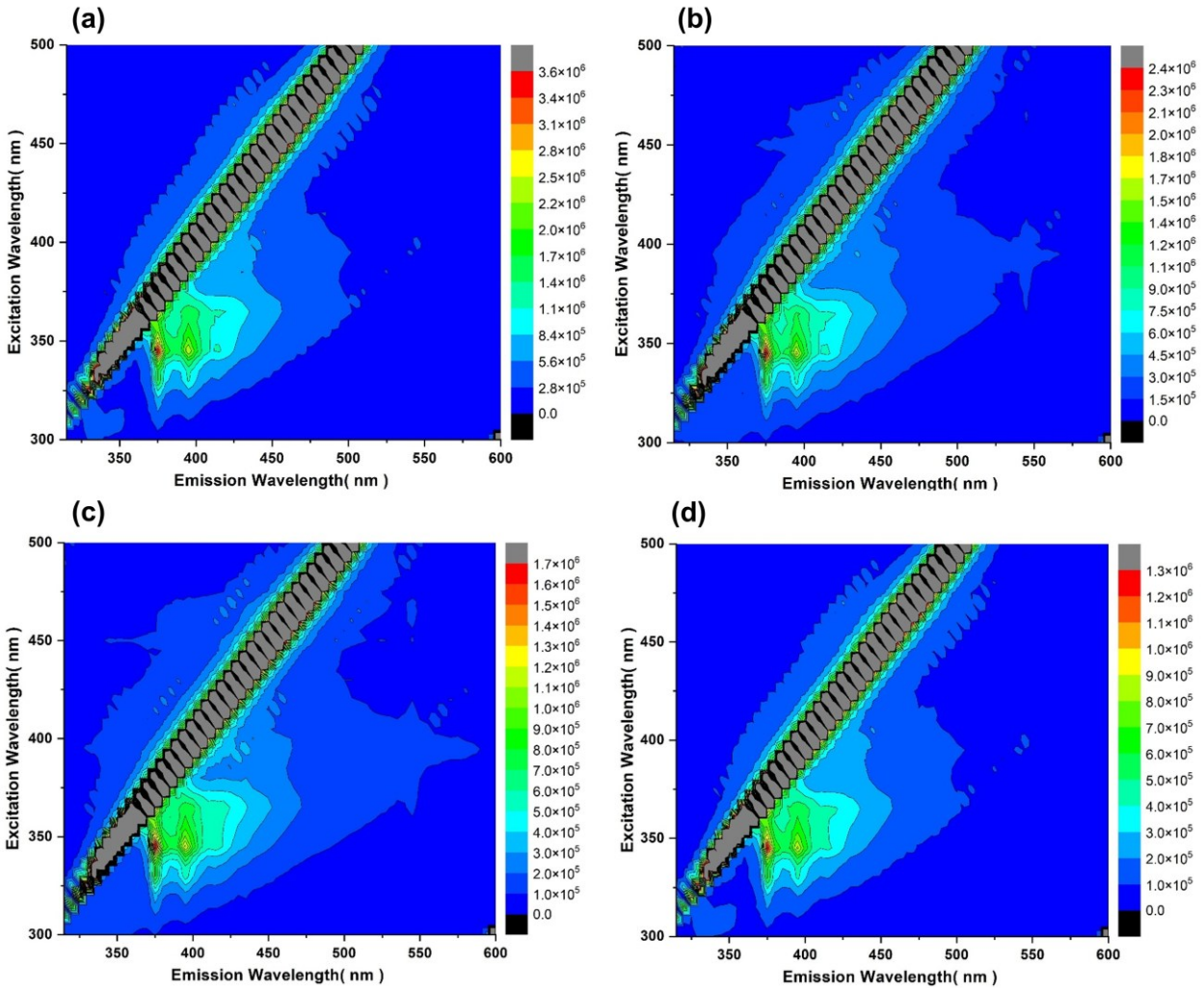

Figure B.1.1: FLE maps of USMNPs-PS of different size ranges. (a) Range 1: MPs larger than 1.2 µm, (b) Range 2: MNPs between 1.2 µm and 400 nm, (c) Range 3: NPs between 400 nm and 100 nm, and (d) Range 4: NPs smaller than 100 nm.

The FLE maps of all four size fractions exhibit similar excitation-emission regions (the strongest FL emission is observed at λ_{ex} 345nm), indicating that the fluorescence characteristics of PS particles remain consistent across different size ranges. However, there is a clear variation in fluorescence intensity, with the largest MPs fraction (Range 1: MPs >1.2 µm) exhibiting the strongest fluorescence signal. As the particle size decreases (Range 2 to 4), the fluorescence intensity decreases, which could be attributed to reduced molecular aggregation, lower sonicated particles concentration per unit volume, or increased scattering effects in smaller particles.

Despite the reduction in intensity, all four size fractions retain distinct fluorescence signals, making FLE mapping a valuable tool for detecting and characterising MNPs in aqueous media. The unique fluorescence fingerprints of PS particles enable their identification, even at the nanoscale, highlighting the potential of this technique in environmental monitoring, contamination assessment, and MNP research.

B.2 FLE Mapping Analysis of USMNP-PET

The FLE maps of USMNPs-PET are shown in Figure B.2.1. These maps are categorised into four size fractions: (a) Range 1: MPs larger than 1.2 µm, (b) Range 2: MNPs between 1.2 µm and 400 nm, (c) Range 3: NPs between 400 nm and 100 nm, and (d) Range 4: NPs smaller than 100 nm. The excitation wavelengths span 300-500 nm, while the emission wavelengths range from 315-600 nm. These maps capture the characteristic fluorescence response of PET particles, which remains consistent across all size fractions in terms of excitation-emission regions. However, similar to USMNPs-PS, significant differences in fluorescence intensity are observed.

Unlike USMNPs-PS, the overall fluorescence intensity of PET particles is substantially lower, showing an approximate 95.3% reduction compared to PS. This decline suggests weaker intrinsic fluorescence properties in PET, likely due to differences in polymer structure and chemical composition. All samples showed strong intrinsic FL emissions at λ_{ex} 380nm. The strongest fluorescence signal is still observed for Range 1 (MPs >1.2 µm), while smaller-sized fractions (Range 2-4) exhibit less FL intensity. As the particle size decreases, the fluorescence weakens further, which may be attributed to reduced molecular interactions and lower particle concentration per unit volume.

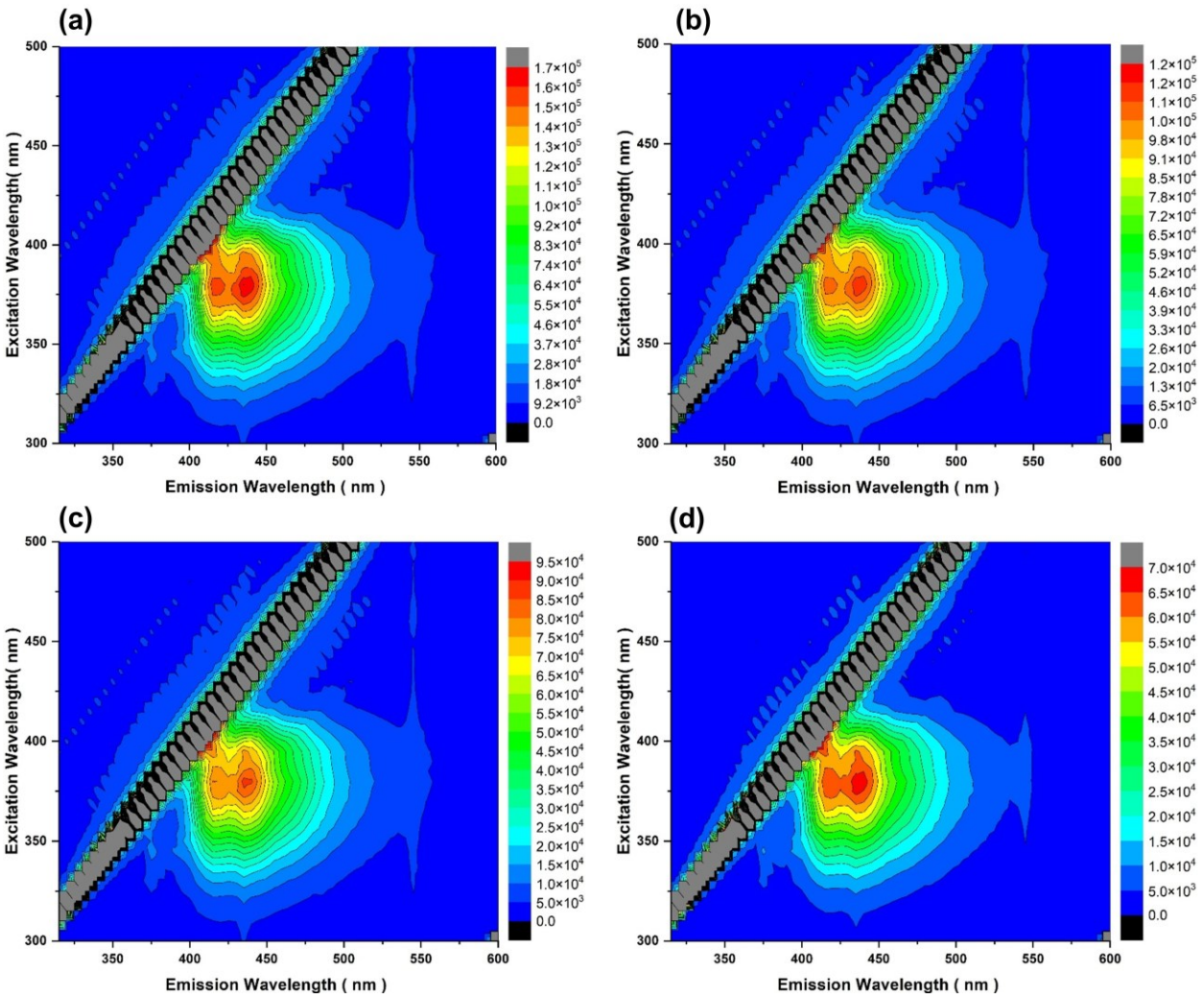

Figure B.2.1: FLE maps of USMNPs-PET of different size ranges. (a) Range 1: MPs larger than 1.2 µm, (b) Range 2: MNPs between 1.2 µm and 400 nm, (c) Range 3: NPs between 400 nm and 100 nm, and (d) Range 4: NPs smaller than 100 nm.

Despite its lower fluorescence intensity, PET retains detectable fluorescence signals across all size ranges. This indicates that FLE mapping remains a useful technique for identifying and tracking MNPs in aqueous environments.

B.3 FLE Mapping Analysis of USMNP-PP

Figure B.3.1 presents the FLE maps of USMNPs-PP, categorised into four different size fractions: (a) Range 1: MPs larger than 1.2 µm, (b) Range 2: MNPs between 1.2 µm and 400 nm, (c) Range 3: NPs between 400 nm and 100 nm, and (d) Range 4: NPs smaller than 100 nm. These maps

illustrate the fluorescence response of PP particles across an excitation wavelength range of 300–500 nm and an emission wavelength range of 315–600 nm, providing insights into their FL spectral characteristics.

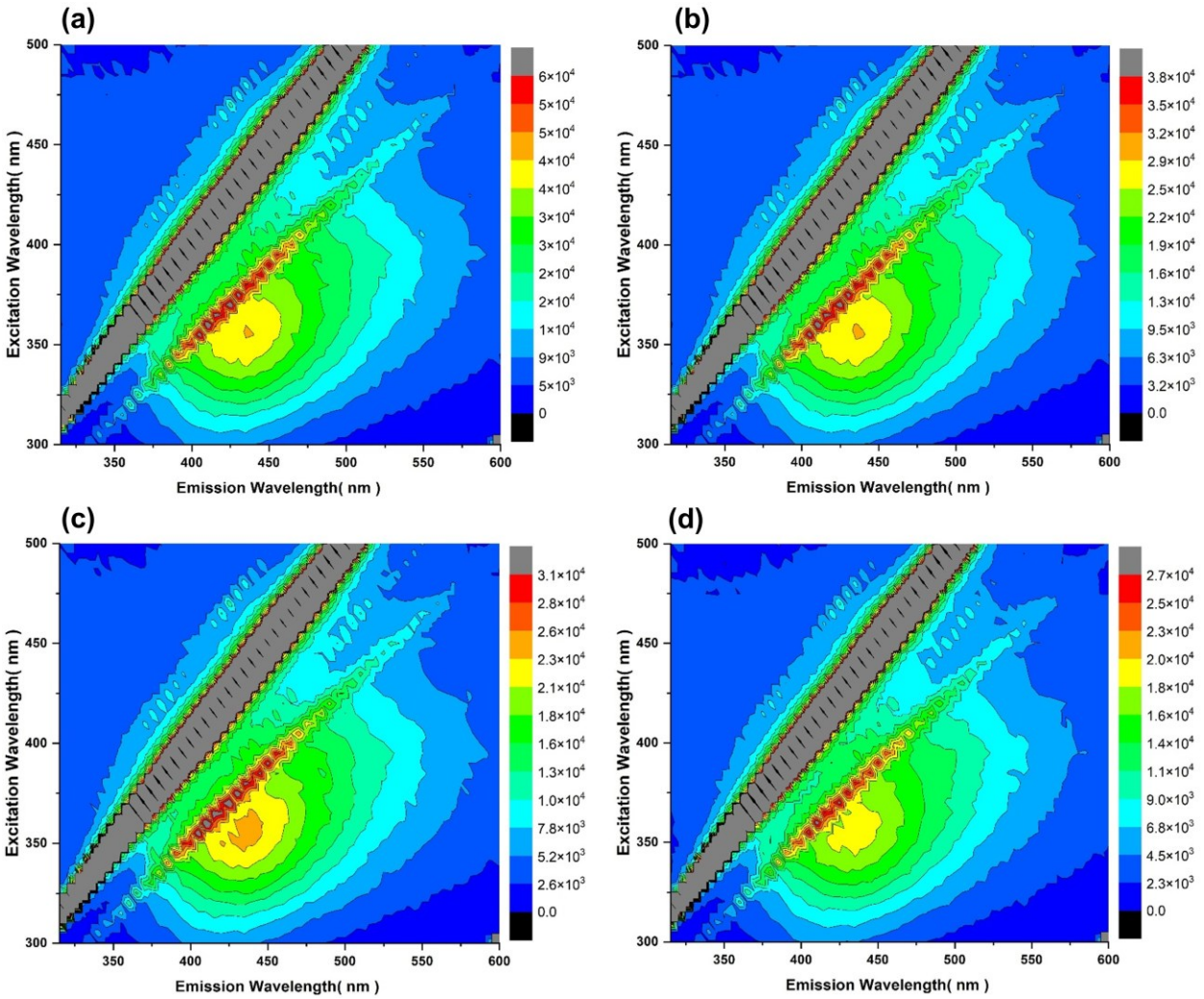

Figure B.3.1: FLE maps of USMNPs-PP of different size ranges. (a) Range 1: MPs larger than 1.2 µm, (b) Range 2: MNPs between 1.2 µm and 400 nm, (c) Range 3: NPs between 400 nm and 100 nm, and (d) Range 4: NPs smaller than 100 nm.

The FLE maps of USMNPs-PP exhibit a strong excitation-emission spectral region with the strongest fluorescence observed around an excitation wavelength of 355 nm. However, in comparison to USMNPs-PS, the fluorescence intensity of USPP is significantly lower, showing a reduction of approximately 98.3%, which is even weaker than USPET. This reduced fluorescence intensity could be attributed to the intrinsic molecular structure of PP, which lacks aromatic rings,

resulting in a lower fluorescence quantum yield. Moreover, the difference in polymer crystallinity and degree of oxidation could also play a role in its weaker fluorescence response (see the section 4.3.2).

In addition to the fluorescence signals, USMNPs-PP exhibits strong Rayleigh and Raman scattering signals, which are observed as diagonal streaks in the excitation-emission maps. The Rayleigh scattering, also observed in USPS and USPET, arises from the elastic scattering of light due to larger microplastic particles and their dispersed nature in aqueous media. The Raman scattering signals are likely due to the vibrational modes of C-H and C-C bonds in PP [282]. These scattering effects make it more challenging to differentiate the pure fluorescence signals of PP compared to PS and PET, which can be removed using the scattering removal technique (see section 4.2.4).

Appendix C: Standard PL measurement protocol for microplastic detection in water using SPPL spectrometer

C.1 PL Measurement Protocol

This section presents the standard PL measurement protocol for detecting microscale plastic particles using the SPPL spectrometer:

1. The first and foremost thing is to select the appropriate light source. Based on EEM mapping data for PS and PET (see Section 2.4.3), a laser source with any wavelength ranging from 325 nm to 370 nm is suitable for exciting and collecting a strong intrinsic fluorescence emission signal. A 325nm UV laser with 30mW output power was utilised, which provided a measurable fluorescence signal for PS and PET. To ensure accurate measurements, the He-Cd laser must be kept in the ON state for two hours to stabilise its output.

2. The spot diameter of the laser beam should be ≈ 1 mm.

3. To get strong fluorescence emission, the number of optical components used should be reduced to avoid incident beam power loss.

4. For precise alignment of the setup, a bidirectional stage with controlled y-axis and z-axis movements should be used.

5. The beam receiving end of the cuvette holder should have enough opening orifice to allow the laser beam to enter and interact with the sample. The incident laser beam can be guided to the sample via optical fibres, but the losses will be maximised in this case.

6. The cuvette head should always be closed with a holder cover to prevent noise in the output signal due to stray light interference.

7. Quartz glass cuvettes should always be used to avoid noise signals in the fluorescence spectra.

8. Fluorescence emission from the sample (microplastic) should be collected at 90 degrees to the incident laser beam.

9. The lid of the cuvette holder, which is placed at the backend of the sample and in line with the incident beam, should always be closed.

10. The SMA-to-SM1 fibre adapter should be tightly fixed to prevent the leakage of fluorescence emissions from the sample.

11. Microplastic samples (solid or in deionised water) should be filled up to 75% of the cuvette volume.

12. It is imperative to handle the sample cuvettes with gloves on. Touching them with bare hands may result in an inaccurate output fluorescence signal.

13. The measurements should be recorded in a darkroom environment in order to prevent room light interaction or interference with the sample.

14. All connections between electronic components and devices should be correct and proper.

15. Considering the laser safety protocols, goggles should always be worn when the UV source is active or the shutter is open.

16. Before measurements, the room light should be switched off, and the room temperature should be ambient. By opening the shutter with the toggle switch, the laser beam passes through the optical components and reaches the microplastic sample. Following the interaction between light and microplastics, the resulting fluorescence signal is captured by the compact USB spectrometer (THORLAB).

17. The fluorescence signal should be recorded using the averaging function in the software of the THORLAB spectrometer.

18. The spectral data should be saved as a text file, which can then be utilised for post-processing with software like Origin or any other data processing tool.

C.2 Semi-Portable PL (SPPL) spectrometer Design

SPPL Spectrometer: The schematic diagram illustrated below (Figure C.2.1) presents the semi-portable photoluminescence (PL) spectrometer for microplastic (MP) detection. The setup consists of three primary components: (i) UV Excitation Source, (ii) Sample Holder, and (iii) USB Spectrometer. The system employs a continuous-wave Helium-Cadmium (He-Cd) UV laser, operating within the 315–360 nm wavelength range, with a peak emission at 325 nm and a power output of 30 mW. This laser serves as the excitation source for microplastic (MP) fluorescence. The laser beam is guided towards the sample using a series of mirrors and a reflector (including two mirrors placed at 45 degrees and one kinematic mount), ensuring precise alignment along the optical path. The sample holder, which accommodates a cuvette containing the MP sample, is positioned on a bi-directional stage for fine-tuned alignment. The system is designed so that the incident laser beam and the emitted fluorescence signal are perpendicular to each other. This orthogonal configuration helps to minimise interference from the excitation source in the recorded fluorescence spectrum. The fluorescence emitted by the excited microplastic sample is collected using a step-index multimode optical fibre, which transmits the signal to the Thorlabs USB spectrometer for spectral analysis. The spectrometer captures and processes the fluorescence data, recording and analysing measurements using Thorlabs spectrometer software.

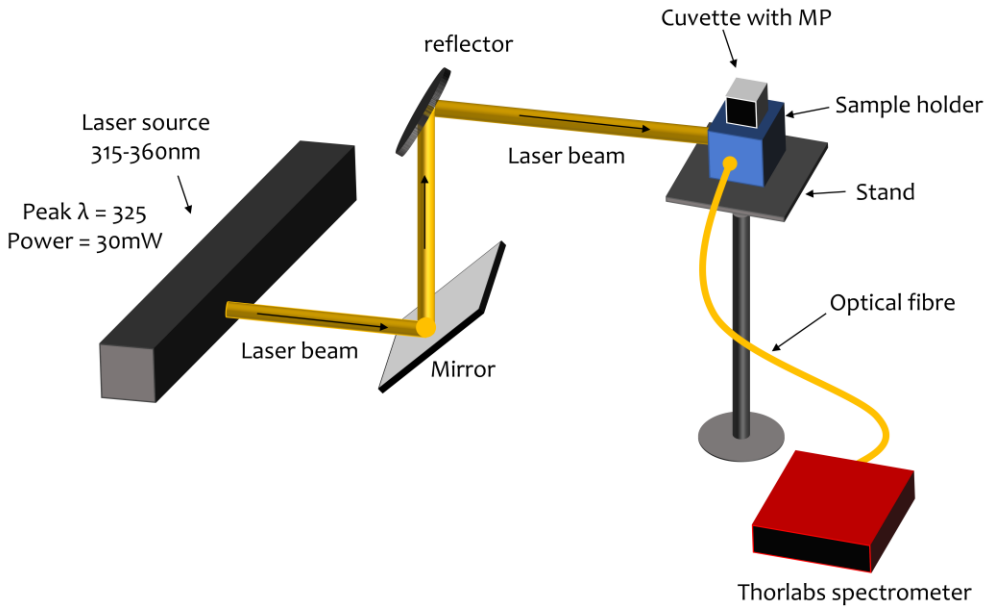

Figure C.2.1: Schematic diagram of the semi-portable PL spectrometer for microplastic (MP) detection. A high-power Helium-Cadmium (He-Cd) laser, operating at λ = 325 nm with a maximum power output of 30 mW, serves as the excitation source. The laser beam is directed through a series of optical components before reaching the sample. The PL emissions from the sample are collected by a USB spectrometer, and the resulting spectral fingerprints are displayed on a computer screen using Thorlabs software.

C.3 Conceptual Fully Portable PL (FPPL) spectrometer Design

Figure C.3.1 illustrates the conceptual design of a fully portable photoluminescence (PL) spectrometer developed for microplastic detection in aqueous media. By “portable,” we refer to a compact, lightweight device that integrates all essential components, including excitation sources, a sample holder, a spectrometer, and a display, into a single enclosure, eliminating the need for external benchtop equipment. The system design is based on a microcontroller unit driving a gear shaft connected to a mechanical turret, which houses multiple laser diodes at different excitation wavelengths. By rotating the turret, the user can sequentially select the desired excitation source for targeted fluorescence analysis. The microplastic (MNP) suspension is placed in a cuvette secured within a sample holder, aligned with the excitation beam path. The emitted fluorescence is then collected and transmitted to a USB-based Czerny–Turner spectrometer for spectral

acquisition. The results are displayed in real time on an integrated LCD screen, ensuring immediate interpretation in the field. Currently, the work demonstrates the feasibility of integrating discrete components into a compact housing. However, further miniaturisation, such as replacing the turret with electronically tunable diode lasers, utilising chip-based spectrometers, and incorporating battery power, would enhance true handheld portability. Robustness for field deployment could be improved by adopting shock-resistant mounting, waterproof housing, and automated calibration functions. The compact and modular design already reduces reliance on bulky instrumentation, marking a significant step towards practical, field-ready PL spectroscopy for environmental microplastic monitoring.

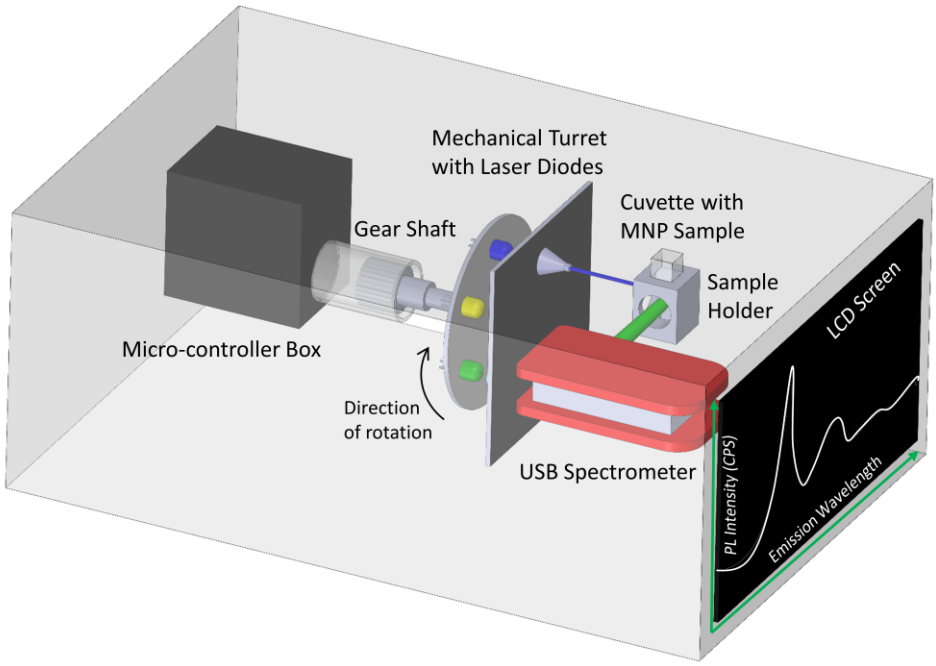

Figure C.3.1: Conceptual design of a fully portable photoluminescence (PL) spectrometer for microplastic detection. The system consists of a microcontroller box driving a gear shaft connected to a mechanical turret with multiple laser diodes for excitation. The cuvette containing the MNP sample is held in a sample holder, with fluorescence collected and transmitted to a USB spectrometer. Processed spectra are displayed in real time on an integrated LCD screen.